Laser damage resistance of coating materials and structures for grating-waveguides

Marek Stehlik

École Doctorale:	ED 352 Physique et Sciences de la Matière
Unité de recherche:	Institut Fresnel
Discipline:	Optique, Photonique et Traitment d'Image

THÈSE DE DOCTORAT
pour obtenir le grade de
DOCTEUR de l'ÉCOLE CENTRALE de MARSEILLE

Etude de la tenue au flux laser de matériaux et structures couches minces pour la réalisation d'optiques diffractives de type GWS (Grating Waveguide Structure)

Marek STEHLÍK

Supervisé par: Laurent Gallais and Frank R. Wagner

Soutenue le 26 Octobre 2022 devant le jury composé de:

LAMAIGNÈRE Laurent	Directeur de Recherche, CEA - Bordeaux	Rapporteur
MELNINKAITIS Andrius	Associate Professor, Vilnius University	Rapporteur
JULLIEN Aurélie	Directrice de Recherche, INPHYNI - Nice	Examinateur
KRAMER Daniel	Senior Scientist, ELI Beamlines - Prague	Examinateur
ABDOU AHMED Marwan	Directeur de Recherche, IFSW - Stuttgart	Invité
GALLAIS Laurent	Professeur, Institut Fresnel - Marseille	Directeur de thèse
WAGNER Frank Rüdiger	Maitre de Conférence, Institut Fresnel - Marseille	Co-directeur de thèse

Affidavit

Je soussigné, Marek Stehlík, déclare par la présente que le travail présenté dans ce manuscrit est mon propre travail, réalisé sous la direction scientifique de Laurent Gallais et Frank R. Wagner, dans le respect des principes d'honnêteté, d'intégrité et de responsabilité inhérents à la mission de recherche. Les travaux de recherche et la rédaction de ce manuscrit ont été réalisés dans le respect à la fois de la charte nationale de déontologie des métiers de la recherche et de la charte d'Ecole Centrale Marseille relative à la lutte contre le plagiat.

Ce travail n'a pas été précédemment soumis en France ou à l'étranger dans une version identique ou similaire à un organisme examinateur.

Fait à Marseille le 18 juillet 2022

I, undersigned, Marek Stehlík, hereby declare that the work presented in this manuscript is my own work, carried out under the scientific direction of Laurent Gallais and Frank R. Wagner, in accordance with the principles of honesty, integrity and responsibility inherent to the research mission. The research work and the writing of this manuscript have been carried out in compliance with both the French national charter for Research Integrity and the Ecole Centrale Marseille charter on the fight against plagiarism.

This work has not been submitted previously either in France or in another country in the same or in a similar version to any other examination body.

Marseille the 18th of July, 2022

Liste de publications et participation aux conférences

Liste des publications réalisées dans le cadre du projet de thèse:

1. M. Stehlik, G. Govindassamy, J. Zideluns, F. Lemarchand, F. Wagner, J. Lumeau, J. Mackenzie and L. Gallais: "Sub-picosecond 1030 nm laser-induced damage threshold evaluation of pulsed-laser deposited sesquioxide thin films", *Optical Engineering*, vol. 61(7), p. 070903, 2022. DOI: 10.1117/1.OE.61.7.070903
2. M. Stehlík, F. Wagner, J. Zideluns, F. Lemarchand, J. Lumeau and L. Gallais: "Beam-size effects on the measurement of sub-picosecond intrinsic laser induced damage threshold of dielectric oxide coatings", *Applied Optics*, vol. 60, No. 27/20, 2021. DOI: 10.1364/AO.433935

Participation aux conférences et écoles d'été au cours de la période de thèse:

1. Conference on Lasers and Electro-Optics Europe and European Quantum Electronics Conference (CLEO®/Europe-EQEC, 2021), conference; oral presentation on "Sub-ps laser damage resistance of optical coatings for reflective components", Munich, Germany (2021).
2. Laser-induced Damage in Optical Materials (SPIE Laser Damage, 2021), conference; oral presentation on "Investigation on beam-size effect on sub-picosecond LIDT of dielectric oxide coatings." Online only (2021).
3. Laser-induced Damage in Optical Materials (SPIE Laser Damage, 2021), conference; poster on "Laser-induced contamination on dielectric coatings in sub-ps MHz regime at 515 nm." Online only (2021).
4. Optical Interference Coatings (OIC, 2022), conference; poster on "Sub-ps laser damage resistance of Magnetron Sputtered dielectric coatings for reflective components." Whistler, Canada (2021).
5. Laser-induced Damage in Optical Materials (SPIE Laser Damage, 2022), conference; oral presentation on "Sub-ps 1030 nm laser-induced damage threshold evaluation of pulsed-laser deposited sesquioxides and magnetron-sputtered metal oxide optical coatings." Rochester, NY, USA (2022).
6. Laser-induced Damage in Optical Materials (SPIE Laser Damage, 2022), conference; poster on "Sub-ps MHz green laser-induced contamination on dielectric coatings in air." Rochester, NY, USA (2022).
7. Forum Interaction Lasers et Plasmas (Forum ILP), summer school; poster on "Sub-ps laser damage resistance of optical coatings for reflective components.", Belambra - Golfe de Lozari, Haute Corse, France (2021).
8. Stuttgart Laser Technology Forum (SLT), tutorial on "Sub-ps Laser Damage of Optical Coatings" within GREAT Networking Workshop, Stuttgart, Germany (2022).
9. Siegman International School on Lasers, summer school; poster on "Sub-ps laser damage resistance of optical coatings for reflective components"; University of Warsaw, Chęciny, Poland (2022).
10. ITN-GREAT Summer School, Online only (2020).
11. ITN-GREAT Winter School, Online only (2020).
12. Seminar on "Laser-induced damage & laser-induced contamination on dielectric coatings in sub-ps regime." ELI Beamlines, Prague, Czech Republic (2022).
13. Seminar on "Laser-induced damage & contamination on dielectric coatings in sub-ps regime." Online for Laboratory of Laser Energetics, University of Rochester, NY, USA (2022).

Title of thesis in English

Laser damage resistance of coating materials and structures for grating-waveguides.

Acknowledgements

I would like to express my gratitude to my supervisors Laurent Gallais and Frank Wagner for guidance, encouragement, and fruitful discussions. Thank you for giving me the opportunity to be a member of the Institut Fresnel and the innovative training network GREAT. The environment of efficient work and international cooperation you established ensured that I never felt bored during the 3 years.

We would like to thank the GREAT consortium partners and all those who contributed to its realization. Among the many people I should list here, I thank a lot to Marwan Abdou Ahmed (project coordinator), Christian Röhrer (project manager) and Jacob Mackenzie (training coordinator). Many thanks to Goby Govindassamy for the productive collaboration, long discussions, visit of the laboratory at Optoelectronics Research Centre in University of Southampton and for providing me a wide spectrum of pulsed-laser deposited samples. I thank to Anton Savchenko and ITO USTUTT institution for the visit of their laboratories and for the collaboration established about the production and testing of samples treated by Ti promoter and Cr mask. I thank also to Fangfang Li for intense work on grating production she did.

I thank Johan Boullet, Adrián Grande and ALPHANOV, Optics & Laser Technology Center for hosting me for secondment and providing me the 150 ps LIDT station. I really enjoyed to share the office with researchers from your group. I thank Daniel Kramer and Irena Havlíčková for the efficient work and the access to the 100 fs LIDT station at Extreme Light Infrastructure Beamlines facility. I also thank HiLASE centre and namely Jan Vanda, Mihai-George Mureșan, Martin Mydlář and Kateřina Pilná to enable me to perform LIDT tests with 1.8 ps Perla B laser.

I am thankful to the whole Institut Fresnel, but especially to Janis Zideluns and Riley Shurvington, with whom I shared an office for the entire three years. It was Janis, who deposited a lot of coatings, which I tested and damaged afterwards. Riley, thank you for the coffee cake recipe. I thank to the coffee distributed in the cafeteria at Institut Fresnel. The high quality coffee contributed significantly to this work as well as the energy resources contained in chorizo and kebab pizzas sold on the corner of campus.

I thank a lot to RCMO team, namely Antonin Moreau for PIAD samples, Aude Lereu for introducing me into the world of s-SNOM microscopy, Camille Petite and Jeanne for the absorption measurement of thin-film coatings. I feel grateful to Marco Minissale from PIIM laboratory for fruitful discussions and work connected to the analysis via X-ray Photelectron Spectroscopy. I thank Jérôme Wenger for the high-quality coverslips, which allowed the XPS study. I would like to thank everyone who participated in the research described in this thesis and whom I have forgotten in the list above.

Last but certainly not least I would like to thank my family, whose infinite support has allowed this thesis to come to life.

This PhD project has received funding from the European Union's Horizon 2020 research and innovation programme under the Marie Skłodowska-Curie grant agreement No 813159.

Abstract

The laser-induced damage and laser-induced contamination are phenomena limiting reliable operation of coating-based optical components in ultrashort pulse high-power lasers. To enhance the damage resistance of optical coatings intended to be used in diffractive components (GWS), testing of various coating materials, development of optimized coating designs, and comparison between deposition methods have been done.

Such developments on coatings rely on a robust laser damage metrology. Despite the efficient excitation of dielectric materials in sub-ps regime, indicating that laser-induced damage threshold (LIDT) should not be dependent on beam size, we found that this statement is not unequivocal in the published literature. Our work on metrology with 500-fs 1030-nm laser source underlines the difficulty of LIDT measurement by very focused laser beams and we suggest beam deformation due to self-focusing in the lens as a possible explanation. We have also identfied testing parameters to obtain reliable and scalable LIDT results.

We performed LIDT tests with pulsed-laser deposited crystalline sesquioxides (Sc_2O_3, Y_2O_3, Lu_2O_3) and amorphous metal oxides (HfO_2, Nb_2O_5, SiO_2) coated by magnetron sputtering. We found the intrinsic LIDT of each material and their evolution with the number of pulses for different laser parameters relevant to the GWS operation.

Following this screening and investigation of coating materials, we investigated the effects of fabrication techniques and designs of GWS on the LIDT. Since the fabrication of diffractive optical components involve multiple and complex fabrication steps, we have investigated the effect of surface processing with adhesion promoter (Ti) and masking layers (Cr) on the LIDT. We observed that the LIDTs of treated surfaces are close to the untreated ones, in our test conditions.

Using 700-fs 515-nm 3.3-MHz setup we studied laser-induced contamination (LIC) growth in dependence on coating material, its deposition technique and its thickness, since LIC is a main issue related to the application. We found a nearly linear relationship between LIC deposit thicknesses and SiO_2 and HfO_2 coating thicknesses. Moreover the deposition technique and hence the material properties has a strong effect on the LIC deposit growth.

Keywords: Laser-induced damage threshold, Laser-induced contamination, Oxide coatings, Sub-ps pulses.

Résumé

L'endommagement laser et la contamination induite par laser sont des phénomènes qui limitent les performances des composants optiques à base de couches minces optiques dans les lasers haute puissance à impulsions ultracourtes. Afin d'améliorer la résistance au flux laser des couches optiques destinées à être utilisées dans des composants diffractifs (GWS), des tests de différents matériaux diélectriques, le développement d'empilements optimisés et l'étude de l'effet de la technique de dépôt ont été réalisés.

De tels développements reposent sur une métrologie robuste de l'endommagement laser. Malgré les processus physiques d'excitation des matériaux diélectriques dans le régime sub-ps, indiquant que le seuil d'endommagement laser (LIDT) ne devrait pas dépendre de la taille du faisceau, nous avons constaté que cette affirmation n'est pas sans équivoque dans la littérature publiée sur le sujet. Notre travail de métrologie avec une source laser de 500-fs 1030-nm souligne la difficulté de la mesure du LIDT par des faisceaux laser très focalisés et nous suggérons la déformation du faisceau due à l'auto-focalisation dans la lentille comme une explication possible. Nous avons également identifié les paramètres de test permettant d'obtenir des résultats LIDT stables et reproductibles.

Nous avons effectué une étude de la tenue au flux laser de sesquioxydes cristallins déposés par laser pulsé (Sc_2O_3, Y_2O_3, Lu_2O_3) et des oxydes métalliques amorphes (HfO_2, Nb_2O_5, SiO_2) déposés par pulvérisation magnétron. Nous avons mesuré les LIDT intrinsèques de chaque matériau et leur évolution avec le nombre d'impulsions pour différents paramètres laser pertinents pour le fonctionnement des GWS.

Après cette sélection et cette étude des matériaux en couches minces, nous avons étudié les effets des techniques de fabrication et le design des GWS sur le LIDT. Puisque la fabrication de composants optiques diffractifs nécessite des étapes de fabrication multiples et complexes, nous avons étudié l'effet de certaines de ces étapes, utilisation de promoteur d'adhésion et couches de masquage, sur la tenue au flux laser. Nous avons observé que les LIDT des surfaces traitées sont proches des LIDT des surfaces non traitées, dans nos conditions de test.

Sur la base d'une source laser 700-fs 515-nm 3.3-MHz, nous avons étudié la dynamique de croissance de la contamination induite par laser (LIC) en fonction du matériau, de la technique de dépôt et de l'épaisseur des couches. Nous avons trouvé une relation quasi linéaire entre les épaisseurs de dépôt de LIC et les épaisseurs de couche de SiO_2 et HfO_2. De plus, la technique de dépôt et donc les propriétés du matériau ont un effet déterminant sur la croissance du dépôt de LIC.

Mots-clés: Seuil d'endommagement induit par laser, contamination induite par laser, couches minces d'oxyde, impulsions subpicosecondes.

Résumé étendu

Depuis l'avènement des lasers, l'endommagement des composants optiques est un phénomène limitant qui a fait l'objet de recherches actives. [1] Les études portant sur cette problématique de dommages laser sont extrêmement importantes non seulement pour améliorer la performance des composants optiques dans les systèmes laser [2] mais aussi pour la recherche sur le traitement des matériaux par laser [3] comprenant l'ablation et l'usinage. [4] La recherche dans le domaine suit les progrès des technologies laser, qui actuellement s'orientent notamment vers la génération d'impulsions ultracourtes à fort taux de répétition. La résistance à l'endommagement par laser des composants optiques, en particulier des miroirs et des réseaux diélectriques, détermine en effet la performance et la fiabilité des lasers solides à impulsions ultracourtes.

C'est la génération des lasers à impulsions ultracourtes qui a créé une demande technologique pour des composants optiques à haute tenue au flux laser, haute réflectivité et à faible distorsion spectrale. Les progrès réalisés dans la conception des couches minces optiques multicouches ont permis de répondre à ces exigences et de faire fonctionner les lasers à impulsions ultracourtes dans des régimes de haute puissance. Les avancées dans ce domaine nécessitent des méthodes de fabrication et des tests pointus dédiés aux couches minces optiques, sur le plan des matériaux et des composants. Afin de qualifier les structures optiques pour des applications laser, de nombreux résultats expérimentaux de tenue au flux laser sur les couches minces optiques et la compréhension des mécanismes physiques de dégradation des matériaux sous flux laser sont nécessaires.

La motivation principale de cette thèse était d'étudier les seuils de dommages induits par laser (LIDT) des matériaux et composants en couches minces et de contribuer au développement de composants mis en œuvre dans les lasers utilisés par exemple dans l'industrie. Pour atteindre ces objectifs, nous avons testé différents matériaux classiques et non traditionnels, des couches minces déposées dans différentes conditions de fabrication et différents types de designs de systèmes muticouches. Les tests ont été réalisés à l'aide de différentes expériences que nous avons développées ou auxquelles nous avons eu accès au cours de cette thèse, dans des conditions aussi proches que possible de l'application prévue des composants.

En effet, le développement de composants optiques à haute tenue au flux laser et les applications laser sont fortement liés. Dans le domaine des lasers à impulsions ultracourtes, une attention considérable a été accordée aux applications industrielles telles que le perçage, la structuration de surface et la découpe, où une qualité et une productivité élevée sont exigées. [5, 6] La mise en œuvre rapide des lasers à impulsions ultracourtes dans les domaines de l'automobile, des communications numériques ou de la santé a mis en évidence la nécessité de disposer de composants fonctionnels résistants aux dommages, capables d'ajuster la longueur d'onde, la polarisation ou la durée d'impulsion du laser. Cet ajustement des propriétés du rayonnement laser peut être réalisé à l'aide d'éléments diffractifs appelés structures de guide d'ondes à réseaux, Grating Waveguide Structures (GWS). [7] Les GWS sont basées sur la combinaison d'un réseau sub-longueur d'onde et d'un guide d'ondes planaire en interface avec un empilement de couches hautement réfléchissantes déposées sur un substrat, voir la Fig. 1.

Le développement des GWS est une tâche essentielle du projet GREAT ITN dans lequel s'inscrit ce travail de thèse. Le projet GREAT (Grating Reflectors Enable laser Applications and Training) est un réseau international de formation (ITN), qui fait partie des actions Marie Skodowska-Curie (MSCA) [8, 9], et qui est décrit dans la première partie du manuscrit. Dans le cadre de la description du projet, le fonctionnement du GWS, ses applications, les objectifs de GREAT et les partenaires du projet sont présentés. Le consortium GREAT comprend à la fois des institutions scientifiques et des entreprises privées, qui possèdent une expertise particulière dans la conception, la fabrication, la caractérisation ou la mise en œuvre de composants optiques dans les systèmes laser.

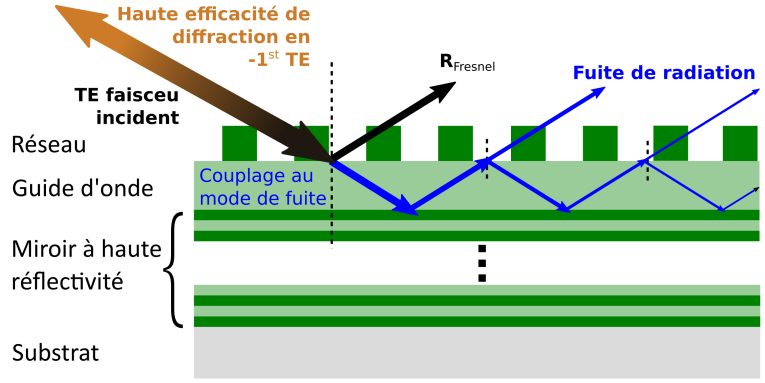

Figure 1: Réseau à guide d'ondes (Grating waveguide structure - GWS).

Pour le projet GREAT et la qualification des GWS, l'un des paramètres clés est la tenue au flux laser. [10] Dans ce travail de thèse, nous avons testé la résistance au flux laser des couches minces et des structures correspondant aux différentes étapes de la chaîne de production des GWS, c'est-à-dire les couches minces monocouches, les miroirs multicouches et la première génération de structures de réseaux gravés dans les substrats. Ce travail sur la tenue au flux laser des GWS est nécessaire pour leur qualification en vue d'une utilisation dans divers systèmes couvrant les lasers à fibre, à disque et les diodes lasers.

Pour être en mesure d'améliorer la résistance des composants optiques, nous devons comprendre les mécanismes physiques qui conduisent à l'endommagement des matériaux couches minces diélectriques. Par conséquent, dans le Chapitre 2, nous faisons le point sur les connaissances relatives à la thématique. Nous résumons les caractéristiques de base de la structure des matériaux diélectriques et leurs spécificités par rapport aux semi-conducteurs et aux métaux. Nous nous concentrons sur ces matériaux diélectriques car ils sont utilisés dans les composants optiques relatifs au projet. Ensuite, nous discutons de l'effet de l'échauffement du matériau, des défauts et des propriétés intrinsèques du matériau sur l'apparition des dommages laser. Nous distinguons les interactions à impulsion unique et à impulsions multiples avec les diélectriques. Nous introduisons les processus d'ionisation et de relaxation et présentons la modélisation par des équations de taux qui peuvent prendre en compte la formation des défauts dans le matériau.

Bien que cette revue se soit concentrée sur les dommages induits par laser dans le régime sub-ps, nous avons également introduit les effets physiques qui sont liés à la formation de dommages par des durées d'impulsion plus longues ou une irradiation CW. Une telle vue d'ensemble est utile car les mécanismes conduisant aux dommages ne dépendent pas seulement de la durée d'impulsion mais aussi, par exemple, du taux de répétition ou du nombre d'impulsions. La formation de dommages pendant une irradiation par impulsions sub-ps avec un taux de répétition élevé peut être associée aux mêmes phénomènes thermiques que dans le régime CW.

Lorsqu'une couches mince diélectrique est irradiée par des impulsions ultracourtes, les électrons de sa structure peuvent absorber l'énergie des photons via des processus non linéaires, notamment l'ionisation multiphotonique ou l'effet tunnel. Ces processus peuvent déclencher une ionisation par impact et une ionisation par avalanche du matériau jusqu'à une densité critique d'électrons dans la bande de conduction qui initie une modification permanente du matériau. Ainsi, dans le régime sub-ps, l'initiation des dommages dans les diélectriques est gouvernée par des processus électroniques.

Dans les couches minces diélectriques, qui sont le théâtre d'effets interférentiels, l'initiation des dommages est liée à la distribution de l'intensité du champ électrique (EFI). Une valeur élevée de l'EFI dans le matériau

facilite son excitation électronique et rend donc l'initiation de dommages plus probable. Les maximas de l'EFI coïncident avec les maximas de la densité électronique. Le choix de la conception d'un système multicouche affecte la distribution de l'EFI et devient donc critique dans l'obtention de composants optiques à haute tenue au flux laser.

Par conséquent, l'amélioration de la résistance des composants optiques nécessite le développement d'un modèle théorique, capable de rendre compte de cette complexité. Dans le Chapitre 3 nous dérivons des équations permettant de calculer la distribution de l'EFI dans une monocouche et son maximum EFI. Ensuite, nous introduisons le terme de fluence LIDT intrinsèque, qui est normalisée par rapport au maximum d'EFI. La fluence LIDT intrinsèque nous permet ainsi de comparer les résultats obtenus dans différentes conditions expérimentales, par exemple l'angle d'incidence, la polarisation, l'épaisseur de la couche ou l'indice de réfraction, qui affectent la distribution de l'EFI dans la couche mince.

Dans le régime sub-ps, les dommages sont principalement dus à l'absorption multiphotonique dans le matériau diélectrique irradié, car les autres processus ne peuvent pas être impliqués dans une courte durée d'impulsion. L'endommagement laser avec des impulsions sub-ps a donc une forte dépendance à l'intensité, et la fluence seuil de dommage est déterministe sans variations statistiques significatives, contrairement aux impulsions nanosecondes par exemple. L'existence d'un seuil d'endommagement déterministe suggère que l'initiation de l'endommagement est lié aux propriétés intrinsèques fondamentales du matériau (largeur de bande d'énergie interdite, indice de réfraction) plutôt que par des défauts distribués de manière stochastique. Ainsi, si le facteur limitant de la résistance au flux laser du matériau semble être les propriétés intrinsèques du matériau, le seuil d'endommagement laser devrait être indépendant de la taille du faisceau laser.

Cependant, ce concept d'apparition de dommages initiés par des impulsions ultracourtes pourrait ne pas être entièrement correct. Des études expérimentales utilisant des impulsions d'une durée comprise entre 30 fs et 1 ps ont montré que les seuils d'endommagement/ablation dépendent de la taille du faisceau (Tableau 3.3). Ainsi, dans le Chapitre 3, nous avons développé une étude métrologique détaillée sur l'effet de la taille du faisceau sur le LIDT dans le cas d'impulsions d'une durée de 500 fs émises à une longueur d'onde de 1030 nm. Nous présentons le dispositif expérimental LIDT utilisé :sa caractérisation, le contrôle de la taille du faisceau laser, la mesure de la stabilité du laser ainsi que l'analyse du profil temporel et spectral sont présentés.

Nous avons mis en évidence certaines limitations sur la détermination du seuil de tenue au flux laser pour des fortes focalisations du faisceau laser, car les incertitudes sur la fluence LIDT, quelle que soit leur nature, sont trop importantes. L'étude souligne la difficulté de ces mesures LIDT avec des faisceaux laser très focalisés, qui pourrait être liée à la déformation du faisceau due à l'autofocalisation dans la lentille. Notre étude recommande, en revanche, l'utilisation d'une focal adaptée, de 30 cm dans notre cas par exemple, pour les tests LIDT de composants optiques destinés à être mis en œuvre dans des systèmes laser à plus grand faisceau. Pour évaluer avec précision les tests de tels composants optiques, nous avons fourni une synthèse des contributeurs d'erreurs identifiés (Tableau 3.4). Nous avons déterminé que l'inexactitude de la mesure de la taille du faisceau était le principal facteur d'erreur dans le meilleur des cas.

Afin de qualifier les couches minces et les structures pour une utilisation dans des systèmes laser liés aux applications du projet, nous avons testé leur résistance au flux laser avec un banc opérant à 500-fs 1030-nm utilisé dans les travaux de métrologie, mais également avec d'autres moyens auxquels nous avons eu accès chez les partenaires du projet. Globalement, dans cette thèse, les tests LIDT ont été réalisé avec 5 stations, qui sont décrites et caractérisées dans le Chapitre 3. Le laser Perla B développé dans le centre HiLASE a permis de réaliser des tests à une durée d'impulsion de 1,8 ps avec de grands faisceaux de diamètre effectif de l'ordre de 315 µm. La Fig. 2 présente des exemples de dommages induits par le laser Perla B. Le laser accessible au centre technologique Alphanov a permis de tester les couches minces avec une durée d'impulsion de 150 ps et une longueur d'onde de 1030 nm, c'est-à-dire dans des conditions proches des impulsions étirées

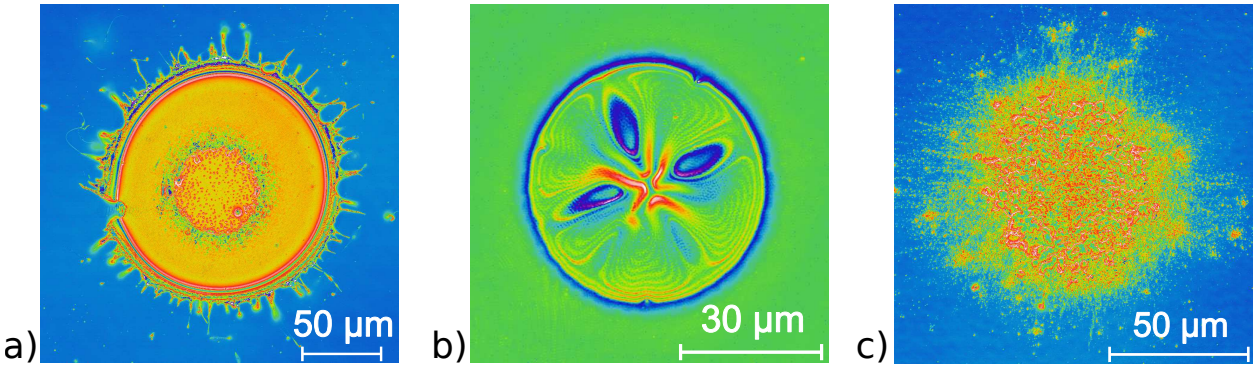

Figure 2: Endommagements de la monocouche de Nb_2O_5 de 450 nm d'épaisseur par des tirs uniques à des fluences intrinsèques de a) 1,47 J/cm^2, b) 1,19 J/cm^2, et par c) 10 tirs à 0,99 J/cm^2. La surface de Nb_2O_5 a été examinée ex-situ avec un microscope confocal OLS5000-SAF (Olympus) équipé d'un objectif à magnification 100X.

existant dans les systèmes laser basés sur la technique d'amplification à dérive de fréquence. En revanche, le dispositif LIDT de l'infrastructure Extreme Light Beamlines a permis de tester le LIDT avec des impulsions aussi courtes que 100 fs dans un environnement sous vide. En plus des installations LIDT dans le proche infrarouge susmentionnéees, fonctionnant à de faibles taux de répétition (1 kHz), nous avons construit une station permettant des tests LIDT en régime MHz par des impulsions de 700 fs émises à une longueur d'onde de 515 nm. Dans l'ensemble, ces installations ont permis de tester des couches minces et des composants diélectriques sur une large gamme de durées d'impulsion allant de 100 fs à 150 ps, à des longueurs d'onde de 515 nm à 1050 nm, à des taux de répétition de 10 Hz à 3,3MHz et avec des diamètres de faisceau effectifs de 40 µm à 315 µm. Cependant, les principales conclusions sur le LIDT résumées dans les paragraphes suivants sont liées aux essais effectués avec des lasers sub-sp dans le proche infrarouge à moins de 1 kHz.

Grâce à la collaboration avec les partenaires du projet produisant les couches minces diélectriques (IF et ORC), nous étudions dans le Chapitre 4 le LIDT de monocouches déposées par différentes méthodes de dépôt. Nous présentons d'abord les méthodes de fabrication des couches minces : dépôt par faisceau d'électrons, dépôt assisté par ions, pulvérisation magnétron, pulvérisation par faisceau d'ions et dépôt par laser pulsé. Ensuite, nous caractérisons les films minces en termes d'indice de réfraction et de bande interdite et nous analysons les structures cristallines des monocouches déposées par laser pulsé par diffraction des rayons X. Ensuite, nous présentons les résultats des tests LIDT effectués sur les monocouches diélectriques par les montages expérimentaux ps/fs accessibles.

En utilisant la station LIDT 500-fs 1030-nm 10-Hz, nous avons effectué des tests avec des sesquioxydes cristallins déposés par laser pulsé (Sc_2O_3, Y_2O_3, Lu_2O_3) et des oxydes métalliques amorphes (HfO_2, Nb_2O_5, SiO_2) déposés par pulvérisation magnétron. Nous avons trouvé des fluences intrinsèques similaires de 1,3 à 1,4 J/cm^2 pour les sesquioxydes optimaux, c'est-à-dire Sc_2O_3 sur saphir, Y_2O_3 sur saphir et Lu_2O_3 sur YAG, lorsqu'ils sont testés avec des impulsions multiples (100 ou 1k).

Les tests LIDT sur le Lu_2O_3 déposé sur saphir ont révélé des seuils de dommages significativement plus bas que le Lu_2O_3 sur YAG. Ce résultat s'explique par la structure polycristalline du Lu_2O_3 déposé sur saphir, déduite de la caractérisation XRD. La structure polycristalline hautement texturée contient des discontinuités dans le réseau qui sont très probablement à l'origine des dommages.

Les sesquioxydes PLD à indice élevé présentent des valeurs d'énergie de bande interdite élevées, ce qui indique une bonne tenue au flux laser des couches minces optiques correspondantes. En termes de seuils de dommages observés, les sesquioxydes peuvent rivaliser avec le HfO_2, un matériau à haut indice fréquemment

utilisé dans les multicouches pour applications laser. L'étude indique que le dépôt par laser pulsé est une méthode de production potentielle et que les sesquioxydes sont des matériaux d'indice élevé prometteurs qui pourraient être utilisés dans des applications liées aux lasers à impulsions ultracourtes de haute puissance.

Le Chapitre 5 étend l'investigation dans le domaine de l'endommagement laser aux composants optiques développés dans le cadre du projet GREAT : miroirs et réseaux diélectriques. Nous commençons par décrire la méthode de la matrice de transfert utilisée pour calculer l'intensité du champ électrique dans les systèmes multicouches. Cette méthode nous permet de déterminer les maximas du champ électrique dans les matériaux couches minces incorporés dans les miroirs. En utilisant ces valeurs et les LIDTs déterminés des monocouches, nous faisons des prédictions des LIDTs pour les miroirs. Nous comparons les LIDT calculés aux données obtenues expérimentalement pour des miroirs testés par des impulsions sub-ps dans le spectre de longueur d'onde du proche infrarouge. Les résultats de cette étude peuvent être utilisés pour concevoir des miroirs avec une distribution optimisée de l'intensité du champ électrique qui conduira a un meilleur seuil de tenue au flux laser des composants.

Dans la partie suivante du Chapitre 5, nous nous concentrons sur le LIDT des réseaux diffractifs et des GWS. Comme la fabrication de telles structures complexes nécessite différentes étapes de fabrication, dans notre cas par exemple l'utilisation de promoteur d'adhésion Ti et de masque dur Cr, nous étudions si le traitement des surfaces optiques avec ces composés peut affecter le LIDT de structures diélectriques et de composants optiques. Nous avons constaté que les LIDT des surfaces traitées sont pratiquement les mêmes que ceux des surfaces non traitées, lorsqu'elles sont testées par 100 impulsions. Ainsi, ces étapes de fabrication ne devraient pas affecter le LIDT des structures visées. Enfin, faute d'accès à des composants finalisés, nous avons prédit le LIDT pour les GWS en utilisant l'analyse rigoureuse des ondes couplées (RCWA) et la connaissance des LIDT pour les matériaux couches minces individuels. Ces résultats devraient être utilisés pour déterminer les conditions pertinentes pour un fonctionnement optimal des systèmes laser, dans lesquels les GWS seront mis en œuvre comme compresseurs d'impulsions ou convertisseurs de polarisation.

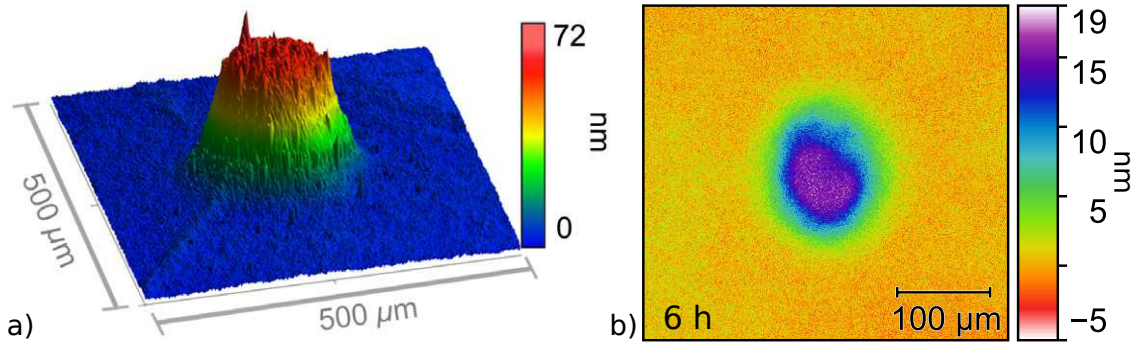

Figure 3: Exemples de dépôts de contamination induits par laser pour: a) un miroir diélectrique [11], b) une couche de SiO_2 de 450 nm d'épaisseur, pulvérisée par magnétron, irradiée pendant 6 h. Les deux échantillons ont été exposés à un laser 700-fs 515-nm 3-MHz avec $\sim$ 35 W de puissance moyenne. Les images des surfaces des échantillons ont été capturées ex-situ par microscopie interférentielle à lumière blanche.

La durée de vie des composants optiques dans les systèmes laser industriels à haute fréquence de répétition peut être limitée par un effet néfaste appelé contamination induite par le laser (LIC). Voir des exemples de dépôts LIC sur la Fig. 3. L'effet LIC a été identifié comme une limitation majeure de l'utilisation des lasers dans les applications spatiales. Dans notre cas, nous explorons l'effet sur des couches minces diélectriques monocouches dans un environnement air ambiant soumises à des impulsions longues de 700 fs émises à une longueur d'onde de 515nm avec un taux de répétition de 3,3 MHz. Après avoir présenté le dispositif

expérimental, nous présentons les résultats sous la forme d'une étude paramétrique. Nous cherchons à décrire l'effet du matériau, de son épaisseur et de la méthode de dépôt sur la croissance des dépôts de LIC. Les dépôts de LIC observés sont caractérisés en utilisant des techniques optiques qui pourraient nous donner des informations sur la morphologie, l'épaisseur ou la composition chimique. Les techniques de caractérisation sont la microscopie interférentielle à faible longueur de cohérence, la microscopie de fluorescence et la spectroscopie photo électronique à rayons X.

Dans le travail sur le LIC, nous essayons de comprendre l'origine et la cause de la formation du LIC sur les couches minces diélectriques dans l'air. Nous avons constaté qu'il existe un effet significatif du matériau et de la méthode de dépôt sur la dynamique de croissance du LIC. Pour les couches minces de SiO_2 déposées par pulvérisation magnétron et de HfO_2 déposées assistance ionique, nous avons trouvé une dépendance approximativement linéaire de l'épaisseur du dépôt par rapport à l'épaisseur de la couche mince. Cette relation pourrait suggérer un effet lié à un mécanisme d'absorption dans la couche. Les résultats de cette étude restent à être approfondis pour comprendre et réduire la croissance du LIC.

Les études menées dans le cadre de la thèse montrent la complexité des processus impliqués dans le domaine de l'endommagement laser. Parmi les nombreuses perspectives à explorer, cette thèse encourage à:

- Etude des couches minces déposées par PLD, y compris le HfO_2 et les composants réfléchissants multicouches.
- Etudes LIDT et LIC avec des taux de répétition allant d'environ 100 kHz jusqu'au régime des GHz. Il devrait être possible de déterminer le temps de relaxation des matériaux de couches minces après l'irradiation par une impulsion sub-ps. Pour le développement de systèmes laser de haute puissance, il pourrait être utile d'identifier le taux de répétition pour lequel les effets thermiques commencent à jouer un rôle significatif dans un matériau en couches mince donné.
- Tests LIDT des matériaux et structures couches minces avec un grand nombre d'impulsions (par exemple 10^8). Comme la reproduction de ces tests prend beaucoup de temps, elle doit être soutenue par des modèles décrivant l'évolution du seuil avec le nombre de tirs.

Contents

Introduction

The laser damage resistance of optical components, such as dielectric mirrors and gratings, represents the limiting factor of useful performance of ultrafast solid-state lasers. [2] Laser induced-damage is intensively studied in terms of damage initiation and the same laws of physics allow to understand material processing [3] comprising laser ablation and laser machining. [4] In the laser damage field, the research follows the advances in laser technologies, such as the generation of ultrashort pulses or high repetition rates, and their applications.

It is the ultrashort-pulse laser generation that has created a technological demand for damage resistant optical components that limit pulse lengthening and spectral distortion. Advances in designs of multilayer optical coatings have made it possible to meet these requirements and enable ultrashort lasers to operate in the high power regime ($> 10\,\mathrm{W}$ mean power). Progress in this field requires state-of-the-art fabrication methods and testing of optical coatings, optical bulk materials and whole components at conditions as close as possible to the intended application. To qualify the optical structures for their use in lasers, numerous experimental results of laser damage resistance on optical coating materials and understanding of the laser damage mechanisms are needed.

In the ultrashort-pulse laser field, industrial applications such as drilling, surface structuring and cutting have gained a considerable attention. The use of ultrashort pulses enables material processing with high quality and productivity. [5, 6] The rapid implementation of ultrashort-pulse lasers in automotive, digital communications or healthcare fields highlighted the need to have systems that can tailor the temporal, spectral or spatial properties of light. In addition, beam tailoring is attractive for research in nuclear physics [12] or for the measurement of gravitational waves. [13]

A possible solution represent diffractive elements based on the combination of a planar waveguide and sub-wavelength gratings, called grating waveguide structures (GWS). [7] The elements are leitmotifs of the GREAT MSCA-ITN-ETN project[1] [8, 9], which is described in Chapter 1 of the thesis. As a part of the description, the project partners (Fig. 4), goals, GWS operation and applications are introduced. For the GREAT project and the GWS qualification, one of the key parameters is their laser damage resistance. [10]

This PhD work deals with laser damage resistance of optical components that need to be qualified for use in various laser designs: fibre, thin-disk or diode lasers. In the thesis, the technological and physical limitations of power handling capabilities of GWS are researched in order to improve the laser-induced damage threshold (LIDT). An important part of the study focuses on the critical topic of LIDT metrology and the development of testing systems for evaluation of laser damage resistance of optical components.

In Chapter 2, we will provide a review of laser damage studies on dielectrics in the sub-picosecond regime. We will briefly summarize the basic characteristics of the material structure of dielectrics and how they differ from semiconductors and metals. Then, the effects of material heating, defects and intrinsic material

[1] Grating Reflectors Enabled laser Applications and Training (GREAT) project is a part of Marie Skłodowska-Curie Actions (MSCA), International Training Networks (ITN) and European Training Networks (ETN).

properties on the LIDT will be discussed. We will briefly describe ionization and relaxation processes relevant to the sub-ps regime. In next part, we will introduce an analytical approach based or rate equations that can be used to predict damage thresholds in optical materials.

In Chapter 2 we will distinguish between single-pulse and multiple-pulse interactions with dielectrics. While the single-pulse interaction is a topic for academic research, the multiple-pulse regime is a practical field relevant for industrial laser applications. For single-pulse interaction, we will review studies on damage fluence dependence on parameters. These studies led to the establishment of scaling laws that are used to compare experimental LIDT results obtained with different irradiation conditions (pulse duration, wavelength) or varying material properties (bandgap, refractive index). In the multi-pulse interaction, we will mention a topic of damage growth with the pulses subsequent to damage initiation. It is the damage growth process on a optical component that limits the operation of lasers.

Chapter 3 is dedicated to metrology work with sub-picosecond laser emitting in near-infrared region. We will firstly derive equations allowing to calculate electric field intensity distribution in monolayers. The determined electric field intensity maximum in a given monolayer will be used to express intrinsic LIDT fluence, characteristic material parameter in sub-ps pulse regime. We will introduce a LIDT experimental setup operating with pulses of 500 fs duration at a wavelength of 1030 nm. As a part of the setup characterization, the laser beam size monitoring, the laser stability measurement as well as the analysis of temporal and spectral profile will be presented.

In Chapter 3 we will investigate whether laser beam-size can affect determined LIDT values in sub-ps regime. The findings of this study should reveal if small beam sizes may be used to test optical components that will be employed in high-energy large-beam lasers. Although effective nonlinear excitation of the material by sub-picosecond pulses results in a deterministic accurate determination of the damage threshold, which should not be thus significantly dependent on defect density and beam size, the studies published so far are not unequivocal on the effect of beam size on LIDT. The work done here will look at the causes of dispersed LIDT values when testing with highly focussed beams. We will summarize identified contributors to errors in LIDT measurement and recommend which focusing conditions should be used for accurate testing of optical components.

Chapter 3 also contains description and characterization of other LIDT setups that enabled to test dielectric coatings and components by a broad range of pulse durations from 100-fs up to 150-ps. The laser Perla B developed in HiLASE centre allowed to carry out tests at a pulse duration of 1.8 ps with large beams of effective beam diameter around 315 µm. The laser accessible in Alphanov technological center permitted to test coatings at a pulse duration of 150 ps and a wavelength of 1030 nm, i.e. in conditions close to pulse-stretched pulses existing in laser systems with chirped pulse amplification technique. By contrast, the LIDT setup in Extreme Light Infrastructure Beamlines facility made possible LIDT testing by pulses as short as 100 fs in vacuum environment. In addition to the aforementioned near-infrared LIDT setups operating at low repetition rates (≤ 1 kHz), we built a station allowing for LIDT tests in MHz regime by 700 fs long pulses emitted at a wavelength of 515 nm.

Chapter 4 deals with dielectric monolayers, thin films that need to be qualified for use in optical components. We firstly introduce thin film fabrication methods: electron-beam deposition, ion-assisted deposition, magnetron sputtering, ion-beam sputtering and pulsed-laser deposition. Then we characterize thin films in terms of their refractive index, bandgap and analyze crystalline structures of pulsed-laser deposited monolayers by X-ray diffraction. Afterwards, we will present results of LIDT tests done on dielectric thin film monolayers by the accessible ps/fs experimental setups. We will compare LIDT results between pulsed-laser deposited crystalline sesquioxides (Sc_2O_3, Y_2O_3, Lu_2O_3) and amorphous metal oxides (HfO_2, Nb_2O_5, SiO_2) coated by magnetron sputtering.

Chapter 5 expands the investigation in the laser damage field to the optical components developed within the GREAT project: dielectric mirrors and gratings. We start the chapter with description of transfer matrix method utilized for electric field intensity calcul in multilayer coatings. The method we use to determine the electric field maxima in materials of coatings incorporated in the mirrors. Using these values and determined LIDTs of monolayers we make predictions of LIDTs for mirrors. We compare the calculated LIDTs to the experimentally obtained data for mirrors tested in sub-ps pulsed regime at near-infrared wavelength spectrum. The results from this study may be used to design mirrors with optimized electric field intensity distribution that will lead to enhanced LIDT of components.

In Chapter 5 we focus also on LIDT of diffractive gratings and GWS. Since the fabrication of such complex structures requires often use of Ti adhesion promoter and Cr hard mask forming thin layers, we will study whether treatment of optical surfaces with these compounds can affect the LIDT of whole dielectric structures and optical components. Finally, using the Rigorous Coupled Wave Analysis (RCWA) and knowledge of LIDTs for individual coating materials, we will make predictions of LIDT for GWS. These findings should be used to determine conditions relevant to reliable operation of laser systems, in which the GWS will be implemented as pulse compressors or polarization converters.

Chapter 6 explores laser-induced contamination (LIC), effect which has a negative impact on the operation of optical components and has been identified as a major limitation for use of lasers in space applications. In our case, we will study LIC effect in air environment by 700-fs long pulses emitted at a wavelength of 515 nm with a repetition rate of 3.3 MHz. After introducing the experimental setup, we will present results in a form of parametric study. We aim to describe the effect of coating material, its thickness and deposition method on LIC deposit growth. The observed LIC deposits will be characterized using optical techniques that could give us information about morphology, thickness or chemical composition of created LIC deposits. The characterization techniques are white-light interference microscopy, fluorescence microscopy and X-ray photoelectron spectroscopy. We will try to understand the origin and cause of LIC formation on dielectric coatings in air. The work might be useful to design optical components that will mitigate the LIC detrimental effect.

Figure 4: GREAT project partners are in Germany, France, Finland, UK and Czechia.

Chapter 1

Grating Waveguide Structures and GREAT project - Motivation

Improved control of the properties of laser light has led to rapid commercial applications of lasers, for example in high value-added manufacturing in the automotive and consumer electronics markets. The possibility to adjust radiation bandwidth has contributed to the development of digital communication. The control of laser light properties is also used in medical applications, biological imaging and surgery. In addition, adjusting the temporal, spectral and spatial properties of light enables new advances across scientific frontiers, for instance in nuclear physics [12] or in gravitational wave measurements. [13]

Diffraction gratings are key optical elements enabling the control of these light properties. Diffraction gratings were discovered in the 18th century and nowadays they are extensively used for spectrometric analysis, whose applications range from probing single molecules of biological samples to analysis of solar systems in astronomy. [14] To produce high-quality diffraction gratings, precise control of the grating period at the nanometer scale is required. The high precision control of the grating period on large scale components was made possible by optical beam lithography, discovered in the 1970s thanks to the advent of lasers in the 1960s. Today, diffraction gratings are seen as a product of modern nanophotonics, which allowed to structure matter at the nanometer scale demanded for light properties tailoring. It is the ability of diffraction gratings to tailor the properties of light that is revolutionizing the field of high-energy lasers.

The earliest designs of reflective gratings were based on metal diffraction gratings. Metals can reflect light with good efficiency, and by periodically structuring the metal surface, diffracted orders show up in the reflection. A preferred material for reflective metal gratings is gold, which exhibits high reflectivity in the spectral range of interest (700 to 1200 nm), in which many lasers operate. In addition to the high optical performance, gold is also a noble metal that has no need for a protective transparent oxide layer like silver or aluminum. [14]

A notable feature of metal gratings irradiated in TM polarization is the broad spectral tolerance of their reflection efficiency. This property is critical for the compression of short pulses with a broad spectrum. This advantage is, however, counter-balanced by low laser-induced damage threshold (only hundreds of mJ/cm^2). [14] One solution to this severe limitation is the fabrication of large gratings that are used at a high incidence angle to reduce the beam intensity. It is however challenging to produce such large metallic gratings with good level of homogeneity needed for both optical performance and LIDT. Large gold gratings are used in many petawatt class laser facilities and in TM polarization they provide diffraction efficiencies of 92 % over a broad bandwidth. [14]

Compared to metals, dielectrics offer two following advantages for chirped pulse amplification (CPA). Firstly, dielectrics show very low losses making them suitable for high optical performance, i.e. the diffraction efficiency of dielectric gratings can reach almost 100 %. [14] Secondly, dielectrics have higher LIDTs in comparison to metals which is of high importance for engineering of damage resistant diffraction gratings. For the dielectric gratings, LIDT values of several J/cm^2 were determined at 500 fs pulse duration. [15]

The dielectric gratings face many challenges including high laser damage resistance and diffraction efficiency. In the pulse compression systems equipped with two to four gratings, the diffracted beam can be significantly distorted by grating wavefront. The wavefront degrades both the focal spot quality and the compressibility of the output pulse.

Moreover, dielectric gratings are suffering from the mechanical stress between the thin films of high and low refractive indices, and also between the stack and the substrate. The mechanical stress is growing with the number of thin film layers and can lead to lower quality of the grating surface. The issue particularly concerns large size dielectric gratings and designs with fused silica substrates. [14]

For the reduction of mechanical stress, optimization of the coating process parameters and/or application of ion assistance (to get denser coatings) are used. The stress can be reduced also by decreasing the number of bilayers while preserving the high reflectivity. A solution is to insert a metallic film between the substrate and the dielectric multilayer. The created hybrid metallo-dielectric designs provide high reflectivity, enable broad bandwidth of the grating and show increased LIDT compared to gold gratings.

To reach high diffraction efficiencies ($\geq$ 99%) with good spectral tolerances while maintaining a high LIDT, low wavefront distortion or reduced mechanical stress, new designs have been developed. Diffraction gratings that aim to overcome the limits of aforementioned metallic, dielectric or hybrid metallo-dielectric gratings are grating waveguide structures (GWS). [7, 16] These gratings are based on a combination of a planar waveguide and a sub-wavelength grating. The GWS have been reported [17–21] as powerful tools for polarization selection [22, 23], as well as for temporal [20] and spectral [24] profile adjustment of high-power laser beams. These diffractive elements can thus adjust the properties of laser radiation. Their design, fabrication, characterization and implementation in lasers is the subject of the Grating Reflectors Enabled laser Applications and Training (GREAT) project. [8, 9]

Thanks to the appropriate design of sub-wavelength gratings integrated with planar waveguides, the GWS can generate interference effects that ensure the high diffraction efficiency. It has been shown that for grating/corrugated waveguide the diffraction efficiency can theoretically reach 100%. [25, 26] Such high diffraction efficiency allows to generate high-power laser beams with tailored properties - filtered polarization (linear, radial, azimuthal) or narrowed, stabilized or tuned emission wavelength. [22] The GWS, however, present a challenge from a fabrication perspective. Their production necessitates an accurate process control due to their performance sensitivity to parameter variations, e.g., refractive index of waveguides and grating profiles. Consequently, it is of utmost importance to develop expertise, tools and methods that either allow the design of parameter-tolerant structures or provide better control of the fabrication processes. The GWS fabrication is made using advanced micro-nanotechnologies and includes coating deposition, lithography and grating etching.

The GREAT project [8, 9] covers the whole development and integration chain of GWS in high-power laser systems, as shown in Fig. 1.1. The project includes GWS design, fabrication, precision characterization and implementation of the qualified component in laser systems. Utilization of the GWS in lasers could meet the requirements of various laser applications covering material processing and relativistic science. The practical objective of this project is focused on laser beam adjustment using the ability to effectively control the spectral, spatial and temporal characteristics of high-power lasers.

In summary, the GREAT project has defined the following research objectives:

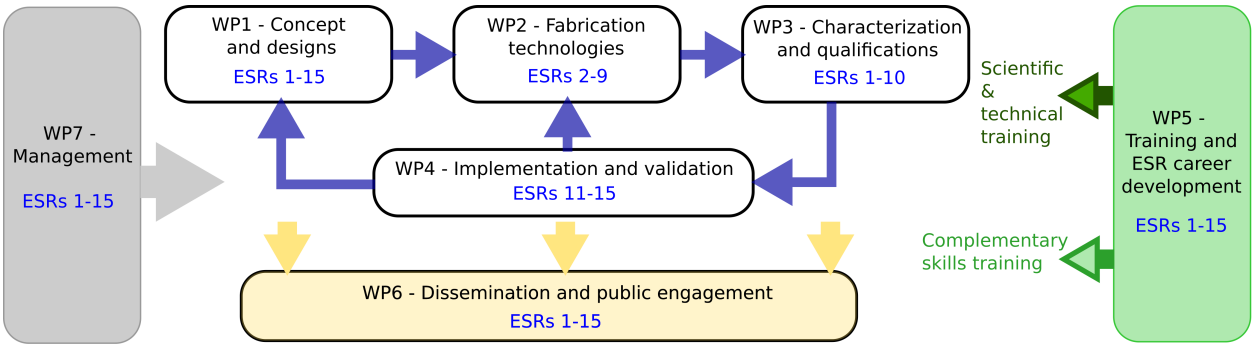

Figure 1.1: Overview of the GREAT project showing the working packages (WP) and involved Early Stage Researchers (ESRs, i.e. PhD students). The work presented in this thesis was made by ESR10. [9]

- To conceive and produce GWSs which are, by design, responding to end-users' needs and products.
- To develop and apply controlled production processes of GWS (gratings and coatings).
- To develop and implement precise measurement and qualification tools.

In addition to these research objectives, the GREAT project has defined training objectives. The GREAT project is indeed an international training network (ITN) that creates a cohort of 15 Early Stage Researchers (ESRs, i.e. PhD students) working collaboratively to deliver systems and solutions responding to real-world problems. [8] Since the mission of GREAT encompasses the full development chain for complex laser systems, the ESRs can well understand both the physical limitations and the requirements from end-users. Forming the highly qualified ESRs in the fields of lasers, beam shaping or micro-nano technologies is one of the crucial objectives of GREAT. The project aims to promote and facilitate the acquisition of complementary skills applicable across sectors and disciplines. Another objective is to establish a collaborative network of highly skilled researchers.

1.1 GREAT partners

The GREAT project is organized by a consortium of scientific institutions, academic partner organizations and private sector partners. The GREAT consortium consists of partners from 5 European countries: Germany, France, UK, Finland and Czechia, see Fig. 4. These partners have unique expertises which are required in different phases of GWS production chain covering design, fabrication, characterization and finally implementation in laser systems. In the following, we introduce the consortium partners and their role in the GREAT project. [8, 9]

Institut für Strahlwerkzeuge (IFSW) of the University of Stuttgart (USTUTT) is a research institute with activities in laser technologies and their applications. [27] Research at the IFSW focuses on the development of laser radiation sources, optical elements and components for beam delivery and beam shaping. In addition to fundamental research, the IFSW is engaged in technology transfer to industry. The laser applications investigated in IFSW cover laser welding, cutting or drilling. [28] The institute gained international reputation thanks to the invention and development of thin-disk laser systems. [29, 30] Within the GREAT project, the IFSW is leading institution in GWS concepts and design and takes care of project management.

Department of Physics and Mathematics of the University of Eastern Finland (UEF) focuses on light-based technologies and their various applications, development of nanotechnology-based experimental photonics and the social impact of photonics. [31] The department has clean rooms facilitating the fabrication

of micro- and nanostructures, equipped with devices for resisting, patterning, etching, and thin-film coating. At UEF, the fabrication methods used include electron beam lithography and nanoimprint lithography. UEF in GREAT is seen as leading institution of the GWS fabrication technologies.

Institut Fresnel is a research laboratory active in the fields of electromagnetism, photonics and signal and image processing. From the perspective of the GREAT project, the role of IF lies in thin-film deposition and laser damage resistance testing of optical materials and structures used for GWS. Institut Fresnel has state-of-the-art deposition machines and associated characterization systems. In GREAT, IF is a leader for GWS characterization and qualification.

ALPhANOV is a technology center that supports innovations in optics and laser fields. The center aims to support research laboratories with the technology transfer process, create collaborative projects, bring technologies to maturity and speed up the introduction of products to the market. [32] For GREAT project, ALPHaNOV represents leading institution in GWS implementation and qualification.

Optoelectronics Research Centre (ORC), based in the Zepler Institute, at the University of Southampton, is an interdisciplinary research centre. The centre has the largest photonics group in the UK with expertise in fibre optics and telecommunication technology. [33] Inventions originating from ORC are used to navigate airlines, cut steel or produce life-saving medical devices. A significant contribution to the expansion of long-distance optical communications was made by the erbium-doped fibre amplifier (EDFA), which was first successfully constructed in ORC. [34] For the GREAT project, ORC is fabricating waveguides and optical layers and it is the leading institution for recruitment and training.

Laboratoire Hubert Curien (LabHC) is a research laboratory specializing in optics, photonics, microwaves, computer science, telecommunications and imaging. [35] In the GREAT project, LabHC is performing laser interference lithography (LIL), direct laser writing, and etching processes for the fabrication of GWS. LabHC also provides ellipsometry measurements for the characterization of thin films. Within GREAT, LabHC is in charge of scientific work dissemination and public engagement.

In addition to the above-mentioned partners playing leading roles in the working packages (WP, Fig. 1.1), the GREAT consortium also includes other partners providing special fabrication technologies or access to experimental laser setups. AMO GmbH company contributes to the GREAT by development and optimization of Nanoimprint Lithography (NIL) and Reactive Ion Etching (RIE) used for fabrication of GWS. Institut für Technische Optik (ITO) of the University of Stuttgart uses interference lithography methods - Scanning Beam Interference Lithography (SBIL) and Stepped Mask Interference Lithography Exposure (SMILE).

The research centres HiLASE and ELI Beamlines allow qualifying coatings and optical components developed in GREAT project using their characterization tools and LIDT setups operating under conditions close to the intended application of the GWS. In Laboratoire Ondes et Matière d'Aqutaine (LOMA), the GWS will be used for pulse compression within picosecond and femtosecond high power ytterbium fibre laser, designed to pump optical parametric oscillators. At Coherent (former DILAS Diodenlaser GmbH), manufacturer of semiconductor laser components, the fabricated GWS will be implemented into diode lasers to stabilize emission wavelength and narrow the spectral bandwidth. [22,24] Furthermore, a partner in project is MarTec Photonics, a spin-off of the IFSW USTUTT and a manufacturer of grating-based laser optics that combine multiple functionalities into one component. [36]

The partners of the GREAT project are also companies producing laser systems (Fibercryst SAS, TRUMPF Laser GmbH, Novae Laser, Amplitude Systèmes) or vacuum thin-film coating technologies (Bühler Leybold Optics). These partners together with RWTH Aachen University and Modus Research and Innovation Limited (MODUS) organisation are training providers or hosts for ESR's secondments.

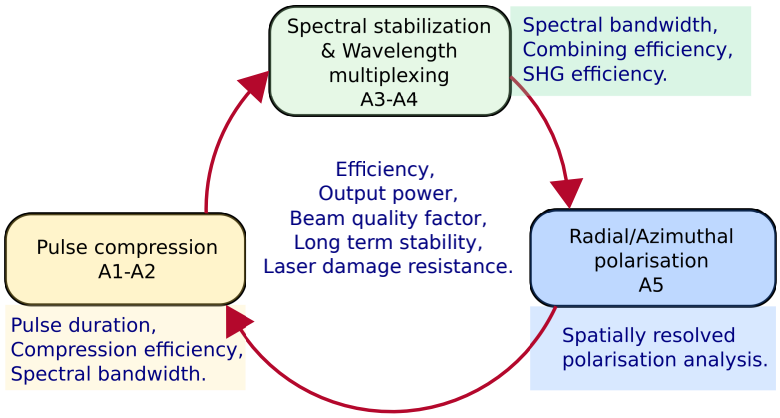

Figure 1.2: Overview of GWS applications and Key Performance Indicators. [9]

1.2 GWS principles of operation and applications

The potential of GWS has been proven for several applications, e.g. the generation of Cylindrical Vector Beams (CVB) with radial and azimuthal polarization, [21, 37, 38], spectral stabilization [39] and wavelength tuning, [17, 40] and pulse compression. [16, 20, 25, 41] However, the application of GWS in high-power lasers have only been investigated by USTUTT in a limited number of scientific papers. [17, 18, 22, 23] Therefore, the GREAT consortium partners join efforts to design, develop, qualify and optimise the GWS for use in high-power lasers. [42, 43]

For GWS applications, the Key Performance Indicators (KPI), summarized in Fig. 1.2, need to be thoroughly analyzed to verify the proper functionalities of the GWS operating in the lasers, for which they have been designed. In sum, the GWS are intended to serve for three purposes in laser systems. The first one is laser pulse compression at 1- and 2- µm wavelengths. These applications are abbreviated as A1 and A2, respectively.[1] The second purpose is to demonstrate spectral stabilization and wavelength multiplexing with diode lasers (A3) emitting in 900-1000 nm range of wavelength. This purpose will be also investigated in the case of solid-state lasers (A4), e.g., Yb:YAG thin-disk and Tm-doped fibre, emitting at 1- and 2- µm respectively. The third purpose is dedicated to generation of Cylindrical Vector Beams (CVB) with radial and azimuthal polarization (A5). The polarization filtering will be realized by the GWS implemented in CW and mode-locked sub-ps pulsed Yb:YAG thin-disk lasers.

1.2.1 GWS principle of operation

The whole idea of GWS is to use the interaction of an incident beam (wave) to the modes that can exist in the waveguide. [16] The operation of GWS is based on resonant diffraction effects. For the clarification of basic principle of GWS operation, we consider the schematics shown in Fig. 1.3. When an incident beam falls on a waveguide (single layer or multi-layer) and there is no grating (Fig. 1.3a), a part of the beam is reflected and other transmitted and no light is coupled into the waveguide. If we implement a grating on the waveguide and the resonance condition is not fulfilled[2](Fig. 1.3b), then the situation is analogous to previous case with exception of additional scattering due to the presence of grating.

[1]The abreviations of applications (A1–A5) are used later in this thesis as parts of description of mirrors and GWS to indicate relevant application.

[2]The resonance condition is occuring only at right wavelength, angle of incidence or polarization

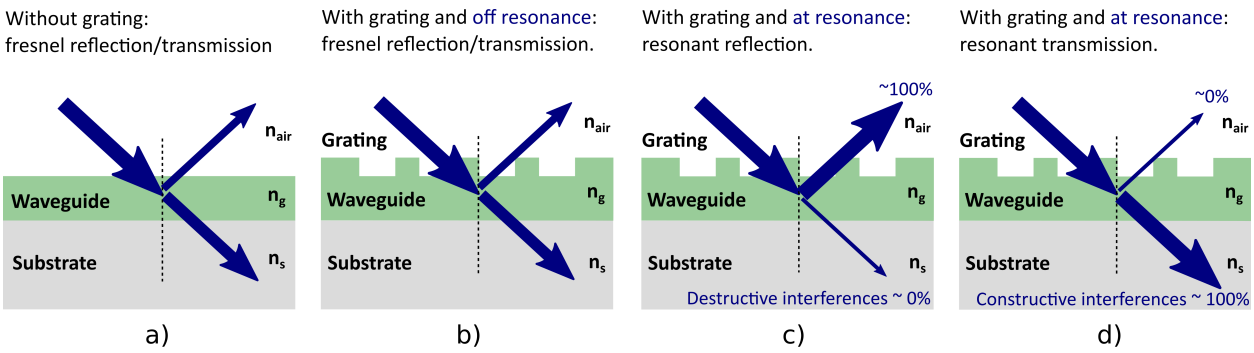

Figure 1.3: Schematics to show role of grating and resonance. Implementation of grating causes additional scattering which is not illustrated.

The mentioned resonance condition occurs only for modes existing in waveguide. To couple the modes into the waveguide, it has to be satisfied the grating coupling condition: [21]

$$n_{\text{eff}} = sin(\theta) + m\frac{\lambda}{\Delta}, \tag{1.1}$$

where n_{eff} is the refractive index of the coupled mode which is depending on the opto-geometrical parameters of the waveguide, θ means the coupling angle of incidence, m stands for the diffraction order, λ is the wavelength of the incident beam and Δ denotes the period of the sub-wavelength grating.

By proper choice of these parameters and waveguide design, the phase shift for destructive interference in transmission can be created (Fig. 1.3c). If we suppress the transmission by the resonant effect, then the very high level of reflectivity can be theoretically reached. Alternatively, the resonant effect can occur with constructive interference in transmission and almost no reflection (Fig. 1.3d). Using appropriate design of the High Reflective (HR) coatings and grating parameters, the incident beam can be diffracted with high efficiency into the 1st diffraction order. The efficiency can theoretically reach 100% thanks to the destructive interference in the zeroth-order reflected beam as shown in Fig. 1.4. [25, 26]

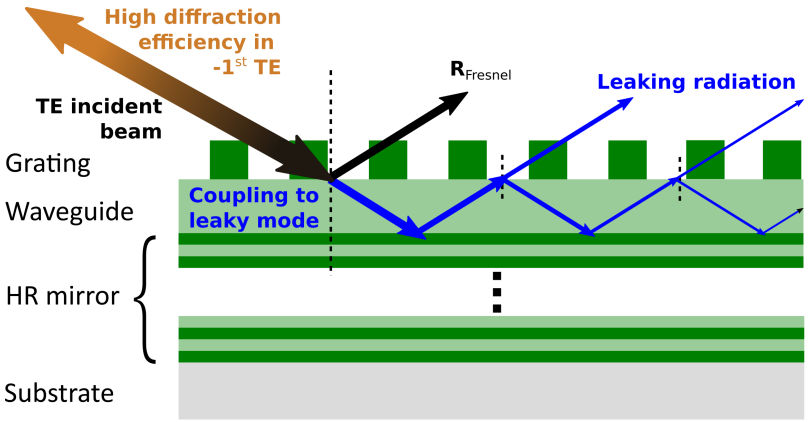

Figure 1.4: Grating waveguide structure in Littrow configuration. [16, 25]

Eq. (1.1) implies that intra- or extra-cavity GWS operating in resonance can be used to control laser beam parameters because the resonant effects occur only for a given wavelength, angle of incidence and effective refractive index. The effective refractive index is a parameter given by the dispersion equation, that is derived

from Maxwell equations and boundary conditions. Since the dispersion equations are different for TE and TM polarizations, the effective refractive indices representing solutions of dispersion equations differ between polarizations. Therefore, at a given angle of incidence and wavelength (and period and diffraction order), the coupling condition (Eq. 1.1) can only be satisfied for one polarization. [21] Using the mechanism to couple the incident free-space beam to leaky waveguide modes can lead to the desired polarization discrimination (Fig. 1.4). The choice of the GWS design thus enables efficient filtering of polarization state.

For TM polarization, the electric field is by definition oscillating perpendicularly to the grating lines, while for TE polarization, it is parallel to the lines. If we consider circular gratings, then the TM electric field has radial shape, whereas TE one shows azimuthal orientation. The GWS with circular lines can thus be used for generation of beams with radially or azimuthally oriented polarizations.

1.2.2 Pulse compression for 1–μm (A1) and 2-μm (A2) wavelength

Commercially available pulse compressors are comprised of gold-coated or transmission gratings and show single pass diffraction efficiencies of only 80-95%. Mixed metallo-dielectric (MMLD) or purely dielectric mirror (MLD[3]) based gratings have been reported [14, 15] with diffraction efficiencies in the -1st order close to 97% and sub-ps laser-induced damage threshold exceeding $1\,J/cm^2$. However, the designs require tight control of the trapezoidal grating shape.

The GWS has been used to demonstrate diffraction efficiencies up to $\sim 99.7\%$ in the 1-μm range. [20] In GREAT, we aim to develop GWS enabling the diffraction efficiency $\geq 99\%$ for a broad spectral bandwidth around 1030 nm, 1070 nm and 2000 nm wavelengths. Besides the diffraction efficiency and broad spectral bandwidth, another parameter limiting performance of high-energy pulse compression gratings is the LIDT. Recently, the GWS based on Ta_2O_5/SiO_2 multilayers showed LIDT around $0.6\,J/cm^2$ for pulse duration of 500 fs at 1030 nm wavelength. [10] The LIDT of GWS can be increased by selection of more resistant coating materials [44] and by design of grating profile (duty-cycle and depth). With such modifications of the GWS design, it is possible to reduce the electric field intensity in the grating ridges as well as the propagation length of the excited mode in the waveguide. [45]

Within GREAT, the ability of GWS to compress pulse duration is intended to be used for development of chirped-pulse amplification (CPA) lasers emitting at 1 μm and 2 μm wavelength. CPA method can be applied to bulk regenerative amplifiers, fiber amplifiers or optical parametric amplifiers and allows the peak power capacity to be extended considerably. [46] We will describe herein the CPA method using an example of femtosecond fiber laser architecture [47] which has similar design to the system to be developed in GREAT.

The CPA system (Fig. 1.5) consists of a passively mode-locked oscillator, a dielectric grating stretcher, three single-pass amplifier stages, and a dielectric grating compressor. [47] The front end oscillator generates femtosecond pulses at high repetition rate (78 MHz) and average power of 150 mW. These pulses are stretched to 800 ps duration using a dielectric reflection grating. Then, the pulses are amplified in three stages comprising double-clad fibres pumped by laser diodes. The stretching to long pulse duration is used since it reduces the peak power to a level, at which detrimental effects (nonlinear pulse distortion or even damage on a component) in the amplifier gain medium are avoided. Finally, the pulses are compressed using two dielectric reflection gratings of 99% diffraction efficiency. Since the compressor gratings are irradiated with very high peak powers, the beam diameter on them has to be large in order to avoid their damage. The CPA technique allowed to produce ultrashort pulses (650 fs) with 10.6 μJ pulse energy at 78 MHz repetition rate providing average power of 830 W. [47]

[3] multilayer dielectric

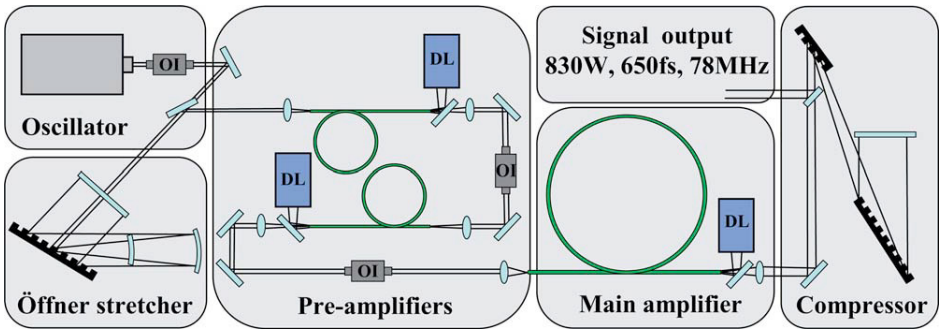

Figure 1.5: Schematic setup of the fibre CPA system. IO - optical isolator, DL - diode laser. The Fig. is taken from [47].

1.2.3 Wavelength multiplexing and spectral stabilization (A3-A4)

The GWS, developed in GREAT, are aimed to be used for spectral stabilization or power scaling via wavelength multiplexing, whose basic principle is shown in Fig.1.6a). These functions of GWS are studied in the GREAT project in both diode lasers (A3) and solid-state lasers (A4). [9] The latter includes Yb:YAG thin-disk, Yb-doped fibre and Tm-doped fibre laser architectures.

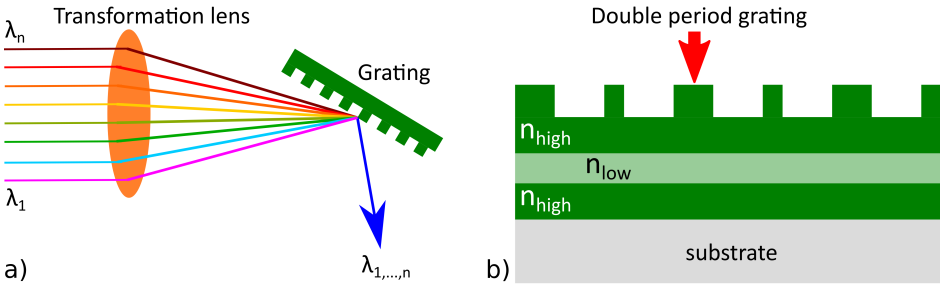

Figure 1.6: a) Schemes of a) wavelength multiplexing and b) double period GWS. [9]

In high-power diode lasers, the wavelength stabilization is commonly realized using Volume Bragg Gratings (VBG). For the diode lasers, GWS represents a promising alternative to VBG. GWS provides a similar spectral response (~ 0.1 nm in FWHM) but shows a broader angular acceptance, which can be achieved by means of a double period grating, see Fig. 1.6b). The GWS operation in diode lasers as wavelength multiplexer is critical for power scaling to reach kW level and high brightness required for the thin-sheet metal cutting.

For solid-state lasers, the wavelength stabilization and selection can be performed using an etalon [48] in combination with thin-film polarizers or Brewster windows. However, such solutions are very limited at high average power due to additional high losses and strong thermal lensing. [9, 16] In GREAT, the GWS will be used as end mirrors of laser cavities, placed at the Littrow angle (-1st order). The project aims to diffraction efficiency exceeding 99.9% ensuring high reflection of radiation back into the resonator. Such a high reflection from GWS exerts a strong wavelength narrowing of laser radiation. In addition, the GWS is polarization selective by design, resulting in a high degree of linear polarization. [22]

In the case of a Yb:YAG thin-disk system, the objective is to stabilize both polarization and wavelength in order to achieve efficient second harmonic frequency conversion inside the laser cavity. As a wavelength and polarisation selective element, the GWS can increase the optical efficiency from 25-30%, reported in [49],

to more than 40% with diffraction limited operation, published in [39]. Furthermore, the GWS can be used as wavelength multiplexing extra-cavity device allowing power scaling of Yb:YAG thin-disk lasers, emitting spectrally stabilized radiation at slightly different wavelengths.

Yb-doped fibre lasers, based on double-clad Large Mode Area (LMA) and large core photonic crystal fibres (PCF) [47] are used in high-power ultrashort pulse amplifiers. The fibre designs are advantageous for high-power operation thanks to their excellent thermo-optical properties, compared to bulk solid-state lasers. For the Yb-doped fibre lasers, the GWS have potential to ensure spectral narrowing, polarization selection or pulse compression of broad band laser emission. Furthermore, the use of GWS as a cavity mirror at close to Littrow angle will avoid the need of an additional polarizer or selective element within the laser cavity.

Tm-doped fibre lasers are promising architectures for high-power generation at 2-µm wavelength range. Although a kW class power was demonstrated [50], the power-scaling is limited by heat generation in the Tm-doped fibre. A solution for power-scaling might be application of GWS as a wavelength multiplexer to spectrally combine several Tm-doped fibre lasers emitting moderate power.

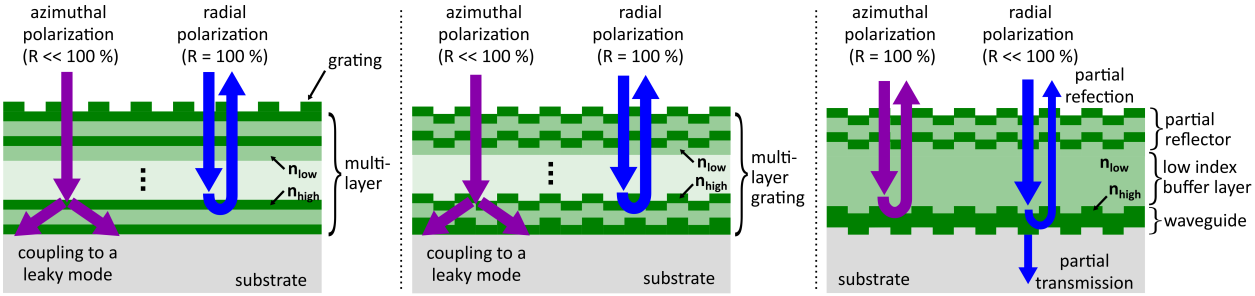

Figure 1.7: Schematic of the GWS with the radial/azimuthal polarizing mechanism. [9]

1.2.4 Radial and azimuthal polarization (A5)

Radially and azimuthally polarized beams are reported to be advantageous for both industrial applications and research. The beams of radial or azimuthal polarizations have significant positive effect on efficiency and quality of material processing, i.e. drilling [51,52], welding [28] and cutting [53] of metals. It has been shown in [54] that a radially polarized beam can be focused to a much smaller size than a linearly polarized one. The result shows potential of radial polarization for data storage [55], lithography [56] or resolution-enhanced microscopy. [57] Radially or azimuthally polarized beams have also gained attention for acceleration [58], trapping [59] and controllable delivery [60] of particles, imaging of molecule orientation [61], or as optical tweezers. [62,63]

In GREAT, the GWS will be used for both intra-cavity generation and extra-cavity conversion of high-power beams. In the case of intra-cavity design, the polarization function will be ensured by a circular grating[4] acting as a cavity end mirror or output coupler. The polarization function is achieved by introducing a significantly higher reflectivity of the lasing polarization state compared to the other polarization states. This is accomplished by coupling the incident beam (polarization to filter out) to a guided or a leaky mode (in the substrate) of the GWS, see Fig. 1.7. [21,37] For the extra-cavity design, the GREAT project aims to use the form-birefringence effect [64] to produce half-waveplates that allow the polarization of the beam to be transformed from linear to radial or azimuthal, see Fig. 1.8.

[4] binary grating with circular grating lines

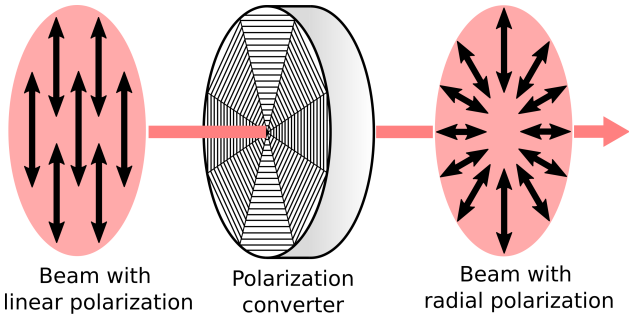

Figure 1.8: Principle example of linear to radial polarization conversion (example with 8 segments of half-wave plates). Conversion to azimuthal polarization can be obtained by a 90° rotation of the incident polarization of the polarization converter. [9]

1.3 Laser damage resistance work within GREAT

To qualify the reflective optical components, developed in GREAT for use in lasers, it is necessary to precisely determine the sample properties at the different stages of the project. This includes properties at a given step of the fabrication, e.g., refractive index of a particular material and grating profile parameters (duty-cycle, groove-depth, period). For the qualification of final reflective components, thin-film multilayer based mirrors and the GWS, the key parameter is the laser damage resistance as this parameter limits the performance and the lifetime of solid-state lasers.

In this thesis, we aim to evaluate the laser damage resistance in terms of laser-induced damage thresholds (LIDT) and laser-induced contamination (LIC). For the evaluation, LIDT and LIC tests of optical materials or structures should be done in conditions as close as possible to the GWS applications. We thus use laser sources working in the femtosecond/picosecond pulse regime, which is relevant to the GWS applications for pulse compression, radial and azimuthal polarization conversion and spectral stabilization.[5]

The experimental work presented in this thesis was done in these GREAT partner institutions: Institut Fresnel, Alphanov technological centre, HiLASE centre and ELI Beamlines facility. The access to LIDT setups in these institutions enabled to make tests at conditions close to the ones of final applications. Furthermore, thanks to GREAT project, we tested broad variety of deposited coatings and several gratings that were designed and fabricated by other ESRs.

Since the GREAT project suffered major delays related to COVID-19, there is no GWS tested within this work.[6] However, the thesis summarizes results on single layers, multilayer coatings and first generation of gratings etched into fused silica substrates. The designs of multilayer coatings are tightly linked to GWS and represent necessary stages of their development. The results obtained with coatings are used as input for theoretical predictions of GWS damage resistance using modeling codes based on the Rigorous Coupled Wave Analysis (RCWA).

[5]The spectral stabilization is of interest for ps/fs Yb fibre architectures and also for CW diode lasers and Yb:YAG thin disk systems.

[6]The LIDT tests with GWS were not done till the time of writing this thesis, but they will be done in the next months.

1.4 Conclusion

Laser applications in areas such as material processing, telecommunication or biochemistry require functional, damage-resistant components that can adjust the wavelength, polarization or pulse duration of light. Such adjustment of laser light properties can be done using Grating Waveguide Structures (GWS), optical elements, whose operation is based on resonant diffraction effects. GWS development includes their design, fabrication, characterization, and implementation in laser systems, and the entire production chain is a central concern of the GREAT project. [8, 9] The role of this PhD work within the GREAT project is to test the damage resistance of coatings and structures corresponding to the various stages of the GWS production chain, namely single-layer coatings, multi-layer reflective structures, and the first generation of grating structures.

Chapter 2

Sub-picosecond laser-induced damage on dielectrics

The chapter is devoted to sub-picosecond laser-induced damage of dielectric materials. The studies of sub-ps laser damage on wide bandgap dielectrics are gaining importance for many practical applications covering industrial micromachining and development of optical components. It is the damage onset on optical components that determines the limit of useful performance of solid-state lasers.

The understanding of damage initiation process on the dielectric materials is important for proper use of high-power solid-state lasers. Based on the knowledge of the material damage thresholds, more resistant optical components can be designed and implemented into lasers. Lasers that can withstand damage of optical components, capable of operating for long periods of time, are demanded in many applications. For example, it is laser cutting, drilling, welding, shock-peening, material structuring, cleaning, engraving/marking or sealing. Sub-picosecond laser pulses can also be used to mitigate surface damages caused by another laser. This application is particularly important for extending the lifetime of large-scale optical components. [65] The role of research in sub-ps laser damage is also increased by the significant number of high-power laser infrastructures existing around the world. [66]

The chapter summarizes fundamental knowledge of laser damage on dielectric materials induced by single or multiple pulses of sub-picosecond duration. In first section, we introduce the class of dielectric materials using their band energy structure. We emphasize the sensitivity of dielectric media to the action of an external intense electromagnetic wave. The media are subjected to the phenomena of nonlinear optics, if a high laser intensity is applied.

In the second section, we define laser damage as an observable irreversible material change and differentiate it from reversible phenomena and non-observable material modifications. We will look at the causes of material damage initiation in different irradiation regimes. We will see that material heating is not only a matter of CW lasers, but also of lasers with high-repetition rates. The causes of damage initiation for nanosecond and femtosecond regimes will be discussed. While the damage in the nanosecond regime arises from defects, the damage threshold in the femtosecond regime is rather due to intrinsic material properties.

In the third section, we will focus on single-pulse laser damage that is of academic interest. The laser damage in sub-ps regime is a consequence of nonlinear excitation processes such as multi-photon and impact ionization. Apart from the ionization processes, we will also describe the relaxation processes including intraband and interband processes. To simulate the damage threshold results, we will show an approach based on rate equations whose predictions correspond to the experimentally observed LIDT scaling laws.

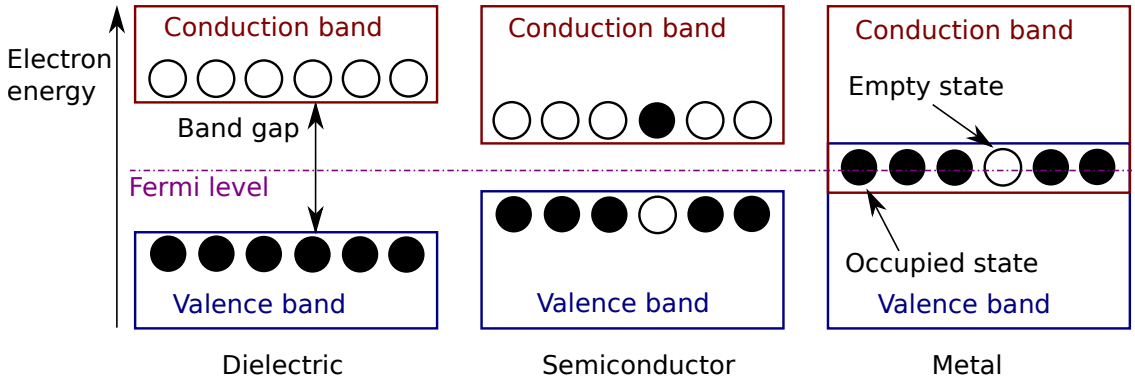

Figure 2.1: Energy bands with electrons of metals, semi-conductors and dielectrics. [67]

The analytical approach is a useful tool for reproduction of experimental trends. The published single-shot results will be presented in dependence on pulse duration, wavelength, material bandgap and refractive index. From the published data, phenomenological scaling laws are deduced. The section devoted to single-shot interaction will terminate with discussion on defect-induced damage and effect of nodular defects on LIDT in sub-ps regime.

The last section deals with multiple pulse interactions that are of practical interest. We will present published damage threshold results on dielectrics using damage characteristic curves. To understand the decreasing damage threshold fluence with increasing pulse number, we will derive an expression for electron density of conduction band. A particular attention will be paid to the damage thresholds generated by two pulses. We will investigate the damage characterisitc curves that provide information about material defects. Finally, the issue of damage growth will be presented.

While the focus of this chapter is on thin films, many implications are valid for bulk materials as well.

2.1 Electronic structure of dielectrics.

In a material, the cohesion of atoms is ensured by the pooling of electrons in more or less directional bonds. A perfectly free electron can have any positive energy level. In an isolated atom, the electrons have energy values corresponding to discrete levels. In a solid material, electrons can have energy values in discrete intervals. The permitted and forbidden bands of a material are defined according to Bloch functions, solutions of the Schrödinger equation. Depending on the filling of the bands with electrons, the material does not exhibit the same electrical behaviour. If there is a band that is not completely filled, then the material behaves as a conductor. If no band is partially filled, then the material is insulating. [67–69]

The Fermi level corresponds to the highest energy of an electron in the ground state, i.e. at a temperature of 0 K. This state allows to classify the materials according to their electronic properties, see Fig.2.1. Metallic materials have a Fermi level in a permitted band, which gives the electrons a great freedom thanks to the directly accessible states which enables electrical conduction. In the case that the Fermi level is located inside a bandgap, then the material is called dielectric. The fully filled band that is closest to the Fermi level is called the valence band and the empty band located above the level is called the conduction band. In the case of low energy band gap (< 3eV), the dielectric material is defined as semiconductor material.

The class of material has influence on the process of damage onset, i.e. energy transfer from the laser pulse to the material. Metals are excited through linear absorption in a thin skin layer near the material

surface. In semiconductors, linear absorption occurs if the photon energy is larger than the energy of the forbidden band. In high quality optical dielectric materials, linear absorption can be neglected and the initial energy deposition occurs via nonlinear absorption. [70]

2.1.1 Electric field generates polarization density in dielectrics.

A dielectric material does not contain freely macroscopically moving electrical charges. The flow of an electric current is therefore impossible, it is an insulator. Glasses, ceramics, most of plastics, oils, pure deionized water or even dry air are all dielectric materials used in electronic and optical applications for their remarkable properties. Although they do not allow to pass a current flow in material, the dielectric medium remains sensitive to the action of an external electric field. [69]

Indeed, at the time t, the electric field $\mathbf{E}$, spatially defined by the position vector $\overrightarrow{r}$, generates in the dielectric material a polarization density $\mathbf{P}$ which is expressed, in a linear medium, according to the Equation (2.1), in which ε_0 stands for the permittivity of the vacuum and $\chi^{(1)}$ denotes the dielectric susceptibility tensor of the material:

$$\mathbf{P}(r,t) = \varepsilon_0 \chi^{(1)} \mathbf{E}(\overrightarrow{r},t). \tag{2.1}$$

According to Maxwell's equations that govern the propagation of an electromagnetic wave, the electric field propagation equation can therefore be developed as:

$$\bigtriangledown \times \bigtriangledown \times \mathbf{E}(\overrightarrow{r},t) + \frac{1}{c^2}\frac{\partial^2}{\partial t^2}\mathbf{E}(\overrightarrow{r},t) = -\frac{1}{\varepsilon_0 c^2}\frac{\partial^2}{\partial t^2}\mathbf{P}(\overrightarrow{r},t), \tag{2.2}$$

where c is the speed of light in vacuum. In the case of an isotropic medium, i.e. χ^1 scalar, the Equation (2.2) can be simplified to formula known as Helmholtz equation:

$$\Delta\mathbf{E}(\overrightarrow{r},t) - \frac{n_0}{c^2}\frac{\partial}{\partial t^2}\mathbf{E}(\overrightarrow{r},t) = 0. \tag{2.3}$$

The refractive index n_0 can be expressed as a function of relative dielectric permitivity of a given material:

$$n_0^2 = 1 + \chi^{(1)} = \varepsilon_r. \tag{2.4}$$

In the case of higher laser intensities, the $\mathbf{P}$ polarization vector can no longer be expressed linearly as in Equation (2.1) and it is necessary to consider the higher orders of its decomposition into the electric field power series:

$$\mathbf{P}(r,t) = \varepsilon_0 \sum_{1}^{i} \chi^{(i)} [\mathbf{E}(\overrightarrow{r},t)]^i. \tag{2.5}$$

Here we introduced the field of non-linear optics. Non-linear effects can have important contributions in our studies and we will come back to it in next sections.

2.2 Laser damage is irreversible material change.

When low-intensity light passes through a transparent substrate, e.g. fused silica, and then falls on a reflective surface or passes through an absorbent medium, there is observed little or no effects. [71] As the beam intensity increases, a whole range of reversible interactions come into action. This includes absorption, temperature rise, expansion, distortion, strain, non-linear absorption/transmission and reflectance. The range of effects covers also electro-optical effects, second and third harmonic generation, optical parametric

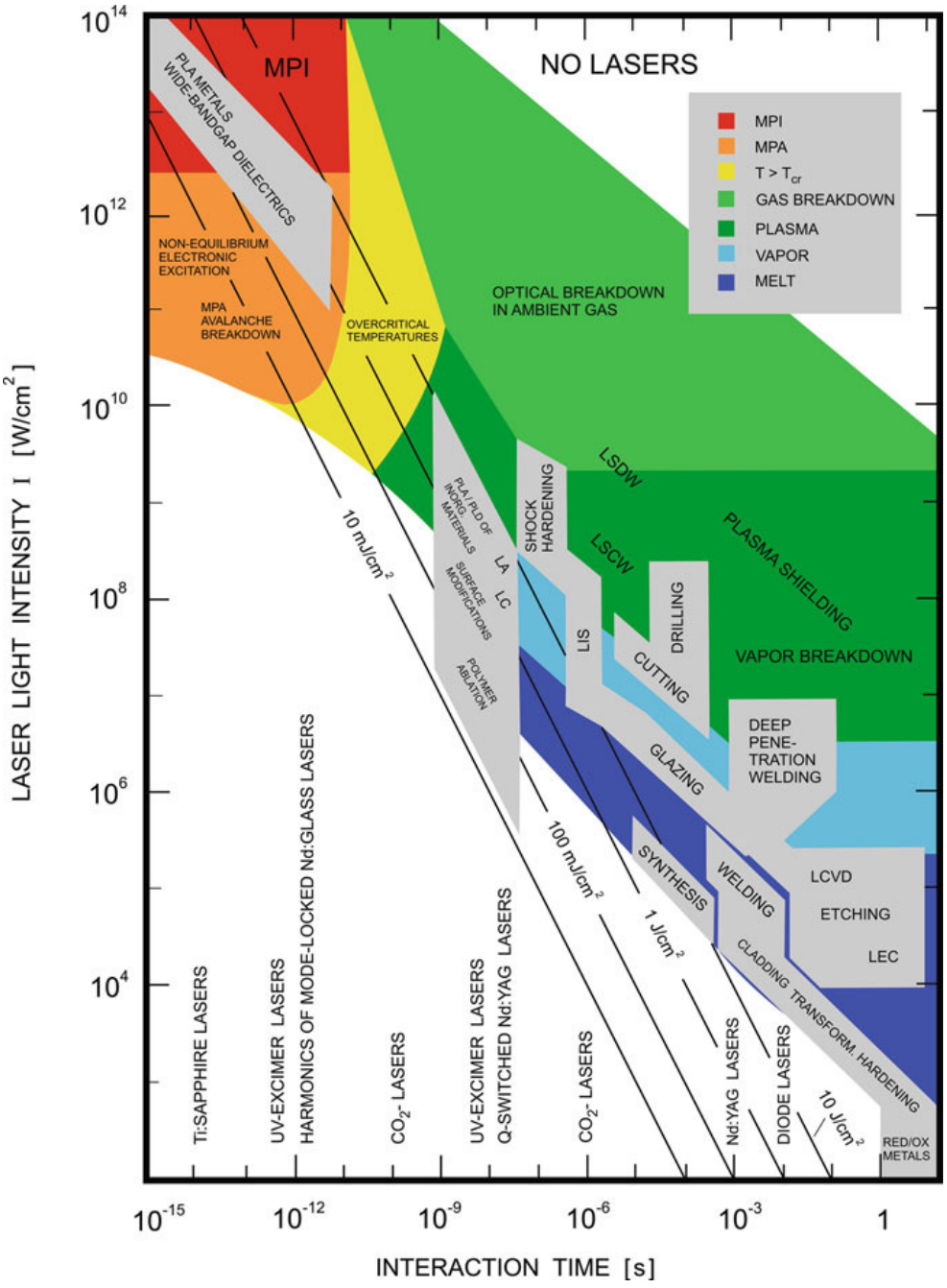

Figure 2.2: Laser applications and processes in material as a function of interaction time, laser-light intensity and pulse fluence. PLA/PLD: pulsed-laser ablation/deposition. Surface modifications include laser-induced oxidation/nitridation of metals, surface doping, etc. LA: laser annealing. LC: laser cleaning. LIS: laser-induced isotope separation/IR-laser photochemistry. MPA/MPI: multiphoton absorption/ionization. LSDW/LSCW: laser-supported detonation/combustion waves. LCVD: laser-induced CVD. LEC: laser-induced electrochemical plating/etching. RED/OX: long pulse or cw CO_2-laser-induced reduction/oxidation. Laser-light intensities exceeding 10^{16} W/cm^2 generate X-rays that gain increasing importance in nanotechnology. Figure taken from [3].

oscillation and self-focusing. Many of these effects can be advantageously used in optical engineering, e.g. for generation of new wavelengths or optical limitation.

In the case of fs pulse of low intensity, the propagation in a dielectric (transparent) material is solely affected by dispersion and diffraction since the interaction process is controlled by a dielectric constant, i.e. refractive index. [70] Laser field activates (almost) immediately the harmonic dipole oscillations and the dielectric material comes back to its initial state after the pulse.

As fluence (intensity) increases, dipolar oscillations evolve into anharmonic, and non-linear optical processes, such as self-phase modulation and harmonic generation, are possible. [72, 73] The non-linear interactions can induce heat effect that can lead to material modifications such as refractive index changes. In the case of certain glasses and polymers, the laser-induced permanent change of refractive index can be used for fabrication of waveguide structures or optical modulators. [74]

A brief overview of laser-induced material processing as a function of interaction time, laser light intensity and pulse fluence is shown on Fig. 2.2. In the diagram, different kinds of laser systems and types of processed materials are included. [3] The diagram summarizes material changes for range of interaction times from several seconds to 1 fs. In the case of wide-bandgap dielectrics that are used in optical components, lasers generating femtosecond (sub-picosecond) pulse duration are relevant for their processing. The corresponding pulse fluences are around 0.1–10 $\mathrm{mJ/cm^2}$ and laser light intensities $\geq 10^{11}$ $\mathrm{W/cm^2}$. Knowledge of the precise levels at which the laser-induced changes take place is useful for laser machining (drilling, welding, cutting - for both the material engineering and laser surgery), for the design of laser cavities and for material research (spectroscopy).

The sufficiently high level of laser beam energy, at which the irreversible and catastrophic material changes occur, is commonly termed laser-induced damage threshold (LIDT). The parameter describing change of optical performance characteristics of the cavity components represents the main limitation in the design and use of laser systems and their miniaturization. [71] Laser-induced damage can occur on the front or rear[1] faces of the optical components, in the bulk part of components or at the interfaces between two components[2]. Damage of laser systems can be caused by reflections between components. In order to avoid laser-induced damage, it is important to know both the component physical parameters and how they are integrated into a laser system.

For femtosecond lasers, the well-defined damage threshold is reached as visible surface (crater) or bulk (void, crack) damage is observed. [70] If the laser fluence is even higher than the damage threshold, then material removal, attractive in micro- and nanostructuring, occurs. [4] Therefore, the damage threshold can be, in a simplified way, interpreted as value between fluences of material modification without removal (refractive index change) and ablation. [70] In this work, however, we define laser damage as any permanent laser-radiation-induced change on a sample, which includes not only ablation but also material modifications without removal observed by an inspection technique, e.g. color changes on films, see Fig. 2.3. In accordance with international standards [75], we mainly prefer to use differential interference contrast microscopy as the inspection technique. For the majority of dielectric materials, the damage thresholds range in relatively narrow band between fluences of typical nonlinear interactions and the laser intensity that allows photo-ionization. [70] The last interaction process is of great importance when the intensity approaches the magnitude of the Coulomb field between electron and nucleus in an atom.

The theory, mechanisms, measurement and improvement of the LIDT of optical components is the subject of intensive research from 1960s to the present. The research in LIDT field remains very active [76] due to the complexity of involved mechanisms, the progress in optical components development and emerging laser

[1] depending on the direction of the laser beam
[2] especially if they are in contact

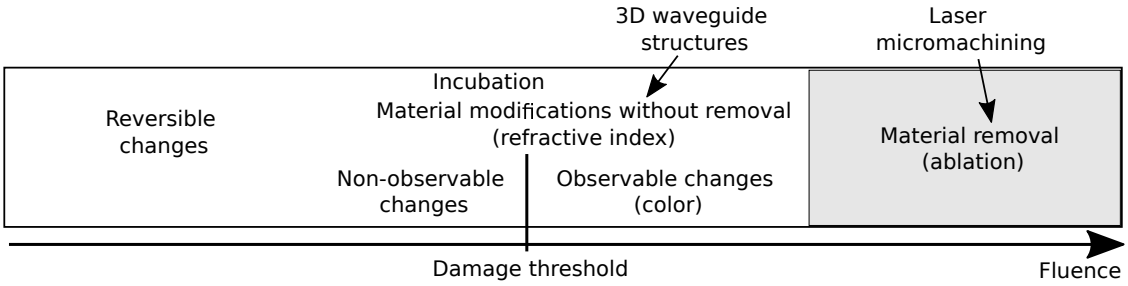

Figure 2.3: Symplified schematic of femtosecond laser-dielectric material interactions in dependence on fluence. [70]

applications. It was the development of stable coatings for ultrashort pulse systems that enabled introduction of femtosecond (fs) lasers, which in turn opened way to industrial and medical applications.

Research in laser-induced damage covers a wide range of optical elements (dielectric and sol-gel coatings, optical glasses, metal films, laser crystals and glasses, crystals used in polarizers, Q-switches, harmonic generators, and parametric oscillators) [2], but our work will be focused on dielectric coatings. The coatings are essential parts in ultrashort pulse laser systems to control the laser emission temporally, spectrally or spatially. Furthermore, the coatings used in mirrors or gratings are one of the main limits for achieving higher performances of lasers.

In the following sections, we will introduce parameters having effect on degradation of optical components. Then we will discuss physical mechanisms involved in ionization or relaxation processes. We will describe characteristics for single-shot and multiple-shot interactions. Finally, a model describing LIDT based on rate equations will be presented.

2.2.1 Material heating can result in laser damage.

When a beam of laser radiation falls on the surface of an optical component or material, a part of the energy is absorbed and then results in heating of the material. [77] The material heating arising from the absorption of laser energy can be a cause of damage in continuous wave (CW) operation, long pulse durations (up to 10^{-8} s) and high-repetition-rate regimes. [71] In the case of ps/fs pulse, the material can be also damaged by heating after the non-linear absorption of energy. Material damage via heating is a function of laser parameters (wavelength, pulse duration and pulse repetition frequency), the relative beam size and the tested material or component; the ambient conditions; the mounting conditions; and the optical, mechanical and thermal properties of the irradiated material. Thermal damage will normally appear on the point of material surface that corresponds to the beam center unless the damage is caused by stress or localized absorbing imperfections within the material.

The evolution of material peak temperature as a function of time in terms of the pulse temporal shape and pulse repetition rate is shown on simplified schematic on Fig. 2.4. In the case of short triangular pulses, Fig. 2.4a), the temperature peak is achieved at or after the intensity maximum of pulse. In contrast, the maximum temperature of square and/or long pulses occurs at the end of the pulse, see Fig. 2.4b). The low pulse repetition rate irradiation regime, Fig. 2.4c), indicates the temperature oscillations in line with the repetition rate and it can grow from pulse to pulse. In the case of short-pulse high repetition rate regime, Fig. 2.4d), the temperature at the center of the sample gradually rises. The temporal evolution, apart from the spiked shape, shows the same characteristic as the temperature of material irradiated by a CW beam, see Fig. 2.4e).

When laser energy is absorbed, the temperature rises, which leads to thermal expansion, deformation,

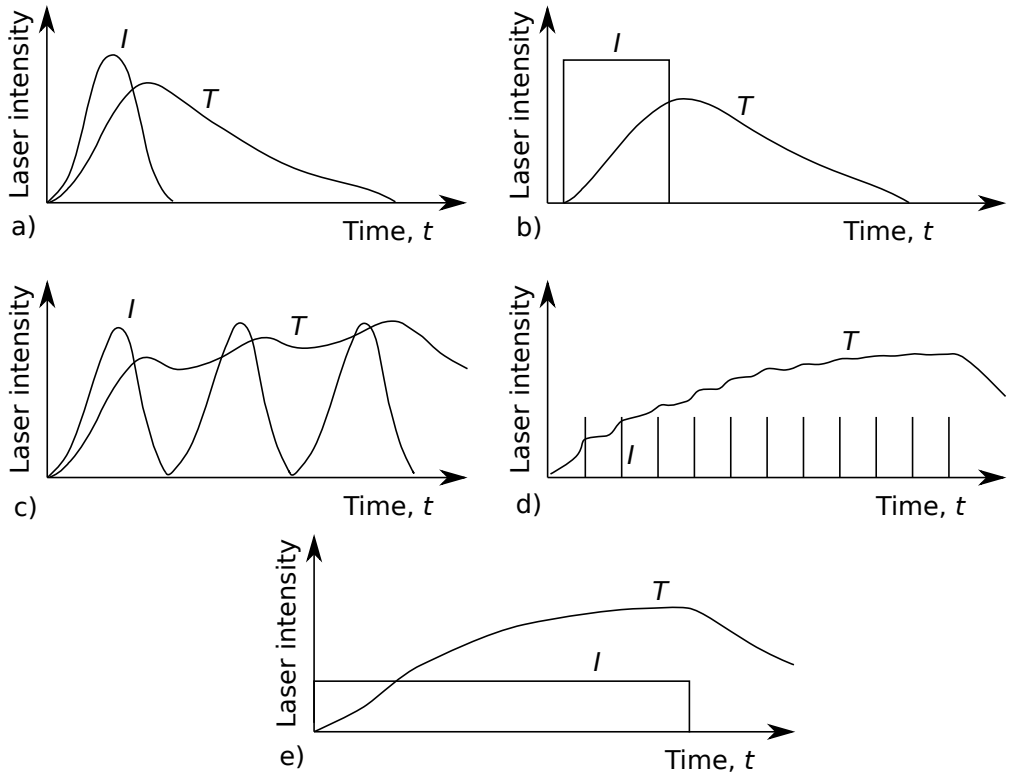

Figure 2.4: Material temperature (T) evolution as a function of laser irradiation regime. The material is irradiated by the laser intensity I. [77]

birefringence, movement of internal defects, cracking, melting and catastrophic shattering. [77] In addition, high peak power densities can result in non-linear absorption and transmittance, electro-optical effects, second harmonic generation, optical parametric oscillation and self-focusing. All these effects can increase the amount of absorbed energy and may lower the observed LIDT. A combination of the above mechanisms may cause a change of beam shape, induce birefringence, or shatter or melt the optical component.

The interaction mechanisms are a function of pulse duration. For long pulse durations of CW exposure, an equilibrium can be reached between the absorbed energy and the dissipated heat by conduction. This is highly dependent on the beam size and the LIDT is therefore size-dependent. For short pulse duration (below 1 µs typically), the amount of absorbed energy per surface unit (J/cm^2) drives the process independently of spot size. However, in the case of high transmission materials, the thermal damage threshold is so high that other damage mechanisms come into play before strict thermal effects occur (before we reach high temperature and damage). The mechanisms include dielectric breakdown of pulse duration of $\sim 10^{-8}$-10^{-10} s, avalanche ionization in the case of pulse durations of 10^{-10}-10^{-13} s, and multiphoton absorption for pulse durations lower than $\sim 10^{-13}$ s. [77]

2.2.2 Defects can initiate laser damage.

An impulse is said to be long when its duration is larger than the relaxation time of the irradiated material, i.e. the time of energy transfer from the electrons to the crystal lattice. [69] In this case, the thermodynamic equilibrium is achieved during the pulse duration and a damage appears when the energy transferred from

the pulse exceeds a threshold that can be related to melting or sublimation temperature of the material.

In the nanosecond regime, the damage process is the result of several physical processes involving absorption, heating, phase changes of materials, hydrodynamic processes and plasma formation. [78] Since nanosecond pulses are relatively long compared to the time scales of these processes, small defect precursors can trigger a cascade of events that can lead to micro-explosion and damage. [78] The laser-induced damage is thus mostly related to the randomly distributed material defect sites, even if their concentration is low. [79] The nanometer scaled particles or structural defects can introduce additional energy levels into the dielectric band gap. [80] These structural defects are located near the surface in micro-fractures resulting from mechanical movements during polishing processes. [81] Other type of defects that were also observed in silica are residues of abrasives produced within the polishing steps, scratches or bubbles of macroscopic size. These imperfections represent the critical factor initiating the damage of optical components in nanosecond scale. The defect absorption can result in spot damage by direct heating and by supplying seed electrons for impact ionization. [82] The imperfections can lead to thermal phenomenon (melting, evaporation) or mechanical disruption (cracking) or serve as light amplifiers causing damage further in the material. [83] The LIDT in nanosecond regime is thus a function of material quality and defect density. Therefore, LIDT determination is a probabilistic phenomenon that requires thorough statistical analysis. [81] The further improvement of nanosecond LIDT of optical components is a question of fabrication technology steps and correct handling in a clean environment.

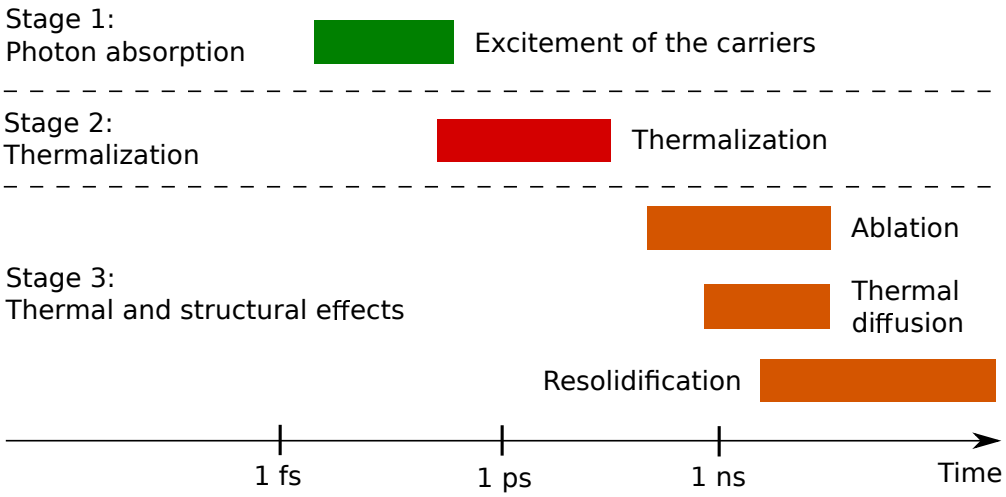

Figure 2.5: The different mechanisms involved in the femtosecond laser-induced damage phenomenon over time. [69]

2.2.3 Intrinsic material properties are important for laser damage in fs regime.

If the pulse duration is shorter than the relaxation time, which is in picosecond range for dielectrics, the excitation and relaxation processes are separated, see Fig. 2.5. [69,80] The ionization of material is driven by multiphotonic absorption since other deposition processes cannot assist due to the short pulse duration. [84] The laser-induced damage process is governed by plasma formation of excited electrons. The damage occurs when the frequency of the electron plasma reaches the excitation frequency of the laser, leading to strong energy coupling in the material.

The femtosecond damage formation of optical components is related to both material characteristics and defects. In comparison to picosecond and nanosecond pulses, the femtosecond laser damage is much more

deterministic. [70, 85] Due to their higher peak intensities, femtosecond pulses can effectively excite band-to-band transitions in dielectric materials via multiphoton ionization, which is dominant in high-quality bulk materials and coatings. [70] Therefore, the femtosecond single pulse damage thresholds of uniform, high-quality dielectric films have uncertainties of only a few percent. This assertion should be however moderated in the case of optical coatings, since macroscopic defects can induce local-intensity enhacement and facilitate the ionization process and thus initiating the localized damage. [86, 87]

By contrast, when multiple femtosecond pulses interact with material at higher repetition rate, the material does not relax completely between the successive pulses. The interaction can result in creation of new midgap levels, i.e. laser-induced defect states. Together with the native traps they facilitate the material ionization and thus decrease the damage threshold.

Since the shorter pulses require lower fluences to produce material disruption, the deposited energy is lower, leading to a more precise ablation or modification of the material. [88] The femtosecond pulses have been applied in areas involving material removal with submicron precision, such as micromachining, electronics, data storage, ophthalmic surgery or drug release. [89] Many experimental and theoretical studies have been carried out to investigate the mechanisms of laser damage by femtosecond pulses. Nevertheless, the theoretical models give only partially satisfactory agreement with the observations made experimentally. Laser damage on ultra-short time scales is still an active area of research. Regarding pulse duration, damage studies on dielectric materials have been extended to pulse durations as short as 5 fs using Ti:sapphire laser. [90]

2.3 Single-pulse interactions

Single-pulse fs interactions are mostly of interest to academics. Single pulse can essentially damage the original material state, i.e. the material without laser-induced changes that accumulate during exposure to a pulse train. [70] The first part to be discussed in this section will be the excitation mechanisms leading to a critical electron density, i.e. formation of a plasma absorbing the incoming laser radiation, in the conduction band of dielectric materials. General scaling laws of the single-pulse fluence-producing damage will be introduced and compared with published experimental data.

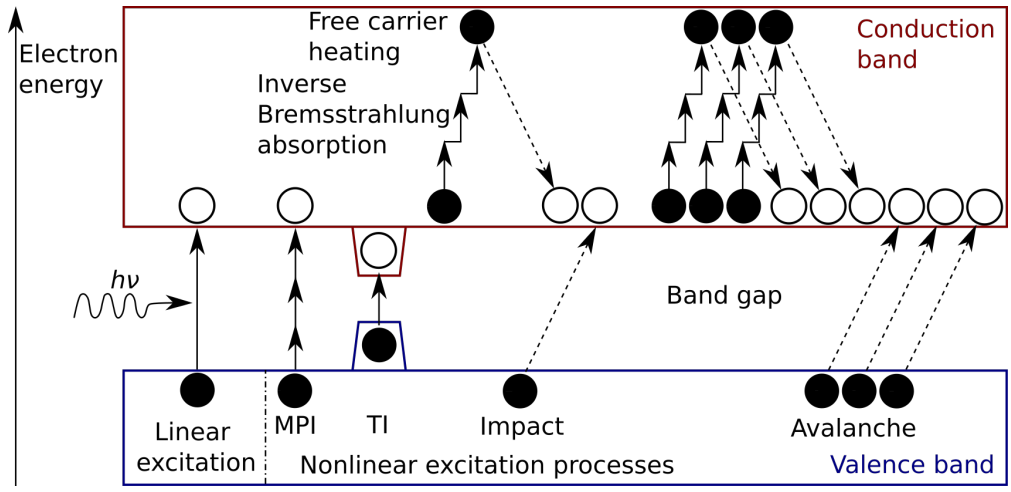

Figure 2.6: Diagram of electron excitation processes. MPI - multiphoton ionization, TI - tunneling.

2.3.1 Ionization processes

When the photon of energy higher than bandgap is passing to the material, the absorbed photon energy can lead using photoelectric effect to excitation of electron from the ground state to the conduction band. For materials of higher-energy electronic bandgaps, the linear photoionization is not possible because one photon does not have the sufficient energy to excite electron through the whole bandgap directly. However, when the material is subjected to a high intensity field, two main non-linear absorption phenomena may be presented: multi-photon ionization (MPI) or tunneling effect (TI). In multi-photon ionization, an electron is excited by the absorption of several photons whose total energy is higher than the width of the band gap. During tunnel effect ionization, a strong electric field helps to lower the Coulomb barrier that binds an electron to its atom and thus facilitates its excitation using a single photon. Once the electrons are in the conduction band, they have the possibility to absorb photons again, which leads them to higher accessible energy states. This phenomenon is called the inverse Bremsstrahlung process. The electron is thus accelerated and has very high energy. By a collision effect with the atoms of matter, this highly energetic electron can yield its energy to a valence electron and promote its transfer to the conduction band. This effect is called impact ionization. The electrons already excited to the conduction band can in turn absorb the photon energy by the inverse Bremsstrahlung process. The repetition of this phenomenon is called electron avalanche. [81]

The inverse Bremsstrahlung process is also known as free-electron absorption, though, a completely free electron is unable to absorb photons since the conservation of energy and momentum cannot be satisfied simultaneously. However, electrons localized in the conduction band interact with the lattice when they interact with the light pulse. The law of momentum conservation is thus fulfilled due to the interaction of electrons with phonons, which leads to the heating of the electrons. [70]

2.3.2 Relaxation processes

The excitation processes lead to the ionization of the irradiated material and the creation of free carriers. The material then tends towards thermodynamic equilibrium which can be achieved through various relaxation phenomena including intraband and interband processes. The intraband processes include electron-electron and electron-phonon relaxations. These processes are very fast, take a few hundred femtoseconds, and can therefore take place within a sub-picosecond laser pulse. [81]

During the electron-electron relaxation, the energy of an excited electron is transferred to another electron. The electron population in the conduction band is not reduced as well as the total energy. This represents also the electrical conduction processes in metals, where the electron density within conduction band is very high. [81]

In terms of electron-phonon relaxations, the charge carriers lose or gain energy and momentum by emitting or absorbing a phonon, i.e. a vibration quantum that corresponds to the harmonic oscillations in the material lattice of ions. Phonons carry a weak energy which is transferred to the lattice and leads to the heating of the material. The process can be shredded by the other electrons in the conduction band. However, in a dielectric, the low electron density in the conduction band makes this electron-phonon relaxation phenomenon very present.

Concerning the interband relaxations, we can distinguish radiative relaxations by direct and indirect recombination. In the case of radiative relaxations by direct recombination, the excited electron reduces its energy by recombining with a hole and emitting a photon. The process has a long duration, around 1 ns, and represents the essence of operation of solid-state lasers.

The indirect recombination relaxation, by contrast, is based on charge trapping, a process in which the electrons are de-excited to energy levels within the band gap. These intermediate levels can be of natural

origin, introduced by crystalline defects, or they can be caused by an excitation of the material. Indeed, when an electron is excited, it leaves a positive charge in the valence band called a hole. The localization of a hole and an electron on neighboring sites can lead to a deformation of the crystalline lattice which makes an intermediate electronic state stable and therefore facilitating the trapping of an electron. This phenomenon of electron self-trapping is called self trapped exciton (STE). If the intermediate states allowing charge trapping are located close to the conduction or valence bands, then the terms of shallow traps (ST) or deep traps (DT), respectively, are used. The characteristic times of these processes vary from a femtosecond to a hundred picoseconds and depend on the materials. [91]

The formation of STE makes the ionization of materials easier. The created intermediate energy levels within bandgap facilitate the access of electrons to the conduction band by reducing the energy required for their excitation and thus they make the photon absorption more efficient. This phenomenon, which appears after several irradiations, corresponds to the material fatigue or incubation effect.

2.3.3 Damage modeling by rate equations

General considerations

The accurate determination of damage threshold in optical materials induced by sub-ps laser pulse is a question that various theoretical models try to answer. The numerous models use a critical electron density as a criterion for dielectric breakdown damage. [70] The most comprehensive models are based on the Boltzmann or Fokker-Planck equations and aim to calculate the density of states[3] within conduction band (occupation vs. energy). [84, 92–94] These models do not only include inter-band transitions, but also electron-electron and electron-phonon interactions. Although they are suitable for reproducing experimental trends, the absolute predictions are very difficult due to the numerous poorly known material parameters. By contrast, the reproduction of sub-ps LIDT experimental data is often possible through an analytical approach based on rate equations, that consider conduction band as a single energy level and use phenomenological cross sections and relaxation times. [84, 89, 94, 95] The results produced in this way indicate the experimentally observed LIDT scaling laws and serve as a useful tool for practical applications.

Single rate equation

Whatever the real damage mechanism, energy must be delivered from the laser to the dielectric material, requiring electronic transitions from the valence band to the conduction band. [70] If conduction band is defined as a single energy level with a population density N, the electron density of conduction band can be expressed using the following rate equation:

$$\frac{dN}{dt} = K(I) + A(I, N) - L(N). \tag{2.6}$$

The electron density in conduction band is thus increased by multiphoton ionization[4] rate $K(I)$ and impact ionization rate $A(I, N)$ and decreased by relaxation process rate $L(N)$ out from the conduction band. The depletion of valence band can be often neglected since the maximum density of excited electrons N_{crit}, removed from the valence band, is several orders of magnitude lower than a typical amount of electron density in the valence band. [70]

For a monochromatic laser radiation, the role of multiphoton ionization rate $K(I)$ is described in the Keldysh theory, see Fig. 2.7. This theory uses the γ parameter, which expresses the relative proportion of

[3] the electron distribution function

[4] Multiphoton ionization together with avalanche ionization is termed as photo-ionization.

multiphoton absorption and ionization by tunnel effect. [96]

$$\gamma = \frac{\tau_t}{T_0} = \frac{\omega_0}{|e\mathbf{E}|}\sqrt{m_{\text{eff}} E_g} \propto \frac{1}{\sqrt{\text{Intensity}}}, \tag{2.7}$$

where τ_t is the tunneling time and T_0 stands for the period of laser field. E_g represents the bandgap energy, m_{eff} effective mass, e electron charge, $\mathbf{E}$ is the linearly polarized electric field amplitude and ω_0 the angular frequency of electric field. [96] In low intensity range ($\gamma \gg 1$), the multiphoton ionization rate is governed by multiphoton absorption and it is proportional to m-th power of electric field intensity, where m is the number of photons, whose sum of energy is sufficient to overcome bandgap. On the contrary, at higher intensities ($\gamma \ll 1$), tunnelling ionization dominates. The simulation using full Keldysh theory, solid line in Fig. 2.7, shows a sequence of gradual drops in the ionization rate with increasing intensity. The decreasing steps correspond to the states, at which an electron needs one more quantum of photon energy to be transferred from valence band to conduction band. [70]

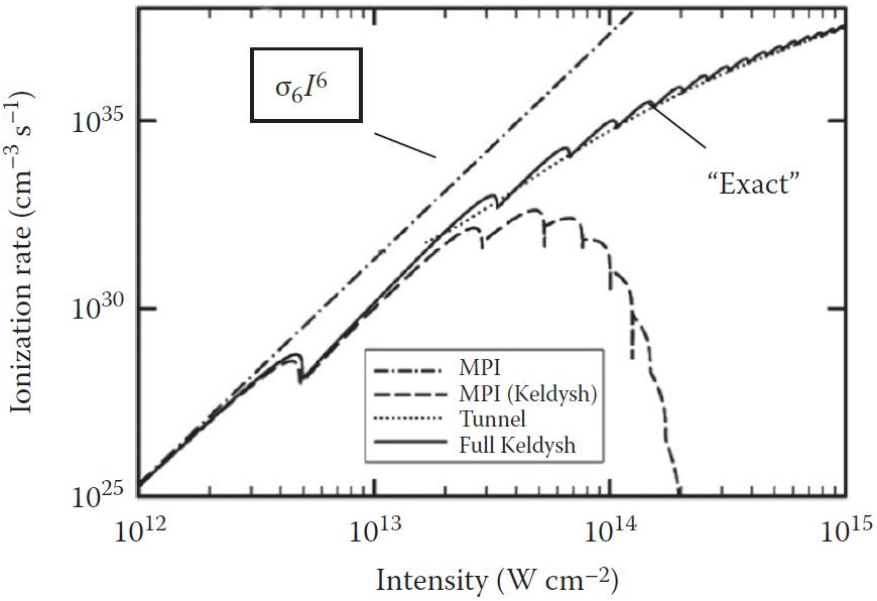

Figure 2.7: Multiphoton ionization rate as a function of intensity. Simulation done according to the Keldysh theory in the case of band gap energy 6 $\hbar\omega_0 < E_g < 7\hbar\omega_0$. The photoionization rate is produced by two processes - multiphoton absorption and tunneling, whose relative weight is given by the Keldysh parameter γ. Under low intensity conditions, the excitation is reduced to multiphoton absorption, whereas at high intensities, the tunneling ionization process dominates. For comparison, simulations of ionization rate corresponding to only tunnel effect or the multiphoton absorption limit ($\sigma_6 I^6$) are also plotted. Figure taken from [70].

The rate of impact ionization, the constituent $A(I, N)$ in Eq. (2.6), can be estimated analytically using the flux doubling model. [84] The approximate approach assumes that when an electron in conduction band reaches the critical energy E_c using inverse Bremmstrahlung absorption, the excited electron immediately collides with an electron localized in valence band. The collision results in two electrons at the bottom of the conduction band. Thereafter, the process is repeated and the avalanche ionization occurs. The rate of impact ionization is thus proportional to the rate, at which the electrons reach the critical energy ($\frac{\sigma_e}{E_c} I$) and the density of electrons in conduction band (N):

$$A(I, N) = W_{\text{imp}} N = aIN = \frac{\sigma_e}{E_c} IN, \tag{2.8}$$

where the coefficients used between the individual equations show different notations of the same impact ionization rate phenomenon used in the literature. [70, 97] W_{imp} means the probability of impact ionization and $a = \frac{\sigma_e}{E_c}$ represents impact ionization coefficient that is also dependent on the light intensity (I) through quiver energy of an electron in an external oscillating field. [70] The effective absorption cross section σ_e is related to the imaginary part of the refractive index n_i by equation:

$$\sigma_e = \frac{2\omega_0 n_i}{cN}, \tag{2.9}$$

where c is the speed of light in a vacuum. The effective absorption cross section σ_e can be derived from Drude's model for the refractive index of a quasi-free electron gas [98] under the assumption of an optically thin plasma, which is valid at the electron densities below dielectric breakdown (damage):

$$\sigma_e = \frac{e^2}{m_{\text{eff}}\varepsilon_0\gamma_e} \cdot \frac{1}{1 + \left(\frac{\omega_0}{\gamma_e}\right)^2}, \tag{2.10}$$

where γ_e is an effective electron collision rate and ε_0 stands for the vacuum permitivity. The effective electron mass m_{eff} and the collision rate γ_e may depend on the electronic energy relative to the edge of the conduction band. However, this dependence is neglected in many applications of the Drude model. [70]

In the multiphoton ionization process by sub-ps pulses in dielectrics, the role of field-assisted collisional ionization is critical. [99] The collisional ionization with "colder" electrons ($\beta_j I^j$) can be included in impact ionization as follows:

$$A(I, N) = aI \left(1 + \sum_{j=1}^{k-1} \beta_j I^j\right), \tag{2.11}$$

where j means the multiphoton order. The field assisted-avalanche need to be taken into account in comprehensive models for laser machining and laser damage in dielectrics.

Using the above assumptions of monochromatic laser radiation, the double flux approximation and by neglecting the relaxation rate $L(N)$ during the interaction with sub-picosecond pulse, the overall rate of increase of the electron density N can be determined by:

$$\frac{dN}{dt} = K(I) + A(I, N) = K(I) + aIN, \tag{2.12}$$

where the multiphoton ionization rate $K(I)$ can be described as Keldysh ionization rate. [70]

Interaction with square pulse

The Eq. (2.12) represents a first-order linear ordinary differential equation for the function $N(t)$. The general solution can be written in the form:

$$N(t) = C_1 e^{a(I)It} - \frac{K(I)}{a(I)I}, \tag{2.13}$$

where C_1 is the constant which can be determined using the initial condition. At time $t = 0$, the electron density is assumed to be $N = N_0$. Therefore, the constant is: $C_1 = N_0 + \frac{K(I)}{a(I)I}$. Let us consider the interaction of the material with a square pulse of duration τ_p and intensity I. The electron density at time τ_p, i.e. immediately after excitation event becomes:

$$N(I, \tau_p) = \frac{K(I)}{a(I)I}\left[e^{a(I)I\tau_p} - 1\right] + N_0 e^{a(I)I\tau_p}. \tag{2.14}$$

The initial electron density N_0 describes background electron density resulting from thermally excited states within the conduction band. The excitation of electrons from midgap states close to the conduction band edge by one-photon absorption has a similar effect. These states are related to native traps and defects, and N_0 should be low for high quality wide-gap materials. [70]

Assuming the multiphoton absorption limit ($K(I) = \beta_m I^m$) and applying the approximation $a(I) \approx a_0$, the Eq. (2.14) provides the electron density as a function of the pulse fluence $F = I\tau_p$:

$$N(F) = \frac{\beta_m}{a_0} \left(\frac{F}{\tau_p}\right)^{m-1} \left[e^{a_0 F} - 1\right] + N_0 e^{a_0 F}. \tag{2.15}$$

From the Eq. (2.15), the damage fluence F_{th} can be computed numerically using the condition $N(F = F_{th}) = N_{crit}$.

The second term in Eq. (2.15) refers to avalanche ionization generated by background electrons. The first term stands for the electrons produced by a combination of avalanche ionization and multiphoton absorption. From Eq. (2.15), it can be concluded that for short pulse durations, the first term dominates while background electron density is less relevant for the electron ionization. Conversely, in the case of longer pulses, the background electron density (N_0) is more critical and provides the seed electrons. Using this consideration, the statistical nature of long pulse LIDT can be explained.

Other consequence arising from the Eq. (2.15) is that the damage fluence depends approximately logarithmically on the critical electron density N_{crit}. A rise of the density N_{crit} by an order of magnitude can lead to the increase of damage threshold fluence F_{th} by only 10 %. A simulation based on Eq. (2.15) describing the damage threshold fluence as a function of critical electron density was done in [100]. The theoretical results assuming four-photon ionization process and a_0 and β_4 parameters of HfO_2 films in the case of two femtosecond pulse durations (20 fs, 320 fs) are plotted on Fig. 2.8a).

If no background electron density ($N_0 = 0$) is present, it is more difficult to produce the conduction band seed electrons needed for avalanche ionization. To produce the seed electrons by longer pulse, higher fluence is required due to its relatively lower intensity (F/τ_p), see Eq. (2.15). Consequently, the impact ionization contributes relatively largely to the overall electron density (exponential term). The impact ionization is triggered by conduction band electrons produced by the multiphoton absorption.

This description of the progressive ionization of the conduction band using multiphoton absorption, impact and avalanche ionization processes explains the sensitivity of the electron density to the pulse beam shape (asymmetry), see Fig. 2.8b). At a given total fluence, the pulse with higher intensity at earlier time generates higher conduction band electron density. Thus, the pulse will more likely reach the critical electron density corresponding to damage onset. The experimental tendencies have been reported in [101]. The work [102] predicts that a flat-in-time pulse will produce damage at approximately 80% of the fluence of a Gaussian pulse of the same duration. In the study [103] of SiO_2, it was shown that the concept of temporal scaling law relies on the temporal shape of pulse. The variation of the temporal shape has impact on LIDT even though the pulse duration measured with an autocorrelator is the same.

Multiple rate equations

Another analytical method allowing a relatively accurate description is an extension of single rate equation (SRE) to a system of multiple rate equations (MRE). [70, 97, 104, 105] The method is based on the splitting of the conduction band into k levels spaced by $\hbar\omega_0$. The MRE allow to take into account the fact that each individual electron needs to gain sufficient energy for impact ionization, whereas SRE considers only mean levels. An electron is heated up to the k-th level using a step-like process within the conduction band, see

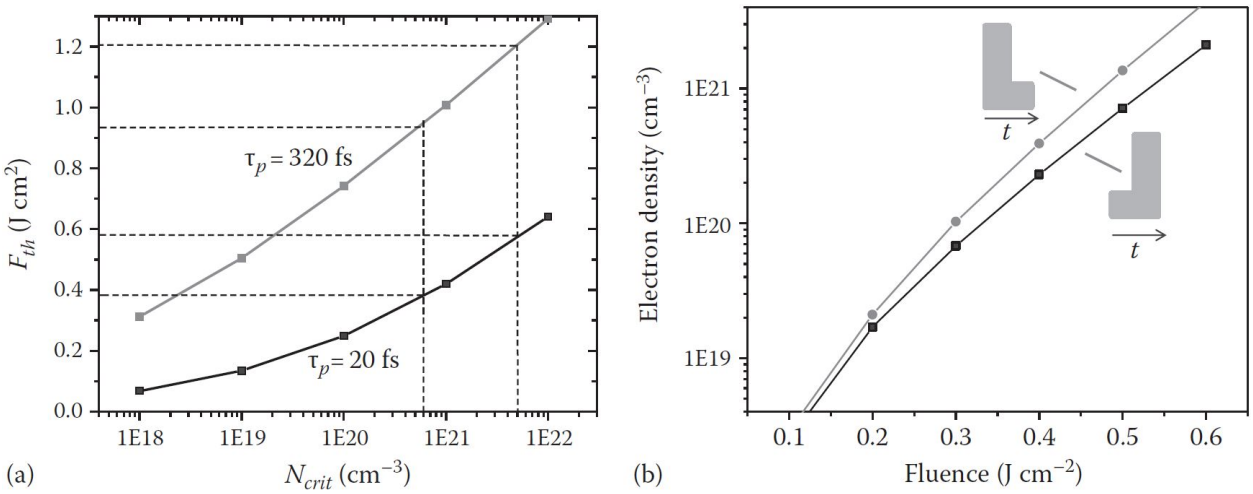

Figure 2.8: (a) Damage fluence (F_{th}) as a function of critical electron density (N_{crit}) in the case of 20 fs and 320 fs pulse durations. The numerical calculation done in study [100] is based on the Eq. (2.15). The simulation assumed four-photon absorption. The a_0 and β_4 parameters corresponded to HfO_2 films. (b) Conduction band electron density (N) of exciting hafnia as a function of pulse fluence (N) for the two different pulse shapes. The pulse duration of each pulse is 50 fs. Figures taken from [70].

Fig. 2.9a). The number k is the positive integer defined using ceiling function as $k = \lceil \frac{E_c}{\hbar\omega_0} \rceil$. The k-th level is thus the first level of energy higher than the critical energy E_c. Immediately, when an electron reaches the E_k energy, the impact ionization occurs, see Fig. 2.9a). The MRE compute the time-dependent electron density N_i of the i-labeled level by considering exchanges of energy with the closest levels in terms of energy, i.e. levels labeled $i-1$ and $i+1$ within the conduction band.[5] By neglecting the relaxation rate from the conduction band, the MRE for femtosecond pulse interaction with dielectric can be expressed as follows: [97]

$$\frac{dN_0}{dt} = \tilde{K}_{pi} + 2\tilde{W}_{\text{imp}} N_k - W_{1pt}(E_0) N_0, \tag{2.16a}$$

$$\frac{dN_1}{dt} = W_{1pt}(E_0) N_0 - W_{1pt}(E_1) N_1, \tag{2.16b}$$

$$\vdots \tag{2.16c}$$

$$\frac{dN_{k-1}}{dt} = W_{1pt}(E_{k-2}) N_{k-2} - W_{1pt}(E_{k-1}) N_{k-1}, \tag{2.16d}$$

$$\frac{dN_k}{dt} = W_{1pt}(E_{k-1}) N_{k-1} - \tilde{W}_{\text{imp}} N_k, \tag{2.16e}$$

where $\tilde{K}_{pi}$ is the photoionization rate from valence band to the 0-th labeled bottom level of conduction band. The symbol $\tilde{W}_{\text{imp}}$ denotes probability of impact ionization and $W_{1pt}(E_i)$ stands for the probability that electron of energy E_i will absorb a single photon from the laser radiation.

Summing up all the Eqs. (2.16) we get:

$$\frac{dN}{dt} = \tilde{K}_{pi} + \tilde{W}_{\text{imp}} N_k, \tag{2.17}$$

[5] This is not fulfilled for the lowest energy level E_0 and the highest energy level E_k of the conduction band since they do not have the two adjacent levels. However, they interact with each other using impact ionization.

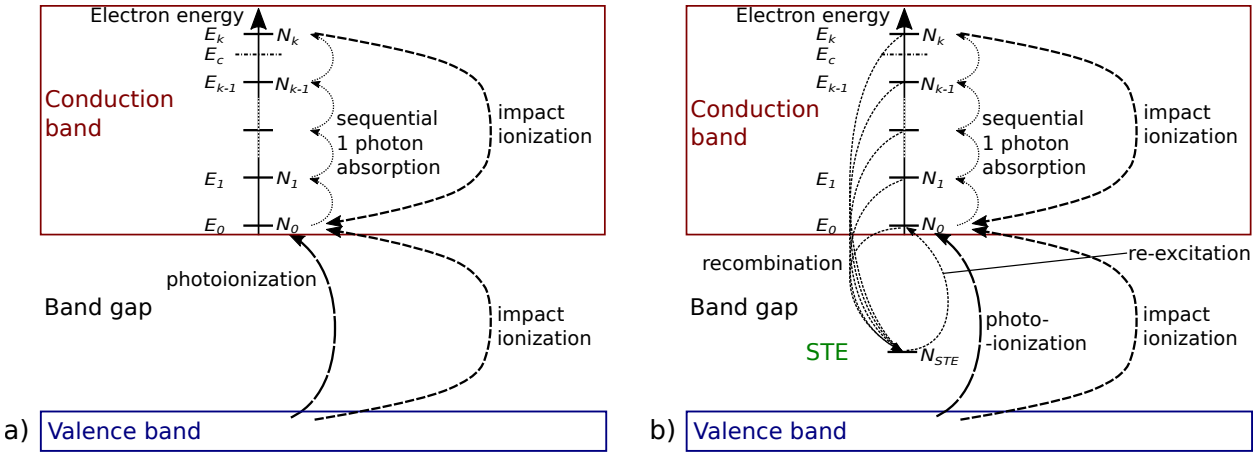

Figure 2.9: Schematic layout of processes involved in multiple rate equation (MRE) models without any recombination of conduction band (a) and with Self trapped exciton state (STE) - (b). The conduction band is splitted into k levels spaced $\hbar\omega_0$. The energy of i-th level is E_i, the corresponding electron density is N_i. E_c means the critical energy. [97, 106]

where N represents the total electron density of the whole conductivity band, i.e. $N = \sum_{i=0}^{k} N_k$. The Eq. (2.17) is thus analogue of the Eq. (2.12) in the single rate equation model with the constituents corresponding to the strong field ionization rate ($\tilde{K}_{pi}$) and the impact ionization rate ($\tilde{W}_{\mathrm{imp}} N_k$). [107] Both these factors are regarded as the most dominant factors in the excitation of electrons in dielectrics. The one-photon excitation probability W_{1pt} is included in the rate equations (2.16) to simulate electron populations (densities) in intermediate levels. [108]

In the MRE models, the strong field ionization generates electrons with low kinetic energy in conduction band, whereas impact ionization is realized by electrons with only sufficiently high kinetic energy. A key advantage of the MRE approach is that only electrons of sufficiently high kinetic energies to conserve both energy and momentum in the ionization process are involved in the impact ionization. This contrasts with the SRE model, in which all electrons are assumed to play a part in the impact ionization, see Eq. (2.8). [108]

Fast recombination and other improvements of MRE

The rate equation models described above did not take into account any interband relaxation. However, for some dielectrics, such as SiO_2, fast interband recombination processes on a timescale of about 150 fs are known. The processes include the ultrafast recombination in self-trapped exciton states (STE) that has been experimentally confirmed in several studies. [91, 109–111] The recombination process to the STE state as well as the re-excitation from the STE state can be taken into account as shown in Fig. 2.9b) and included

as additional terms into the following modified multiple rate equations: [106]

$$\frac{dN_{STE}}{dt} = \frac{N}{\tau_{\text{recomb}}} - W_{STE}N_{STE}, \tag{2.18a}$$

$$\frac{dN_0}{dt} = \tilde{K}_{pi} + 2\tilde{W}_{\text{imp}}N_k - W_{1pt}(E_0)N_0 - \frac{N_0}{\tau_{\text{recomb}}} + W_{STE}N_{STE}, \tag{2.18b}$$

$$\frac{dN_1}{dt} = W_{1pt}(E_0)N_0 - W_{1pt}(E_1)N_1 - \frac{N_1}{\tau_{\text{recomb}}}, \tag{2.18c}$$

$$\frac{dN_2}{dt} = W_{1pt}(E_1)N_1 - W_{1pt}(E_2)N_2 - \frac{N_2}{\tau_{\text{recomb}}}, \tag{2.18d}$$

$$\vdots \tag{2.18e}$$

$$\frac{dN_{k-1}}{dt} = W_{1pt}(E_{k-2})N_{k-2} - W_{1pt}(E_{k-1})N_{k-1} - \frac{N_{k-1}}{\tau_{\text{recomb}}}, \tag{2.18f}$$

$$\frac{dN_k}{dt} = W_{1pt}(E_{k-1})N_{k-1} - \tilde{W}_{\text{imp}}N_k - \frac{N_k}{\tau_{\text{recomb}}}, \tag{2.18g}$$

where N_{STE} stands for the density of electrons in exciton states. The recombination rate is defined using recombination time τ_{recomb} and the re-excitation rate is W_{STE}. The other parameters are analogous to that used in Eqs. (2.16).

The influence of ultrafast interband relaxation processes as recombination in STE states was simulated using the Eqs. (2.18) in study [106]. Results for a pulse duration of 200 fs showed a delayed increase in electron density and thus a lower peak of electron density with decreasing characteristic recombination time. Note that when considering longer pulse durations up to picosecond regime, the recombination processes are becoming progressively more important. [105]

Besides the inclusion of ultrafast recombination processes, several improvements and applications of multiple rate equations have been published. Models of MRE have been successfully applied to simulate experimental observations of laser damage and ablation caused by tailored femtosecond pulse shapes. [101, 112,113] The study published by Christensen and Balling [108] extended the MRE modelling for an influence of light propagation into the material. The MRE model has improved energy conservation in the impact ionization process and the optical parameters were considered as varying during irradiation. The laser damage was simulated in dependence on laser fluence, wavelength, pulse duration or material band gaps and the results were compared with experiments. In the work, the limitations of MRE were discussed and the inclusion of defects was suggested as important aspect of material description. Other improvements of MRE modelling cover nonlinear light propagation in fused silica [114,115] and relaxation processes, such as Auger recombination to valence band [116] or plasma energy relaxation into the phonon gas. [114] Simulations employing extended multiple rate equations (EMRE) and ordinary differential equation (ODE) have shown the influence of strong pulse chirps, which can naturally arise from the non-linear propagation. The pulse chirps results in ionization dynamics that are not captured by the standard monochromatic approach to laser-induced plasma formation. [114]

Apart from the large number of publications considering the free electron density as the crucial parameter for laser damage of dielectrics, there are several studies that use the absorbed energy as a criterion ultimately responsible for material modification. The final material modification should be an effect of energy accumulation in the material lattice, rather than an electronic effect. [117] On the other hand, it is the electrons that directly absorb the energy of the laser radiation. The transfer to the lattice structure occurs after femtosecond irradiation. The criterion of electron density seems to be appropriate since the damage threshold is related to changes in electronic properties, i.e. optical properties of the created electron-hole

plasma.

Even though the electron density criterion is related to the damage threshold [117, 118], in study [119] it has been found a situation where the electron density exceeded its critical value, but no material damage has been observed in the corresponding experimental work [120]. Nevertheless, good agreement with the sub-picosecond experimental results was obtained using a thermal criterion based on the effect of lattice melting. [119] In work [121], both criteria, i.e. an electron density criterion and an energy density criterion, were used for the calculation of ablation depth. The results of both criteria were identical within a wide range of incident fluences.

The study [121] showed that modeling based on MRE can reproduce experimentally obtained quantities such as phase shift, absorption, reflectivity or depth of the ablation crater using a single set of model parameters. In work [103], the MRE fitted well observed experimental trends of temporal LIDT scaling law with the effect of temporal beam shape. A numerical model employing MRE showed results corresponding well to the experimental data of the LIDT at 100 fs as a function of material bandgap and laser wavelength. [122] The use of such a model, based on reasonable physical assumptions, is important for thin-film materials, for which it is difficult to measure or estimate their physical properties.

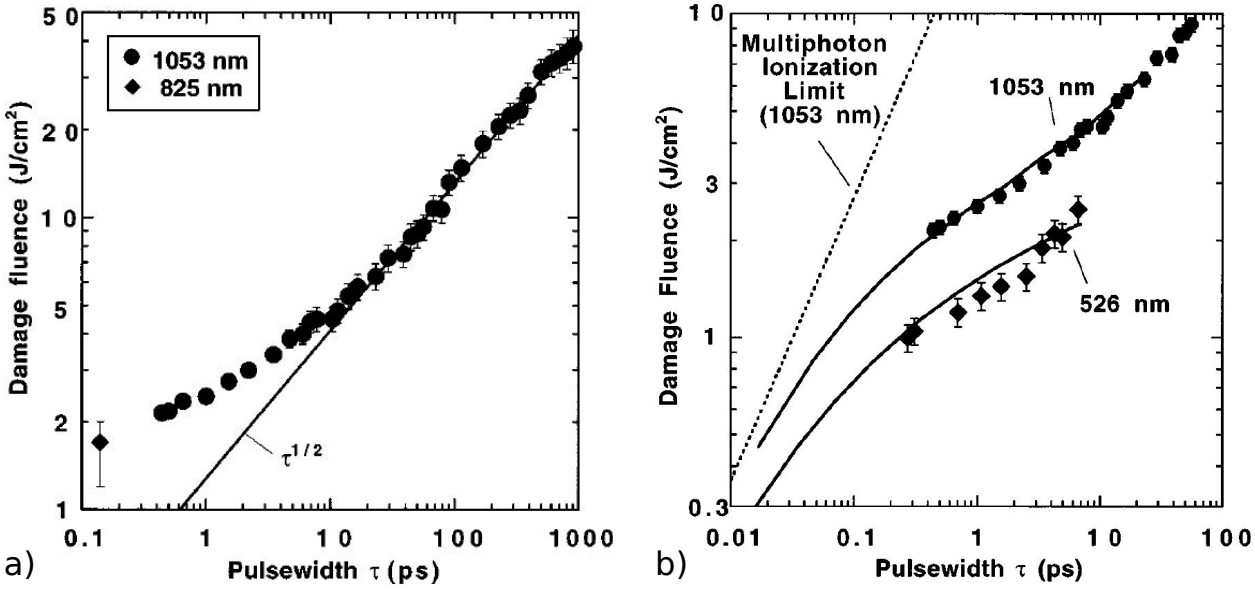

Figure 2.10: Damage threshold fluence of fused silica as a function of pulse durations. a) Comparison to the scaling law $\sim \tau_p^{0.5}$. b) Comparison of measured and calculated (solid lines) results for different wavelengths: 1053 and 526 nm. Dashed line shows calculated damage limit originated from multiphoton ionization. Figures taken from [84].

2.3.4 Damage fluence dependence on parameters.

Pulse duration

In the laser-induced damage field, one of the most studied dependencies is the damage threshold fluence of a given material as a function of pulse duration. [84,89,90,95,100,123] Generally, the damage fluence increases with increasing pulse duration. For pulse durations longer than ∼10 ps, the interaction is driven by the phenomenon of thermal relaxation and the damage threshold fluence (F_{th}) is approximately proportional to square root of pulse duration (τ_p), i.e. $F_{th} \propto \tau_p^{0.5}$, see Fig. 2.10a). [84] However, in the case of pulse shorter than ∼10 ps, there is a significant deviation in the behaviour of the damage threshold. An example of such dependence on pulse duration is depicted in Fig.2.11a), where threshold fluences of SiO_2, Al_2O_3, HfO_2, Ta_2O_5 and TiO_2 oxide thin films are shown in the pulse duration range from 25 fs to 1.3 ps. [100] The value of power exponent κ in the scaling law $F_{th} \propto \tau_p^{\kappa}$ was found to be ∼ 0.3 for all these oxides. However, optical dielectric materials indicate broad range of κ values ranging from 0.1 for fused silica and CaF_2[6] up to 0.35 in the case of borosilicate. [124] According to a phenomenological rate equation model, the material damage dependence on pulse duration is related to the interaction of multiphoton ionization, impact ionization and sub-picosecond relaxation of electron out of the conduction band. The magnitude of power exponent κ is associated to avalanche ionization initiated by photoionization. [100]

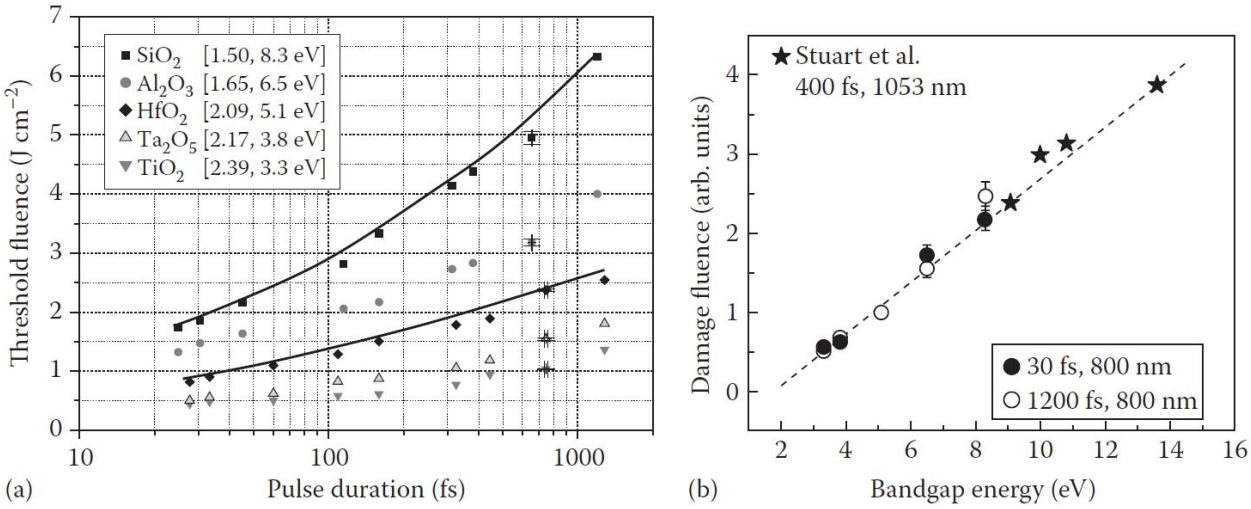

Figure 2.11: (a) Single-pulse damage fluence as a function of pulse duration for oxide thin films. Laser wavelength 800 nm. Values of refractive index and bandgap corresponding to each oxide are shown in brackets. The solid lines reflect the predictions derived from the scaling law - Eq. (2.19). [100] (b) Relative damage fluence as a function of bandgap energy. The pulse duration was 30 fs (solid circles) and 1.2 ps (open circles). Damage fluence is normalized to the point at bangap energy $E_g = 5.1$ eV. The data shown by asterisks correspond to bulk fluorides BaF_2, CaF_2, MgF_2, and LiF and were taken from [84]. Both graphs were taken from [70].

Wavelength

Thanks to the various studies [84, 85, 125–128], a general behaviour can be deduced: a decrease of the threshold with the shorter wavelength from 1050 to 250 nm. There are more diverse explanations for this phenomenon. For instance, in Stuart's study [84] the surface laser damage of amorphous silica was measured

[6]The power exponent value $\kappa = 0.1$ was determined from data of mulitple pulse experiment.

for different pulse durations at two different wavelengths, see Fig. 2.10b). The change from 1053 to 526 nm wavelength results in a decrease in the damage threshold, which was explained by the number of photons necessary for multiphoton ionization. Indeed 4 photons are needed at 526 nm while 8 photons are required to obtain multiphoton ionization at 1025 nm. Since the probability of absorption is lower in the case of 8-photon process, the damage threshold is increased.

By irradiating an amorphous silica using 110 fs pulse duration, Schaffer observed only very small difference in damage threshold at 400 and 800 nm wavelength. [125] The explanation was based on a difference in the absorption mechanism. The results indicate that at 400 nm the absorption occurs by multiphoton ionization while at 800 nm the photoionization occurs by tunnel effect process.

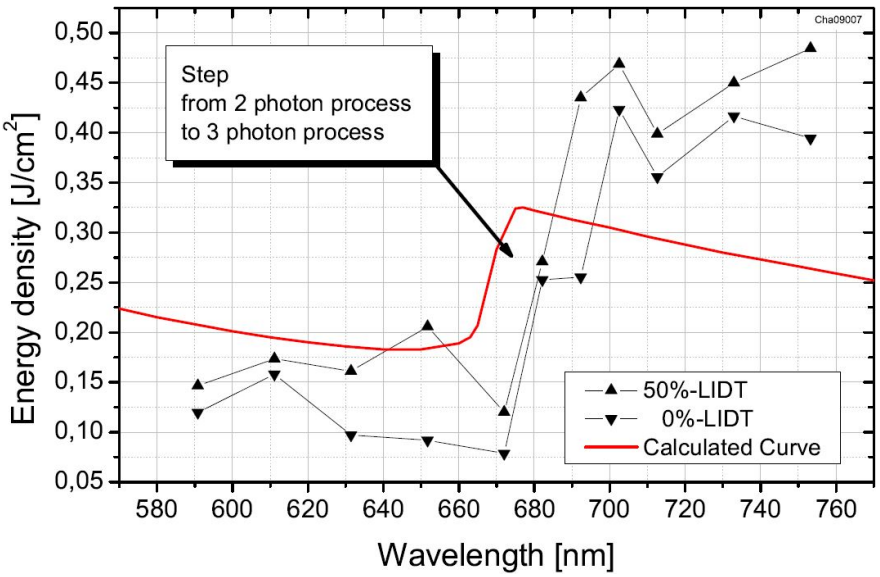

Figure 2.12: Evolution of the damage threshold of TiO_2 monolayer as a function of laser wavelength. Pulse duration 130 fs. The absorption below 670 nm is carried out by 2 photon process. The jump around 680 nm corresponds to the skip from 2 to 3 photon process. Figure taken from [129].

Work [129] done on a TiO_2 monolayer by 130 fs pulse duration have shown the dominant role of multiphoton ionization. The damage threshold was studied for different wavelengths between 580 and 770 nm, see Fig. 2.12. The results showed a significant jump at damage threshold that corresponds to the transition between 2-photon and 3-photon absorption. The jump clearly confirmed the theory done by Bloembergen [130] that predicts changes in damage threshold at the transitions in which number of photons needed for passing through the bandgap is changed. The decrease of LIDT with decreasing wavelength was observed also with SiO_2, HfO_2 and Nb_2O_5 coatings investigated at 343, 515 and 1030 nm for a broad range of pulse numbers (1 to 100k). [128]

Bandgap

For a fixed pulse duration and laser wavelength, a linear damage threshold dependence on the material bandgap was recognized, as shown on Fig. 2.11b). Experimental study on TiO_2, Ta_2O_5, HfO_2, Al_2O_3 and SiO_2 oxides [100] as well as the analysis of data on BaF_2, CaF_2, MgF_2 and LiF fluorides [84] suggests a following scaling law:

$$F_{th}(E_g, \tau_p) = (c_1 + c_2 E_g)\, \tau_p^{\kappa}, \tag{2.19}$$

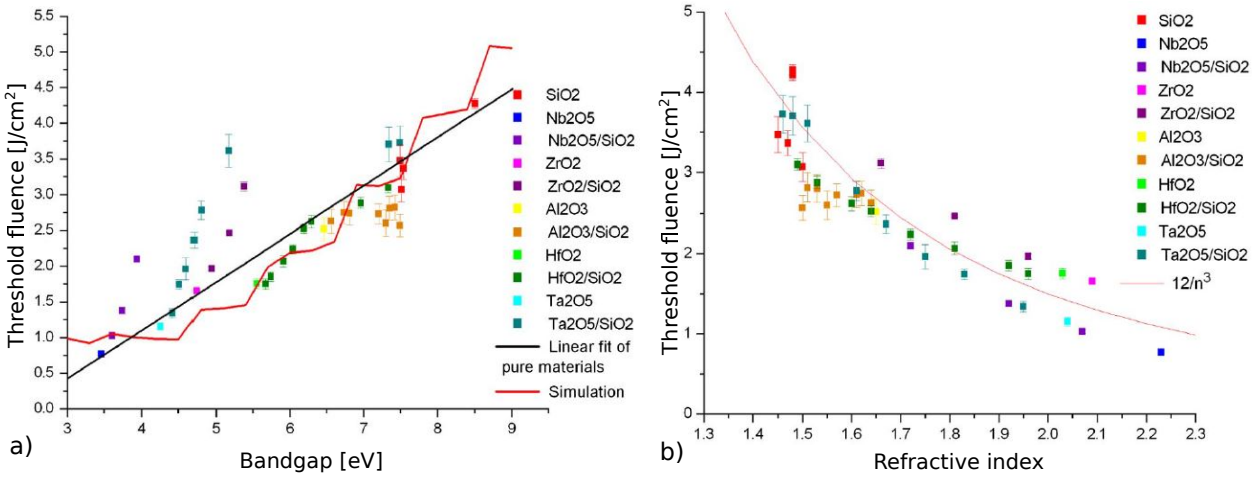

Figure 2.13: Damage threshold fluence as a function of bandgap (a) and refractive index (b) for pure oxides and their mixtures. Pulse duration 500 fs, laser wavelength was 1030 nm. Figures taken from [44].

where $c_1 = -0.16 \pm 0.02$ J cm^{-2} fs$^{-\kappa}$, $c_2 = -0.074 \pm 0.004$ J cm^{-2} fs$^{-\kappa}$ eV^{-1} and $\kappa = 0.30 \pm 0.03$. The damage fluence threshold F_{th} means the internal fluence value. The linear dependence on bandgap has been verified in studies of binary oxide films, $Ti_xSi_{1-x}O_2$ [131] and $Hf_xSi_{1-x}O_2$ [132], in which the proportion of particular material components was continuosly tuned by changing the composition parameter x. The values of coefficients c_1 and c_2 in Eq. (2.19) are slightly influenced by film deposition and post-deposition treatment, e.g. annealing. [70] The linear scaling character of the bandgap on LIDT has been found also in bulk crystalline fluorides. [133] The extensive material study [44] confirmed a linear dependence of the LIDT on bandgap in the case of pure oxides including ZrO_2 and Nb_2O_5, see Fig. 2.13a).

However, in the case of Ta_2O_5/SiO_2, Nb_2O_5/SiO_2 and ZrO_2/SiO_2 oxide mixtures, deviations from the linear behaviors were observed. This more complex behaviour is not surprising in view of the variability of the band structure of ternary alloys depending on the composition of the individual alloy, which is well known for single-crystal materials. [134] The deviations from linear dependency of LIDT on material bandgap (Eq. 2.19) were observed also by Melninkaitis [135] in oxide mixtures with silica content.

The dependence of the damage threshold on the material bandgap is extremely interesting for the design of dielectric mirrors, since it can be easily used in the development process of a multilayer component. In study [136], for instance, the damage threshold of optics was enhanced by a factor of 2 by adjusting the multilayer structure in order to have electric field maximum localized inside the layer of the material that shows the highest bandgap.

Refractive index

For the optimization of multilayer optical components with enhanced damage fluence, the critical material parameter is refractive index of particular thin films. Damage fluence as a function of refractive index is shown for more than 50 samples on Fig. 2.13b). The results indicate a clear continuous trend that is independent on the sample nature. The evolution of threshold fluence as a function of refractive index could be approximately fitted by equation: [44]

$$F_{th} = \frac{12}{n^3} \text{ [Jcm}^{-2}\text{]}. \tag{2.20}$$

The phenomenological scaling law can predict roughly the damage threshold of particular material and it could be very useful in the coating design process.

2.3.5 Defect-induced damage

Since the advent of a laser as a technology that allows extreme spatial and temporal concentration of light energy, it has been found that localized defects in optical components are a key factor in laser-induced damage. [83] Thanks to the continuous progress in the optical technology, the optical components are fabricated in higher optical quality with lower defect density and smaller size of the imperfections. Nevertheless, with ever-increasing demands on laser power densities, e.g. in laser fusion facilities, even nanoscale absorption defects are still a main source of damage. Furthermore, the presence of defects is an inherent feature of the thin films produced by the physical vapor-deposition processes.

In the sub-picosecond regime, the laser-induced damage threshold (LIDT) is related to both material properties (energy bandgap, refractive index) and laser parameters (pulse duration, wavelength). [44,100,128] These material and laser parameters affect the distribution of the electric field intensity. Since the damage resistance of material depends on the laser intensity, any local enhancement of the electric field should lead to a decrease in the LIDT. [86,124] The damage threshold dependence was confirmed in the case of multilayered diffractive gratings with various designs of pillars influencing electric field maximum. [15, 137] The local electric field enhancement can be found also in dielectric coatings on nodular defects, i.e. macroscopic defects embedded in the structure, originating from the manufacturing processes of functional coatings. [124, 138] The nodules behave like microlenses, focusing light into a coating, and thereby reducing the laser resistance of the coating. [139] The results obtained in [140] study showed that nodules, and potentially any macroscopic defects, e.g. cracks, grooves, voids or pores, that could modify the distribution of the electric field, are a serious issue in the sub-picosecond laser field. [141] Nodular defects initiate damage at very low fluence compared to the intrinsic damage threshold and the initiation threshold can be estimated using electric field enhancement simulation.

In order to evaluate the effect of nodular defects on LIDT in sub-picosecond regime, Sozet et al. analyzed behavior of three high-reflective (HR) mirrors with HfO_2/SiO_2 coatings. [86] The typical images of defect sites after single shot irradiation by 675 fs pulse at 1053 nm wavelength are shown on Fig. 2.14. Observations of DIC microscopy revealed morphological differences between the damage sites irradiated by laser fluences lower and higher than the LIDT value of the tested mirror (3.4 J/cm^2). In the case of fluences below the LIDT value, the sites are small and localized (Fig. 2.14a), whereas for fluences above the LIDT value, a large structuring of the upper layer is apparent (Fig. 2.14b).

The mirrors were tested also by the rasterscan procedure to determine damage density. It was found that damage events occur even for fluences significantly lower than the single shot LIDT value. Therefore, the previously determined damage thresholds of tested dielectric mirrors are doubtful. The damage density should be thus considered as important parameter for the characterization of optical components used in various laser systems where precise knowledge of material behavior is needed. The view on material defects in the sub-picosecond regime make high demands on the thin film fabrication using optimized coating manufacturing processes. A thorough analysis of defect-induced damage could also result in a better prediction of the lifetime of the optics under operating conditions, i.e. after irradiations of multiple pulses with large laser beam size.

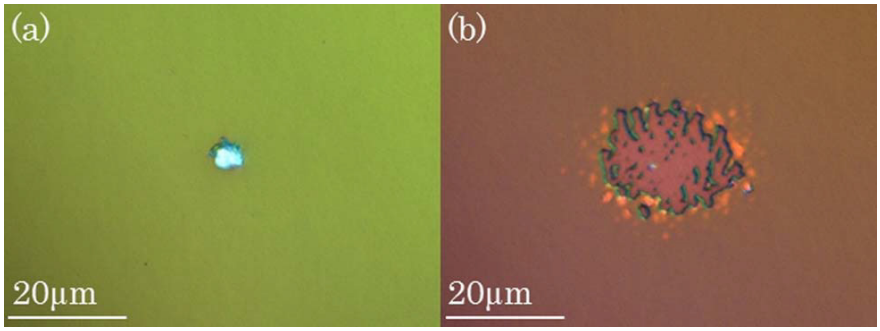

Figure 2.14: Examples of DIC of damage sites after single shot tests (675 fs, 1053 nm) on dielectric mirror performed below (a - 3.16 J/cm^2) and above (b - 3.56 J/cm^2) the LIDT value of 3.41 J/cm^2. The mirror was produced by an e-beam deposition process and designed as [Glass: (HL)ˆ11 H 2L: Air]. Figure taken from [86].

2.4 Multiple pulse interactions

While the single pulse interaction is of interest to academics, the material damage induced by multiple pulses is important for practical applications, e.g. laser machining or testing of optical component resistance. [70] The multiple-pulse damage test means that the same sample site is irradiated by multiple pulses. In an S-on-1 damage test, one sample site is irradiated by a train of S identical pulses that are equidistantly spaced in time.

2.4.1 Damage characteristic curve illustrates the incubation

The measured damage threshold, $F_{th}(S)$, decreases as the number of pulses increases. [70] The process called incubation results from laser-induced material changes prior to damage onset. [142, 143] Damage should logically occur during the last pulse and all previous pulses are causing non-visible material changes. When the irradiation is done using sufficiently high number of pulses, the threshold approaches a constant value, F_∞, the multi-pulse damage threshold. Reliable and safe operation of the optical components is possible at fluences lower than the value ($F < F_\infty$). The curve of damage threshold (F_{th}) as a function of number of pulses (S) is called the damage characteristic curve and illustrates the incubation nature. An example of the $F_{th}(S)$ dependence in the case of fused silica is shown on Fig. 2.15.

The fact that the fluence damage threshold after the S pulses is lower than the single pulse damage threshold means that the material does not fully recover between pulses. The behavior can be explained using the existence of defect states within the dielectric bandgap. The first excitation event (pulse) excites electrons from the valence band to the conduction band through a combination of multiphoton and impact ionization. Since the material does not fully relax between consecutive pulses, the defect states, whether native traps or laser-induced defects, remain occupied. The further excitation of the midgap states by subsequent pulses increases the electron density in the conduction band, thereby enhancing the impact ionization and lowering the damage threshold. [70] The irradiation by multiple pulses can induce also pre-damage changes in the optical properties of material, e.g. the change of thin film reflectance, although no visible damage is observed, see Fig. 2.15b). [144]

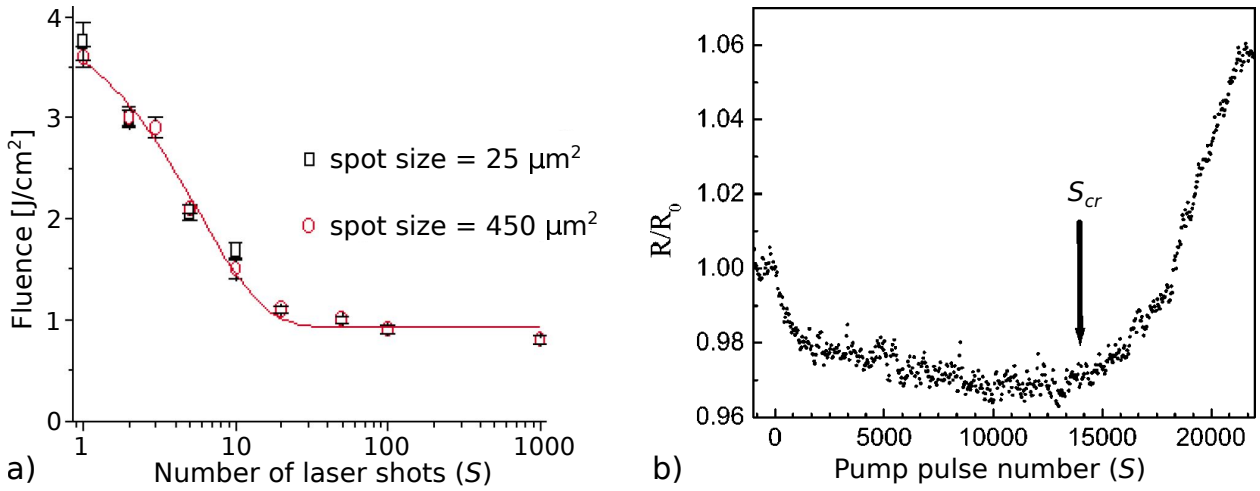

Figure 2.15: a) Damage threshold fluence as a function of number of laser shots for fused silica. Pulse duration 100 fs, laser wavelength 800 nm. [142] b) Influence of pulse number (S) on the reflectance (R/R_0) of Ta_2O_5 film deposited by IBS technique on fused silica. Repetition rate 1 kHz, pulse duration 40 fs, wavelength 800 nm. Value of pulse fluence was between the single and multiple pulse damage thresholds. The visible material damage was detected at pulse number $S = S_{cr}$. [144]

2.4.2 Damage thresholds can be fitted by multiple-pulse model

For a better understanding of damage process arising from multiple pulse experiments, let us consider the following simplified case. A dielectric material is exposed to a train of identical pulses that are repeated with a period T. The pulses have duration τ_p and fluence lower than the single pulse damage threshold ($F < F_1$). According to the Eq. (2.15), the first pulse yields an electron density of conduction band: [70]

$$N_1 = \frac{\beta_m}{a_0}\left(\frac{F}{\tau_p}\right)^{m-1}\left[e^{a_0 F} - 1\right] + N_0 e^{a_0 F} = Q + N_0 e^{a_0 F}, \tag{2.21}$$

where the first term on right side (Q) denotes the electron density produced by multiphoton absorption and impact ionization. The second term ($N_0 e^{a_0 F}$) stands for the avalanche ionization induced by background electrons. Taking only band-to-band relaxation into account, see Fig. 2.16a), and assuming the lifetime of the conduction band electrons T_{cv}, the electron density decreases to the value $N_{02} = N_1 e^{-\frac{T}{T_{cv}}}$ before the arrival of the second pulse. The electron density (N_2) of conduction band after the second pulse is therefore:

$$N_2 = Q + N_{02} e^{a_0 F} = Q + Qp + N_0 p e^{a_0 F}, \tag{2.22}$$

where the parameter $p = e^{a_0 F - \frac{T}{T_{cv}}}$ is used to reflect the balance between amplification by avalanche ionization ($e^{a_0 F}$) and relaxation losses ($e^{-\frac{T}{T_{cv}}}$) from conduction band to valence band. By repeating this procedure the electron density of conduction band after S pulses can be expressed in the form of a geometric progression:

$$N_S = Q\sum_{n=0}^{S-1} p^n + N_0 e^{a_0 F} p^{S-1} = Q\frac{1-p^S}{1-p} + N_0 e^{-a_0 F} p^{S-1}. \tag{2.23}$$

Using the Eq. (2.23) the conduction band electron density as a function of time during the pulse train irradiation was calculated. The results are shown on Fig. 2.16b),

When the material is exposed to the train of pulses, the peak of electron density increases with each subsequent pulse. In the case of control parameter $p < 1$, the electron density converges for $S \to \infty$ to

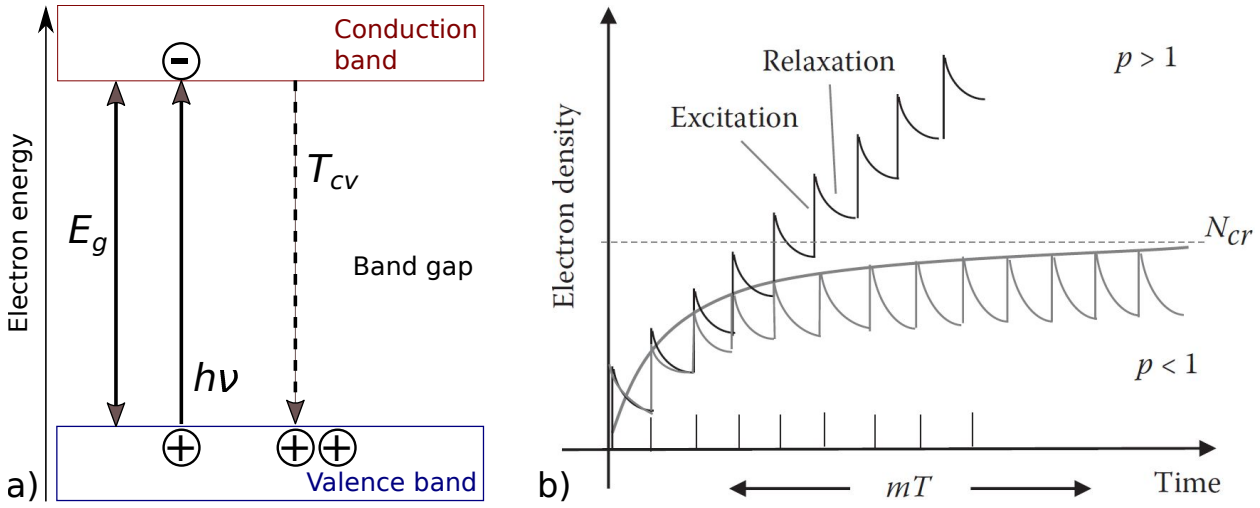

Figure 2.16: a) Energy level diagram illustrating the conduction band electron generation and electron relaxation with a characteristic decay time T_{cv}. b) The increase in electron density as a function of time in the case of irradiation by a train of identical pulses spaced by the period T. In dependence on the parameter p, the electron density either saturates or continues to increase. [70]

$N_\infty = \frac{Q}{1-p}$. If $N_\infty < N_{crit}$, the material remains resistant to damage regardless of the number of pulses. However, if $N_\infty > N_{crit}$, the material damage occurs after irradiating by a critical number S_{cr} of pulses that allow the reaching of critical electron density. In the case of control parameter $p > 1$, the electron density (N_S) is divergent for $S \to \infty$ and the material is always damaged at a certain number of pulses. The value of control parameter p for a given fluence F is a function of the material (a_0) and the pulse repetition period T. If the period is shorter, the importance of relaxation process between pulses is decreasing and the case ($p > 1$) indicates a higher susceptibility to damage. [70]

This discussion explains the main feature of multiple pulse damage, i.e. the decreasing damage threshold fluence with increasing pulse number. The explanation was based on the simplest form of material incubation: the incomplete relaxation of conduction band electrons between the consecutive pulses.

2.4.3 Two-pulse damage thresholds depend on native midgap states

The effect of material relaxation can be well described by the damage fluence $F_{th}(2)$ of two pulses (2-to-1) as a function of delay between them. [70] $F_{th}(2)$ fluences of fused silica and borosilicate glass are shown on Fig. 2.17a). [145] For delays between pulses shorter than 200 fs, $F_{th}(2)$ is up to 30 % lower than the near constant value of delays between pulses longer than 200 fs.

This time scale matches the formation time of the self-trapped exciton in silica glasses. In the case of HfO_2, relaxation was studied on a broad time scale over 13 orders of magnitude, see Fig. 2.17b). [146] For delays between pulses longer than 1 s, the HfO_2 does not show any decrease in damage threshold on arrival of the second pulse. The HfO_2 has fully relaxed before the irradiation by second pulse. The flat area in the ns and µs delay region indicates that the HfO_2 recovers in two steps. The fast relaxation takes approximately 100 ps and the slow one $\sim$ 100 ms.

To explain the observed trends, a rate equation model that considers one additional state between conduction band (CB) and valence band (VB) was applied. [146] Its results are shown using the solid line in Fig. 2.17b). The first fast transient process occurs via relaxation of electrons from CB, while the second

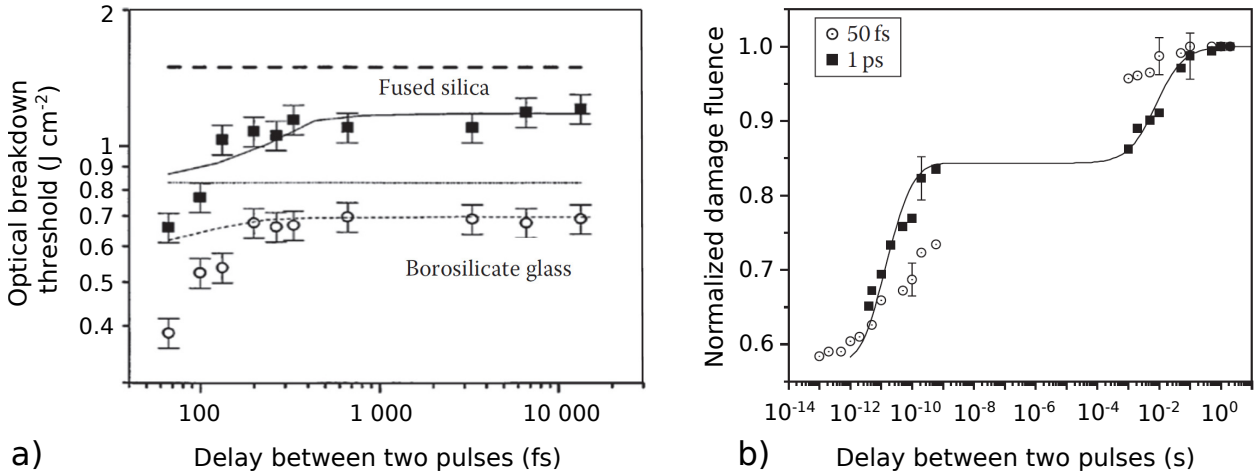

Figure 2.17: Damage fluence of two pulses as a function of their delay: a) for fused silica and borosilicate glasses, [145] b) for HfO_2 film with normalized damage fluences to $F_{th}(1)$. [146]

slower one occurs by relaxation of electrons from the midgap state to VB. For 1 ps long pulses, the height of flat area in the ns and µs delay region is determined by the absorption cross section of the midgap state and the branching ratio of two relaxation processes out of the CB - into VB and the midgap state. [146] In the case of material excitation by 50 fs pulses, additional states are photo excited by the second pulse. A detailed examination revealed that the material does not fully recover even after minutes. The decrease in damage thresholds is connected to formation of laser-induced defects that play a role only for higher numbers of pulses. [147]

2.4.4 Damage characteristic curves reveal material defects

Damage characteristic curves, i.e. $F_{th}(S)$ functions, give information about the properties of the native midgap states and the generation rate of laser-induced defects (Fig. 2.18). The experimental data can be compared to appropriate models based on rate equations. The models consider the formation, occupation and re-excitation of midgap states and predict the CB electron density during the material irradiation by pulse train. [70]

Laser-induced damage thresholds of a typical $F_{th}(S)$ curve can be characterized with fit functions, see Fig. 2.15a). According to the International Standard Organization, the damage threshold curve $F_{th}(S)$ is fitted by empirical law: [148]

$$F_{th}(S) = F_\infty + \frac{F_1 - F_\infty}{1 - \frac{log_{10}(S)}{\Delta_D}}. \tag{2.24}$$

The Eq. (2.24) describes $F_{th}(S)$ using single-pulse (F_1) and multiple-pulse (F_∞) threshold fluences and a fit parameter Δ_D. Another function in the form of

$$F_{th}(S) = F_\infty + (F_1 - F_\infty)\exp\left[-k(S-1)\right] \tag{2.25}$$

was used to fit the quartz data from Fig. 2.15a). The Eq. (2.25) uses the empirical constant k to describe the rate of trap generation with pulse number S. [142] The fit assumed that the damage threshold change after the $(S+1)_{th}$ pulse $[F_{th}(S+1) - F_{th}(S)]$ is proportional to $[F_{th}(S+1) - F_\infty]$.

The $F_{th}(S)$ curve can be also derived from a simplified material model which relates fit parameters to basic material features. Within the processes depicted on Fig. 2.18, we consider only the excitation, cf.

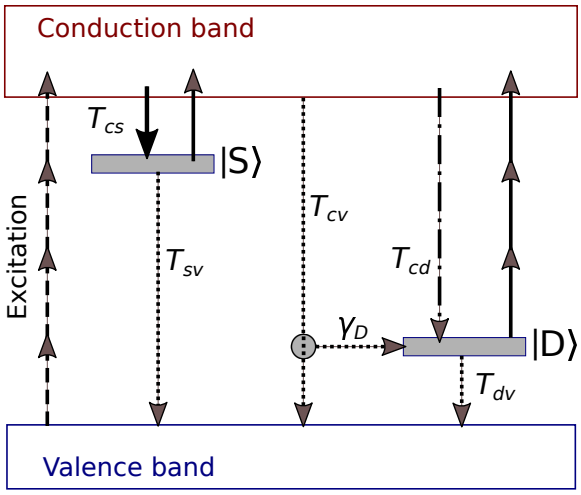

Figure 2.18: Excitation and relaxation processes considered in the interaction of dielectric material with laser pulses. Electrons in conduction band can relax to shallow ($|S\rangle$) and deep traps ($|D\rangle$) or directly back to the valence band. The parameter γ_D express possibility that during the relaxation new laser-induced defect states form. Constants T_i represent relaxation times. [70]

Eq. (2.15), the formation and occupation of a laser-induced defect with time constant T_{LD}, and relaxation from the CB to the VB with time constant T_{cv}. The shallow traps have their number density N_{ST} and it is assumed that they are completely ionized by each pulse and reoccupied before each pulse arrival. Using these simplifications, we can derive expression for the damage characteristic curve: [144]

$$[F_{th}(S)]^m \approx F_\infty^m + (F_1^m - F_\infty^m)\left(1 - \frac{T_{cv}}{T_{LD}}\frac{N_1}{N_{ST}}\right)^{S-1}, \tag{2.26}$$

where m means the order of the multiphoton absorption needed for excitation from VB to CB. The term $\frac{T_{cv}}{T_{LD}}\frac{N_1}{N_{ST}}$ ensures the limit approach $F_{th}(S) \to F_\infty$ and relates to the relaxation branching ratio $\frac{T_{cv}}{T_{LD}}$ and to the ratio between CB electron density generated by the first pulse interacting with the nascent material (N_1) and the number density of shallow traps (N_{ST}).

In fact, the material response is more complex than has previously been considered. To explain experimental data of damage characteristic curves $F_{th}(S)$, the full set of processes outlined in Fig. 2.18 is needed. Such a comprehensive model based on rate equations was used to explain characteristic damage curves of dielectric materials with a broad range of excitation conditions. [149] The model was used to simulate the $F_{th}(S)$ curves for a HfO_2 film (Fig. 2.19a) excited by trains of 50 fs and 1 ps pulse durations.

The $F_{th}(S)$ differ significantly in shape between the excitation by 50 fs and 1 ps pulses. The curve shapes give information about the effect of deep and shallow states in HfO_2. In the simulations, fitting well the experimental data by solid lines in Fig. 2.19a), high maximum density of laser-induced deep traps and a lower density of native shallow traps were used. For pulses of 50 fs duration, the damage threshold fluence is higher and the deep traps are photo-ionized more efficiently than at long pulse durations. Consequently, the shape of $F_{th}(S)$ is characterized by the slow accumulation of these deep traps since they reach higher densities than shallow traps. [70]

In contrast, the $F_{th}(S)$ for 1 ps pulse is dominated by the occupation of shallow traps due to the lower excitation fluence and therefore lower ionization efficiency of deep traps by the multiphoton process. Due to the longer pulse duration, the role of avalanche ionization is more pronounced (see Section 2.3.3). Even

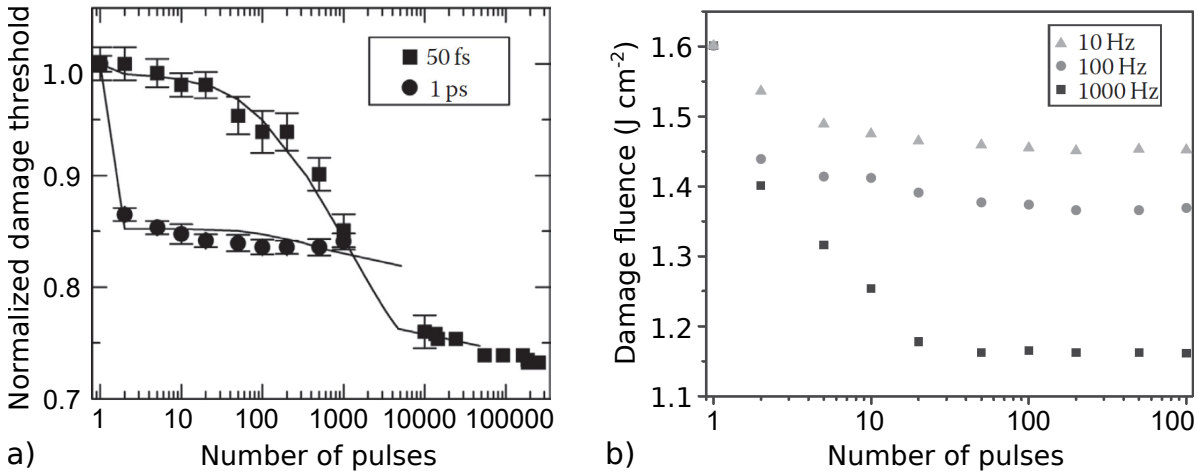

Figure 2.19: (a) Experimental data of characteristic damage curve of HfO_2 obtained using 50 fs and 1 ps pulse durations. The damage thresholds are normalized to F_1. The solid lines correspond to the model based on rate equations taking into account processes depicted in Fig. 2.18. The model assumes low-density ($\sim 10^{18}\,\mathrm{cm}^{-3}$) of native shallow states and a high-density ($\sim 10^{20}\,\mathrm{cm}^{-3}$) of laser-induced deep states. [149] (b) Effect of pulse repetition rate on characteristic damage curves $F_{th}(S)$. Pulse duration 1 ps. [70]

a small number of occupied shallow traps can yield a larger proportion of seed electrons in CB compared to the excitation by shorter pulses.

Another parameter that affects the shape of characteristic damage curve $F_{th}(S)$ is the repetition rate. Comparison of multiple-pulse damage fluences for HfO_2 film irradiated at 10 Hz, 100 Hz and 1000 Hz is shown in Fig. 2.19b). The results clearly show that with increasing repetition rate the multiple-pulse damage fluence is decreasing. The significant damage fluence decrease at 1 kHz is in agreement with the two-pulse damage data, cf. Fig. 2.17, showing that shallow traps of HfO_2 are depopulated within the ms time scale. [70]

In summary, an ideal optical material would show no incubation effects. It has been shown that doping with nitrogen ions, known to alter the properties of shallow traps [150], can eliminate the incubation effect in HfO_2 coatings irradiated by pulses of 800 fs duration. [151]

2.4.5 Damage growth

In the laser damage community, there are two definitions of the term "damage". [2, 152] Somebody may consider damage as the physical appearance of a defect in the material, for another damage is the deterioration of the output quality of the laser system. From the perspective of the laser system user, performance deterioration is more important than the physical appearance of a defect in the material. Often, the presence of a minor imperfection or defect has no effect on laser system performance. Therefore, it is critical to evaluate whether the defect remains constant or grows over time to a size that leads to laser failure.

The tendency of damage to grow under successive pulses is called damage growth. In study [87], the phenomenon in sub-picosecond regime at a wavelength of 1030 nm was simulated on engineered circular defect. In the simulation, a material volume was assumed to be exposed to electric-field intensitites complying with damage threshold conditions. The material was heated and promoted plasma formation. The damage growth predictions were in very good agreement with experimental results. It was found that after the damage onset, the modified areas tend to grow linearly with the number of subsequent pulses. The experiments on high-reflective dielectric coating show the growth process triggering in the case of fluences as low as 50 % of

the intrinsic damage threshold. It should be mention that the damage initiation mechanism in the nodule can be understood and predicted with simulations. [124] However, the damage growth mechanism is much more complex and difficult to be predicted with our current knowledge.

2.4.6 Effect of ambient environment

Most optical materials are employed in atmospheric environment, and their damage resistances are commonly reported and compared for surrounding air. [70] However, to prevent undesirable nonlinear optical processes in gases (air), high-intensity femtosecond laser systems require that some optical components be operated at low pressure (vacuum). Studies in the nanosecond pulse regime, inspired by the use of optical systems in space, indicate that the ambient environment influences LIDTs. [153] This result was explained by the photolysis of background organics, particularly aromatic compounds, which caused the formation of absorbent graphitic layers. When activated by a laser pulse, these deposits are normally cleared by oxygen in the air.

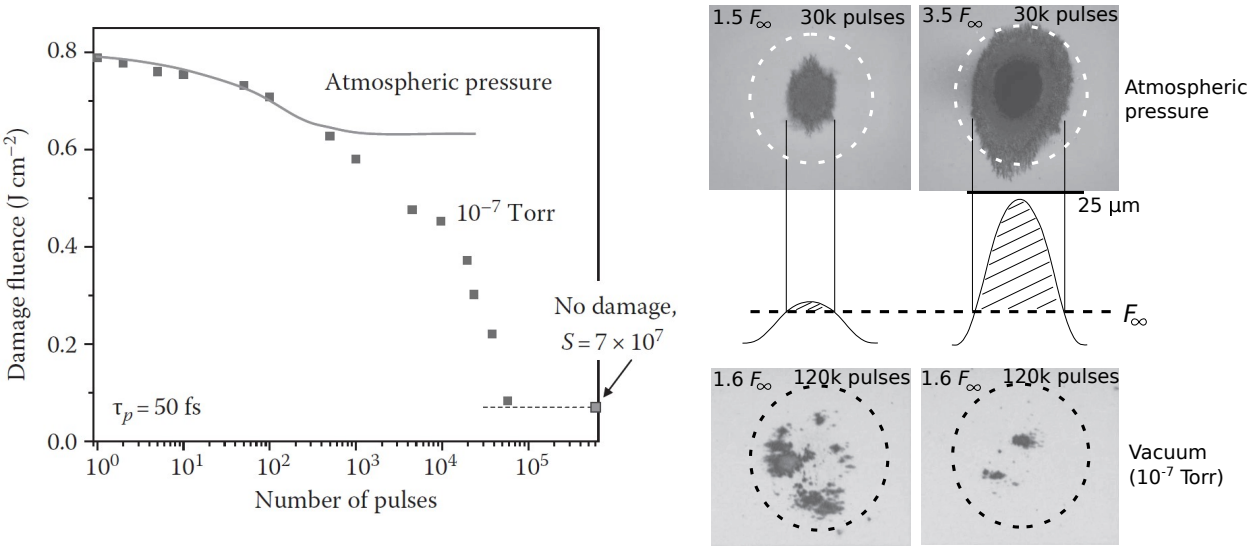

Figure 2.20: Characteristic damage curve of ion-beam-sputtered HfO_2 coatings in air and under vacuum corresponding to testing at a pulse duration of 50 fs and a wavelength of 800 nm. [70]

In the case of femtosecond pulse exposure, the LIDTs of oxide films also vary with ambient gas composition and pressure [154], but for diverse reasons than those discussed for nanosecond pulses. Figure 2.20 illustrates that in vacuum, the multiple-pulse LIDT fluence decreases to roughly 10% of single-shot LIDT at atmospheric pressure. Pressure has no effect on single-pulse thresholds, and there is minimal variation in the $F_{th}(S)$ curves for number of pulses $S < 1000$. However, as the number of pulses increases, not only the LIDT but also the damage morphology changes. While damage at atmospheric pressure is very deterministic and initiates in the laser beam center, where the highest fluence is present, damage begins at random locations inside the beam spot in a vacuum environment, see Fig. 2.20.

Figure 2.21a) depicts the LIDT values with 300k pulses as a function of pressure for the three most prevalent components of air - pure nitrogen, oxygen, and water vapor. In vacuum conditions, the damage threshold can be enhanced by a presence of water vapor. Oxygen has also a little impact on LIDT in low pressure, while nitrogen has no effect on the LIDT. It should also be noted that pressure has no effect on

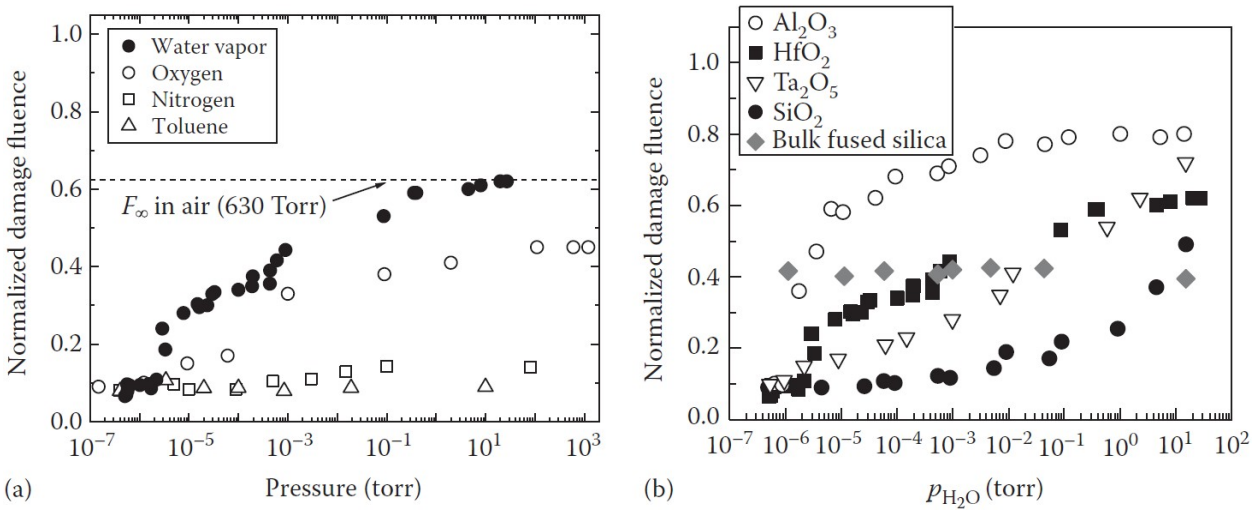

Figure 2.21: (a) Multiple-pulse (S = 300,000) damage thresholds as a function of pressure of various ambient gases. [154] (b) LIDT (S = 300,000) of Al_2O_3, HfO_2, Ta_2O_5, SiO_2 oxide films and bulk fused silica in respect to water vapor pressure (p_{H_2O}). [70]

the multiple-pulse damage threshold of bulk fused silica surfaces, see Fig. 2.21b). However, it does influence LIDT of Al_2O_3, HfO_2, Ta_2O_5, SiO_2 oxide films. The forms of curves illustrating LIDT dependency on pressure differ between these materials.

As can be predicted by multiple-pulse damage modelling, the damage threshold decreases as damage density increases. It has been proposed [154] that the incubation in oxides is caused by the laser-induced generation of oxygen vacancies. The vacancy density in the oxide film might be attributed to the pressure of oxygen and water vapor in the surrounding atmosphere, see Fig. 2.21a).

From atmospheric air pressure to $\sim 3 \times 10^{-6}$ Torr, the damage crater initiates deterministically at the center of the beam and expands in diameter as the fluence increases. [154] At pressure lower than $\sim 3 \times 10^{-6}$ Torr, damage begins at random spot within the exposed area of hafnia film. This might be because water vapor cannot form a monolayer at such low pressure. As a consequence, defect density saturation and hence LIDT is observed. These spots are likely generated at predisposed locations in hafnia such as grain boundaries between crystallites, or crystalline and amorphous material phases.

2.5 Conclusion

In this Chapter 2, we provided a review of laser damage studies on dielectrics in the sub-picosecond regime. We summarized the basic characteristics of the material structure of dielectrics and how they differ from semiconductors and metals. Then, the effects of material heating, defects and intrinsic material properties on the LIDT were discussed. We described ionization and relaxation processes relevant to the sub-ps regime. Finally, we introduced an analytical approach based or rate equations that can be used to predict damage thresholds in optical materials.

We distinguished between single-pulse and multiple-pulse interactions with dielectrics. For the single-pulse interaction, we reviewed studies on damage fluence dependence on parameters. These studies led to the establishment of scaling laws that are used to compare experimental LIDT results obtained with different irradiation conditions (pulse duration, wavelength) or varying material properties (bandgap, refractive

index). In the multi-pulse interaction, we introduced a topic of damage growth, i.e. tendency of damage to grow with the pulses subsequent damage initiation. We should emphasize that it is not the damage initiation but the damage growth process on a optical component what causes laser failure.

Chapter 3

Metrology of sub-ps LIDT tests

Metrology refers to the set of measurement tools and processes that are put in place to ensure the highest possible quality of the measurements made. In this chapter, we present the metrology associated with the study of laser damage to dielectric materials using sub-picosecond and picosecond pulses.

In the sub-ps regime, damage initiation in dielectrics is governed by electronic processes, as it was discussed above. In dielectric thin films, that are the scene of interferential effects, damage initiation is related to the distribution of the electric field intensity. Any increase in electric field intensity within the film facilitates its electronic excitation and thus causes damage initiation at lower fluences of incoming radiation. Therefore, we will firstly present the calculus of the electric field intensity distribution that enables us to determine electric field intensity (EFI) maximum in the case of a monolayer. Then, we introduce the term of intrinsic LIDT fluence, which is normalized to the electric field intensity maximum. The intrinsic LIDT fluence thus allows us to compare results obtained under different experimental conditions, e.g. angle of incidence, polarization, layer thickness or refractive index, that affect the electric field intensity distribution in the thin film.

In the second part of this chapter, we will provide the description of sub-ps near-infrared laser damage station, which was used to obtain the majority of the results reported in this thesis. The description covers damage detection and laser radiation characteristics in energy, temporal and spatial domain. As a part of laser characterization, we summarize variations of laser stability parameters that provide error bars of LIDT fluences experimentally determined in this work. In general, the sub-picosecond laser damage station represents a robust apparatus that enables to adjust multiple irradiation parameters: pulse energy, number of pulses, pulse repetition rate, pulse duration, wavelength, angle of incidence, beam polarization and beam size. For example, the effect of laser wavelength and number of pulses on dielectric coatings LIDT was studied with this station in [104].

In the next section, we will focus on beam-size effects on the measurement of sub-picosecond intrinsic LIDT of dielectric oxide coatings. The study is motivated by published works [155–158] indicating beam-size effects on LIDT measurements, which is in contradiction to the concept of damage initiation given rather by intrinsic material properties than by defects. The concept of intrinsic and thus deterministic single pulse damage was confirmed in early sub-ps studies with fused silica. [142,159] After introducing the topic, we will describe the tested dielectric thin films, used damage test procedure, method of matching between LIDT pulse energies and beam sizes expressed in effective areas. We will show LIDT results carried out with two lenses enabling LIDT tests at different focusing conditions. Then we will analyze and discuss possible causes of observed differences: self-focusing in air and self-focusing in the lens, effect of beam divergence, alignment,

camera errors.

We will then summarize error margins for identified contributors in the best case scenario of LIDT tests performed with this in detail characterized 500-fs 1030-nm LIDT station at Institut Fresnel. The metrological study tells us how accurately we are able to determine LIDT. The summary is applicable for LIDT tests performed on dielectric single layers or optical components characterized within the thesis.

Afterwards, we will present laser damage stations, which were available at GREAT partner institutions: ALPHANOV technological center, HiLASE centre and Extreme Light Infrastructure (ELI) Beamlines. The stations enabled to test dielectric coatings or optical component at conditions which are relevant to the intended applications of GWS. The station at HiLASE centre operates at a pulse duration of 1.8 ps with large beams of effective beam diameter around 315 µm. With the laser available at the Alphanov center, it was possible to perform testing at a pulse duration of 150 ps and a wavelength of 1030 nm, i.e., at conditions close to the stretched pulses existing in laser systems with chirped pulse amplification techniques. The LIDT station at ELI Beamlines, on the other hand, allowed testing using pulses as short as 100 fs generated at a wavelength of 1050 nm. Apart from these near-infrared LIDT stations operating at low repetition rates (≤ 1 kHz), we have built a testing station working with pulses in MHz regime at a pulse duration of 700 fs and at a wavelength of 515 nm.

3.1 Laser-Induced Damage Threshold

According to the international standards [75], the laser damage is any permanent laser-radiation-induced change in the characteristics of the surface of specimens which can be observed by an inspection technique and at a sensitivity related to the intended operation of the product concerned. The term laser-induced damage threshold (LIDT) describes the highest quantity of laser radiation incident upon the optical component, for which the extrapolated probability of damage is zero. The quantity of laser radiation may be expressed in fluence (energy density) in J/cm^2 or power density in W/cm^2.

From a LIDT test with a dielectric layer, we can get directly damage threshold value expressed in F_{ext} external fluence. The fluence at the laser-induced damage threshold is obtained by dividing E, the pulse energy, by the beam size expressed using A_{eff}, the effective beam area: [75]

$$F_{\text{ext}} = \frac{E}{A_{\text{eff}}}. \tag{3.1}$$

The relative uncertainty of the laser-induced damage threshold fluence is thus obtained from the uncertainties of pulse energy and effective area as:

$$\frac{\Delta F_{\text{ext}}}{F_{\text{ext}}} = \frac{\Delta E}{E} + \frac{\Delta A_{\text{eff}}}{A_{\text{eff}}}. \tag{3.2}$$

In this work, we express the uncertainties using 3σ values, which give a 99.7 % confidence interval. Within this thesis, the dielectric layers are irradiated in sub-picosecond regime, in which the external damage threshold fluence is dependent on electric field intensity distribution.

3.1.1 Electric Field Intensity in monolayers on a substrate

Optical thin films are the scene of interferential effects that must be taken into account when investigating damage thresholds, especially in sub-picosecond regime where electronic processes govern. As the distribution of the electric field is not homogeneous, the generation of free electrons depends on the z position (Fig 3.1) considered within the film or component. Therefore, the maxima of the laser-induced electron density in the

conduction band coincide with the maxima of the electric field. The choice of the design to be used then becomes critical in obtaining optical components with high laser damage fluence resistance. The improvement of the resistance of current optical components thus requires the development of a specific theoretical model, capable to account for this complexity.

Before we move on to calculate the electric field intensity for transversely electric (S) and transversely magnetic (P) polarization, we derive the phase difference on a thin film and then express the Fresnel coefficients. These coefficients will be needed to calculate the electric field intensity.

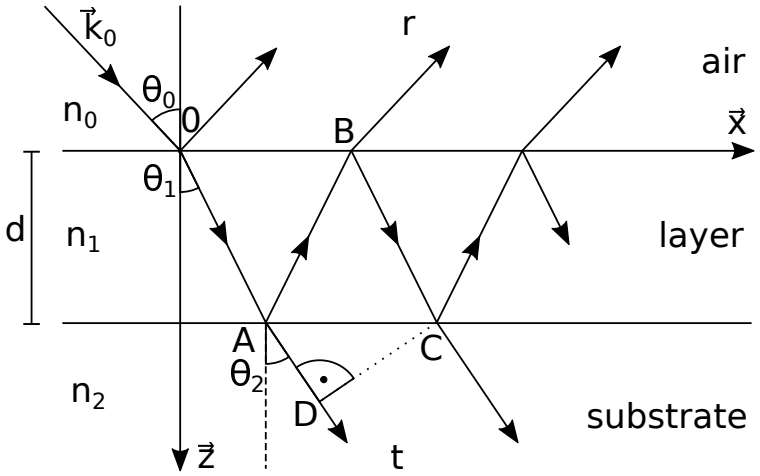

Figure 3.1: Schematic drawing of monolayer design indicating total reflection (r) and total transmission (t) coefficients. The electromagnetic radiation of $\vec{k_0}$ wave vector falls at θ_0 incidence angle on a layer of d thickness deposited on the substrate. Refractive indices of air, layer and substrate are represented by n_0, n_1 and n_2 symbols, respectively.

Phase difference

Consider a simple layer on the substrate, see Fig. 3.1. An electromagnetic wave, characterized by the wave vector $\vec{k_0}$, falls on the air-layer interface. There are two succesive waves that passed through the layer of thickness d and refractive index n_1 and then they are propagating inside the substrate of refractive index n_2. The phase difference (2φ) between these two successive waves in the substrate is:

$$\begin{aligned}
2\varphi &= \varphi_{AB} + \varphi_{BC} - \varphi_{AD} \\
&= \frac{2\pi}{\lambda} n_1 \left(|AB| + |BC|\right) - \frac{2\pi}{\lambda} n_2 |AD| \\
&= \frac{2\pi}{\lambda} n_1 \left(|AB| + |BC|\right) - \frac{2\pi}{\lambda} n_2 \cdot |AC| \cdot \sin(\theta_2) \\
&= \frac{2\pi}{\lambda} n_1 \left(\frac{d}{\cos(\theta_1)} + \frac{d}{\cos(\theta_1)}\right) - \frac{2\pi}{\lambda} n_2 \cdot 2d \tan(\theta_1) \cdot \sin(\theta_2) \\
&= \frac{2\pi}{\lambda} \frac{2d}{\cos(\theta_1)} \left[n_1 - n_2 \sin(\theta_1) \cdot \sin(\theta_2)\right]. \\
&= \frac{2\pi}{\lambda} \frac{2d}{\cos(\theta_1)} \left[n_1 - n_1 \sin^2(\theta_1)\right] = 2 \cdot \frac{2\pi n_1 d \cos(\theta_1)}{\lambda}.
\end{aligned} \tag{3.3}$$

The 2φ phase difference between two successive waves corresponds to the phase difference gained during two one-direction, forward and backward passes over the entire layer of d thickness at θ_1 angle, see Fig. 3.1.

Fresnel coefficients

The reflection (r_{ij}) and transmission (t_{ij}) coefficients at the interface of two environments are defined using Fresnel relations derived from continuity of tangential components of electric and magnetic fields.

$$r_{ij} = \frac{\widetilde{n}_i - \widetilde{n}_j}{\widetilde{n}_i + \widetilde{n}_j}, \tag{3.4a}$$

$$t_{ij} = \frac{2\widetilde{n}_i}{\widetilde{n}_i + \widetilde{n}_j}, \tag{3.4b}$$

where $\widetilde{n}_i$ is the effective refractive index of environment, in which the incident wave propagates and falls on the interface with the second environment of $\widetilde{n}_j$ effective refractive index. The effective refractive indices differ for the state of polarization perpendicular to the plane of incidence (S, TE - Transverse Electric) and the state of polarization parallel to the plane of incidence (P, TM - Transverse Magnetic):

$$\widetilde{n}_i = n_i \cdot cos(\theta_i), \qquad (S) \tag{3.5a}$$

$$\widetilde{n}_i = n_i / cos(\theta_i). \qquad (P) \tag{3.5b}$$

The t total transmission and r total reflection coefficients, as illustrated in Fig. 3.1, can be calculated as:

$$t = t_{01}e^{\imath\varphi}t_{12} + t_{01}e^{\imath\varphi}r_{12}e^{\imath\varphi}r_{10}e^{\imath\varphi}t_{12} + t_{01}e^{\imath\varphi}r_{12}e^{\imath\varphi}r_{10}e^{\imath\varphi}r_{12}e^{\imath\varphi}r_{10}e^{\imath\varphi}t_{12} + ..., \tag{3.6a}$$

$$r = r_{01} + t_{01}e^{\imath\varphi}r_{12}e^{\imath\varphi}t_{10} + t_{01}e^{\imath\varphi}r_{12}e^{\imath\varphi}r_{10}e^{\imath\varphi}r_{12}e^{\imath\varphi}t_{10} + ... \tag{3.6b}$$

These infinite geometric series can be summarized using the formula:

$$\sum_{n\to+\infty}(1 + x + x^2 + ... + x^n) = \frac{1}{1-x}. \tag{3.7}$$

The resulting total transmission and reflection coefficients in the case of single layer are:

$$t = \frac{t_{01}t_{12}e^{\imath\varphi}}{1 - r_{12}r_{10}e^{2\imath\varphi}}, \tag{3.8a}$$

$$r = r_{01} + \frac{t_{10}t_{01}r_{12}e^{2\imath\varphi}}{1 - r_{12}r_{10}e^{2\imath\varphi}}. \tag{3.8b}$$

S polarization

Consider the case of S polarization. The $\vec{\mathcal{E}}_i^+(z)$ electric field is propagating in i-labeled environment, e.g. 0-labeled air on Fig. 3.2a. The $\vec{\mathcal{E}}_i^+(z)$ vector is parallel to $\vec{y}$ direction and oscillates in the tangential plane (perpendicular to the incidence plane). Thus, the $\mathcal{E}_i(z)$ entire electric field containing the $\mathcal{E}_i^+(z)$ incident and retro-propagating $\mathcal{E}_i^-(z)$ part,

$$\mathcal{E}_i(z) = \mathcal{E}_i^+(z) + \mathcal{E}_i^-(z) = E_i^+(z)e^{\imath k_i z} + E_i^-(z)e^{-\imath k_i z}, \tag{3.9}$$

satisfies the following continuity conditions at $z = 0$ and $z = d$ interfaces:

$$E_0^+(0)e^{\imath k_0 \cdot 0} + E_0^-(0)e^{-\imath k_0 \cdot 0} = E_1^+(0)e^{\imath k_1 \cdot 0} + E_1^-(0)e^{-\imath k_1 \cdot 0}, \tag{3.10a}$$

$$E_1^+(d)e^{ik_1 \cdot d} + E_1^-(d)e^{-ik_1 \cdot d} = E_2^+(d)e^{ik_2 \cdot d} + E_2^-(d)e^{-ik_2 \cdot d}. \tag{3.10b}$$

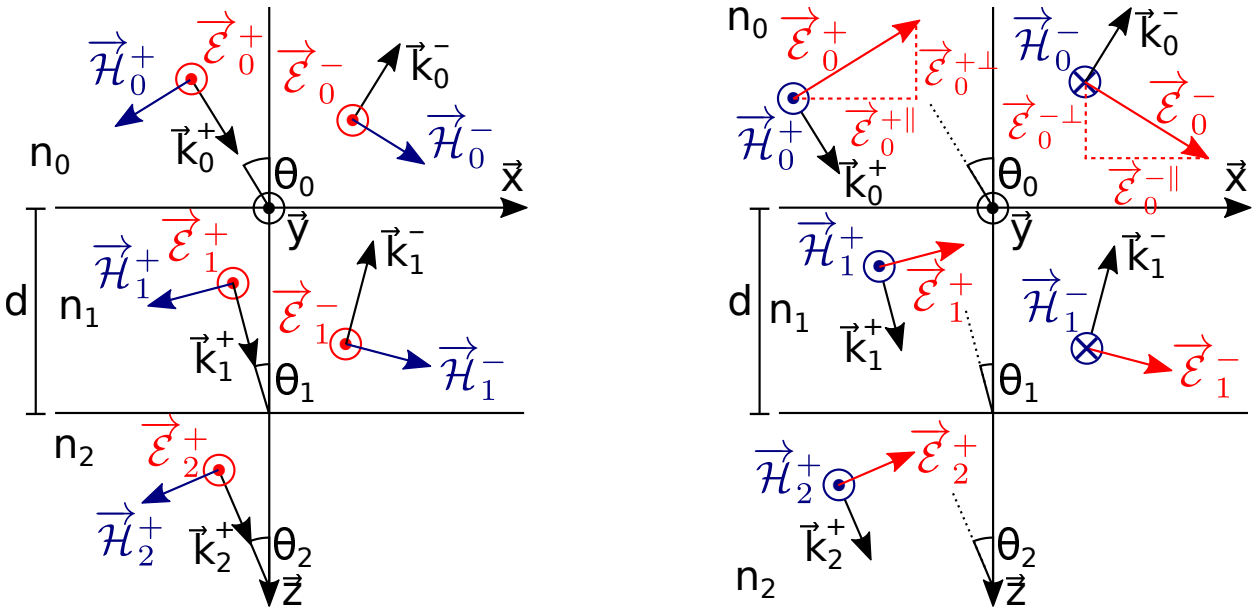

(a) S-polarized beam.

(b) P-polarized beam.

Figure 3.2: Schematic layout of S-polarized (3.2a) and P-polarized (3.2b) beam falling on single layer deposited on substrate.

The $E_2^-(d)$ amplitude is assumed to be 0 that means the substrate is considered of unlimited thickness, i.e. without reverse electromagnetic wave propagating to the layer, see Fig. 3.2a. The total transmission and total reflection coefficients can be written as:

$$t = \frac{\mathcal{E}_2^+(d)}{\mathcal{E}_0^+(0)} = \frac{E_2^+(d)e^{\imath k_2 \cdot d}}{E_0^+(0)e^{\imath k_0 \cdot 0}} = \frac{E_2^+ e^{\imath k_2 \cdot d}}{E_0^+}, \tag{3.11a}$$

$$r = \frac{\mathcal{E}_0^-(0)}{\mathcal{E}_0^+(0)} = \frac{E_0^-(0)e^{-\imath k_0 \cdot 0}}{E_0^+(0)e^{\imath k_0 \cdot 0}} = \frac{E_0^-}{E_0^+}. \tag{3.11b}$$

From the precedent Eqs. (3.10) and (3.11), it can be derived the E_1^+ and E_1^- electric field amplitudes of the layer environment:

$$E_1^+ = (1+r)\,E_0^+ - E_1^-, \tag{3.12a}$$

$$E_1^- = E_0^+ \frac{t-(1+r)e^{\imath k_1 \cdot d}}{e^{-\imath k_1 \cdot d} - e^{\imath k_1 \cdot d}}. \tag{3.12b}$$

Using the electric field amplitudes and the Eq. (3.9), the electric field intensity within the different environments can be plotted as a function of z position,

$$EFI_S = \left| \frac{\mathcal{E}_i(z)}{\mathcal{E}_0^+} \right|^2. \tag{3.13}$$

P polarization

In the case of P polarization, see Fig. 3.2b, the electric field $\mathcal{E}_i(z)$ in i-labeled environment contains the normal component $\mathcal{E}_i^{\perp}(z)$, perpendicular to the environment interface, and the tangential component $\mathcal{E}_i^{\parallel}(z)$,

parallel to the interface along x axis. This fact is reflected in the definition of electric field intensity for P-polarized beam:

$$EFI_P = EFI_i^{\parallel} + EFI_i^{\perp} = \left| \frac{\mathcal{E}_i^{\parallel}(z)}{\mathcal{E}_0^{+}} \right|^2 + \left| \frac{\mathcal{E}_i^{\perp}(z)}{\mathcal{E}_0^{+}} \right|^2, \tag{3.14}$$

where $\mathcal{E}_i^{\parallel}(z)$ and $\mathcal{E}_i^{\perp}(z)$ denote electric field components in tangential plane and normal orientation to interface, respectively. Both electric field components meet the following equations:

$$\mathcal{E}_i^{\parallel}(z) = \mathcal{E}_i^{\parallel+}(z) + \mathcal{E}_i^{\parallel-}(z) = E_i^{\parallel+}(z)e^{\imath k_i z}\cos(\theta_i) + E_i^{\parallel-}(z)e^{-\imath k_i z}\cos(\theta_i) \tag{3.15a}$$

$$\mathcal{E}_i^{\perp}(z) = \mathcal{E}_i^{\perp+}(z) - \mathcal{E}_i^{\perp-}(z) \tag{3.15b}$$

where the minus sign in the Eq. (3.15b) corresponds to the retro-oriented direction of the reflected vector of the electric field normal component to the incident vector normal component, see Fig. 3.2b.

The $E_i^{\parallel}(z)$ electric field tangential component meets the condition of continuity at the environment interfaces at $z = 0$ and $z = d$, analogous to the case of S polarization:

$$E_0^{\parallel+}(0)e^{\imath k_0 \cdot 0}\cos(\theta_0) + E_0^{\parallel-}(0)e^{-\imath k_0 \cdot 0}\cos(\theta_0) = E_1^{\parallel+}(0)e^{\imath k_1 \cdot 0}\cos(\theta_1) + E_1^{\parallel-}(0)e^{-\imath k_1 \cdot 0}\cos(\theta_1), \tag{3.16a}$$

$$E_1^{\parallel+}(d)e^{\imath k_1 \cdot d}\cos(\theta_1) + E_1^{\parallel-}(d)e^{-\imath k_1 \cdot d}\cos(\theta_1) = E_2^{\parallel+}(d)e^{\imath k_2 \cdot d}\cos(\theta_2) + E_2^{\parallel-}(d)e^{-\imath k_2 \cdot d}\cos(\theta_2). \tag{3.16b}$$

The total transmission and total reflection coefficients are:

$$t = \frac{E_2^{\parallel+}(d)e^{\imath k_2 \cdot d}\cos(\theta_2)}{E_0^{\parallel+}(0)e^{\imath k_0 \cdot 0}\cos(\theta_0)} = \frac{E_2^{\parallel+}e^{\imath k_2 \cdot d}}{E_0^{\parallel+}} \cdot \frac{\cos(\theta_2)}{\cos(\theta_0)}, \tag{3.17a}$$

$$r = \frac{E_0^{\parallel-}(0)e^{-\imath k_0 \cdot 0}\cos(\theta_0)}{E_0^{\parallel+}(0)e^{\imath k_0 \cdot 0}\cos(\theta_0)} = \frac{E_0^{\parallel-}}{E_0^{\parallel+}}. \tag{3.17b}$$

The $E_1^{\parallel+}(0)$ and $E_1^{\parallel-}(0)$ electric field amplitudes can be expressed from the Eqs. (3.16) and (3.17) as:

$$E_1^{\parallel+} = (1+r)\,E_0^{\parallel+} \cdot \frac{\cos(\theta_0)}{\cos(\theta_1)} - E_1^{\parallel-}, \tag{3.18a}$$

$$E_1^{\parallel-} = E_0^{\parallel+}\frac{t - (1+r)e^{\imath k_1 \cdot d}}{e^{-\imath k_1 \cdot d} - e^{\imath k_1 \cdot d}} \cdot \frac{\cos(\theta_0)}{\cos(\theta_1)}. \tag{3.18b}$$

Using the electric field amplitudes and the Eq. (3.15a), the $E_i^{\parallel}(z)$ electric field intensity corresponding to the tangential component can be determined.

The $\mathcal{E}_i^{\perp}(z)$ electric field normal component, by contrast, does not meet the continuity condition at the interface. Its $\mathcal{E}_i^{\perp+}(z)$ incident and $\mathcal{E}_i^{\perp-}(z)$ retro-propagating components can be expressed using goniometric relations with the $\mathcal{E}_i^{\parallel+}(z)$ and $\mathcal{E}_i^{\parallel-}(z)$ counterparts in the tangential plane:

$$\mathcal{E}_i^{\perp+} = \mathcal{E}_i^{\parallel+}\tan(\theta_i) \tag{3.19a}$$

$$\mathcal{E}_i^{\perp-} = \mathcal{E}_i^{\parallel-}\tan(\theta_i). \tag{3.19b}$$

From the Eq. (3.15b), the $\mathcal{E}_i^{\perp}(z)$ entire electric field normal component size can be determined and used for the electric field intensity calculation using Eq. (3.14). [69, 80, 81, 104, 134, 160] The above described model of the electric field intensity calculus was implemented in MATLAB environment and compared with the results obtained by commercial COMSOL software. We provide the validated code in Appendix B.

3.1.2 Intrinsic LIDT fluence

Since the optical layers are the scene of interferential effects, the distribution of electric field inside layer irradiated by laser is not homogeneous. The electric field distribution is critical for understanding the sub-ps LIDT results because the excitation of dielectrics is governed by electronic processes, see Chapter 2. [70] To compare LIDT results with different conditions having an influence on electric field distribution, e.g. angle of incidence, polarization, layer thickness or refractive index, it is necessary to rescale the LIDT results with the electric field intensity maximum (EFI_{max}) within the given layer. The EFI_{max} can be determined using the model for monolayer described in previous Sec. 3.1.1. The value is used to calculate the rescaled LIDT results expressed by F_{int} intrinsic fluence:

$$F_{\mathrm{int}} = EFI_{\mathrm{max}} \cdot F_{\mathrm{ext}} = \left| \frac{E_{\mathrm{max}}}{E_{\mathrm{inc}}} \right|^2 \cdot F_{\mathrm{ext}}, \tag{3.20}$$

where F_{ext} means experimentally used external fluence, the E_{max} represents the maximum value of electric field in the layer and the E_{inc} means incident electric field amplitude. [161] The correction factor of incidence angle is taken into account within the EFI_{max} calculation. The distribution of electric field intensity for used Nb_2O_5 layer with our experimental conditions is shown on Fig. 3.3. It should be noted that LIDT results reported in this thesis correspond to the F_{int} intrinsic fluence.

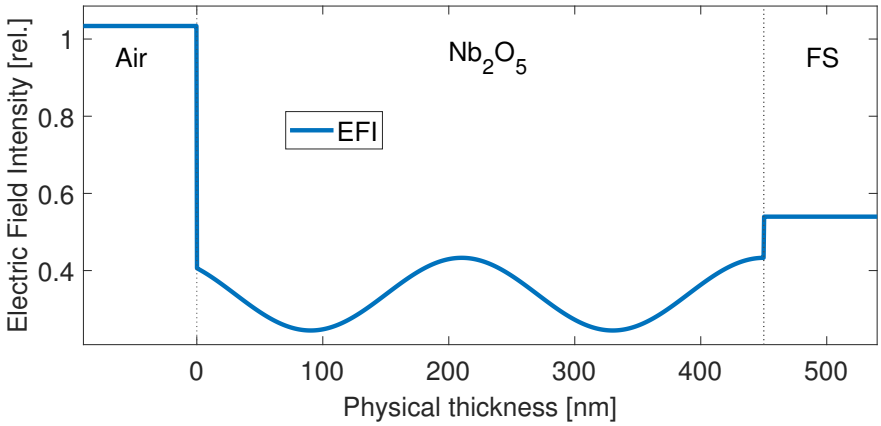

Figure 3.3: Distribution of electric field intensity (EFI) inside Nb_2O_5 layer of 450 nm thickness (refractive index 2.26 at 1030 nm). Fused silica substrate (FS, refractive index 1.45 at 1030 nm). Polarization P, angle of incidence 45°. The EFI is normalized to the incident electric field amplitude in air.

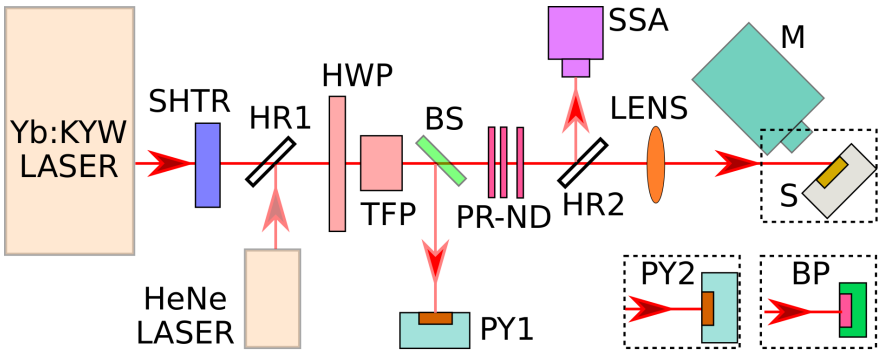

Figure 3.4: Schematic drawing of sub-ps near-infrared LIDT station. HeNe laser is intended for station alignment. SHTR - shutter, HR1/HR2 - high reflective flip-flop mirrors, HWP - half-wave plate, TFP - thin film polarizer, BS - beam splitter, PY1/PY2 - pyroelectric detectors, PR-ND - partially reflective @1030nm and neutral density filters, LENS - focusing lens, S - sample, BP - beam profiling camera, SSA - single shot autocorrelator. More details are given in Section 3.2.

3.2 500-fs 1030-nm LIDT experimental setup

Laser damage tests were done by using a commercial diode pumped Yb:KYW laser (Amplitude Systemes S-pulse HP). The system emits radiation of nearly Gaussian spatial profile ($M^2 \approx 1.15$) in the near-infrared wavelength around 1030 nm. The emitted pulses have pulse duration of 500 ± 50 fs that was measured by a single shot autocorrelator (AVESTA ASF 70 fs–3 ps, Acore software). The experimental set-up is described in Fig. 3.4.

We used the Yb:KYW laser at 10 Hz repetition rate. The maximum pulse energy was 1 mJ. The single shot mode was achieved using a mechanical shutter (SHTR, Thorlabs SH05). The pulse energy was adjusted by a 0-order half-wave plate (HWP), mounted on a motorized rotation stage, and a thin-film polarizer (TFP). The beam that passed through the polarizer falls on the beamsplitter (BS) which directs a small part of pulse energy ($\approx 5\,\%$) to a pyroelectric energy meter (OPHIR PE9) recording the energy of each pulse. The energy meter is calibrated to the energy incident on the tested sample (S) which was measured using a second pyroelectric meter (PY2, OPHIR PE9F) placed behind a focusing lens (LENS).

The beam used for LIDT testing is linearly polarized and focused by a plano-convex lens on the tested sample (S) which was placed at 45° incidence angle. The LIDT testing was performed in ambient air at room temperature. Positioning of the tested sample is done using a motorized 2D translation stage. The laser damage station is equipped with a He-Ne laser which is used for beam alignment.

The focused laser radiation of pulse energy reduced by 6 to 7 orders of magnitude using a combination of partially reflective and neutral density filters (PR-ND) is analyzed by a beam profiling camera (BP) connected to an imaging software. The camera was placed instead of holder with sample (S), see Fig. 3.4, and its sensor was oriented perpendicularly to the beam direction. In this study, two focusing plano-convex lenses with focal lengths of 30 cm and 15 cm were used. Both lenses had a diameter of 25 mm and were made of AR-coated N-BK7 material. Examples of measured beam profiles at different lens positions for both lenses are shown on Fig. 3.5. For $z < 0$, the camera is close to the focusing lens (before the focal plane).

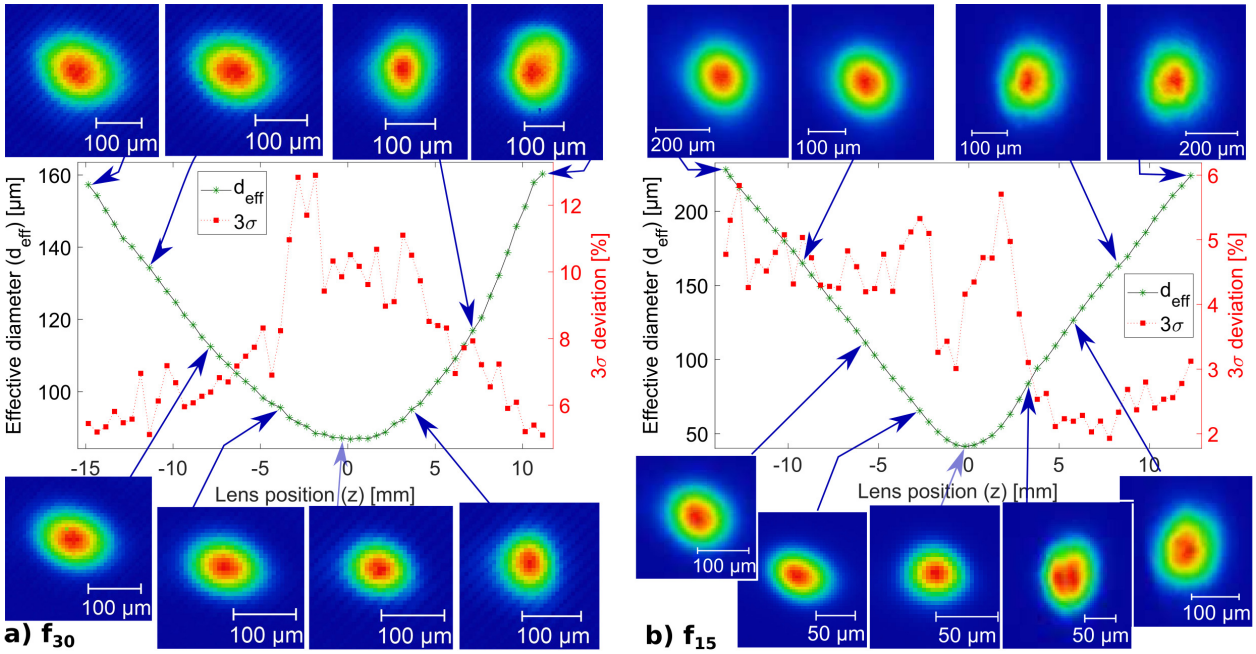

Figure 3.5: Effective beam diameter (d_{eff}) and 3x standard deviation (3σ) of effective area as a function of lens position, with typical normalized beam profiles at different positions. For $z < 0$, the camera is close to the focusing lens (before the focal plane). Comparison of lenses with different focal lengths: a) $f_{30} = 30\,\text{cm}$, $d_{\text{eff,min}} \approx 86\,\mu\text{m}$, b) $f_{15} = 15\,\text{cm}$, $d_{\text{eff,min}} \approx 40\,\mu\text{m}$.

3.2.1 Beam size measurement

Particular attention in this study was given to the determination of beam size with its statistical deviation in dependence of lens position. The beam size is expressed using the effective diameter (d_{eff}), defined using square root of the effective area (A_{eff}) divided by π: [75]

$$d_{\text{eff}} = 2 \cdot \sqrt{\frac{A_{\text{eff}}}{\pi}}. \tag{3.21}$$

For beam with transverse profile of optical intensity described using Gaussian function, the diameter at $1/e^2$ peak intensity is $d_{1/e^2} = \sqrt{2} \cdot d_{\text{eff}}$. The effective area is obtained by the ratio of pulse energy E and maximum energy density (F_{max}) of the laser pulse in the target plane, i.e. [75]

$$A_{\text{eff}} = \frac{E}{F_{\text{max}}} = \frac{\sum_{\text{pixel}} E_{\text{pixel}}}{\frac{E_{\text{max}}}{S_{\text{pixel}}}}, \tag{3.22}$$

where E_{pixel} is the signal measured on a pixel, S_{pixel} denotes the surface of one pixel and E_{max} stands for maximum signal of the beam captured on one pixel of used sensor.

For both used lenses, the beam profiles were measured at discrete lens positions with maximum lens position step of 0.5 mm. The beam profile after lens of 30 cm focal length, see Fig. 3.5a), was measured by WinCam UCD23 camera (DataRay Inc.) with CCD sensor of 6.45 µm pixel length. In the case of lens with 15 cm focal length, the beam profiles were analyzed by two different cameras: the WinCam UCD23 and BP87 (Femto Easy) whose parameters are listed in Table 3.1. The results recorded by these cameras were analogous but the ones of BP87 were preferred because the used CMOS sensor provided higher lateral

Camera	WinCam	BP87
Sensor type	CCD 14-bit	CMOS 12-bit
Pixel size [µm]	6.45 x 6.45	3.45 x 3.45
Exposure time	41 µs	39 µs
Noise per signal max.	1-2%	0.1%

Table 3.1: Parameters of beam profilers.

resolution due to its 3.45 µm pixel length, which was important for the smallest beam around the focal plane. Another advantage of BP87 beam profiler was its lower noise in comparison to the WinCam. The statistical results, see Fig. 3.5b), were derived from 100 frames per lens position.

The measurement of the effective areas in dependence of the lens positions allowed us to determine accurately focal plane corresponding to the lens position with minimum of effective area. The obtained data points of effective beam area were then linearly interpolated between each measured point in order to determine subsequently the effective beam areas of specific lens positions corresponding to the LIDT tests.

The values of three standard deviations (3σ) from a mean were calculated using the formula:

$$3\sigma = 3 \cdot \sqrt{\frac{\sum_{i=1}^{N} \left(A_i - \bar{A}\right)^2}{N-1}}, \tag{3.23}$$

where A_i represents i-th area value and $\bar{A}$ the average (mean) area value within the sample size of N values, i.e. number of beam profile frames per given lens position. The 3σ deviations were also linearly interpolated between each measured point to be defined at lens positions corresponding to the LIDT tests. Thus, the 3σ deviations shown in LIDT results are only estimations since they were not measured at exactly the same lens positions.

3.2.2 Laser stability

The accuracy of damage threshold depends on the laser stability. Instabilities in temporal or spatial beam profile can affect damage threshold and lead to erroneous results. [103] The stability parameters of used near-infrared LIDT station were measured and their 3σ deviations are summarized in Table 3.2. To determine the variations of laser pulse energies, pyroelectric meter recorded the energy values for several hours and the results are shown in Fig. 3.6. For reliable pulse duration determination, the measurement with AVESTA ASF autocorrelator was repeated with various calibration delays, see Fig. 3.7, showing absolute uncertainty in tens of fs. Thanks to the low variations in pulse energy, pulse duration and beam size, the station enables to perform laser damage tests with high accuracy and limits the errors in measurement.

Parameter	f	3σ	Sampling
Effective area	30 cm	< 13 %	64 / lens pos.
	15 cm	< 6 %	100 / lens pos.
Pulse energy		0.7 %	30000
Pulse duration		1.2 %	1600

Table 3.2: Variations of laser stability parameters, expressed in pulse-to-pulse 3σ deviations. Effective beam area was measured for two lenses of different focal length (f). The 3σ deviation of effective area depends on lens position, see Fig. 3.5. Sampling expressed in number of pulses.

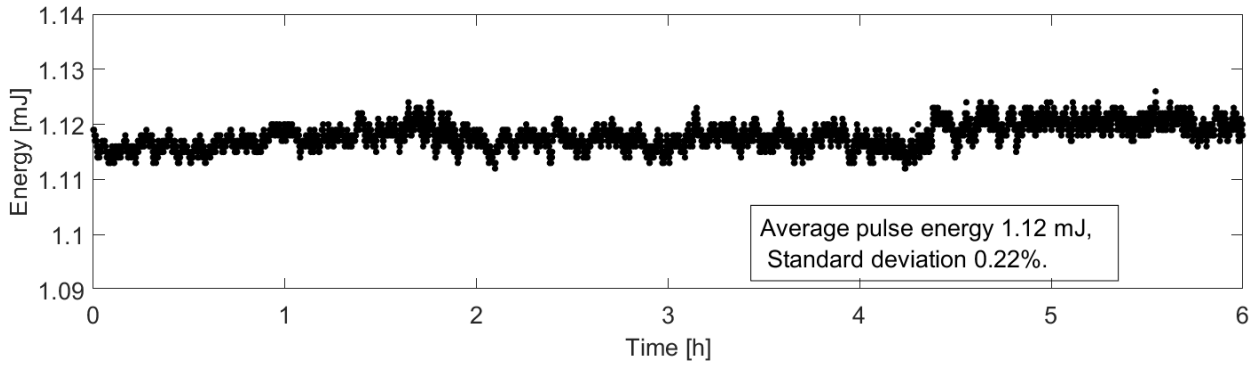

Figure 3.6: Endurance of laser used for LIDT tests. Measured by PE9F (OPHIR) pyroelectric meter.

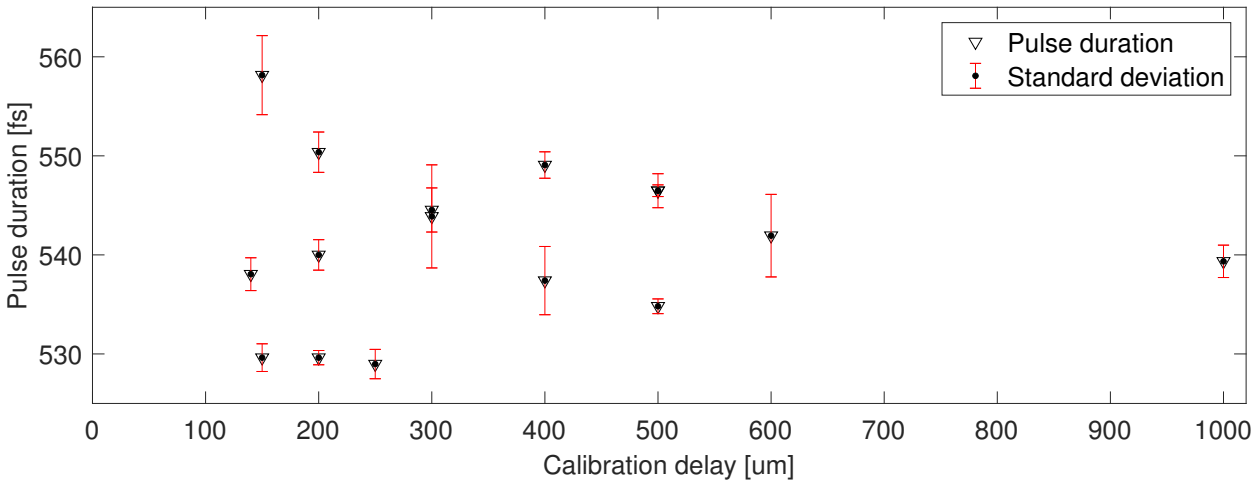

Figure 3.7: Pulse duration of laser used for LIDT tests. Measured by AVESTA ASF single-shot autocorrelator connected to Acore software. Since the determined pulse duration was dependent on autocorrelator calibration delay and differs between individual measurements, we estimate absolute error margin ±50 fs.

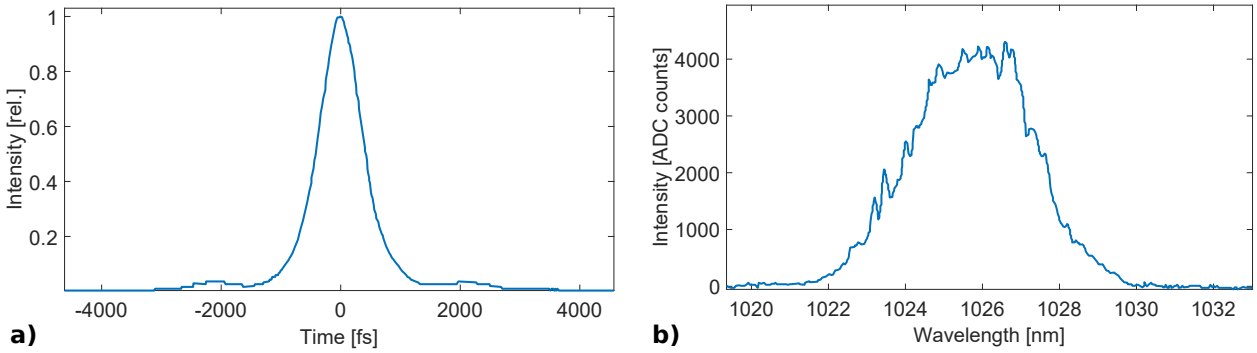

Figure 3.8: Laser pulse characterization: a) autocorrelation trace, b) spectral profile measured at 1 kHz repetition rate. From autocorrelation trace, pulse duration full width at half maximum of 525 fs (sech^2) has been determined. Pulse duration determined using discrete Fourier transformation from spectral profile is 410 fs.

3.2.3 Temporal and spectral profile of pulse

The spectral profile was measured by a high-resolution spectrometer (AvaSpec-3648) connected to imaging software (AvaSoft). The characteristic profiles of the temporal pulse and the spectral distribution are shown on Fig. 3.8. From the autocorrelation trace, we can determine the pulse duration using the relation:

$$\tau = I_{\mathrm{FWHM}}/C_p, \tag{3.24}$$

where I_{FWHM} means full width at half maximum (FWHM) of intensity and C_p signifies deconvolution factor. Assuming a beam of sech^2 temporal profile, we use $C_p = 1.543$ giving pulse duration of 525 fs.

Another way to estimate the pulse duration is by using a discrete Fourier transform from the frequency to the time domain. Using the discrete Fourier transformation applied on the spectral profile in Fig. 3.8b) we determined pulse duration ~ 410 fs.

The minimum pulse duration we can determine using the Heisenberg uncertainty principle which relates the temporal FWHM width $\Delta\tau$ of a pulse to its spectral FWHM $\Delta\nu$ expressed in frequency: [73, 162]

$$\Delta\nu \cdot \Delta\tau \geq K, \tag{3.25}$$

where K means a factor whose value depends on the shape of the temporal profile. The spectral FWHM can be expressed as:

$$|\Delta\nu| = |\nu_2 - \nu_1| = \left|\frac{c}{\lambda_2} - \frac{c}{\lambda_1}\right| = \left|\frac{c\cdot\Delta\lambda}{\left(\lambda_0 + \frac{\Delta\lambda}{2}\right)\left(\lambda_0 - \frac{\Delta\lambda}{2}\right)}\right| = \left|\frac{c\cdot\Delta\lambda}{\lambda_0^2 - \frac{1}{4}\Delta\lambda^2}\right|, \tag{3.26}$$

where c is the speed of light in vacuum, λ_0 the central wavelength and $\Delta\lambda$ spectral FWHM.

Heisenberg's uncertainty principle states that the broader the spectral width of a pulse, the shorter its pulse duration can be. This relation allows us to calculate this theoretical minimum once the spectral width is known (the pulse is then said to be Fourier limited). In our case, $\Delta\lambda = 3.8$ nm, central wavelength $\lambda_0 = 1026$ nm and the K factor for sech^2 temporal beam profile is 0.315. According to Heisenberg's uncertainty principle (Eq. 3.25) we get minimum $\Delta\tau$ pulse duration of 293 fs.

3.3 Beam-size effect on LIDT with 500-fs 1030-nm pulses

After the advent of the laser, it was soon recognized that laser-induced damage in optical components is frequently initiated by defects, such as pits, grooves, cracks, absorbing inclusions, scratches, pores, impurities or material contamination. [141, 163–167] The defects, that act as laser damage precursors, are inherently stochastically distributed and thus provide explanation of non-deterministic behavior and damage threshold dependence on laser beam size. [163, 168] Larger beams increase the probability that a defect is present within the irradiated area. The defect dominated damage behavior was observed in long-pulse (nanosecond) regime, in which the damage is consequence of several physical processes involving absorption, heating, phase changes of materials, hydrodynamic processes and plasma formation. Since nanosecond pulses are relatively long compared to the time scales of these processes, small defect precursors can trigger a cascade of events that can lead to micro-explosion and damage. [78, 169] However, if the pulse duration is shorter than the relaxation time, i.e. energy transfer from electrons to atomic network, which lasts several picoseconds for dielectrics, the processes of excitation and relaxation are decoupled in time. [84] In such ultra-short regime, the damage is mainly driven by multiphotonic absorption in the irradiated material because the other processes cannot be involved within the short pulse duration. Laser damage with sub-ps pulses has

therefore a strong nonlinear dependence on intensity and the damage threshold fluence is deterministic without significant statistical variations, as opposed to nanosecond pulses. [85, 95, 170–172] The evidence of deterministic damage threshold suggests that damage initiation is given by fundamental intrinsic material properties (energy bandgap, refractive index) rather than by stochastically distributed defects. Thus, if the limiting factor of material damage resistance seems to be the intrinsic material properties, then the laser damage threshold is expected to be independent on laser beam size. This was confirmed in the early studies on this topic with fused silica irradiated by 400 fs pulses within the beam diameters ranging from 0.4 to 1.0 mm. [159] The fused silica LIDT independence on beam size was confirmed at 100 fs with number of pulses ranging from 1 to 1000. [142]

3.3.1 Independence of LIDT on beam-size might not be entirely correct.

Material - reference [-]	LIDT [J/cm^2]	Beam diameter [μm]	Beam size effect [-]	τ [fs]	λ [nm]	Non1 [-]	f [kHz]	Explanation [-]
Fused silica [155]	26 – 6	1.6 – 22	Yes	450	1025	1	-	Defects
Sapphire crystal [156]	45 – 1	6 – 110	Yes	100	800	1	1	Plasma shielding
Fused silica [173]	6.5 – 6	30 – 100	$< 15\,\%$	1000	1053	1	-	
E-beam Si coating [173]	5.5 – 5	30 – 100	Ambiguous	1000	1053	1	-	
PIAD Si coating [173]	4.5 – 4	30 – 100	Ambiguous	1000	1053	1	-	
Borosilicate glass [157]	1.0 – 0.2	40 – 800	Yes	30	800	1000	1	Defects
Ion phosphate glass [158]	0.8 – 0.3	160 – 560	Yes	30	795	1000	1	Defects
Fused silica [159]	2.3	400 – 1000	No	400	1053	600	0.01	
Fused silica [142, 174]	$\sim$ shots	5.6; 23	No	100	800	1-1k	≤ 0.02	
Silicon [175]	1.0 – 0.2	20 – 400*	Yes	30	790	1-10k	1.7	Defects
Silicon [176]	0.5 – 0.1	3.2 – 9.6	Yes	60	800	100	1	Defects
Dentin [177]	0.7 – 0.5	260 – 520	$\sim$ rep. rate	130	800	1000	0.1 - 1	Thermal effects
Polystyrene [178]	1.2 – 0.4	20 – 400	Yes	30	790	1-10k	1.7	Defects
Stainless steel [175]	1.1 – 0.3	20 – 400*	Yes	30	790	1-10k	1.7	Defects
Stainless steel [176]	0.4–0.03	3.2 – 9.6	$\sim$ treatment	60	800	100	1	Defects

Table 3.3: Review of some studies on beam size effect on damage threshold by ultrashort pulses. Symbols: τ - pulse duration, λ - laser wavelength, Non1 - number of pulses irradiated on the same site, f - pulse repetition rate. The symbol * refers to additional experiments done with other laser ($\lambda = 800$ nm, $\tau = 60$ fs, 2.6 μm beam diameter). For more details, see references.

However, this attitude to damage onset initiated by ultra-short pulses might not be entirely correct. There are experimental studies employing pulses of duration between 30 fs and 1 ps showing damage/ablation thresholds dependent on the beam size. These experiments were done on stainless steel [175, 176], silicon [175, 176], or even dielectric materials (fused silica [155], barium borosilicate glass [157], ion phosphate glass [158], dentin [177], sapphire monocrystal [156], polystyrene [178]). In the studies [155, 157, 158, 175, 176, 178] the beam size dependence of laser damage was described using defect-site models distinguishing two laser-induced damage regimes - extrinsic defect-dominated regime for larger beam sizes and intrinsic regime for smaller ones. The defect-site models fitted well the experimental results, even though the nature of defect sites initiating damage remains often unclear. [157, 158, 179] In the work [176], the effect of material treatment on the damage threshold was studied. Both the AlO_x slurry treatment on silicon and grit sandpaper treatment on stainless steel led to an increase of defect density, increasing the effect of beam-size on LIDT. The effects of defects in the studies (Table 3.3) are potential explanations, but they are not demonstrated. The role of defects in dentin [177], stainless steel [175, 176], polystyrene [178] or slurry treated silicon [176] could

be affected by the fact that the opaque materials do not show optical quality or sample homogeneity. In addition, the multiple shot tests reflect presence of cumulative effects including laser-induced defects that facilitate electronic excitation which differs from fundamental interaction of a sub-ps pulse with a monolayer of dielectric material that we aim to study in this work. In the study of damage threshold on dentin [177], the effect of beam size was significantly affected by repetition rate. At 100 Hz, the ablation threshold was almost independent on beam size whereas at higher repetition rates, 1 kHz and 500 kHz, the beam size dependence of ablation thresholds was evident and heat accumulation was proposed as an explanation. Recently, E-beam deposited and PIAD silica thin films together with fused silica were tested by broad range of picosecond pulse durations (1 – 60 ps) and results were compared for three sizes of beam waists (30, 50, 100 µm in FWHM). [173] The results obtained by 1 ps pulses are ambiguous with respect to the beam size effect. The highest threshold fluences were measured with smallest beams (30 µm) in all three optical materials but the thresholds achieved with 50 µm beam waists were lower than the 100 µm ones for both coatings.

The comparison of above mentioned published results (Table 3.3) is difficult since the experiments have not been done in the same conditions. The laser parameters differed in pulse duration, laser wavelength, number of pulses, repetition rate or spot size range. The tests were done on various samples of different properties (material, surface state, fabrication, polishing, cleaning, contamination, prior history etc.). The study of beam-size dependence in femtosecond range could be also affected by nonlinear effects which were observed in bulk fused silica below damage threshold in the case of smaller numerical apertures, i.e. larger beam sizes. [180] Apart from the experimental conditions, the laser damage dependence on beam size is a function of the used threshold definition. The results published in nanosecond study [181] suggest damage threshold independence of beam size if damage threshold is defined as fluence of 0 % damage probability. However, if damage threshold is considered as fluence of 50 % damage probability, the effect of beam-size is evident. In general, in presence of defects, the effect of beam size is growing with increasing probability of damage used for threshold definition. Additionally, the damage threshold results may vary by a few percents because of used calorimeters or beam profiling cameras that have influence on possible deviations of measured pulse energies or beam areas. [182]

The motivation of this study is to test laser damage resistance of dielectric materials that are used in coatings of optical components which determine the limit of reliable operation of high energy sub-picosecond solid-state lasers. [2] The effect of beam size on the damage threshold is extremely important for qualifying optical components for use in high power lasers. The results in this work should indicate whether small beam sizes can be used for the testing of optical components that will be implemented in high-energy large-beam lasers, such as in the applications of GREAT project. The limit to this approach is the role of macroscopic defects, such as nodules, that were evidenced in the sub-ps regime. [140] In that case only Raster scan testing procedures are relevant for laser damage testing. [86] We will focus on the single shot testing method to study fundamental interaction of a sub-picosecond pulse with a monolayer of dielectric material (HfO_2, Nb_2O_5) and to exclude the complexity of cumulative effects and interference phenomenon in a multilayer stack.

3.3.2 Tested Samples

The tested samples were monoloayers of HfO_2 and Nb_2O_5. The HfO_2 sample of 150 nm thickness was deposited by electron-beam evaporation with ion assistance on BK7 substrate. The refractive index is 1.93 determined at 1053 nm with spectrophotometry. [183] The Nb_2O_5 monolayers are deposited on fused silica substrates with magnetron sputtering process controlled by HELIOS system. [184] The refractive index was determined by spectrophotometry to be 2.26 at 1030 nm wavelength. The thickness of the tested Nb_2O_5 layers were 150 and 450 nm.

3.3.3 Damage Test Procedure

The LIDT test consisted of a procedure adapted to the study of beam size effect on damage threshold. The different beam sizes were achieved by focal lens positioning using a motorized stage. At a given lens position, the sample was irradiated at different spots with unique pulse energies that were changed with $\sim 1\,\%$ energy increment. The damage threshold was then determined as an average between the lowest fluence with damaged spot and the highest fluence with zero probability of damage. The LIDT results on both Nb_2O_5 and HfO_2 were deterministic.

3.3.4 Damage detection

Laser damage was detected *in situ* by optical microscopy with a 20x magnification of objective mounted on BXFM Olympus microscope. The technique allows real time estimation of the irradiated sample surface state. After the LIDT testing, an *ex-situ* damage inspection was performed using an Zeiss Axiotech differential interference contrast (DIC) microscope with objective of 20x magnification. Due to the better contrast with DIC microscopy, the *ex-situ* observation technique was preferred for the determination of damage threshold results presented in this work.

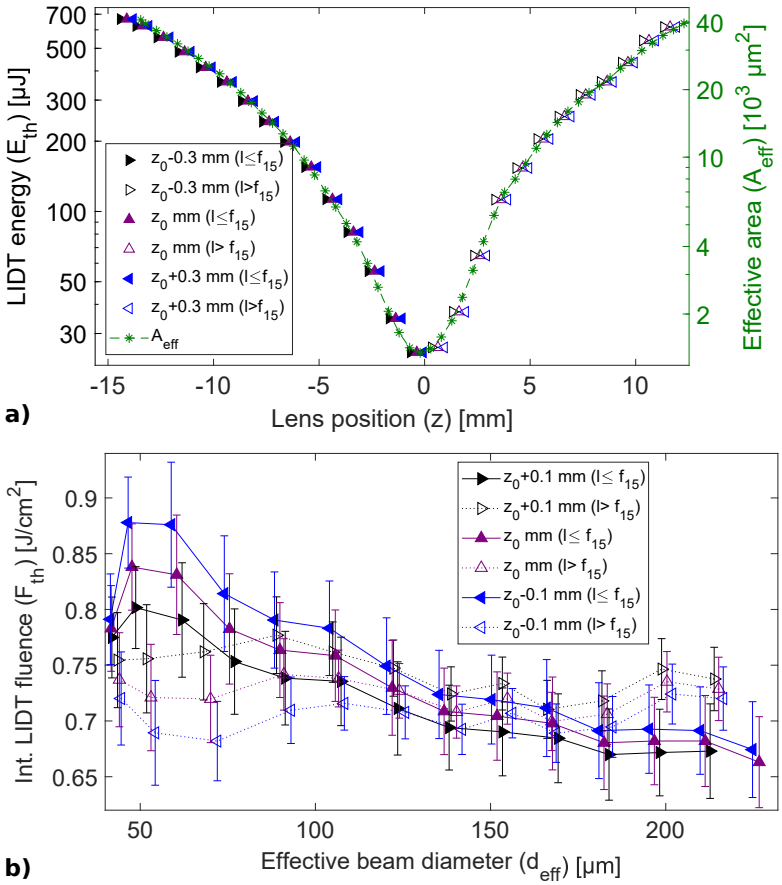

Figure 3.9: LIDT results of Nb_2O_5 sample tested with lens of $f_{15} = 15\,\text{cm}$ focal length: a) Fitting of LIDT pulse energy dataset to the A_{eff} effective area curve using a linear relationship between them, b) Influence of shift in lens position by 0.1 mm to the intrinsic LIDT fluence with respect to effective beam radius. Symbols: z_0 means one specific lens position, l is distance from lens to the surface of tested sample.

3.3.5 LIDT pulse energies are matched to effective areas.

Since the effective area was measured at discrete lens positions before or after the LIDT tests, it was needed to match the effective area data to the LIDT energies. To do that, we firstly determined the z lens position coordinate, for which the effective beam area was smallest ($z = 0$). Knowing the effective areas before ($z < 0$) and after ($z > 0$) the lens focal length, we described the evolution of effective areas in both directions from the waist. Then we tried to shift the data of LIDT pulse energies to correspond well to the evolution of effective beam areas as it is shown on Fig. 3.9. The results clearly show high sensitivity of determined fluences on the lens position shift and should be considered as a significant source of fluence inaccuracy in this work.

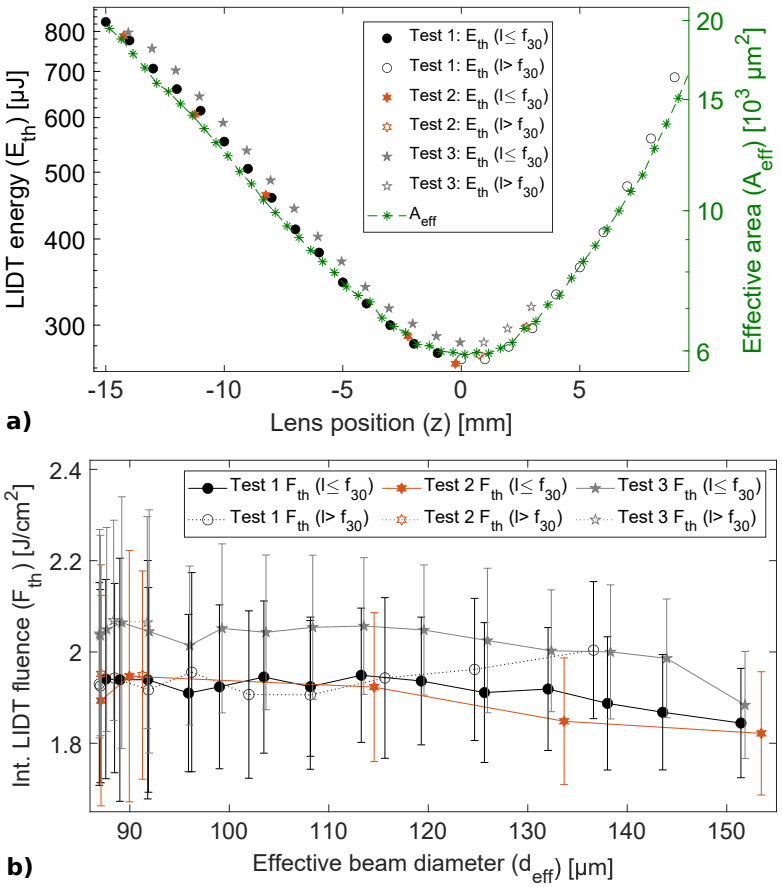

Figure 3.10: Summary of LIDT results with HfO_2 sample tested by lens of $f_{30} = 30$ cm focal length: a) LIDT energy and effective area as a function of lens position. The two y axis are linked by linear scaling law. Figure b) shows the intrinsic LIDT fluence in dependence of effective beam radius. Tests 1 and 2 were evaluated using the preferred *ex-situ* microscopy. Test 3 corresponds to the *in-situ* damage detection. Length l means distance from lens to the tested sample surface.

3.4 500-fs 1030-nm LIDT results and discussion

3.4.1 Results with 30 cm focal length are independent on beam size.

The LIDT testing by lens with 30 cm focal length was repeated three times for HfO_2 sample. The results of tests 1 and 2 were evaluated using the preferred *ex-situ* DIC microscopy while the ones of test 3 correspond to the *in-situ* damage detection. The LIDT results on Fig. 3.10 underline the critical effect of damage detection on LIDT determination. In our case it adds an offset that seems consistent. Fig. 3.10a) illustrates the damage threshold pulse energies together with effective area values in dependence of lens position. Both effective area and damage threshold energies indicate similar dependence on increasing distance from focal plane. The behavior can be evidenced by independence of intrinsic LIDT fluence on the beam size as shown on Fig. 3.10b). The small deviations ($< 10\%$) for larger effective beam diameters ($> 130\,\mu m$) could be connected with beam divergence influencing angle of incidence and thus EFI maxima. Also the real beam size at the spot on tested sample can be different since the sample was inclined at 45° and beam position slightly shifts in dependence on lens position. However, the observed deviations of intrinsic LIDT fluences are still in compliance with the shown error bars summarizing 3σ deviation of effective beam area, 3σ deviation of pulse energy and uncertainty given by $\sim 1\%$ energy increment in damage test procedure. For this measurement, we thus do not see a significant beam size effect on intrinsic LIDT fluence.

3.4.2 Results with 15 cm focal length are difficult to interpret

The beam-size effect on LIDT fluence was studied also with lens of 15 cm focal length. The results for Nb_2O_5 and HfO_2 samples are shown on Figs. 3.11a) and 3.11b), respectively. In contrast to the previous results with the lens of 30 cm focal length (Fig. 3.10), the interpretation of LIDT fluences in dependence of beam size is difficult in the case of lens with 15 cm focal length since we observe differences of threshold values up to 20 % around focal plane. Also, for the large beam sizes, we see differences in LIDT values between tests performed with lens-sample distances smaller and larger than focal length. In the following sections we shall analyse the possible cause of LIDT deviation when changing the spot size.

3.4.3 Analysis of potential self-focusing effects in air

Since the sub-picosecond systems have high peak powers of pulses, they can create conditions for nonlinear effects that can modify the beam profile. The important phenomenon, that can introduce errors in the damage testing, is self-focusing. The evaluation of self-focusing for Gaussian beams is possible by estimating the self-focusing power: [185]

$$P_{SF} = \frac{0.149\lambda^2}{n_2 n_0}, \tag{3.27}$$

where n_0 signs for linear refractive index and n_2 is nonlinear refractive index of air, defined by $n = n_0 + n_2 I$, where I means intensity.

For femtosecond pulses (≤ 200 fs) at 800 nm wavelength, the nonlinear refractive index n_2 of air can be found in several publications [186–189], in which its value ranges between 10^{-23} and $6 \cdot 10^{-23}\,m^2/W$ in dependence on wavelength, pulse duration or refractive index measurement method. [190] In 2014, Mitrofanov et al. [191] determined the nonlinear refractive index of air to be $n_2 \sim 5 \cdot 10^{-23} m^2/W$ at 1030 nm wavelength, 200 fs pulse durations, which are parameters close to the irradiation conditions of our LIDT setup (540 fs pulse duration, 1030 nm wavelength). Substituting the value in Eq. (3.27), the self-focusing power for our setup is $P_{SF} \sim 3.2$ GW, that is 2 times larger than the highest used peak power of 1.6 GW corresponding

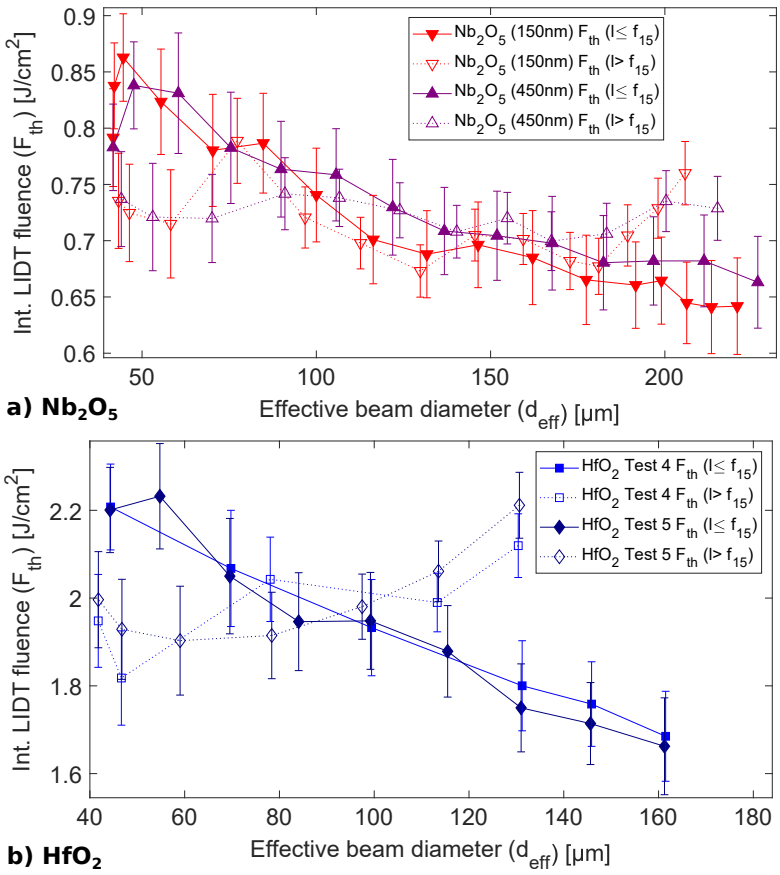

Figure 3.11: Summary of intrinsic LIDT results obtained using the lens of $f_{15} = 15\,\text{cm}$ focal length: a) intrinsic LIDT of two Nb_2O_5 coatings of different thicknesses ($\bigtriangledown$ 150 nm, $\bigtriangleup$ 450 nm) obtained in two different LIDT test campaigns, b) intrinsic LIDT fluence of HfO_2 sample determined in two different LIDT test campaigns. The $\bigtriangleup$ and $\diamond$ datasets were obtained with very accurately aligned beam whose maximal shift of peak caused by lens positioning was around 30 µm. In the case of $\bigtriangledown$ and $\square$ tests, it was around 400 µm.

to pulse energy of 0.85 mJ. Thus, the beam propagation should not be exposed to self-focusing phenomenon in air. In addition, this question is relevant only in the case of LIDT testing at sample-lens distances larger than focal length with pulse energies close to our maximum, i.e. for the largest beam sizes.

3.4.4 Self-focusing effects in the lens

A potential cause of the evolution of LIDT with spot size could be self focusing in the lens material. If our results are affected by the effect, the influence is largest for the highest pulse energies that correspond to the farthest lens positions from the focus. For the sample-lens distances closer than focal length ($l < f_{15}$), the effect can cause more intense focusing and lower damage threshold energy. Since the beam profile measurement was performed with pulse energies reduced by 6-7 orders of magnitude compared to the LIDT tests, the determined effective areas may not correspond to the real ones affected by self-focusing. The effect could thus be interpreted as decrease of intrinsic LIDT fluence for the lowest sample-lens distances ($z < 0$) as it is shown on Fig. 3.12.

The more intense focusation can thus lead to shift of focal plane to shorter sample-lens distances but also

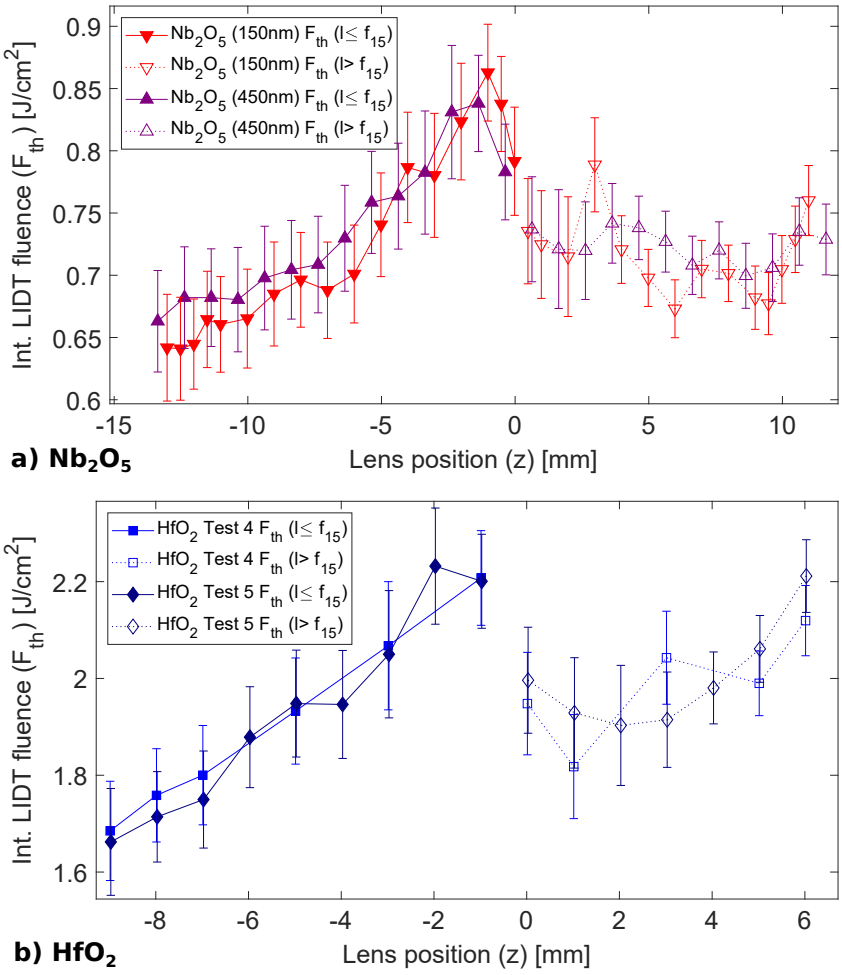

Figure 3.12: Intrinsic LIDT fluence results for a) Nb_2O_5 and b) HfO_2. The results are the same as in Fig. 3.11, but here they are plotted as a function of z lens position.

to faster divergence (defocusation) in dependence on z posititon. Therefore, the apparent LIDT thresholds could be higher for the largest sample-lens distances ($z > 0$) which again correlates with the results on Fig. 3.12.

For the effective beam diameters in the range from 75 µm to 175 µm, see Fig. 3.11, the more pronounced discrepancy between the damage thresholds before and after the focal length in the case of HfO_2 sample than in the Nb_2O_5 tests correlates with the higher pulse energies in the HfO_2 tests. This also suggest a potential self-focusing effect since the damage threshold energies of HfO_2 were approximately 3 times larger for the same beam diameter.

3.4.5 Effect of beam divergence

In the LIDT determination procedure, it is assumed that a plane wave propagates in the sample to calculate the electric field distribution. Because of the Gaussian nature of the laser beam, this is not the case when LIDT tests are performed out of the focal plane. We have therefore tried to estimate the consequences on EFI calculation.

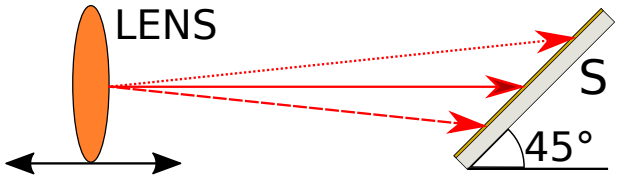

Figure 3.13: Schematic layout of beam alignment. Lens position influence on beam position on sample (S).

Assuming that our beam is close to the Gaussian beam profile (see Fig. 3.5b), and characterized with a certain M^2 factor, we can calculate the θ divergence half-angle using the relation:

$$\theta = M^2 * \frac{\lambda}{\pi w_0}, \tag{3.28}$$

where w_0 stands for $1/e^2$ beam radius at the beam waist. The meaning of half-divergence angle is that the angle from beam axis should cover 86.5% of the pulse energy in the case of ideal gaussian beam in far field from focal plane. It could thus be assumed that the half-divergence angle would also define the range of incidence angles and positions where the material damage is initiated. For our beam, the half-divergence angle of lens with focal length of 15 cm is around 0.7°. Performing the calculation of electric field intensity maxima for different incidence angles around 45°, we estimate the maximum difference in EFI maxima to be 1.4%. Thus, we can not explain the observed differences in LIDT fluences using the beam divergence determined by the Gaussian beam approximation. However, the difference in EFI maxima could be added into the error bars when the sample plane was far from focus.

3.4.6 Alignment

During the LIDT test we changed the positions of focusing lens along the beam axis. As the lens was moving step by step from one extreme position to the second one, there was a gradual movement of the beam peak in the plane perpendicular to the beam propagation. This movement occurred in both horizontal and vertical coordinates and was recorded by a beam profiling camera. Since the LIDT tests were done at 45° incidence angle, see Fig. 3.13, the change of peak position in horizontal plane can be projected also along the beam axis and thus influence the lens-sample distance.

Assuming approximately the same distance changes along the beam axis as in horizontal coordinates ($\Delta x \approx \Delta z$), we can estimate the error in LIDT fluence by expressing the ratio between effective areas located at lens positions of Δz difference. We estimate the effective area (A_{eff}) difference as:

$$\frac{\Delta A_{\text{eff}}}{A_{\text{eff}}}(z_i) = \frac{\max\left[A_{\text{eff}}(z_i + \frac{\Delta z_i}{2}), A_{\text{eff}}(z_i - \frac{\Delta z_i}{2})\right]}{\min\left[A_{\text{eff}}(z_i + \frac{\Delta z_i}{2}), A_{\text{eff}}(z_i - \frac{\Delta z_i}{2})\right]}, \tag{3.29}$$

where z_i means i-th lens position. For the large range of lens positions associated with horizontal movement of beam $\sim 400\,\mu$m, i.e. $\bigtriangledown$ and $\square$ datasets on Fig. 3.11a) and 3.11b), respectively, the beam positioning error could be $\sim 5\,\%$. In the case of $\bigtriangleup$ and $\diamond$ datasets, the error caused by 30 µm peak position movement can be neglected ($< 0.5\,\%$). The data of pointing stability show standard deviation lower than 10 µm and thus the parameter can be ignored.

The move of peak position indicates that there could be also some influence on incidence angle (and EFI maximum) when the lens is moved. We can estimate the incidence angle change as:

$$\Delta\theta \sim \arctan\left(\frac{\Delta x}{f_{15}}\right). \tag{3.30}$$

In the case of $\Delta x = 400\,\mu\text{m}$, the $\Delta\theta \sim 0.15°$ corresponds to difference in EFI maxima $\leq 0.3\,\%$. Thus, the influence of beam positioning on EFI maxima does not play an important role. However, the effective area differences due to beam displacement calculated using Eq. 3.29 could be used for explanation of the differences between the LIDT test campaigns presented on Fig. 3.11.

3.4.7 Camera errors

Noise error

The BP87 camera shows very low noise level around 0.1 % of signal maximum. Furthermore, several beam profile measurements with different background area selection confirmed the same A_{eff} results. Thus, we do not consider the noise error as important.

Pixel size error

The effective area determination is limited by the spatial resolution of the beam profiler given by the pixel size. [192] In the tests with lens of 15 cm focal length, the pixel size $l_{\text{pixel}} = 3.45\,\mu\text{m}$. Taking into account an absolute error of effective beam diameter determination, i.e. $\delta d_{\text{eff}} = \pm l_{\text{pixel}}$, we assess the relative error: [192]

$$\epsilon_{\text{pixel}} = \frac{\delta A_{\text{eff}}}{A_{\text{eff}}} = \frac{\frac{\pi}{2} d_{\text{eff}} \delta d_{\text{eff}}}{\pi \frac{d_{\text{eff}}^2}{4}} = \pm \frac{2 \cdot l_{\text{pixel}}}{d_{\text{eff}}}. \tag{3.31}$$

The problem of spatial resolution is a serious issue when beam profilers are used to measure relatively small spots. For our lens with 15 cm focal length, the minimum effective beam diameter $d_{\text{eff}} \approx 40\,\mu\text{m}$ corresponds to the relative error $\epsilon_{\text{pixel}} \approx 17\,\%$. This error could be one of the main reasons why the LIDT results on Figs. 3.11a) and 3.11b) show such high dispersion for smaller beam sizes.

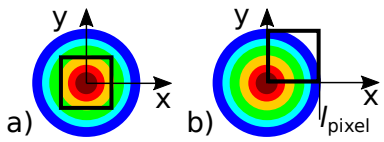

Figure 3.14: Schematic drawing of Gaussian beam intensity peak: a) at the center of pixel, b) at the corner of pixel.

Maximum pixel intensity error

We will estimate an error of maximum intensity value measured on one pixel of our camera by considering difference between two extreme cases of maximum pixel positioning, i.e. the case of peak at the center of pixel (Fig. 3.14a) and the case when maximum intensity is at the corner of pixel (Fig. 3.14b). Assuming Gaussian intensity profile, we can determine h, the mean value of intensity within the S_{pixel} pixel area by:

$$h = \iint_{S_{\text{pixel}}} \exp\left(\frac{-4\left(x^2 + y^2\right)}{d_{\text{eff}}^2}\right) dx\, dy / S_{\text{pixel}}, \tag{3.32}$$

where d_{eff} is the effective beam diameter and x, y are transverse coordinates. Integrating the Eq. 3.32 from $-l_{\text{pixel}}/2$ to $l_{\text{pixel}}/2$ over both x, y coordinates, we defined the h value in the case of intensity peak at the center of pixel, see Fig. 3.14a). For the intensity peak at the corner of pixel, the integral was from 0

to l_{pixel} in both x, y coordinates. Using the $l_{\text{pixel}} = 3.45\,\mu\text{m}$, the maximal difference between h values is $\epsilon_{\text{max pixel}} \approx 1.5\,\%$. In the case of intensity peak at pixel corner, the h value is by 2 % lower than intensity peak of Gaussian beam with $d_{\text{eff}} = 40\,\mu\text{m}$.

3.4.8 Other errors

Other errors in measurement might include the accuracy of motorized stage movements or the accuracy of microscopic observation. The latter mentioned we estimate to be around low percentage units.

3.5 Summary of 500-fs 1030-nm LIDT metrology

In our particular case, the LIDT results, obtained with lens of 30 cm focal length in the range of effective beam diameters between 80 and 160 µm, show that the sub-picosecond damage threshold of dielectric coatings is independent of beam size as shown on Fig. 3.10b). In order to evaluate the tests of such optical components as accurately as possible, we provide in Table 3.4 a synthesis of identified contributors to errors. As the major error contributor in the best case scenario, we detected the 3σ variations of beam size (6%). The influence of contributors related to beam alignment, i.e. beam positioning at 45° incidence angle, pulse energies and effective areas matching, beam divergence or effect of incidence angle on EFI maximum, could be minimized by damage testing at normal incidence or by beam profile measurement at the same incidence angle as the tests are performed.

No.	Contributor	Error bar
1	Beam size variations (3σ)	6%
2	Damage detection	5%
3	Beam positioning at 45° AOI	3%
4	Calorimeter	3%
5	Pulse energies and A_{eff} matching	2%
6	Pulse energy variations (3σ)	0.7%
7	Pulse energy increment	0.5%
8	Effect of beam divergence	0.5%
9	Effect of AOI on EFI maximum	0.3%
	Total budget	21%
	Quadratic summation	9%

Table 3.4: Synthesis of error margins for identified contributors in the best case scenario of LIDT tests with lens of 30 cm focal length. A_{eff} - effective beam area, AOI - angle of incidence, EFI - electric field intensity. With quadratic summation, an accuracy of 9% can be achieved for the determination of LIDT fluences. The pulse energies and A_{eff} matching error corresponds to shift in lens position by 0.1 mm.

In contrast to the results with lens of 30 cm focal length, it is difficult to determine the relation between beam size and LIDT fluence in the case of lens with smaller focal length of 15 cm. The different fluences before and after the beam waist (Fig. 3.12) could suggest potential beam deformation related to self-focusing in the lens. Another error could rise from beam profile measurements, especially for smaller beam sizes. This could be related to pixel size error of 17 % or maximum pixel intensity error of 1.5 %. Last but not least, it is necessary to emphasize the significant effect of the chosen shift in lens positions to the intrinsic LIDT fluence in respect to the effective beam diameters, see Fig. 3.9.

From the practical point of view, this study recommends in our case the lens of 30 cm focal length to be used for LIDT testing of optical components intended e.g. for use in larger beam laser systems. The lens of 15 cm focal length, by contrast, should not be used for damage testing since the uncertainties in LIDT fluence, regardless of their origin, are too large. For work done in this thesis using 500-fs 1030-nm setup, we use the lens of 30 cm focal length with a tested sample placed at focal plane.

On the more general perspective, this work underlines the difficulty of LIDT measurements with very focused laser beams. Despite our best efforts, the deviations of LIDT are quite large and we believe similar issues should have been encountered in previous studies related to this topic, see Table 3.3, where spot size dependences were observed for highly focused beams.

In the remaining part of this chapter we will introduce other laser damage setups that were used in this thesis to test dielectric coatings.

3.6 1.8-ps 1030-nm 1-kHz LIDT setup (Perla B, HiLASE)

A compact regenerative laser amplifier based on the Yb:YAG thin-disk technology [193] is the laser source for the LIDT test station, which is shown schematically in Fig. 3.15. The LIDT station was used to test Nb_2O_5 monolayer coatings whose results will be shown in Sec. 4.4. The automated LIDT station [194] that fulfills ISO 21254 standards is used at the HiLASE centre, which develops high-power large-beam pulsed lasers. The laser source emits radiation with a pulse duration of 1.8 ps at a wavelength of 1030 nm at a repetition rate of 1 kHz. [195] A generated pulse has a near Gaussian spatial profile and an achievable energy of up to 10 mJ. The number of pulses is regulated by the BBO crystal Pockel's cell. The pulse energy is attenuated by a combination of half-wave plate and thin-film polarizer. After the attenuator, the beam is directed by highly reflective mirrors and focused on a tested sample using a concave dielectric mirror (HR3) with focal length of 6 m.

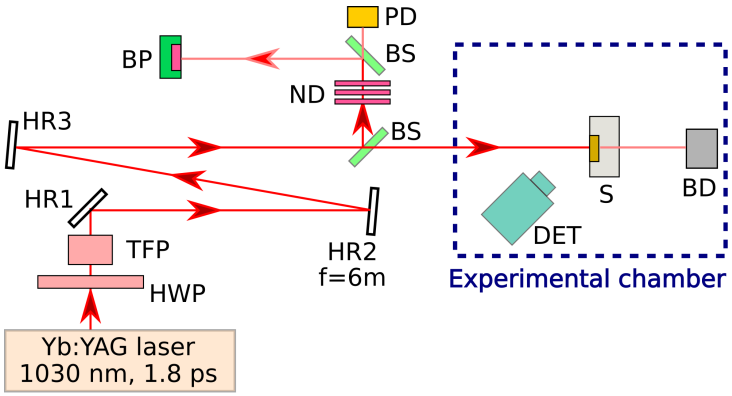

Figure 3.15: 1.8-ps 1030-nm 1-kHz LIDT station. TFP - thin film polarizer, HWP - half-wave plate, HR - highly reflective mirror, BS - beam splitter, S - sample, ND - filters, PD - photodiode, BP - beam profiler, BD - beam dump. [195]

In the beam path, a beam splitter is placed to separate less than 1% of the energy to the diagnostic branch. The branch allows to measure pulse energy and beam profile on-line during the LIDT tests. To measure the beam profile equidistant to the tested sample, a CMOS[1] camera (UI-5370CP Rev. 2, IDS) with ISO-compliant characterization software and 5.5 µm pixel length is used. The testing station is located in

[1] Complementary metal-oxide-semiconductor

a clean room laboratory with regulated humidity, temperature, and dust particle concentrations that meet ISO class 6 cleanliness standards. [195]

The tested sample and damage detection equipment are put in an experimental chamber intended for vacuum testing with pressure up to 10^{-3} mbar or for overpressure testing in a non-corrosive environment with pressure up to 1.4 bar. [195] The tested sample is mounted on a remote-controlled micrometric translation 2-axis stage. To detect a damage online, a camera continuously monitors the exposed site on tested sample surface. In order to thoroughly analyze the LIDT results, the sample surface is examined ex-situ with a laser scanning confocal microscope (OLS5000-SAF) before and after the LIDT tests.

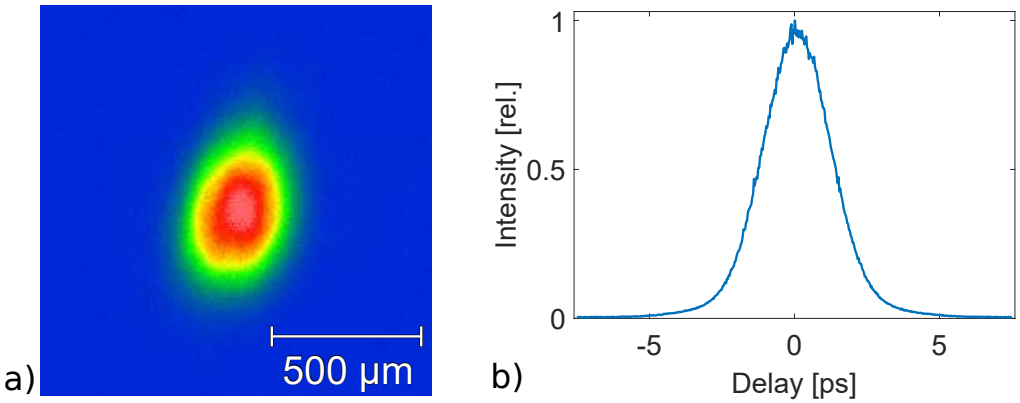

Figure 3.16: Characterization of 1.8-ps 1030-nm 1-kHz LIDT setup at HiLASE centre. Beam profile (a) at the focal plane used for sample testing. The effective beam diameter is around 315 µm. Pulse duration (b) was measured by APE autocorrelator. The sech^2 pulse fit corresponds to $\sim$ 1.8 ps pulse duration.

The energy variance between pulses of the laser source is less than 5%. [195] A typical beam profile used for LIDT testing is shown in Fig. 3.16a). Using a set of 20 beam profile images, we determined a mean effective beam diameter of 315 µm and a standard deviation of 3% for pulse-to-pulse beam area variations. With an APE autocorrelator, a pulse duration of $\sim$ 1.8 ps was confirmed, see Fig. 3.16b). The standard deviation of pointing stability was around 5 µm.

3.7 150-ps 1030-nm 1-kHz LIDT setup (Alphanov)

As mentioned in Sec. 1.2.2 on page 26, we aim in GREAT consortium to develop gratings for pulse compression that will be implemented in the lasers based on chirped-pulse amplification. To qualify the optical materials and components for use in the CPA systems, we should test them at conditions corresponding to the compressed pulse as well as the streched pulse. Therefore, we used a laser source generating a pulse duration of 150 ps which is close to the conditions, at which stretched pulses of CPA systems operate. In this thesis, the 150-ps laser was used to test Nb_2O_5, HfO_2 and SiO_2 dielectric coatings and obtained LIDT results will be shown in Sec. 4.5.

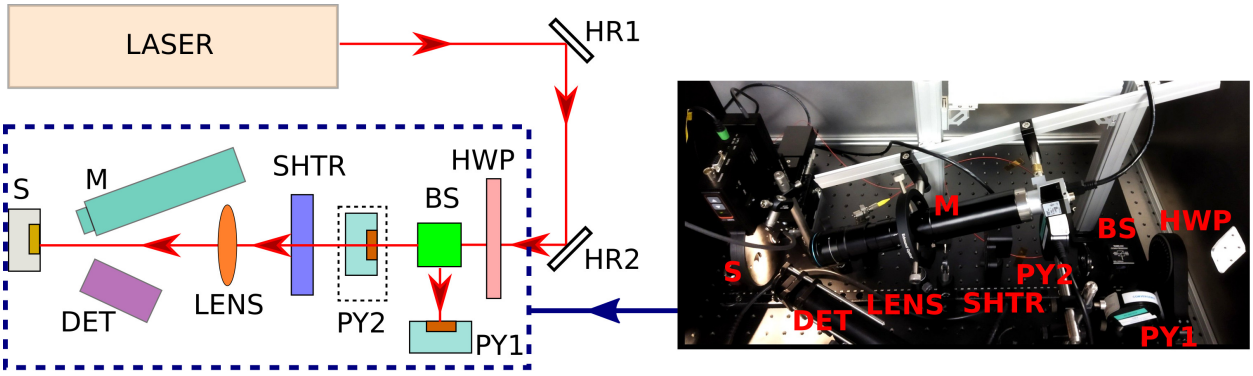

Figure 3.17: 150-ps 1030-nm 1-kHz LIDT station at Alphanov technological center. HR – high-reflective mirror, HWP – half-wave plate, BS – polarizing beam splitter cube, PY1/2 – pyroelectric sensors (both PE10-C, Ophir), SHTR – mechanical shutter, LENS – focusing lens, S – sample, M – in-situ surface monitoring, DET – detector of scattered light.

For the LIDT tests at a pulse duration of 150 ps, we used the experimental station shown in Fig. 3.17. The laser source of this station emits pulses at a wavelength of 1030 nm with a repetition rate of 1 kHz. The emitted pulse beam is directed by a set of high reflective (HR) mirrors to the half-wave plate (HWP) that adjusts the polarization orientation before it arrives to the polarizing beam splitter (BS) cube CCM5-PBS203/M. The HWP and BS determine the energy level used for damage testing. Pulses that pass through the mechanical shutter (SHTR) are then focused by lens (LENS, $f \approx 20$ cm) and reach the tested sample (S) surface at focal plane. Positioning of the sample is controlled by a holder (FW102C, Thorlabs). During the tests, the sample surface is monitored by in-situ imaging (M, Basler acA1920-40um camera) and the changes of scattered light are analyzed by detector (DET).

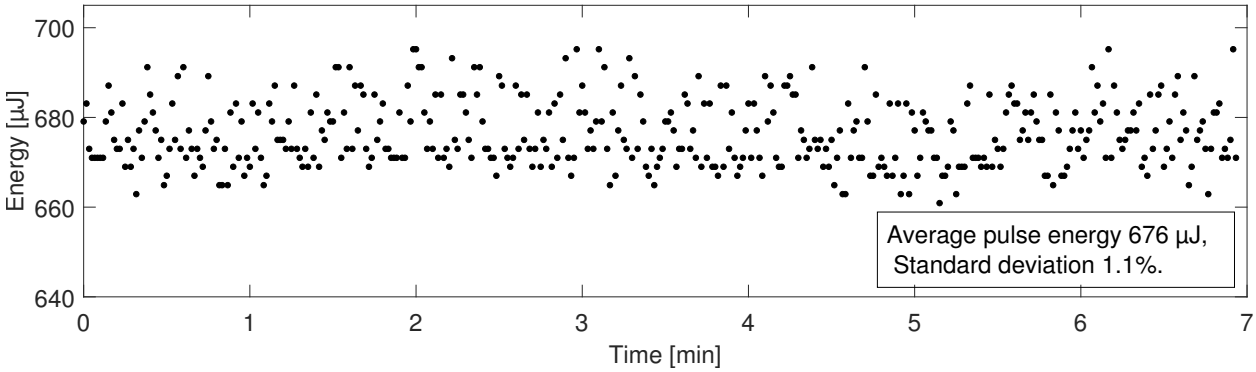

Figure 3.18: Endurance of 150-ps 1030-nm 1-kHz laser source. Measured by PE10-C (Ophir) pyroelectric meter.

3.7.1 Energy stability

A pyroelectric meter PE10-C (PY1) was used to measure the pulse energy stability throughout a 7-minute irradiation, see Fig. 3.18. The average pulse energy was 676 µJ at 1 kHz repetition rate. The value of three standard deviations (3σ) was 3.3%.

3.7.2 Pulse duration and repetition rate

For the measurement of pulse duration, a fast photodiode (2 µm InGaAs PIN Detector ET-5000) was used. The photodiode has bandwidth > 10 GHz and thus can be used for measurement of pulse duration around 150 ps. The photodiode was connected to KEYSIGHT DCA-X 86100D wide-bandwidth oscilloscope. Measured pulse duration was around 170 ps at FWHM, see Fig. 3.19a). The value is in agreement with the value of 150 ps given by manufacturer since the photodiode has both rise and fall time of 28 ps. The measurement confirmed also repetition rate of 1 kHz, see Fig. 3.19b).

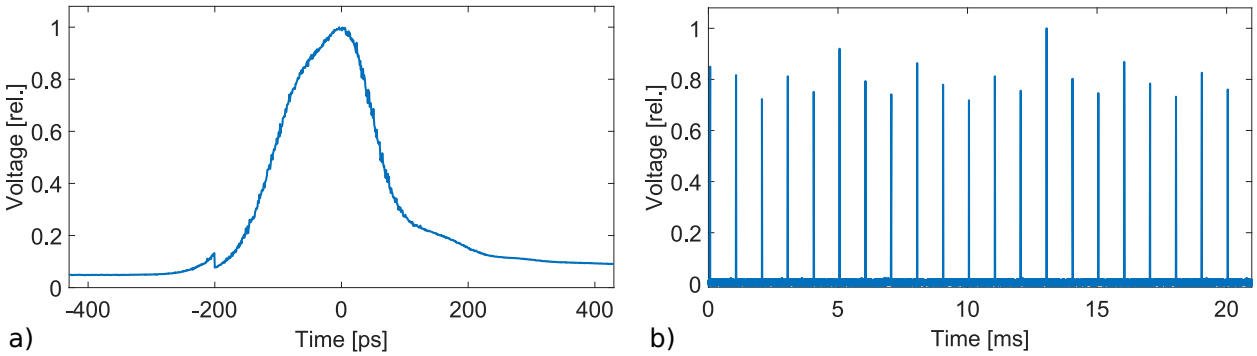

Figure 3.19: Characterization of laser source in time domain using a fast photodiode connected to an oscilloscope: a) pulse duration with FWHM around 170 ps; b) repetition rate of 1 kHz.

3.7.3 Beam profile

The measurement of beam profile at focal plane was done before the secondment at ALPHANOV, the effective beam diameter is around 78 µm, see Fig. 3.20.

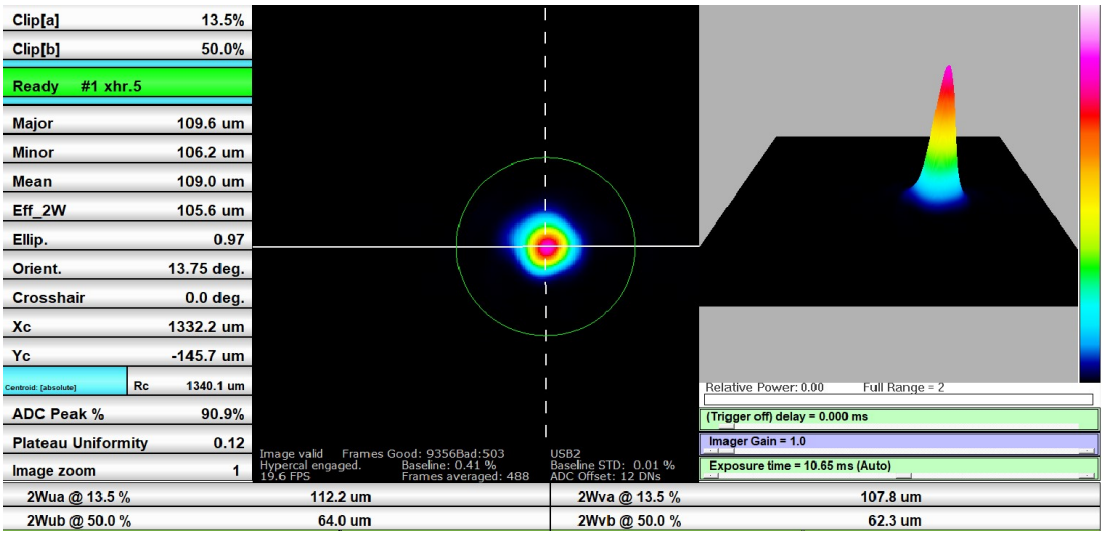

Figure 3.20: Beam profile at focal plane shows near-Gaussian shape and an effective beam diameter of 78 µm.

3.8 100-fs 1050-nm 500-Hz LIDT setup (ELI Beamlines)

For the investigation of laser damage resistance of optical materials developed within GREAT consortium, the ultrashort regime with pulse duration around 100 fs is relevant. The final products, GWS, are planned to be implemented in Yb-doped fiber lasers to ensure the compression of the generated broad band laser pulses. The testing of optical coatings in 100 fs pulse regime was performed using the LIDT station at ELI Beamlines facility. The results of LIDT tests carried out with this station will be reported for dielectric monolayers in Sec. 4.6 and for mirrors in Sec. 5.3.2.

The input beam of the LIDT station originates from a commercial Ti:sapphire CPA laser (Astrella, Coherent), which is emitting pulses of $\sim$ 40 fs duration at a wavelength of $\sim$ 800 nm. [196–198] The pulse repetition rate is set to 500 Hz for this experiment. The 800 nm laser source is used to generate both the OPA seed pulse and to pump nonlinear amplification stages based on BBO and KTA crystals. [199] For the LIDT testing of optical coatings, we used a laser source obtained by means of these amplifiers.

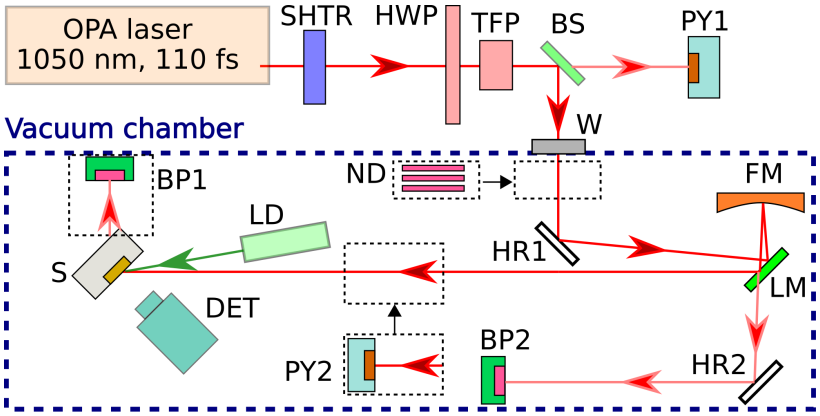

Figure 3.21: Simplified scheme of 100-fs 1050-nm LIDT station at ELI Beamlines. SHTR – shutter, HWP – half wave plate, TFP – thin film polarizer, BS – beam splitter, PY1/PY2 – pulse energy meters, W – window, ND – neutral density filters, HR – highly reflective mirror, LM – leaky mirror, FM – focusing mirror, S – sample, BP – beam profiling camera, DET – damage detector using scattered light, LD – laser diode. [196]

The scheme of laser damage station is shown in Fig. 3.21. The OPA laser has a pulse duration of 100 fs, a central wavelength of 1050 nm and a spectral bandwidth of 20 nm. Coatings tested with this station were irradiated by S-polarized beam. Number of pulses was reduced using mechanical shutter (SHTR, SH05 Thorlabs). Pulse energy was adjusted by a combination of half-wave plate (HWP) and thin-film polarizer (TFP). A small part of beam passed from beam splitter (BS) to the reference energy meter (PY1, PD10-PJ-C, Ophir). The reference energy meter was calibrated with an energy meter (PY2, PE25-C, Ophir) placed in the beam path after the last optical element. A larger part of pulse energy was directed from beam splitter through window (W) into the vacuum chamber, see Fig. 3.22. In the case of beam profile measurement, pulse energy was significantly reduced by multiple neutral density (ND) filters. However, during the LIDT tests, the filters were not used.

Inside the vacuum chamber, see photographs in Fig. 3.22, the beam was directed by highly reflective mirror (HR1) and leaky mirror (LM) to the focusing mirror (FM). Less than 1% of pulse energy passes through the leaky mirror to a vacuum compatible CMOS camera (BP2) which monitors the beam profile on-line at an equivalent distance to the tested surface sample plane. The last spherical mirror has a focal distance of 80 cm and enables LIDT tests with a beam effective diameter of $\sim$ 130 µm near focal plane.

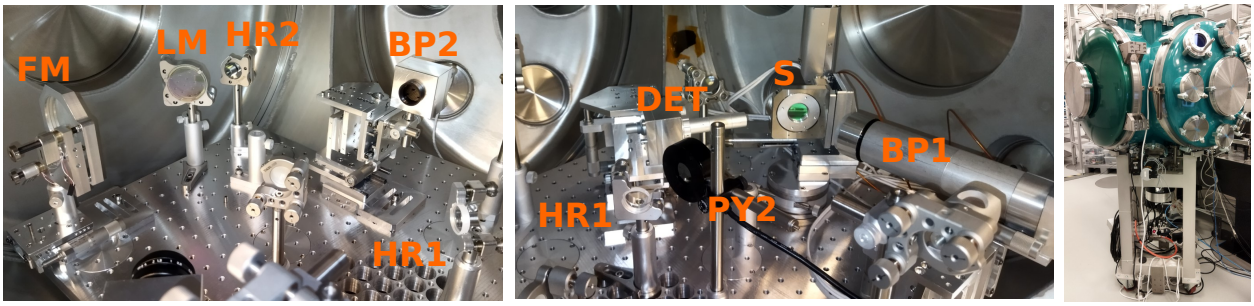

Figure 3.22: Mobile station for femtosecond LIDT tests in vacuum at ELI Beamlines facility. The labels of optical elements inside the chamber correspond to the description of simplified scheme in Fig. 3.21.

Using a beam profiler (BP1) we measure directly the beam size at the plane of the sample surface. The tested sample (S) is placed near the focal plane on a rotary stage. The in-situ sample surface observation is done by a damage detection (DET, FemtoEasy) camera with the scattering light from the 532 nm continuous wave laser diode (LD, LDS5 Thorlabs). To confirm the laser beam stability, the measurements using leaky and direct beam profiling cameras are repeated before and after the LIDT tests as well as pulse energy calibration.

The LIDT tests were done with a pressure around 10^{-6} mbar, which is close to the conditions in which optical components at ELI facility are used. The vacuum chamber was evacuated by scroll turbomolecular pumps. [200] An advantage of the LIDT station enclosed in the vacuum chamber is its mobility allowing to perform tests by different laser sources located at ELI Beamlines facility, see photograph of the chamber on the right in Fig. 3.22.

3.8.1 Energy stability

The pulse energy stability was measured with PE25-C (PY2) pyroelectric meter during 5 minutes long irradiation, see Fig. 3.23. The average pulse energy was around 125 µJ at 500 Hz repetition rate. The value of three standard deviations (3σ) was 4.2%.

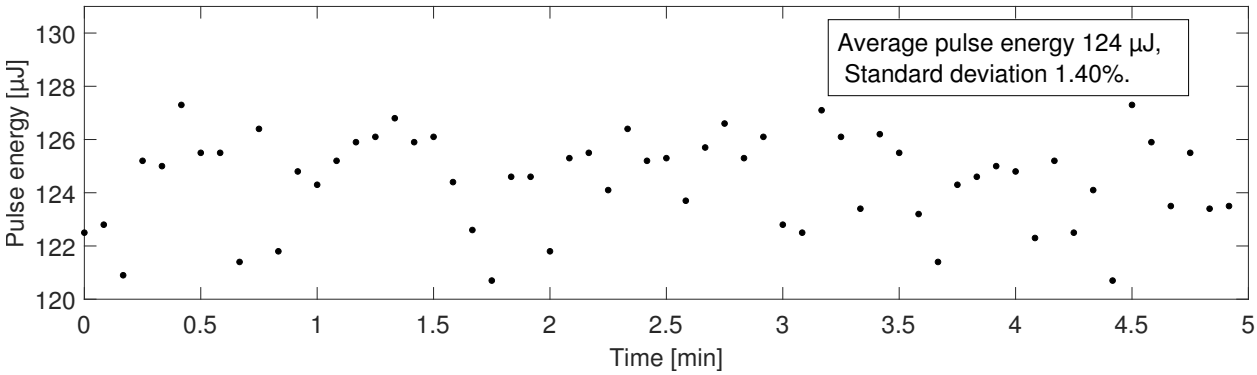

Figure 3.23: Pulse energy stability of OPA laser source of LIDT station at ELI Beamlines.

3.8.2 Beam profiling

Using the BP2 camera we determined effective beam diameter to be around 130 µm. The value was confirmed by BP1 direct camera monitoring beam profile on a sample positioned at 45° AOI, see Fig. 3.24. The pulse-to-pulse variation of measured effective areas expressed in three standard deviations (3σ) is 3.9%.

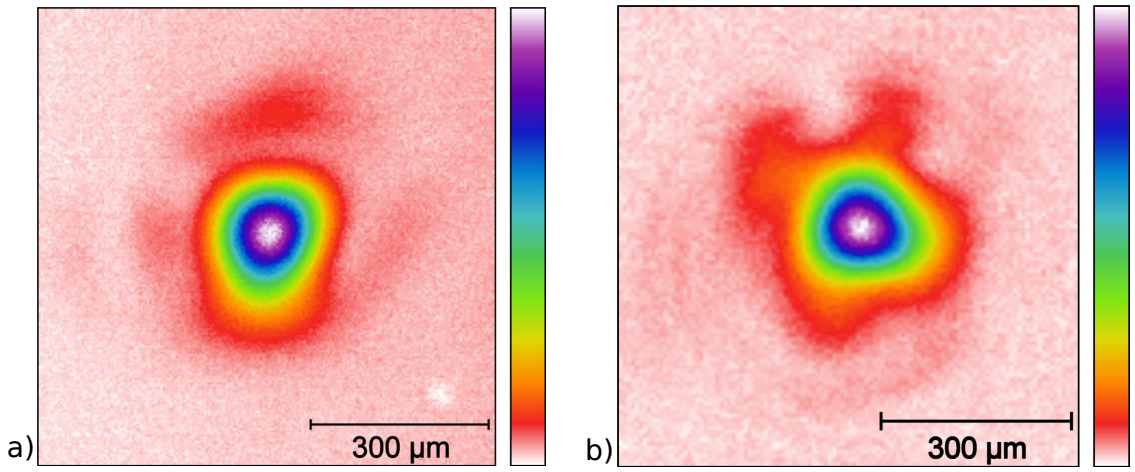

Figure 3.24: Beam profile at focal plane obtained for a) direct BP1 and b) leaky BP2 cameras. The BP1 camera monitored beam profile at 45° AOI while the CMOS chip of BP2 camera was placed in normal to the beam direction.

3.8.3 Pulse duration

Pulse duration was measured using a single-shot pulse row optical autocorrelator (Femto Easy). We found sech^2 fit pulse duration of ~ 100 fs, see temporal profile in Fig. 3.25a).

3.8.4 Spectral profile

Spectral profile was characterized using a STS-NIR spectrometer (Ocean Optics) over a broad range of wavelengths in the near-infrared region with a step of $\sim 0.5\%$. The central laser wavelength is 1050 nm with FWHM of 10.8 nm, see Fig. 3.25b).

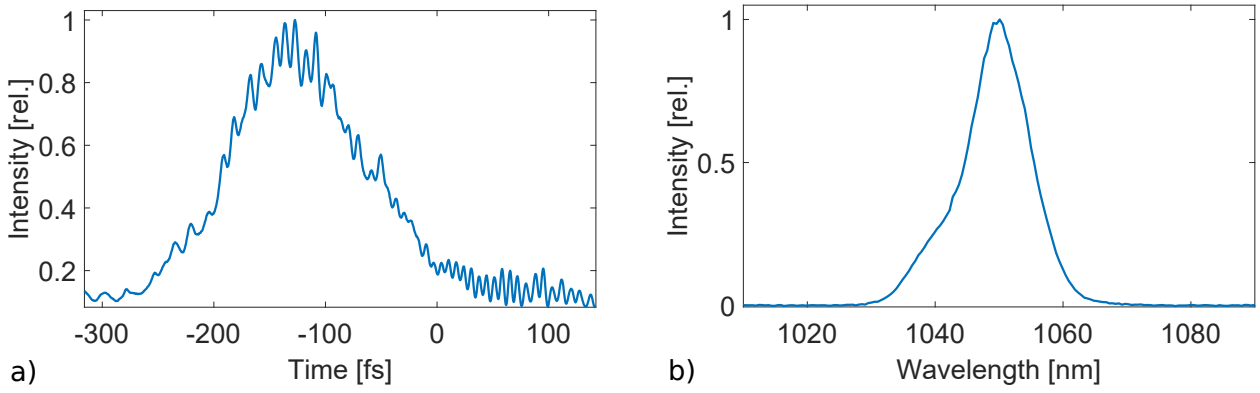

Figure 3.25: Temporal (a) and spectral (b) profile of LIDT laser source at ELI Beamlines.

3.9 700-fs 515-nm MHz LIDT setup (IF)

For high-repetition rate ($\geq$ 500 kHz) LIDT testing of dielectric coatings (Sec. 4.7), we used the setup depicted in Fig. 3.26 based on a high-power industrial laser source emitting radiation with a pulse duration of 700 fs at a wavelength of 515 nm. The emitted radiation is reflected by the dielectric mirror to the mechanical shutter that reduces the irradiation time and number of used pulses.[2] To control the energy of emitted pulses, an attenuator consisting of a half-wave plate (HWP) and a thin-film polarizer (TFP) placed at Brewster angle was used.

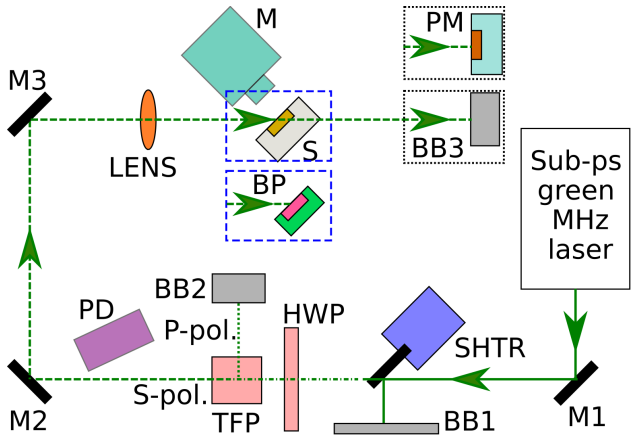

Figure 3.26: Experimental setup of sub-ps green high-repetition rate LIDT station. MX – x-th mirror, SHTR – shutter, HWP – half-wave plate, TFP – UVFS thin film polarizer, S – tested sample, OM – optical microscope (BXFM Olympus), BBX – x-th beam blocker, PM - power meter with thermal sensor, BP - beam profiler, PD - photodiode.

After passing through the attenuator, the laser beam is reflected by two mirrors and directed into the focusing lens (LENS) of approximately 30 cm focal length. The lens was placed on a motorized stage enabling move along the beam axis. The LIDT tests are performed with samples (S) positioned at the focal plane at an angle of incidence of 45°, see Fig. 3.26. The irradiation of samples was carried out with vertically S-polarized beam. Behind the tested sample, a beam blocker was positioned to suppress the laser energy transmitted through the sample.

The power of laser beam was measured using a power meter (PM) with thermal sensor. The values measured on this device were calibrated to the positions of HWP. At 500 kHz repetition rate, the maximum power used for LIDT testing was 7 W, which corresponds to a pulse energy of 14 µJ.

3.9.1 Pulse energy stability

The energy stability was measured using a Si-biaised photodiode DE10A/M connected to fast Tektronix DPO 7254 Digital Phosphor Oscilloscope (2.5 GHz, 40GB/s). The energy stability measurement lasted 2 h and counted 64k values. We found the 3× standard deviation (3σ) of pulse energy stability 1.3%.

[2]Since the laser source is not equipped with Pockel's cell, the picking of individual pulses is not allowed. Thus, the minimum number of shots is limited by the mechanical shutter opening time, which we defined to ∼10 ms using a fast photodiode connected to an oscilloscope (ISO-TECH IDS-1054B). At the lowest accessible repetition rate of this laser source of 500 kHz, it means the minimum number of pulses is 5000.

3.9.2 Beam profile

The beam profile was measured using WinCam UCD23 (DataRay Inc.) camera positioned at an angle of 45° to the incident beam. More information about the camera is listed in Table 3.1 on page 71. For beam profile measurement, the laser source operated in low-power mode with a power of ≈ 0.1 W. The power was reduced also by the rotation of half-wave plate. To avoid any damage on the camera sensor, a neutral density filter (ND-4) was mounted on the camera.

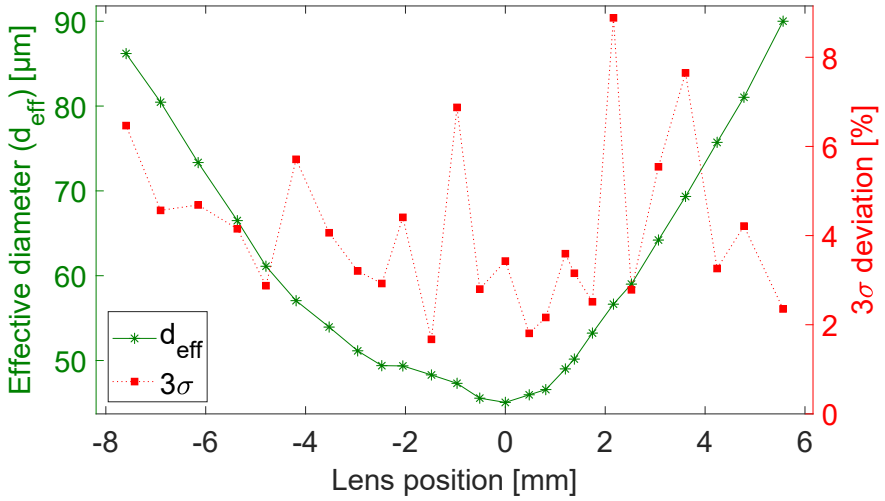

Figure 3.27: Beam profile measurement of MHz sub-ps green laser which was used for LIDT testing of samples placed at focal plane. Effective beam diameter (d_{eff}) and 3σ standard deviation of effective area as a function of lens position. For lens positions < 0, the camera is closer to the lens than the focal length.

By moving the lens along the beam direction, the beam size incident on the camera sensor was changed. The results of beam profile measurement are shown in Fig. 3.27. The effective beam diameter in the focal plane was 45 µm. Movement of the camera sensor by 1 mm from the focal plane represents a difference of $\sim 10\%$ in the effective beam area.

3.10 Conclusion

In Chapter 3, we presented measurement tools and processes that we use to get the high quality of measured data. We described the metrology relevant to the study of laser damage using sub-picosecond and picosecond pulses. Because dielectric excitation is driven by electronic processes, we provided in the first part of this chapter the calculus of electric field intensity distribution in monolayer coatings. We introduced the term of intrinsic LIDT fluence which is normalized to the electric field intensity maximum inside given layer and thus enables comparison of LIDT results obtained with different conditions having an impact on electric field distribution, e.g angle of incidence, polarization, layer thickness or its refractive index.

Despite the efficient excitation of material in the sub-ps regime, which indicates that LIDT should be independent of beam size, we found that this statement is not consistent in the published literature. Thus, we carried out extensive metrology research on the effect of beam size on LIDT determined by pulses of 500 fs duration emitted at a wavelength of 1030 nm. The metrology work emphasizes the difficulties of measuring LIDT with very focused laser beams, which could be attributed to beam deformation caused by lens self-focusing. We identified focusing conditions for LIDT testing of optical components that will be

implemented in lasers with larger beams than the test beam. To reliably evaluate the testing of such optical components, we presented a synthesis of identified error sources. In the best-case scenario, we identified beam size measurement inaccuracy as the largest error source.

To qualify the dielectric coatings and structures used in designs of GWS it is needed to perform LIDT tests at conditions close to the aimed applications of GWS. Since the GWS applications have targeted performances differing in pulse duration, wavelength, pulsed/CW regime or repetition rate, the qualification of coatings requires access to LIDT stations providing such irradiation conditions. Therefore, we took advantage of availability of five LIDT stations located at GREAT partner institutions: Institut Fresnel, HiLASE centre, Alphanov technological center and ELI Beamlines.[3]

Overall, the access to these setups enabled testing with pulse durations ranging from 100 fs up to 150 ps, at wavelengths of 515, 1030 and 1050 nm, at repetition rates from 10 Hz to 3.3 MHz and with effective beam diameters from 40 µm up to 315 µm. In the Fig. 3.28, we provide an overview of available conditions for LIDT testing.

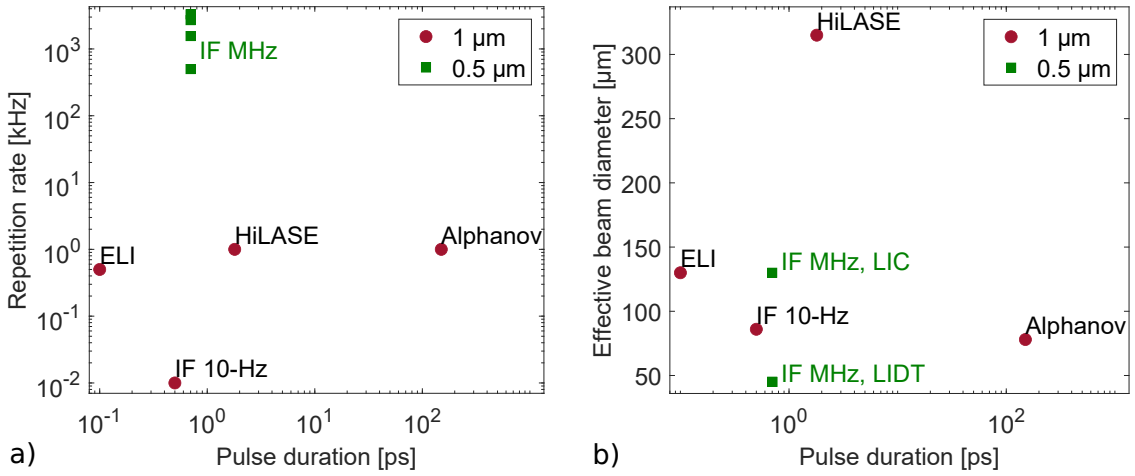

Figure 3.28: Conditions available for LIDT testing: a) repetition rate as a function of pulse duration, b) effective beam diameter as a function of pulse duration. The legend refers to laser wavelength and labels to the station locations in GREAT consortium institutions. The MHz laser source at Institut Fresnel (IF) was used for both LIDT and laser-induced contamination (LIC). Since the focusing conditions, repetition rate, beam characterization as well as on-line detection was different, we will describe the setup used for LIC separately in Sec. 6.1 on page 150.

[3]Due to project delays connected to covid19, we did not have access to LIDT station operating at CW regime. However, the testing in CW regime will be performed in the first month after submission of this thesis.

Chapter 4

Investigation of monolayers for use in optical components

In this chapter, we explore thin film dielectric materials and deposition tools available to the GREAT consortium. The deposition tools represent following fabrication methods: Electron Beam Deposition (EBD), Ion Assisted electron beam Deposition (IAD), Magnetron Sputtering (MS), Ion Beam Sputtering (IBS) and Pulsed Laser Deposition (PLD). The choice of fabrication method has an impact to thin-film properties including refractive index, extinction coefficient, roughness, crystallinity, and finally the LIDT.

In the first part of this chapter, we give a brief overview of the above-mentioned optical thin film fabrication methods. The results obtained in thin film damage competitions within annual Boulder Damage Symposium show which deposition methods provide coatings with higher damage resistance at given testing conditions. [76] The coatings made by EBD and IAD methods proved to be suitable for nanosecond pulsed regime at a wavelength of 1030 nm. The e-beam processes are used for fabrication of large optics placed in petawatt laser facilities. [201] The IAD is also utilized for depositing gratings, since the method reduces crazing by higher density of coatings. [14]

By contrast, the sputtering methods (MS, IBS) show high damage resistance in sub-ps and ps pulse durations for wavelengths around 800 nm. [76] Thanks to the high accuracy in layer thicknesses, both sputtering procedures became widely utilized in the manufacture of dispersive mirrors. [202] IBS is less commonly employed in industrial mass manufacturing due to its poor deposition rate. [203] However, recent advances in the IBS deposition technique demonstrated that it can produce large size[1] dielectric petawatt mirrors with 100k-on-1 LIDT of 0.9 J/cm^2 at a pulse duration of 42 fs and a wavelength of 805 nm. [196]

Magnetron sputtering is a technique used for coating production with various functions such as antireflection [204, 205], hydrophobicity [206], low emissivity [207] and conductivity [208]. Magnetron-sputtered anti-reflective coatings are used for solar cells [204, 209], hydrophobic feature is perspective for self-cleaning windows. [206] Glasses coated with low-emissive layers can ensure energy conservation in buildings by reflecting infrared radiation. [207] Magnetron-sputtered transparent conducting oxide coatings are used in liquid crystal displays. [210] The success of magnetron sputtering in optics-related applications is attributed to its high deposition rate as well as its precision. [202, 203]

In addition to these standard optical thin film fabrication techniques, we will focus our attention to PLD. PLD is one of the most versatile and powerful method [211] that has been used for deposition of a wide

[1] The mirrors for ELI Beamlines facility have dimensions: $44 \times 29 \times 7.5\,\mathrm{cm}^3$.

range of materials covering metals, semiconductors or biomaterials. [212] Despite the fact that PLD is not a common approach to make optical thin films, recent studies [213–217] suggest it has potential for optical coating fabrication.

The primary group of materials of interest to the GREAT consortium are oxides. These materials are excellent for creating optical components for high-power lasers because they have the high physical, chemical, and optical resilience. In the visible or near-infrared range, where the majority of subpicosecond lasers operate, it is mainly the group of oxides that is used for production of thin-film based optical components. [203,218] Oxides allow for the formation of dense, abrasion-resistant films with very low residual absorption. These materials are mechanically and chemically stable and the dense ones have even low environmental sensitivity. [203] In addition, they allow access to a wide range of refractive indices needed for functional designs of optical components. [219]

In the next part of this chapter, we will sum up the optical properties of thin-film coatings that were fabricated within the GREAT consortium. For the design and production of optical components and GWS, a thorough understanding of thin-film optical qualities is required. The refractive index must be measured to an accuracy of 10^{-3} in order to offer adequate modeling data for the development of optical components. We will report the bandgap values of explored thin-film materials, as it has been found that this parameter is in correlation with laser-induced damage thresholds, see Sec. 2.3.4 on page 50. The homogeneity of PLD thin-film materials is investigated using an X-ray diffraction characterisation method that will be described. The information supplied here on the characterization of the optical characteristics of coating materials will be used in the GREAT project's modeling part. Material characterisation will determine design constraints and choices for the GWS and related application areas.

Because the LIDT of thin-film materials used in optical components is the limiting factor of useful performance of ultrafast solid-state lasers [2,70], we will devote the remaining parts to LIDT testing of these materials. Here, we will present LIDT results of dielectric oxides obtained by testing with available laser sources at Fresnel Insitute and at partners locations. The laser sources allowed us to test oxides using a pulse duration ranging from 100 fs up to 150 ps with the main wavelength of 1 µm. The number of pulses ranges from 1 to 100 millions and the repetition rate from 10 Hz to 3 MHz. Finally, we will compare LIDT results obtained by different setups and summarize our findings on damage resistance of dielectric oxide coatings.

4.1 Fabrication methods

For the deposition of optical coatings used in laser components, there are numerous techniques that can and are utilized. [220] The most prevalent group of techniques is termed "physical vapour deposition (PVD)". The PVD processes are carried out in vacuum chambers in order to avoid turbulence effects and reactions with molecules in the atmosphere. In PVD processes, material heating or bombardment leads to evaporation, ejection, and direct condensation from the vapour phase to the solid phase on a substrate.

In a simplified sense, the term 'physical', as opposed to 'chemical,' denotes the lack of any chemical interactions during the film's deposition. In fact, PVD does involve chemical processes, however the term chemical vapour deposition (CVD) refers to a group of procedures in which the growing film differs significantly in composition and characteristics from the vapour phase materials. [220]

For industrial thin film fabrication, there are various fundamental requirements, whose importance vary with the application. The optical and mechanical properties of thin films must be reproducible with high accuracy. The deposition process should be done at high rates and must allow to create homogeneous films over large areas. The layer thickness must be precisely monitored in order to terminate the deposition process

accurately. In addition, a high level of automation, a fast thin film growth, and availability of low-cost, non-toxic deposition materials are crucial parameters from an economic point of view. [203] In this section, we will describe PVD coating technologies that are used for optical thin film coating fabrication.

4.1.1 Electron Beam Deposition

An effective technology for industrial manufacture of optical thin film coatings is electron beam deposition (EBD), which uses an electron beam to directly heat the coating material within a crucible, see Fig. 4.1. To make uniform evaporation of coating material, the electron beam is deflected by coils. Also an optional crucible's rotating movement can assist to uniform evaporation. Furthermore, multi-crucible electron beam sources enable the successive evaporation of different coating materials in a single deposition process; alternatively, the EBD devices are provided with two or more sources. [203]

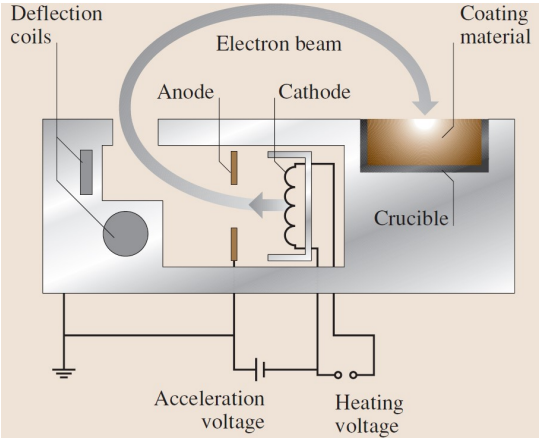

Figure 4.1: Electron beam evaporation source. Electrons are accelerated by a potential difference of several kV and are directed by a magnetic field into a water-cooled crucible. Additional deflection coils allow the beam to write customized patterns on the material to achieve uniform evaporation. [203]

Thanks to the high energy densities of the electron beam, the EBD method enables the evaporation of materials with high melting points. When it comes to rate control, the electron-beam sources benefit from a low inertia combined with their good stability. On the other hand, one of the EBD drawbacks is that high local temperatures can cause decomposition, if chemical compounds are utilized as coating materials. For oxides, this decomposition issue can be overcome by an extra oxygen inlet providing partial pressure around $1 - 3 \times 10^{-2}$ Pa. [203]

Depending on the EBD process conditions, thin films generated by thermal evaporation show diverse microstructures. Columnar growth with microstructural voids is common in evaporated films due to the condensing particles' restricted surface mobility and shadowing effects. To minimize voids, the process parameters are optimized and an additional substrate heating, typically around 300°C, is used. [203]

A serious disadvantage resulting from the presence of microstructural voids in thin films is the penetration of moisture from the surrounding atmosphere. Adsorbed water and bound OH groups induce optical absorption losses, especially in the near- and mid-infrared (MIR) wavelengths. Water adsorption also affects the value of effective refractive index of the layer. Due to fluctuating water content, the spectral characteristic of porous multilayer interference filters reveals a significant dependency on external variables such as temperature and humidity. [203] The sensitivity to environmental conditions can be overcome with ion

assistance, which produces densified films.

4.1.2 Ion Assisted Deposition

Ion Assisted electron beam Deposition (IAD)[2] represents widely used technique for optical thin film fabrication. [203] This technique uses an ion source (Fig. 4.2), which is integrated into the vacuum chamber alongside the evaporation sources, to improve process stability as well as optical and mechanical thin film qualities. The ion source is overlaid on the flow of condensing particles, causing the growing layer to densify as needed. However, the ion source can produce ions of excessive energies that might create ion-induced stoichiometry defects. To maintain dense homogeneous layers with low optical losses, a possible solution is to use oxygen as a reactive gas to assist oxide coating deposition.

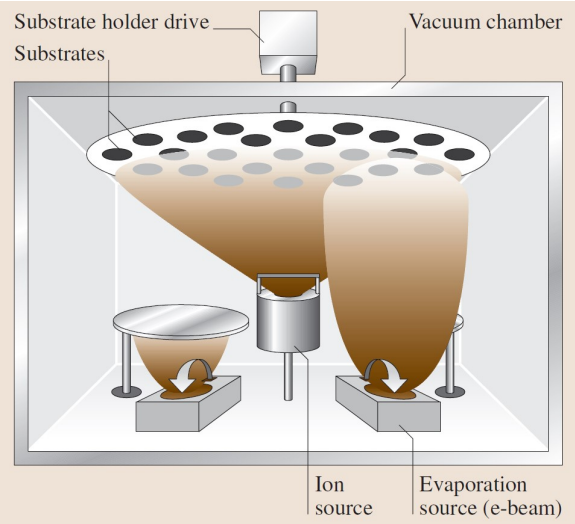

Figure 4.2: Basic configuration of an ion-assisted deposition (IAD). In addition to the electron beam evaporators, an ion source is located in the vacuum chamber. A low-energy ion beam is used to irradiate the substrates, resulting in greater energy transfer to the growing layer. [203]

The IAD deposition can be done using a Bühler SYRUSpro 710 machine employing plasma-ion source to assist the e-beam evaporation process. The substrates are set on a revolving sample holder. According to the deposited material, either low or high index, the corresponding ion source is turned on. Typical deposition rates of low and high index materials are around 0.5 nm/s and 0.25 nm/s, respectively. The control of the thickness of each of the layers is carried out using an OMS 5100 optical monitoring system (Bühler).

The advantages of IAD technique include fast deposition process, ability to deposit dense layers and a wide range of available materials. In turn, the IAD method has the following disadvantages. The deposition rates can be unstable depending on the materials. The maximal total coating thickness is around $10-15\,\mu m$ and the uniformity is limited to 1% over an aperture of 100 mm diameter.[3]

[2] The IAD technique also incorporates Plasma-Ion Assisted Deposition (PIAD).

[3] In this thesis, we studied IAD HfO_2 coating as a part of metrology work in Chapter 3. In Chapter 6, we tested PIAD HfO_2 and SiO_2 coatings at MHz repetition rates to study laser-induced contamination.

4.1.3 Magnetron Sputtering

Plasma assisted reactive magnetron sputtering (PARMS) is a technique for depositing diverse materials at high rates by bombarding a target material with ionized atoms in the presence of a magnetic field. Magnetron-sputtered (MS) thin films within GREAT consortium are produced with a Helios coater developed by Bühler Leybold optics, see photograph in Fig. 4.3. [221]

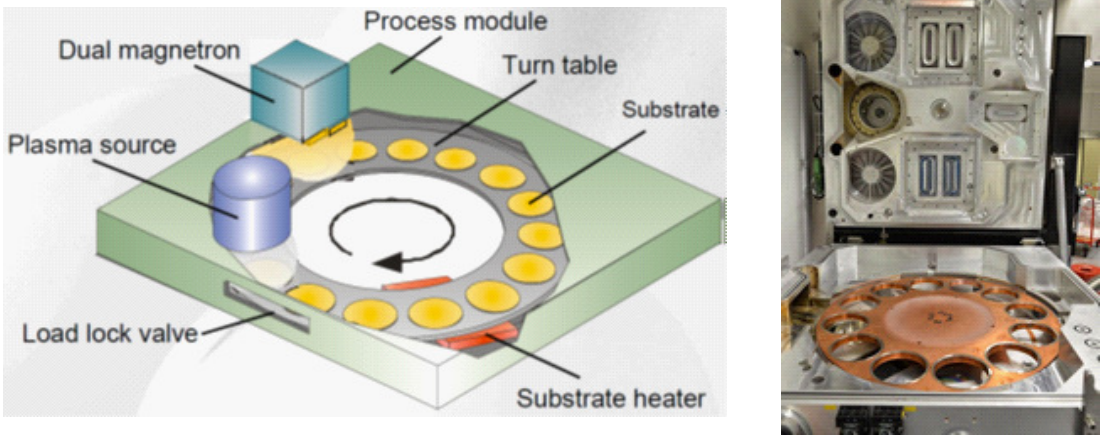

Figure 4.3: Schematic overview and photograph of Helios coater.

The main vacuum chamber incorporates two treatment zones for dielectric materials (MF magnetron sputtering) and one for oxygen plasma assistance. Depending on the deposited material, either low- or high-index, one of the MF magnetron sputtering cathodes is turned on. Using the oxygen plasma assistance the coating densification and stoichiometric layer production is achieved. [184] Typical pressure inside the vacuum chamber during deposition is $5{\cdot}10^{-5}$ mbar. An argon and oxygen mix is used as process gas for MS, while oxygen is used as the source gas in the plasma for thin-film oxidation.

Inside the Helios coater, the substrates intended for deposition are placed on a 12-position rotating sample holder (rotation at 240 rpm[4]). At first the sample passes under a mid frequency dual magnetron, where a thin substochiometric layer is deposited from a metallic target. Then the sample passes under radio frequency plasma source where the thin layer is oxidized. The speed of rotation and power of magnetron is adjusted to deposit ~ 0.1 nm of thin-film in each rotation. Low- and high-index materials have typical deposition rates of 0.40-0.45 nm/s and 0.5-0.6 nm/s, respectively. Within one production cycle, both high- and low-index materials can be coated.

Each individual thin-film-layer thickness is controlled by in-situ optical monitoring. Optical measurement is performed at each passing of the substrate under the measurement window. This allows the single-layer thickness to be controlled to better than 1 nm accuracy. The thickness of the layers is monitored using the OMS 5100 optical monitoring system (Bühler). Both monochromatic and broadband monitoring can be used in this setup.

For MS, we can highlight as advantages the fast and stable deposition process, dense layer production without limit for total thickness, good uniformity and absence of cross contamination when multiple materials are deposited. Disadvantages of this technique include high cost, limitation to planar substrates and high level of contamination.

Previous studies at Institut Fresnel have been conducted on films produced by this machine and their

[4]revolutions per minute

LIDT values were compared to a large set of samples produced by different methods and manufacturers, exhibiting LIDT in accordance with state of the art. [44,124,128] More details about production of magnetron-sputtered samples, which were tested in this thesis, can be find in [222].

4.1.4 Ion Beam Sputtering

When an ion beam is used to sputter a solid target of the material to be deposited, the process is known as Ion Beam Sputtering (IBS). The concept of IBS is depicted schematically in Fig. 4.4. IBS uses a separate chamber (ion gun) to generate the ions that are then extracted and directed towards the target placed in the deposition chamber. [220] The localization of ion gun out of the deposition chamber improves the quality of films. The IBS setup contains a revolving holder with substrates on which sputtered particles from the target condense into thin films.

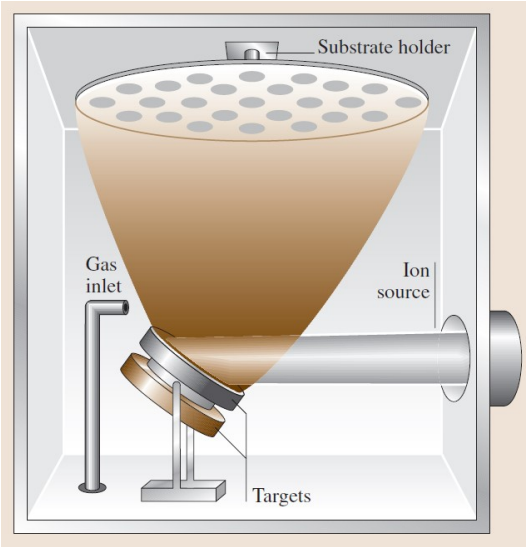

Figure 4.4: Diagram of the ion beam sputtering process. A separate ion source is directed towards the target, from which particles are sputtered and condensed on rotating substrates. By using automatic target exchange, the production of multi-layer coatings is possible. [203]

In common IBS process conditions, argon ions with kinetic energies around 1 kV are used. [203] For the deposition of compound layers from metallic targets, an additional reactive gas inlet is employed. Furthermore, the IBS setup may include a second ion source that is directed to the substrates, allowing for both pre-cleaning of the substrate and assistance with layer growth.

Compared to magnetron sputtering, IBS offers a number of advantages. The low working pressure combined with the absence of interactions between the substrates and the plasma leads to high quality thin films with minimal contamination and defects. IBS coatings are amorphous and can achieve total optical losses below 1 ppm, making them ideal for ultra-low-loss components. The IBS technique is used to produce optics of the highest quality and its advantages include dense layers, access to a wide range of materials and high LIDT. [203]

However, in the commercial mass manufacturing of optical coatings, ion-beam sputtering is less common. IBS possesses significant economic drawbacks, including a poor deposition rate and low thickness homogeneity for large areas. Typical IBS deposition rates for precision optics are approximately 10 times lower than for magnetron sputtering. Despite the aforementioned drawbacks, IBS technology has established its place in

the market for the production of high-end precision optics such as complex chirped mirrors for femtosecond lasers and next-generation lithography. [203] Here, we should note that IBS limitations related to large-scale optics seems to be technologically overcome now. Recent advances in IBS enabled production of large-scale highly-resistant transport mirrors for ELI Beamlines facility. [196] In this thesis, we tested one IBS HfO_2 coating in terms of laser-induced contamination (Chapter 6).

4.1.5 Pulsed Laser Deposition

In addition to established conventional coating techniques in precision, laser and consumer optics, there are now manufacturing methods that can be relevant to other applications. One of the most versatile and powerful methods is Pulsed Laser Deposition (PLD), in which the target material is ablated by laser pulses in a vacuum chamber and the ejected plasma plume is afterwards deposited on substrates. For growing thin films of organic and inorganic compounds, the PLD technique provides an excellent reproduction of the target stoichiometry. However, expanding this method to large coating surfaces and high deposition rates is challenging and currently too expensive. [203]

Contrary to other deposition techniques such as sputtering, or chemical vapor deposition (CVD), PLD enables crystalline thin-film growth at relatively low substrate temperatures. [223, 224] PLD also provides the ability to deposit several multi-component materials in-situ with preserved stoichiometry. [225] Since the pioneering PLD work from Smith and Turner in 1965 [226], the technique has been used for deposition of a wide range of materials [212] and recently proved to be a reliable method for optical-coating fabrication. [213–217]

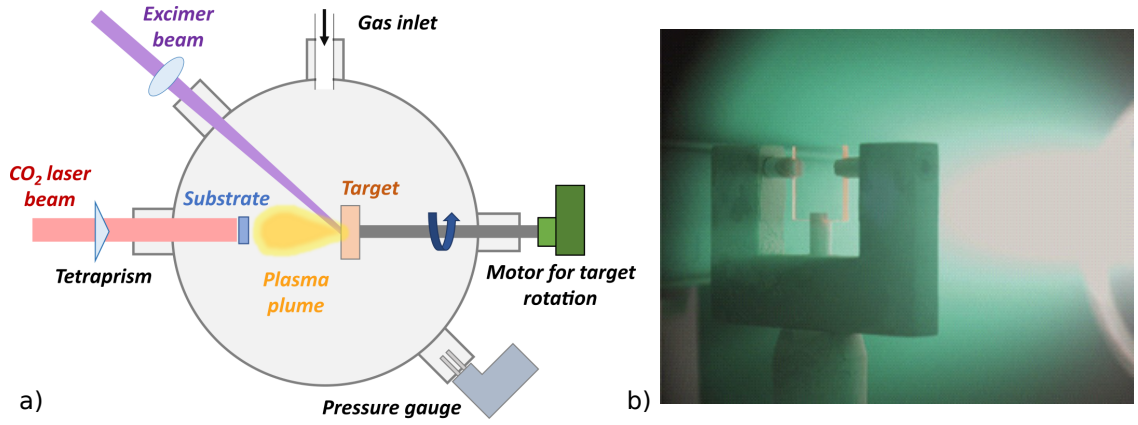

Figure 4.5: Pulsed-laser deposition setup (a) and photograph of ejected plasma plume directed to the substrate (b).

The deposition of the films investigated in this study was performed with the PLD setup depicted schematically in Fig. 4.5 and described in more details in Refs. [216, 227, 228]. The targets were fabricated by sintering powders of the materials of interest, which ensures a stoichiometric proportion of the elements, and had a final mass of $\sim 85\%$ of the expected mass for the pure crystalline material of the same volume. Target ablation was achieved using a KrF excimer laser operating at 248 nm, with a pulse duration of ~ 30 ns and a repetition rate of 100 Hz, yielding growth rates ranging from 10 µm/h (Lu_2O_3) to 20 µm/h (Sc_2O_3). The motion of the target was configured to obtain an effective bi-directional ablation, which was proven to significantly reduce the amount of scattering points in the as-grown films [227]. A Metricon (Model 2010) prism coupler equipped with a prism, and a HeNe laser source operating at 633 nm was used to determine the refractive index and thickness of the films investigated.

To achieve crystalline-film growth, during deposition the rear surface of the substrate was heated by a CO_2 laser operating at 10.6 µm. The original Gaussian intensity distribution of the beam was transformed by a ZnSe tetraprism [229] into a nearly-uniform 10 x 10 mm square profile, which fits the substrate's dimensions. The substrate temperature used for the deposition of the samples ranged from 950°C to 1100°C, depending on the material.

The background pressure of the vacuum chamber could be tuned by manually adjusting an oxygen gas in-flow. All sesquioxide films analysed in this report were deposited at a background pressure of 20(±2) µbar.

Substrate material & orientation	Film	Target ablation fluence	Heating power	(222) XRD peak position	Film lattice constant
YAG <100>	Lu_2O_3	1.21 J/cm^2	26.7 W	29.79°	10.390 Å
sapphire <0001>	Lu_2O_3	1.27 J/cm^2	26.2 W	29.76°	10.399 Å
sapphire <0001>	Y_2O_3	1.19 J/cm^2	18.0 W	29.10°	10.632 Å
sapphire <0001>	Sc_2O_3	1.24 J/cm^2	24.0 W	31.50°	9.840 Å

Table 4.1: Deposition parameters and lattice properties of the sesquioxide films grown on sapphire (Al_2O_3) or yttrium aluminium garnet (YAG) substrates. The measurements of the XRD peaks and lattice constants are detailed in Sec. 4.2.4. The precision on the position of the (222) XRD peak is limited by the angular resolution of the incident beam, ±0.01°. The film lattice constant is calculated for a Cu Kα wavelength of 1.5418 Å and the resolution error is ±0.004 Å.

The deposition parameters of the investigated PLD samples are listed in Table 4.1. An optimisation of the parameters had been conducted previously and PLD the samples for LIDT measurements were selected based on their crystalline properties and surface homogeneity (in terms of the number of scattering points visible under a dark field microscope).

4.2 Characterization of thin films

The goal of this section is to sum up available data of the optical characteristics of thin-film coatings and layers that are used in the GREAT project. For the design and production of optical components including GWS, a thorough understanding of these qualities is required. The refractive index must be measured to an accuracy of 10^{-3} in order to offer adequate modeling data for the construction of effective designs. The information provided here on the characterisation of the optical properties of the coating materials to be utilized will be used to support modeling and specify design restrictions and choices for the GWS and related application areas.

4.2.1 Samples for tests at 500-fs 1030-nm

The tested samples were monolayers of Y_2O_3, Sc_2O_3, Lu_2O_3, HfO_2, Nb_2O_5 and SiO_2, see Table 4.2. The crystalline sesquioxide materials (Y_2O_3, Sc_2O_3, Lu_2O_3) were deposited on a <0001>-oriented sapphire substrate. In the case of Lu_2O_3 material, one sample was deposited on a <100>-oriented yttrium aluminium garnet (YAG) substrate. The amorphous metal oxides (HfO_2, Nb_2O_5, SiO_2) were deposited on fused silica (FS) using the magnetron sputtering process. In the metrology work (Chapter 3), we tested also HfO_2 made by IAD technique.[5]

[5] In Chapter 6, we study also IBS and PIAD coatings in terms of laser-induced contamination at high repetition rate (3.3 MHz) at a wavelength of 515 nm. Description and available data of these samples are reported in Sec. 6.1.3 on page 152.

Material	Thickness	n	Bandgap	Deposition	Substrate
Sc_2O_3	1750 nm	1.97	5.74 eV	PLD	sapphire
Y_2O_3	1310 nm	1.90	5.44 eV	PLD	sapphire
Lu_2O_3	970 nm	1.91	5.43 eV	PLD	sapphire
Lu_2O_3	1000 nm	1.91	5.43 eV	PLD	YAG
$HfO_2^{\star}$	250 nm	2.03	5.25 eV	MS	FS
Nb_2O_5	450 nm	2.26	3.41 eV	MS	FS
SiO_2	450 nm	1.47	8 eV †	MS	FS
HfO_2	150 nm	$1.93^{\diamond}$		IAD	BK7

Table 4.2: Thin-film materials intended for LIDT tests at 500 fs and 1030 nm. Summary of their parameters, n means refractive index at 1030 nm wavelength. The Sc_2O_3, Y_2O_2 and Lu_2O_3 sesquioxides were PLD-grown in the Optoelectronics Research Centre (Southampton, UK). The HfO_2, Nb_2O_5 and SiO_2 were magnetron-sputtered (MS) in the Institut Fresnel (Marseille, France). The IAD deposited HfO_2 was tested only in metrology work (Chapter 3) and its refractive index ($^{\diamond}$) corresponds to 1053 nm. $^{\star}HfO_2$ is not pure but contains $\sim 1-2\,\%$ of SiO_2 admixture. [230] †The SiO_2 bandgap was taken from [128].

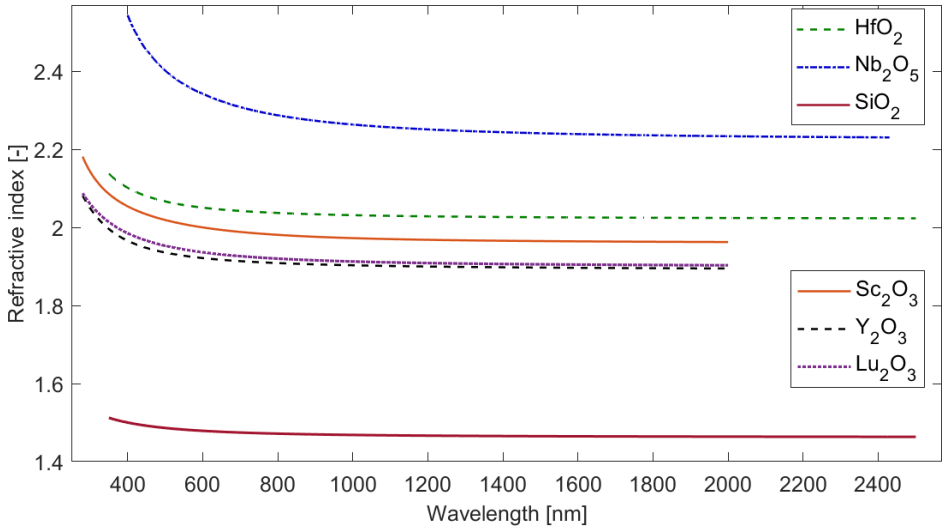

Figure 4.6: Dispersive curves of PLD Sc_2O_3, Y_2O_3, Lu_2O_3 and magnetron-sputtered HfO_2, Nb_2O_5 and SiO_2.

4.2.2 Refractive index measurement

The refractive indices of the magnetron-sputtered samples were determined by spectrophotometry using numerical fitting methods to the transmittance and reflectance measurements in the low-absorptance spectral region. The values of refractive indices at 1030 nm are listed in the Table 4.2. The dispersion curves are shown in Fig. 4.6. In the case of PLD materials, the dispersion curves were determined using ellipsometry. The refractive indices of Y_2O_3 (1.90 @1030nm) and Sc_2O_3 (1.97 @1030nm) correspond well with published values [231, 232]. Extinction coefficients were measured by ellipsometry, however given the uncertainty of the method, we can only assess that the extinction coefficient values are below 10^{-2} at 1030 nm. In the case of MS SiO_2, the measured refractive index (1.47 @1030nm) corresponds well to the value (1.47 @1030nm)

published in [233]. For MS HfO_2, we have index of 2.03 @1030nm, which is also very close to the value (2.02 @1030nm) of MS film reported in [128]. The refractive index of our MS Nb_2O_5 (2.26 @1030nm) is same as the one provided as a part of study [234].

4.2.3 Bandgap measurement

The optical bandgap values of the tested samples were derived from each film's intrinsic absorption coefficient, α, by plotting $(\alpha E)^{1/2}$ as a function of the photon energy E and extrapolating the linear curve to the abscissa axis. The bandgap error margins were estimated using the photon energies corresponding to absorption coefficients of 10^3 and $10^4\,\mathrm{cm}^{-1}$. [235, 236] The value of SiO_2 bandgap was taken from Ref. [128] because the absorption edge could not be reached with our instruments.

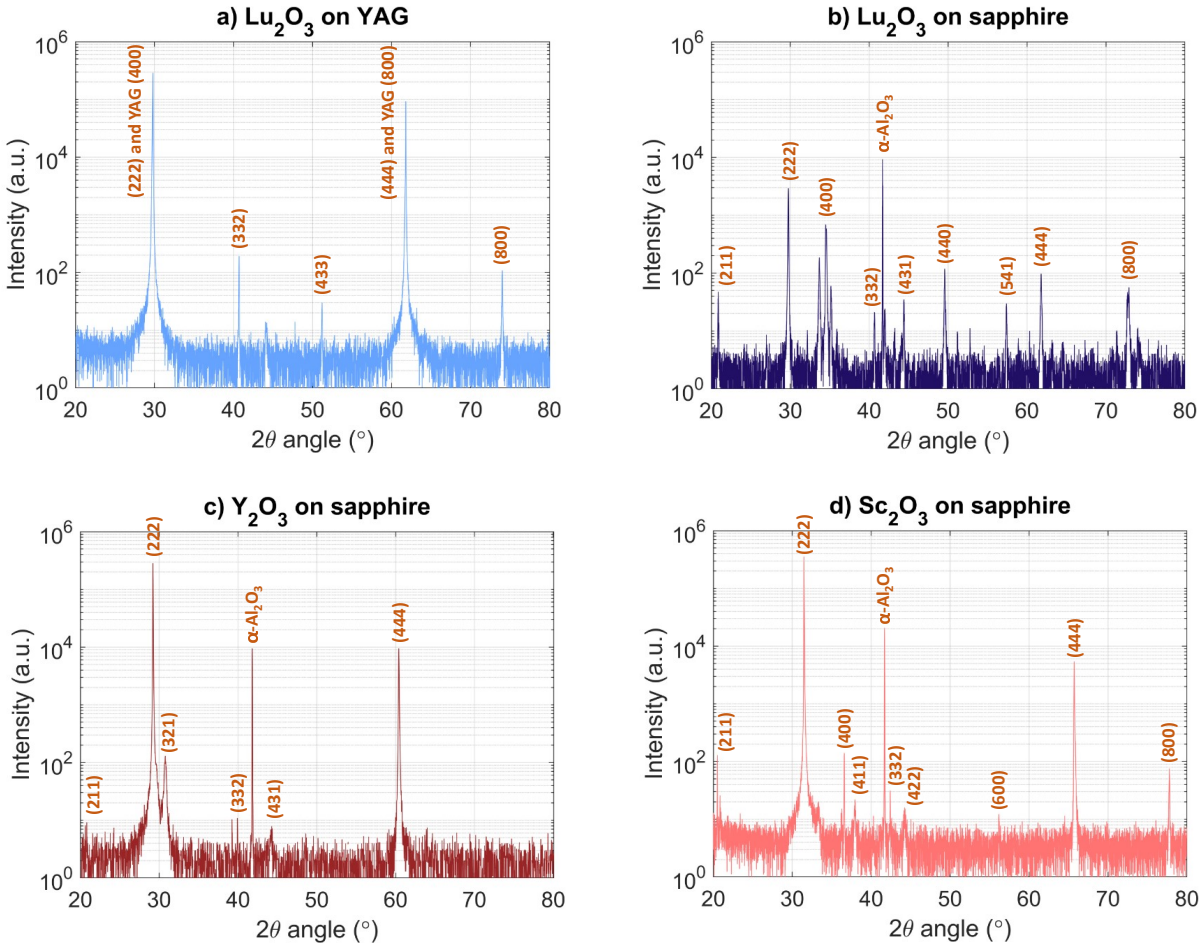

Figure 4.7: Wide XRD scans of the PLD samples: a) Lu_2O_3 film on YAG substrate, b) Lu_2O_3 film on sapphire substrate, c) Y_2O_3 film on sapphire substrate, d) Sc_2O_3 film on sapphire substrate.

4.2.4 X-ray diffraction on PLD films

Epitaxial growth of the Y_2O_3, Lu_2O_3 and Sc_2O_3 films on the <0001>-cut sapphire was expected to be predominantely in the <111>-direction, since the lattice mismatch in this orientation is the smallest with

substrate orientation, i.e., 4.9 %, 2.9 % and 2.5 %, respectively. Similarly, Lu_2O_3 <111> has a quasi-perfect lattice match with <100>-cut YAG, that facilitates growth of that orientation.

The out-of-plane X-ray diffraction (XRD) patterns from the samples were recorded by a Rigaku Smartlab, equipped with a Ge(220) 2-bounce monochromator. Two different sets of parameters were selected for the scans. A wide scan with a 2Θ value from 20° to 80° and a step size of 0.02° was used to compare the proportion of the different orientations in the film. Since the films were expected to grow preferentially in the <111>-direction, the (222) diffraction peak was our main peak of interest. Secondly, an additional high-resolution scan with a step size of 0.002° was made around this primary peak.

Fig. 4.7 displays the XRD patterns of the films with each peak labelled with the corresponding orientation. The Y_2O_3 and Sc_2O_3 films grew primarily in the <111>-orientation, as demonstrated by the dominance of the (222) peak. The height ratio between the (222)-peak and the peaks corresponding to other orientations is greater than 3000. However, the Lu_2O_3 film grown on sapphire exhibits strong polycrystalline characteristics, with several orientations that have a height ratio of less than 30 with the (222) peak. On the contrary, the growth of <111>-oriented Lu_2O_3 is clearly favoured on the YAG substrate: the XRD results also show that the (222) peak is 1500-times stronger than the next visible orientation (332) and is nearly perfectly superimposed with the YAG (400) peak at a 2Θ angle of 29.8°. This aspect is highlighted in the high resolution XRD pattern of that sample in Fig. 4.8b), with a clear double-peak lying at 29.8°.

Fig. 4.8 compares the position of the (222) peak of the different films, which was used to calculate their lattice constants. The results, summarized in Table 4.1, show that the lattice constant of the as-grown films is close to the value reported for the corresponding bulk materials. [237, 238]

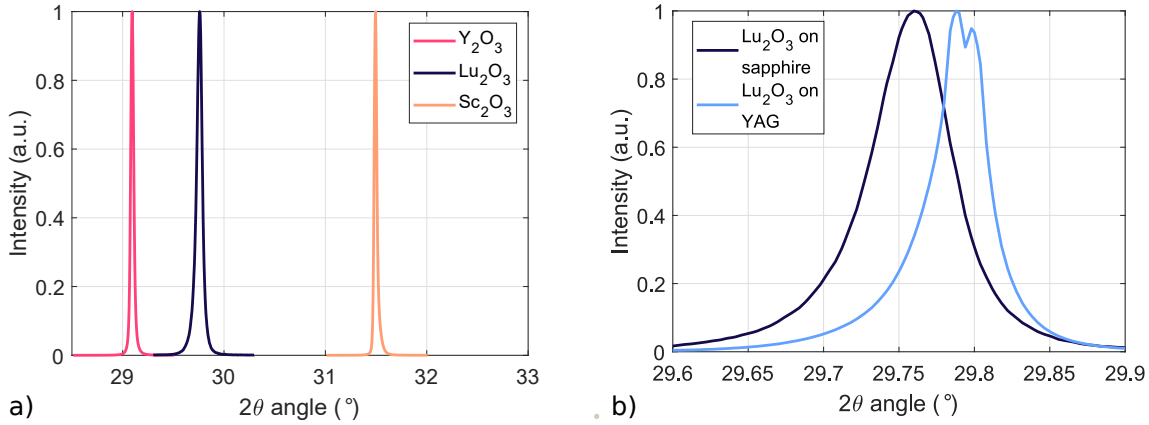

Figure 4.8: a) (222) XRD peaks of the Y_2O_3, Lu_2O_3 and Sc_2O_3 films grown on <0001>-sapphire; b) (222) XRD peak of the Lu_2O_3 films grown on <0001>-sapphire and <100>-YAG.

4.3 500-fs 1030-nm LIDT of PLD sesquioxides and magnetron-sputtered metal oxides

In the past decade, mirrors based on the combination of HfO_2, as high refractive index, and SiO_2 as low index materials, received considerable attention. [132, 183, 239] However, the published sub-ps LIDT results for Sc_2O_3 or Y_2O_3 films, indicate that sesquioxides might be good alternatives for HfO_2. [240–243] Especially Sc_2O_3, which is a promising high refractive index material that exhibits slightly larger optical bandgap

(5.7 eV) [244] than HfO_2 (5.55 eV). [124, 245] In fact, EBD Sc_2O_3 and Y_2O_3 thin films, tested at 500 fs and 1030 nm by single shots and 100 shots at 10 Hz repetition rate, showed LIDTs comparable to that of HfO_2. [240] The laser damage resistance at 500 fs and 1030 nm was also measured for IBS Sc_2O_3 for which its 1-on-1 internal damage threshold reached a value of 3.1 J/cm^2. [241] It has to be pointed out that most of the laser damage studies of Sc_2O_3 have been motivated by the development of optical interference coatings in the UV range. [244, 246–248] To the best of our knowledge, all the LIDT studies conducted on sesquioxide films focused either on amorphous or polycrystalline films. Consequently, the results might differ from films produced via PLD method, which has the potential to grow single-crystal films. [216, 228, 249]

For the testing at a pulse duration of 500 fs and a wavelength of 1030 nm, we prepared magnetron-sputtered amorphous SiO_2, HfO_2 and Nb_2O_5 thin films and pulsed-laser deposited crystalline sesquioxides (Sc_2O_3, Lu_2O_3 and Y_2O_3). Thicknesses, bandgaps and refractive indices at a wavelength of 1030 nm for these samples are listed in Table 4.2. SiO_2, HfO_2 and Nb_2O_5 thin films are standard optical materials whose damage thresholds have been reported in several studies comparing them with a variety of optical-coating materials. [44, 124] In contrast, PLD sesquioxides are non-traditional materials for optical applications but recent studies indicate that PLD coatings have potential for use in high-power pulsed laser systems. [213–217]

4.3.1 LIDT test procedure

The test station used for LIDT tests with a pulse duration of 500 fs was described in Sec. 3.2 on page 69. For the results reported here in this section, the pulses of nearly Gaussian spatial profile at $\sim$ 1030 nm wavelength were incident on a sample. Characterization of the spatial and temporal profiles as well as an energy calibration were carried out before and after the LIDT test campaign. The LIDT tests were performed with samples placed at focal plane of the lens with 30-cm focal length. The effective beam diameter, as defined by international standards, [75] was 84 µm in a plane perpendicular to the beam propagation. The LIDT tests were performed in an air environment at a room temperature of 25 °C and humidity around 27 %.

Each sample was irradiated at different spots with unique pulse energies that were changed with a $\sim$ 1 % energy increment in order to get statistical data. The procedure was repeated for different numbers of pulses - from single-shot up to 1000 shots at a repetition rate of 10 Hz. The LIDT tests were done at 45° incidence angle with P-polarization. The irradiated sites were analyzed ex-situ using a Zeiss Axiotech differential interference contrast microscope with 20x-objective magnification. Any observable material modification was evaluated as damage. The damage threshold was determined as the highest fluence that is lower than the lowest fluence causing damage in the experiment. The LIDT error bars correspond to sum of 3σ variations of effective beam area near focal plane ($\sim$ 3 %), pulse energy ($\sim$ 0.7 %) and a half of pulse energy increment ($\sim$ 0.5 %). The results reported here are expressed in intrinsic fluences according to the description provided in Sec. 3.1.2 on page 68.

4.3.2 Laser Damage Results and Discussion

Deterministic 0-1 transition

To evaluate the uniformity of the tested materials in terms of laser damage, the transition range of the damage probability, as indicated in Fig. 4.9a), was calculated for each material and number of shots used, see Fig. 4.9b). The 1-on-1 laser damage tests with Sc_2O_3, Y_2O_3, SiO_2, HfO_2, Nb_2O_5 show deterministic results, i.e., narrow transition ranges of damage probability from 0 to 1. The transition range of damage probability was only a few percent in fluence, which suggests that the LIDT is limited by intrinsic material properties rather than by defects or impurities caused by the deposition process. [100] However, in the case

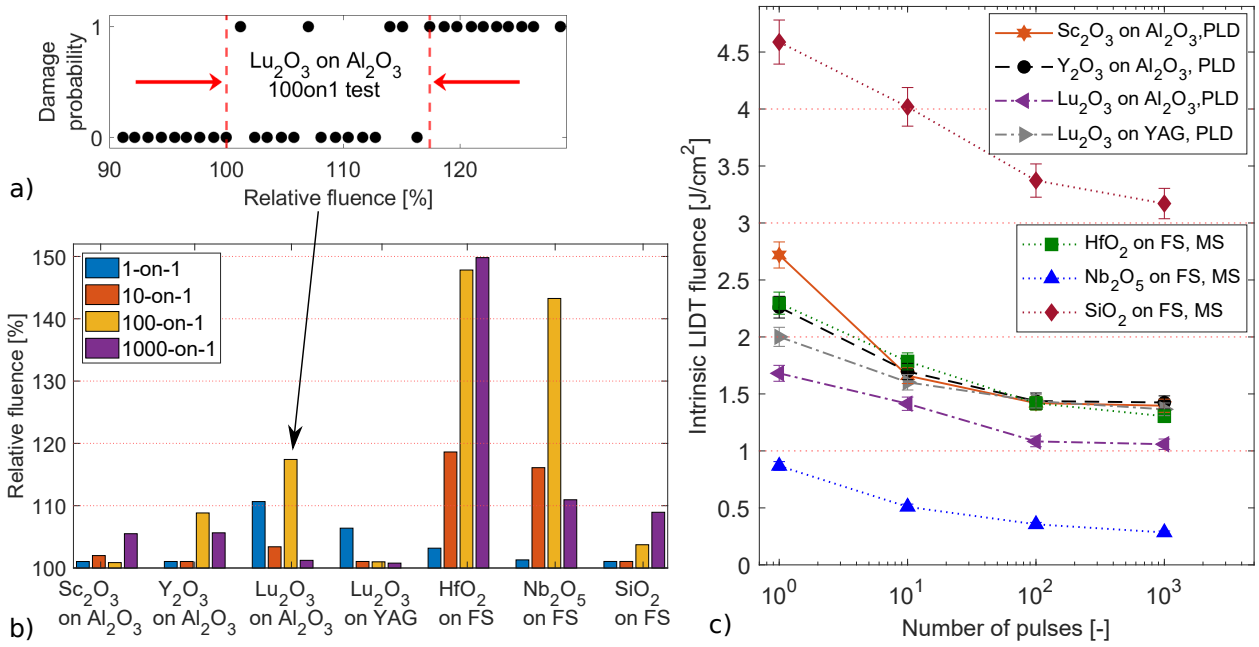

Figure 4.9: Laser damage results for materials used in GWS: a) example of the damage probability results in the case of 100-on-1 tests with Lu_2O_3 deposited on sapphire; b) transition ranges for the damage probability expressed in relative fluence, as indicated in Fig. 4.9a); c) intrinsic LIDT fluence as a function of shot number. The Sc_2O_3, Lu_2O_3, and Y_2O_3 films were fabricated by pulsed-laser deposition, while HfO_2, Nb_2O_5 and SiO_2 by magnetron sputtering. All samples were tested with pulse duration of 500 fs at 1030 nm.

of Lu_2O_3 we found wider transition ranges that could be a consequence of film imperfections, see Fig. 4.10, especially in the case of the film grown on sapphire that could be connected to the polycrystalline nature of this film. The larger ranges for the multiple-pulse tests may be due to the stochastic formation of deep and shallow traps in the bandgap, which facilitate electron excitation and material modification. [70]

LIDT - single shots

The intrinsic LIDT fluence as a function of shot number for different thin-film materials is shown in Fig. 4.9c). On Figs.4.10 and 4.11 we show examples of damage morphologies for PLD and magnetron-sputtered coatings. Among the tested materials, the SiO_2 film shows the highest LIDT while Nb_2O_5 shows the lowest. In between, we find the other high-index materials, namely HfO_2, Sc_2O_3, Y_2O_3 and Lu_2O_3, that are interesting for high-power applications.

HfO_2, a widely used high-index material in optical mirrors, showed a single-shot LIDT of 2.3 J/cm^2, which is higher than the values around 2.0 J/cm^2 published in previous works [240, 250, 251] performed for conditions close to ones used in this study (1030 nm, 500 fs). The higher LIDT of the tested HfO_2 can be explained by the inclusion of SiO_2 in the deposited film, which was estimated from dispersion curve to be around 1-2 %. [230] This effect of the SiO_2 admixture on the HfO_2 damage threshold is in agreement with previous work. [44].

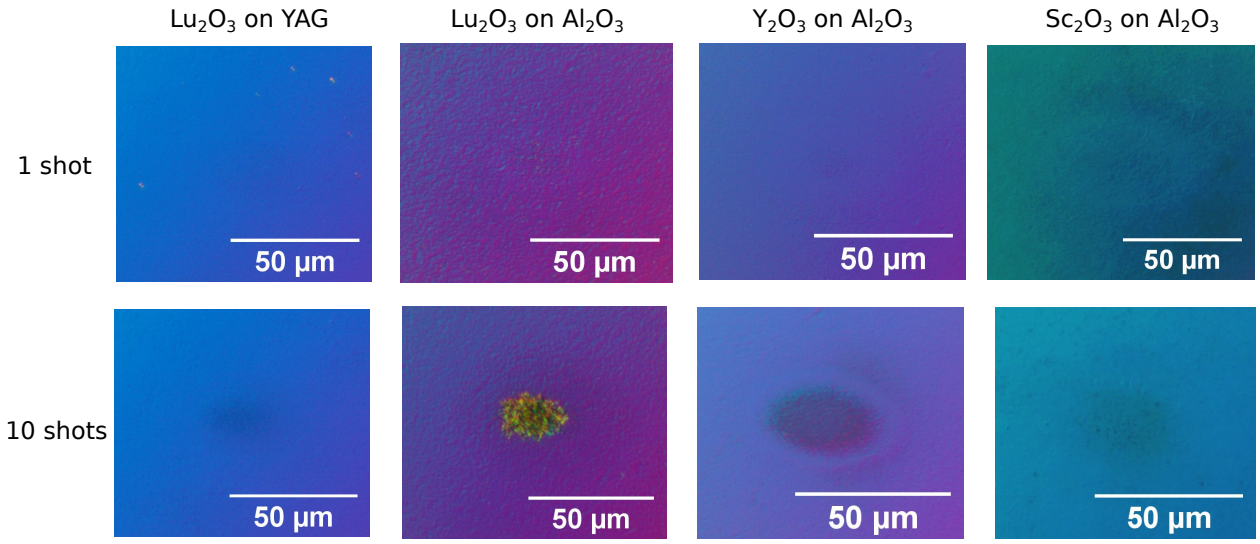

Figure 4.10: Laser-induced damage morphologies for the tested crystalline sesquioxide films. Presented spots were irradiated at fluences slightly higher ($\sim 10\%$) than the determined damage thresholds.

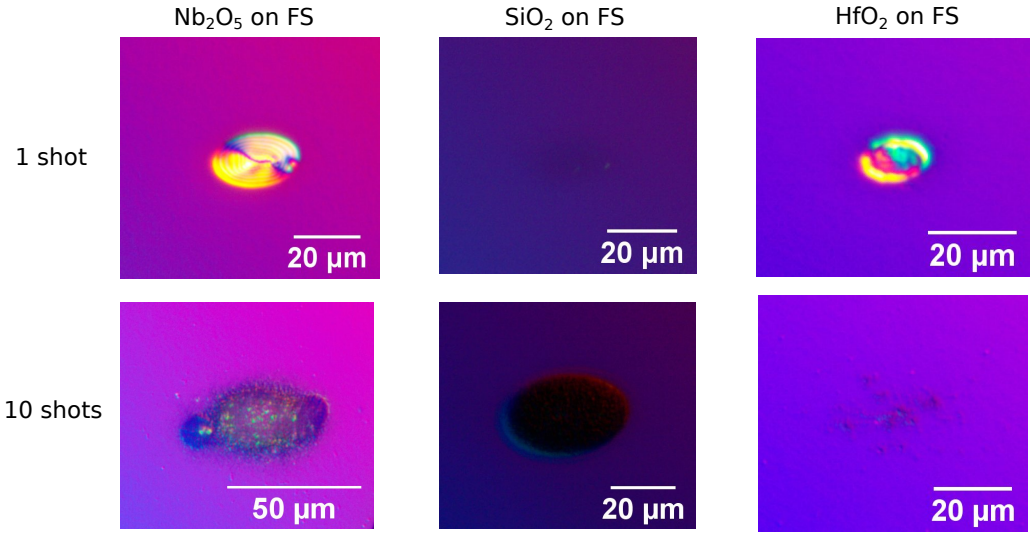

Figure 4.11: Laser-induced damage morphologies on magnetron-sputtered coatings deposited on fused silica (FS). Presented spots were irradiated at fluences slightly higher ($\sim 10\%$) than the determined damage thresholds.

LIDT - multiple shots

For all materials, the LIDT is decreasing with an increasing number of shots, see Fig. 4.9c). The results show a drop of $> 20\%$ of the threshold within the first 100 shots. In contrast, at the transition from 100 pulses to 1000 pulses we observe only a small decrease. These tendencies were already observed in works performed at similar irradiation conditions with metal oxide coatings. [128, 240, 252] The gradual decrease is associated with the formation of laser-induced defects, leading to accessible energy levels within the bandgap. The deep or shallow traps can capture electrons from the conduction band even after a sub-threshold irradiation, thus facilitating the promotion of electrons to the conduction band. [149]

In the case of Sc_2O_3, the drop in LIDT is more noticeable than for the other sesquioxides and reaches that of HfO_2. The larger 1-on-1 LIDT of Sc_2O_3 compared to HfO_2 was also observed in work with IBS films [241] which could be related to imperfect damage detection. Going to a higher number of pulses, the HfO_2 deposited on FS, Y_2O_3 on Al_2O_3, Sc_2O_3 on Al_2O_3, and Lu_2O_3 on YAG, samples show very similar LIDT, indicating that any of these materials could be recommended for high-power applications, as far as LIDT is concerned. The 1-on-1 and 100-on-1 LIDT values of Y_2O_3, Sc_2O_3 and HfO_2 materials are also close to each other in the study [240], which is devoted to electron-beam deposited single-layers on FS substrates. The LIDT tests were performed at identical conditions to this work (500 fs, 1030 nm, 10 Hz).

In the case of Lu_2O_3 deposited on an Al_2O_3 substrate, we observe significantly lower LIDT values, which could be explained by the polycrystalline and highly textured nature of the film (Fig. 4.10). The presence of multiple crystal orientations implies the existence of discontinuities in the lattice that may potentially modify the local bandgap of the material. These boundaries between domains of different orientations may initiate the damage at lower fluences.

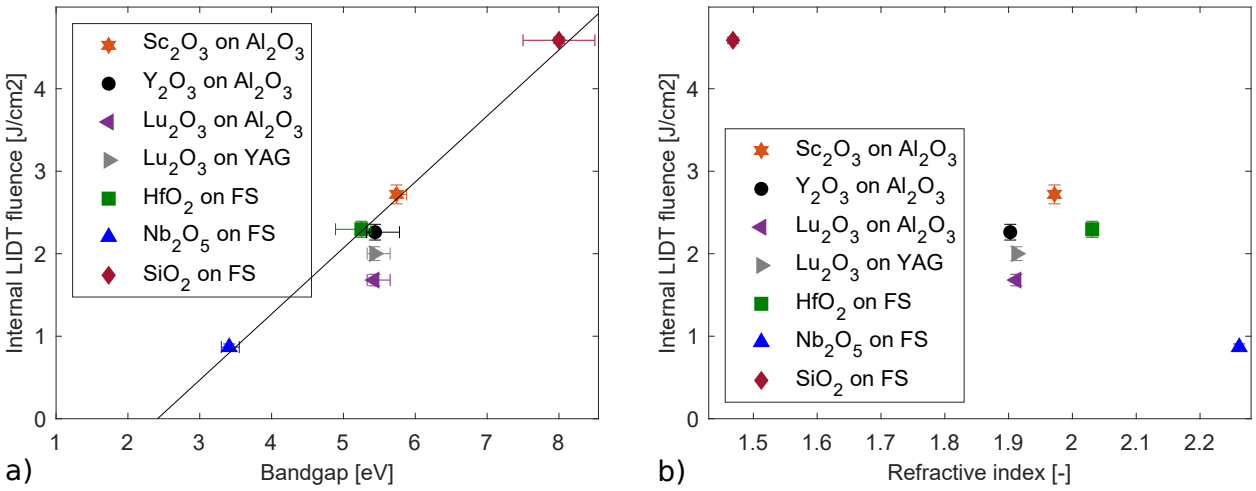

Figure 4.12: Single-shot intrinsic LIDT fluence as a function of material bandgap (a) and refractive index (b). The bandgap was determined using the Tauc method.

Bandgap

Since laser-damage initiation in the sub-ps regime is driven by nonlinear ionization, the bandgap represents a critical parameter that correlates with the laser-damage resistance. [100] The behavior can be explained by taking into account the electron excitation processes playing a dominant role at the beginning of damage formation, i.e. multi-photon and impact ionization. [70] The intrinsic threshold fluences of tested materials are plotted as a function of their bandgap values in Fig. 4.12a). We observe a linear tendency of increasing single-shot LIDT with a larger bandgap value that is in agreement with the studies performed at similar irradiation conditions in Refs. [124, 170]

The deviations from the linear tendency in Fig. 4.12a) can be explained by the challenges faced to observe material modifications induced by single-shot irradiation, see Fig. 4.10. Moreover, some of the sesquioxide crystal films exhibit imperfections that include defect sites. For example, the lower LIDT of Lu_2O_3 on sapphire could have been caused by its polycrystalline structure, enabling lower local bandgap values at domain boundaries for different lattice orientations. It should be highlighted that the Tauc method provides

a measure of the bandgap at a macroscopic scale, while on the microscopic level there are likely to be numerous defects in the polycrystalline film. Even in the case of the near single-crystal Lu_2O_3 on YAG, the error bars on the bandgap would be larger than that determined from the Tauc measurement method used.

In this work, the LIDT (in J/cm^2) tendency on bandgap E_g (in eV) can be well fitted by the relation:

$$LIDT = 0.8 \times E_g - 1.93. \tag{4.1}$$

The equation shows a higher slope, i.e., more dynamic dependence on the bandgap than the empirical description in Ref. [124] derived from results for numerous materials deposited by various methods. The differences from the published data could be explained by the limited number of tested samples or the selected method of bandgap determination.

The bandgap values of sesquioxides are very close to each other with slightly larger bandgap in the case of Sc_2O_3, see Fig. 4.12, whose single-shot LIDT was determined as the highest within the high-index materials. The determined bandgap value for the Sc_2O_3 film tested (5.7 eV) is close to the bandgap of ion-beam sputtered Sc_2O_3 (5.6 eV) [241]. However, larger bandgaps have been reported for electron-beam deposition (EBD) of Sc_2O_3 (6.5 eV) or Y_2O_3 (6.1 eV) [240] compared with the samples tested here grown by PLD i.e., Sc_2O_3 (5.7 eV) or Y_2O_3 (5.4 eV).

In the case of magnetron-sputtered oxides, the values are close to the ones published in studies [124,128].[6] Here determined bandgap for MS Nb_2O_5 of 3.41 eV is the same as for IAD one and slightly lower than IBS Nb_2O_5 (3.46 eV). [135] The bandgap of our MS HfO_2 of 5.25 eV is within the range of values (5.22–5.36 eV) published with EBD HfO_2. [124,250] It should be noted that care should be taken when comparing bandgaps across publications, since the bandgap is not exactly defined and can be determined using different methods.

Refractive index

For the design of multilayer components and GWS in our case, the critical parameter is the refractive index. Thus, in Fig. 4.12b), we plot the intrinsic 1-on-1 LIDT of the tested materials as a function of refractive index at 1030 nm. The results confirm the trend of increasing refractive index with decreasing intrinsic 1-on-1 LIDT, which was also observed in works [44,124] performed at similar irradiation conditions (500 fs, 1030 nm). Amorphous magnetron-sputtered and single-crystal PLD materials appear to follow the trend, while polycrystalline sesquioxide, such as Lu_2O_3 on Al_2O_3, seems to be susceptible to a lower LIDT. This could be due to local defects associated with domain boundary interfaces and the highly textured surface, see Fig. 4.10. Based on the comparison, Sc_2O_3 seems to be the most promising of the sesquioxides, showing both high damage resistance and a high refractive index value. Furthermore, the PLD Sc_2O_3 (1.97 @1030nm) shows higher refractive index @1030nm than the IBS one (1.93) [241] or the EBD Sc_2O_3 (1.82 @1030nm) [240]. The refractive index of the PLD Y_2O_3 samples studied here is same as that of EBD Y_2O_3 (1.90 @1030nm). [240]

For magnetron-sputtered oxides, the values of refractive indices at 1030 nm are very close to the ones of coatings produced by the same technique whose results are published in [128]. For the same material, the values differ by no more than 0.01. Such a low or no difference is even between refractive indices of SiO_2 coatings deposited by magnetron-sputtering (1.47 @1030nm), IAD (1.47 @1030nm) [128] and IBS (1.46 @1030nm) [135] techniques. The refractive index of here investigated magnetron-sputtered Nb_2O_5 is higher than the value for Nb_2O_5 coating deposited by IAD (2.21 @1030nm) [128] and IBS (2.23) [135] methods. The magnetron-sputtered HfO_2 (2.03 @1030nm) shows higher refractive index than EBD (1.83–1.95) and IAD (1.93 @1030nm) HfO_2. [240]

[6] The SiO_2 bandgap used in our study was taken from [128].

Deposition methods

The LIDT of magnetron-sputtered SiO_2, HfO_2 and Nb_2O_5 coatings have already been studied at identical conditions (500 fs, 1030 nm) in [128] and results for these materials have been compared to a broad range of optical-coating materials. [44, 124] The LIDT results of MS films done by Douti [128] are close to the ones we obtained here. Douti compared MS coatings to IAD deposited films. While for Nb_2O_5 and SiO_2 materials both methods showed similar results, in the case of HfO_2, the MS coatings had by approximately 25 % higher damage thresholds than IAD HfO_2, which was attributed to a small content of silica.

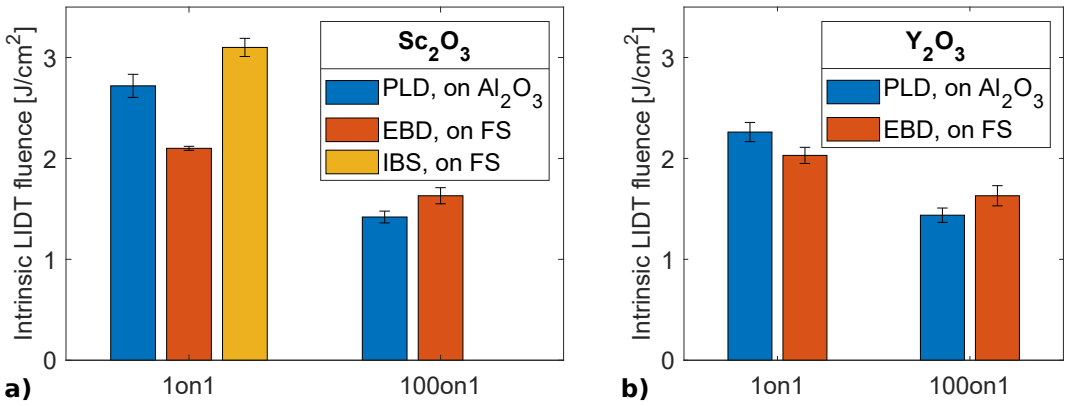

Figure 4.13: Intrinsic LIDT fluence for a) Sc_2O_3, b) Y_2O_3. Comparison of deposition methods. The results of electron-beam deposited (EBD) and ion-beam sputtered (IBS) samples are taken from [240] and [241], respectively. All samples were tested under identical conditions using the same experimental setup with 500 fs pulse duration at 1030 nm wavelength.

Thanks to the LIDT studies [240, 241] performed in identical conditions using the same experimental setup as this work (500 fs, 1030 nm), we can compare the LIDT values of sesquioxides deposited by different fabrication methods as shown in Fig. 4.13. For both Sc_2O_3 and Y_2O_3, the laser damage resistance of the PLD samples is comparable to that of EBD layers. The thresholds of both PLD and EBD samples indicate similar fatigue effect - decrease between the 1-on-1 and 100-on-1 thresholds. In the case of 1-on-1 Sc_2O_3 thresholds, the differences between PLD, EBD and IBS deposition methods can be explained by the difficulty in detection of material changes. Furthermore, the higher 1-on-1 LIDT of Sc_2O_3 layer fabricated by IBS compared with that of the PLD grown layer could be explained by a 1.6 % Si fraction of Sc+Si content in the IBS layer. [241]

Sesquioxides in multilayer coatings

Lattice-matching constraints strongly limit the potential combinations of materials involving crystalline sesquioxides. Among the materials studied, Sc_2O_3 and α-Al_2O_3 have the largest refractive index contrast, i.e., 0.2 at the wavelength of 1030 nm. Despite a lattice mismatch of only 2.5%, the fundamentally different lattice structure of Sc_2O_3 and α-Al_2O_3 (space group $Ia\bar{3}$ and $R\bar{3}c$, respectively) can potentially make the fabrication of Sc_2O_3/ α-Al_2O_3 multilayer coatings more complex than pairs of cubic sesquioxides. However, for example, the lattice mismatch of a Sc_2O_3/Y_2O_3 combination is too large, at 7.6%, for robust thick-multilayer epitaxial growth. Another challenge derives from the lower index contrast between these PLD-grown sesquioxide materials. For instance, a quarter-wave stack of HfO_2/SiO_2 needs a minimum of 25 layers to reach 99.9% reflectivity at normal incidence for wavelength of 1030 nm, while an equivalent Sc_2O_3/α-

Al_2O_3 mirror would require 73 layers. The resulting multilayer stack would have a full thickness on the order of 20 µm, which is within the scope of PLD crystalline growth. [217] Furthermore, owing to the high deposition rates achievable ($\sim 15 - 20$ µm/h), around 10 times faster than magnetron sputtering, 10's-µm dimensions are entirely feasible within reasonable growth-run times.

4.3.3 Summary of LIDT tests at 500-fs 1030-nm

Using a pulse duration of 500 fs and a wavelength of 1030 nm, we tested magnetron-sputtered amorphous HfO_2, Nb_2O_5, SiO_2 and PLD crystalline Sc_2O_3, Y_2O_3 and Lu_2O_3. The LIDT tests were done for number of pulses ranging from 1 to 1000 at a repetition rate of 10 Hz. The results of magnetron-sputtered oxides correspond to the previous LIDT study [128] performed at identical conditions with the same materials deposited by the same technique.

In the case of PLD films, similar intrinsic LIDT fluences of 1.3 - 1.4 J/cm^2 were found for the well-grown sesquioxides, i.e. Sc_2O_3 on sapphire, Y_2O_3 on sapphire and Lu_2O_3 on YAG, when tested with multiple pulses (100 or 1k). The LIDT tests on Lu_2O_3 grown on sapphire revealed significantly lower damage thresholds than Lu_2O_3 on YAG. This result is explained by the polycrystalline structure of Lu_2O_3 grown on sapphire, deduced from XRD characterization. The highly textured polycrystalline structure contains discontinuities in the lattice that most probably initiate the damage. The high-index PLD sesquioxides show high bandgap values indicating good damage resistance in optical-coatings.

Our comparative work on LIDT shows that PLD sesquioxides can compete with magnetron-sputtered HfO_2, a frequently used high-index material in dielectric multilayers. The study shows that pulsed-laser deposition is a candidate for optical-coating fabrication and that the sesquioxides are promising high-index materials that could be used in applications relating to high-power ultrashort-pulse lasers.

4.4 Laser damage testing of monolayers at 1.8 ps

Using the 1.8-ps 1030-nm 1-kHz LIDT station at HiLASE centre, described in Sec. 3.6, we tested three magnetron-sputtered Nb_2O_5 monolayers of varying thickness. The monolayers of 150 nm, 300 nm, 450 nm thicknesses were deposited on 2 mm thick fused silica substrates at Institut Fresnel. A bare fused silica substrate was also tested with this LIDT station. At the moment of these tests, other materials were not available.[7]

The LIDT tests were done at an angle of incidence close to normal (2°) for number of pulses ranging from 1 up to 100k at a repetition rate of 1 kHz. During the testing, we irradiated 4 spots with the same fluence and number of pulses. The spot-spot distance was 1.6 mm for an effective beam diameter of 315 µm. Such a long distance is critical to avoid surface pollution from pulses hitting other regions, especially in the case of multiple-shot large beam tests. However, due to the selected long spot-spot distance, each 1-inch sample provided only 120 sites within its central region of 20 mm in diameter. Thus, to perform tests with 6 different number of pulses, we used only 20 sites per number of pulses. For each number of pulses, only 5 different fluence values were used.

For the evaluation of LIDT data reported here, the sample surface was examined ex-situ with a OLS5000-SAF confocal microscope (Olympus) equipped with a 100X magnification objective. The LIDT results of Nb_2O_5 monolayers and fused silica substrate are shown in Fig. 4.14. The indicated error bars correspond to the sum of 3σ effective beam area deviations (9%), pulse energy variations (5%) and half of the pulse energy increment (mostly $\sim 4\%$).

[7] The LIDT tests at 1.8 ps were done 2 months after the start of PhD, when Nb_2O_5 material was the only one available.

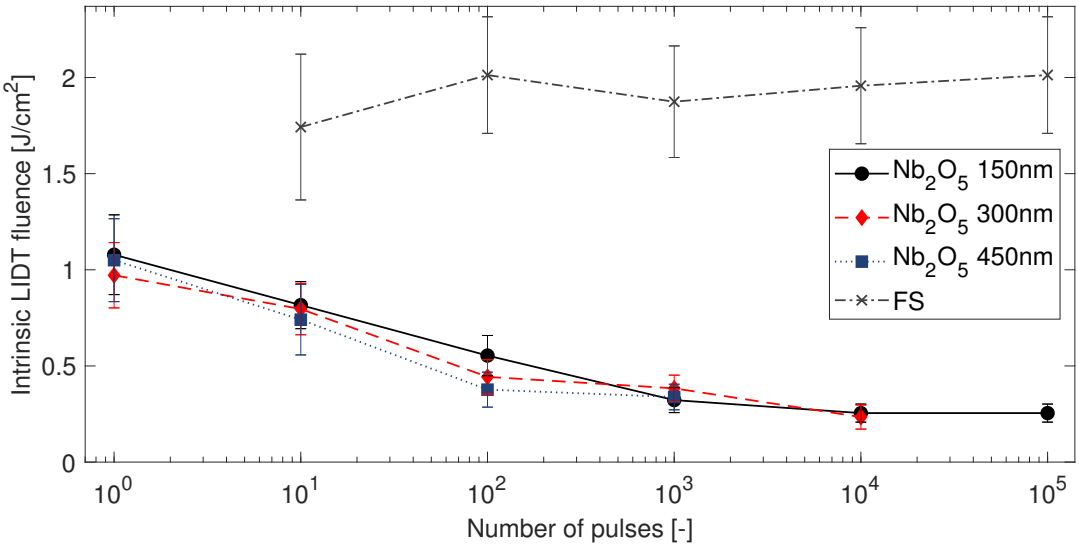

Figure 4.14: Intrinsic LIDT fluence for Nb_2O_5 monolayers of different thicknesses and fused silica (FS) substrate.

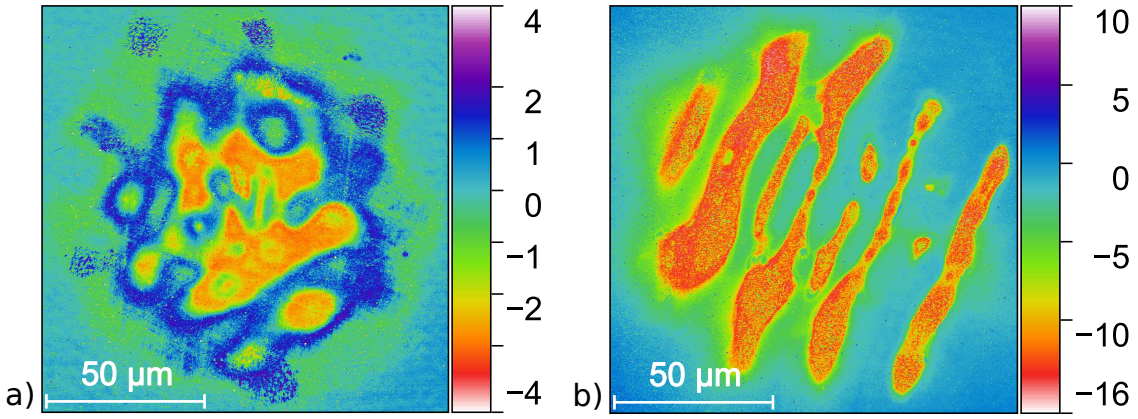

Figure 4.15: Spots on fused silica substrate irradiated in 1on1 (a) and 10on1 (b) procedures by an intrinsic fluence of 2.7 J/cm^2. The lateral scale is only relative. The images were captured ex-situ by a laser confocal microscope with 100X objective magnification.

The intrinsic damage threshold of fused silica substrate was significantly higher than for Nb_2O_5 monolayers. We did not identify the single-shot threshold of fused silica since the irradiation at maximal safely accessible pulse energy (3.1 mJ) did not reveal any damage with in-situ observation technique. However, the detailed ex-situ inspection of substrate with the confocal microscope showed clear surface modifications induced at this fluence, see Fig. 4.15a). Thus, for the used beam of 315 µm effective diameter and the calculated electric field intensity maximum in substrate (0.67) normalized to the incident electric field amplitude in air, we can tell that the 1on1 intrinsic LIDT of fused silica is lower than 2.7 J/cm^2. In the multiple-shot regime, the damage thresholds of fused silica were determined and they did not show incubation effect. This suggests that the damage, which is observed, is formed within the first 10 pulses and the subsequent pulses do not play a significant role at a given fluence level below damage threshold for 10 pulses. The damage tests with different numbers of pulses show the same thresholds within the indicated error bars. An example of fused silica surface modified by 10 shots is shown in Fig. 4.15b).

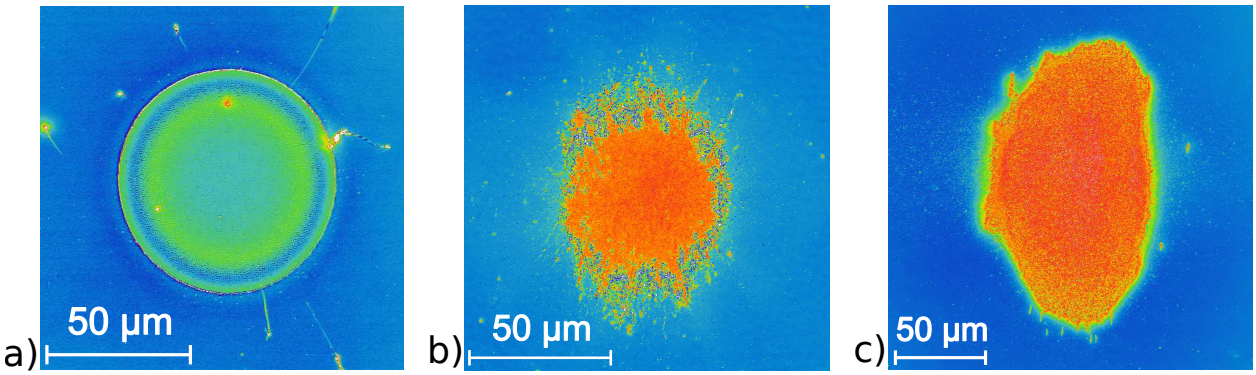

Figure 4.16: Damages on spots of 150 nm thick Nb_2O_5 monolayer induced by: a) single-shot at an intrinsic fluence of 1.19 J/cm^2, b) 10-shots at 0.93 J/cm^2, c) 1280-shots at 0.34 J/cm^2.

Examples of surface modifications on the 150 nm, 300 nm and 450 nm thick Nb_2O_5 monolayers are shown in Figs. 4.16, 4.17 and 4.18, respectively. The single-shot damage (Fig. 4.16a) induced by a fluence slightly higher ($\sim$ 10%) than the determined threshold has very regular shape which confirms high-quality of the used near-Gaussian beam profile. In contrast, the structure of damage in Fig. 4.16b) produced by a serie of 10 consecutive pulses is more irregular, which may be the result of stochastically present laser-induced defects. The modification in Fig. Fig. 4.16c) produced by an irradiation with 1280 pulses with a fluence of approximately 3% higher than the damage threshold for 1000 pulses shows a sharper boundary for the ablated part of the surface. This sharper boundary could be related to the slow growth of damage with a large number of pulses at a fluence very close to the damage threshold.

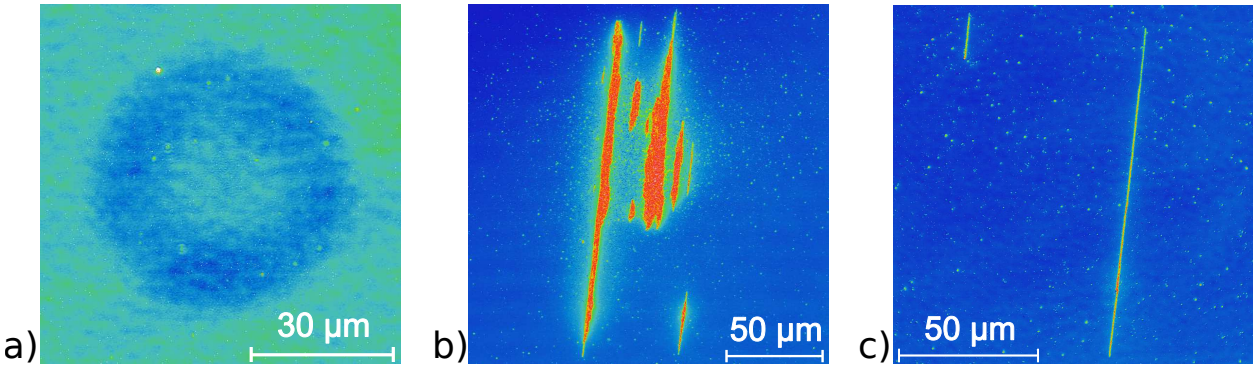

Figure 4.17: Surface modifications of 300 nm thick Nb_2O_5 monolayer induced by conditions close to the damage thresholds: a) single shot at an intrinsic fluence of 1.04 J/cm^2, b) 10k-shots at 0.32 J/cm^2, c) 100k-shots at 0.23 J/cm^2.

Fig. 4.17a) shows a slight modification (discoloration) of the 300 nm thick Nb_2O_5 that was detected using a confocal microscope and image processing with an appropriate color gradient. A similar discoloration morphology was found on the surface of multi-layer dielectric optical coatings irradiated by a pulse duration of 37 fs with a center wavelength of 800 nm. [197] The gentle nature of the damage may not have a substantial impact on reflectivity, but it may cause the staining to spread with the accumulation of pulses. At greater fluences and/or longer exposures, this might be a precursor to catastrophic damage. [197]

After a certain number of pulses, laser-induced nanostructures (nanocracks) were found on the surface of 300 nm thick Nb_2O_5, see Figs. 4.17b) and c). In the femtosecond regime [253], it has been illustrated that the

formation of nanocracks could begin with the generation of nanobumps, i.e. changes in surface roughness. For the 500-fs 1030-nm multiple pulse exposures, the nanocrack formation was observed on oxide thin films and studied as a function of polarization orientation. [254] It has been shown that nanocracks are due to damage growth connected to nano-ablation and electric field enhancements. Our findings in the picosecond regime show the nanocrack growth on magnetron-sputtered Nb_2O_5 with the increasing number of pulses. The growth was also observed in [254]. It should be noticed that some of the nanocracks were not observed in-situ, but disclosed by the ex-situ surface inspection using the confocal microscope with 100X objective magnification. Because of the presence of such modifications, we cannot determine the LIDT of 300 nm thick Nb_2O_5 for 100k shots. However, the threshold is lower than the intrinsic fluence of $0.23\,J/cm^2$.

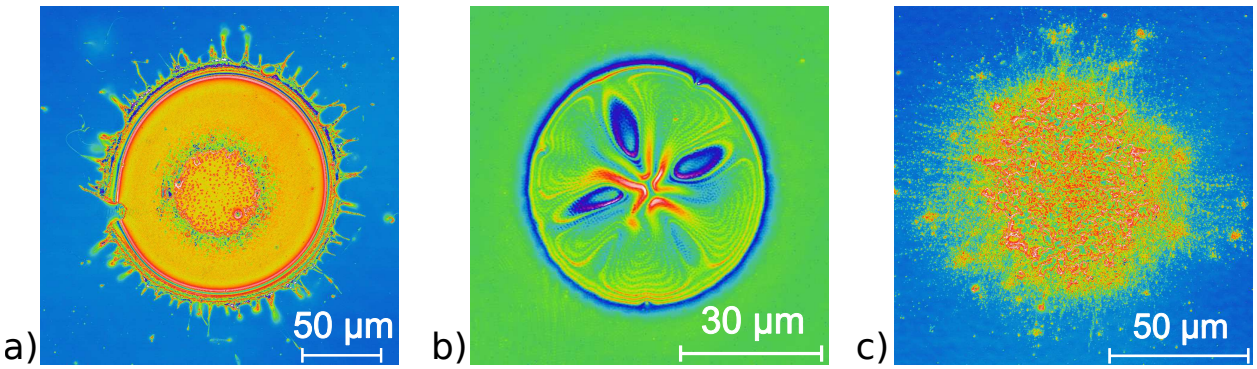

Figure 4.18: Damaged spots of 450 nm thick Nb_2O_5 monolayer induced by single shots at intrinsic fluences of a) $1.47\,J/cm^2$, b) $1.19\,J/cm^2$, and by c) 10-shots at $0.99\,J/cm^2$.

Surface modifications of 450 nm thick Nb_2O_5 caused by single-shots of varied intrinsic fluences 40% and 13% above the determined damage threshold are shown in Figs. 4.18a) and b), respectively. While the higher fluence caused an ablation of area with $\sim 140\,\mu m$ diameter, the fluence near the damage threshold modified the material over a smaller area with $50\,\mu m$ diameter. The ablated material irradiated by the lower fluence regrouped into a radially oriented structure, which is not the case in the higher fluence test. The morphologies of ablated sites were explained in study [255] using the electric field distribution showing multiple maximas within the films. However, for practical industrial applications of lasers, it is more relevant to study the interaction and resistance of optical materials irradiated with large numbers of pulses. As can be seen for instance from Figs. 4.16, 4.17 and 4.18, the surface modifications at higher numbers of pulses are significantly different from the material changes induced by single pulse.

4.5 Laser damage testing of monolayers at 150 ps

For the high-power laser community, laser damage resistance at a pulse duration close to 150 ps is critical since it is the regime in which dielectric coatings of pulse stretchers, components of chirped pulse amplification systems, operate. Laser damage tests at close to the 150 ps pulse duration were performed in studies [173, 256, 257]. The LIDT of broadband low dispersion mirrors in this regime was a topic of thin film damage competition at Laser Damage Conference in 2015. [258] Within the GREAT consortium, we had access to the LIDT station operating at a pulse duration of 150 ps. The station is located at Alphanov technology center and was described in Sec. 3.7.

4.5.1 Test procedure

The 150-ps station at Alphanov allowed us to test three magnetron sputtered coatings - Nb_2O_5, HfO_2 and SiO_2, whose surface was irradiated by the beam oriented at the normal incidence. The coating thickness was 150 nm for HfO_2 and SiO_2, whereas in the case of Nb_2O_5 it was 300 nm. On each tested sample, a tested zone schematically shown in Fig. 4.19a) was irradiated. The tested zones consist of lines scanned by the beam with experimental fluences ranging from 0.4 up to 14.6 J/cm^2. The distance between neighboring lines is always 200 µm. The schematic in Fig. 4.19b) corresponds to the 1st pretest done on Nb_2O_5.

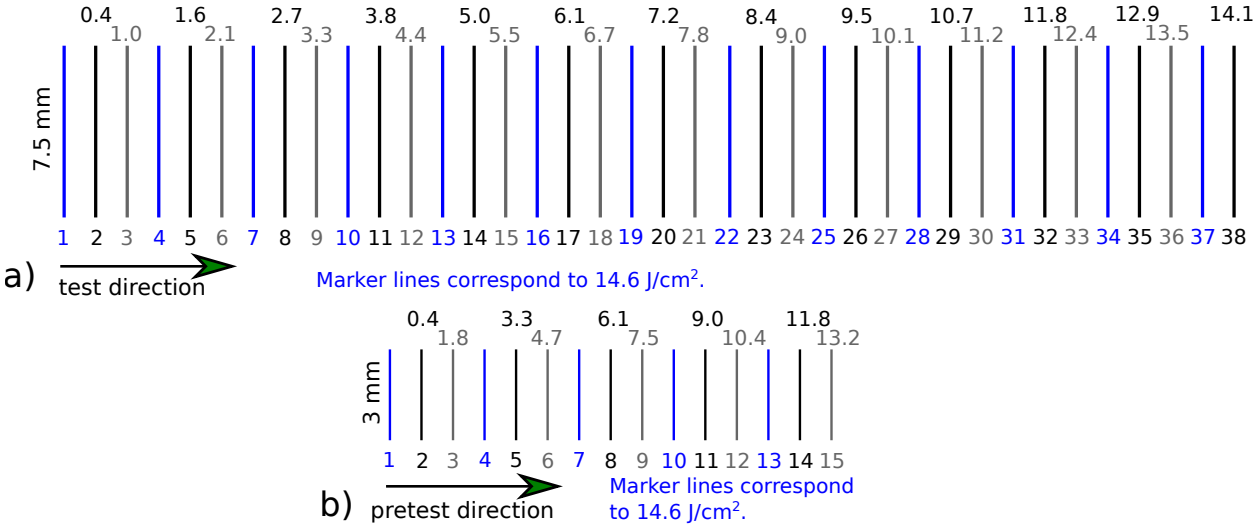

Figure 4.19: Diagram of the tested zones applied on the three samples - Nb_2O_5, HfO_2 and SiO_2. The numbers above the lines correspond to the used experimental fluence in J/cm^2. The schematic b) corresponds to the 1st pretest done on Nb_2O_5.

During the testing, the beam of 78 µm effective beam diameter ($d_f = 110$ µm at $1/e^2$) was moving with the v_s speed of 300 µm/s at the repetition rate $f_{rep} = 1$ kHz. Using these parameters we can determine the pulse overlap:

$$PO = \left(1 - \frac{v_s}{d_f \times f_{rep}}\right) = 99.73\%. \tag{4.2}$$

The test procedure is thus corresponding to multiple shot irradiation on the same site (Son1). In our case, the displacement between each shot is 0.3 µm. Within the beam diameter of 110 µm (at $1/e^2$), we have 367 shots. Since the beam is of near-Gaussian profile, we can say we have hundreds of shots per site.

4.5.2 Experimental results

Using the in-situ imaging device (Edmund Optics, camera BASLER acA1920-40um), a clear ablation was observed for Nb_2O_5 and HfO_2 but not in the case of SiO_2 even at the maximal experimental fluence of $14.6\,J/cm^2$. Examples of the damaged zones observed by in-situ camera are shown in Fig. 4.20. More detailed inspection was performed ex-situ at Institut Fresnel using differential contrast microscopy. Examples of ablated lines on Nb_2O_5 and HfO_2 observed ex-situ are shown in Fig. 4.21. In the case of Nb_2O_5, the ablation occurred even at the lowest fluence (0.4 J/cm2) used within the test. However, in the 1st pretest damage at this fluence was not found. Thus, the threshold for Nb_2O_5 is below the value of 0.4 J/cm^2 but we suppose near this value.

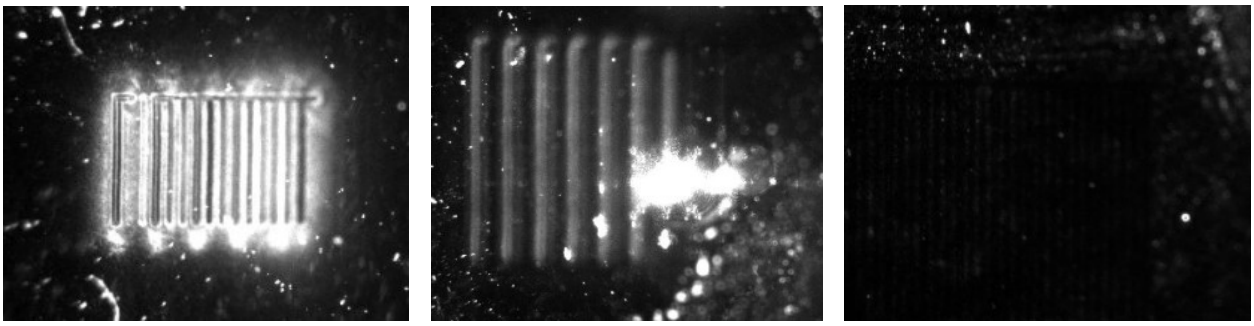

Figure 4.20: In-situ observation on Nb_2O_5 (a), HfO_2 (b) and SiO_2 (c). The distance between neighboring lines is always 200 µm.

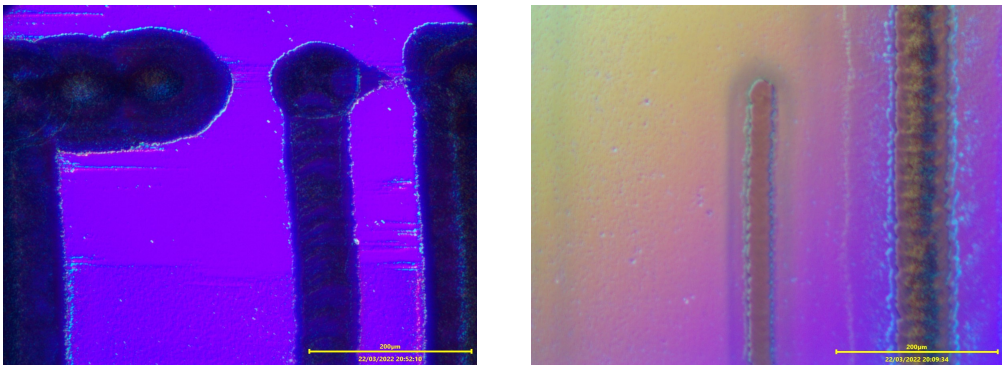

Figure 4.21: Images of irradiated lines captured via differential interference contrast microscope with 10X magnification: a) Nb_2O_5 (lines 1-4); b) HfO_2 surface containing ablated lines 21 and 22, see schematics in Fig. 4.19. The lowest fluence causing ablation of HfO_2 was $7.8\,J/cm^2$. For Nb_2O_5, we observed ablation even at $0.4\,J/cm^2$ but not in the case of pretest. In the case of SiO_2, no damage was observed ex-situ even at the maximum experimental fluence level of $14.6\,J/cm^2$.

For HfO_2, we plotted damage probability as a function of experimental fluence, see Fig. 4.22. At two fluences slightly higher than the determined threshold ($7.2\,J/cm^2$), the ablation started later than at the line beginning. In these cases, we plot rough relative proportion of the ablated part of line to the whole line.

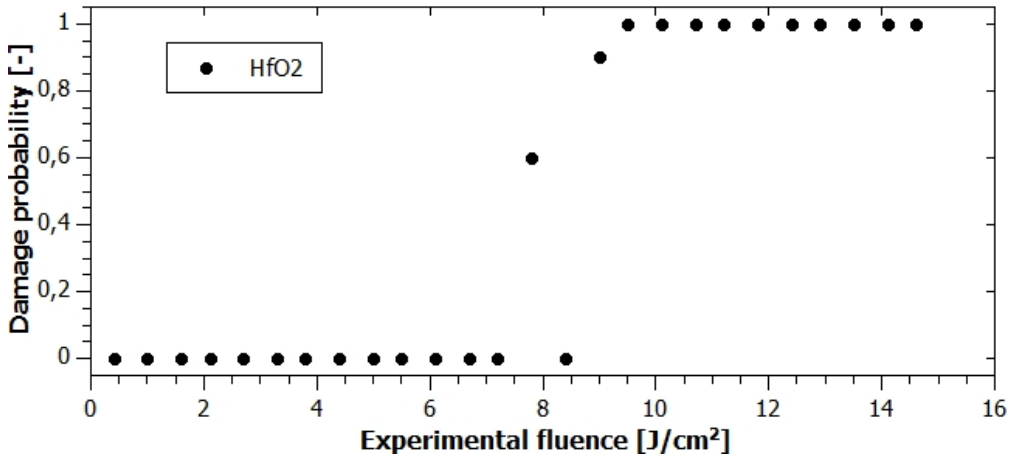

Figure 4.22: Damage results for HfO_2. The probabilities between 0 and 1 are rough estimation of relative part of given line showing ablation.

4.5.3 Summary and discussion

In summary, the tests performed with 150-ps 1030-nm 1-kHz LIDT station at ALPHANOV technological center confirmed significant difference in damage threshold resistance between Nb_2O_5, HfO_2 and SiO_2 coatings, see Fig. 4.23. We should mention that precedent lines could create debris and degrade damage resistance for further damage sites.

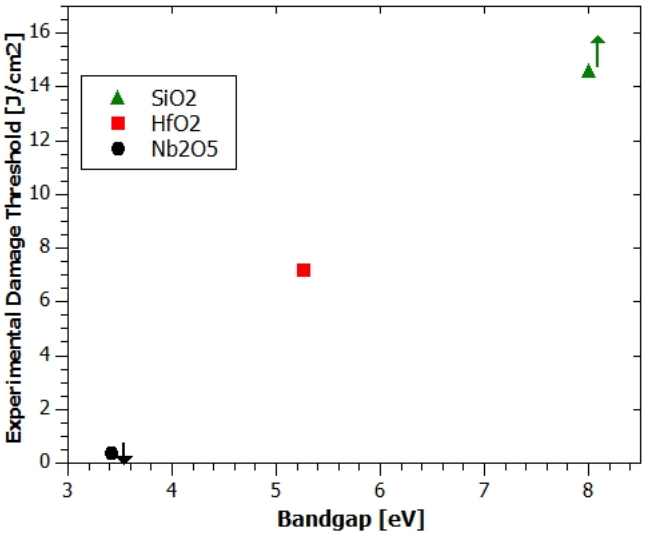

Figure 4.23: Evaluation of experimental damage (ablation) thresholds based on ex-situ differential interference contrast microscopy. Threshold for SiO_2 is higher than 14.6 J/cm^2, while the threshold for Nb_2O_5 should be lower than 0.4 J/cm^2.

The laser damage tests close to the 150 ps pulse duration were studied in [173, 256, 257]. Damage tests of mirrors at a pulse duration of 150 ps were a topic of thin film damage competition at the SPIE Laser Damage Conference in 2015. [258] The topic is of high interest since the broadband low dispersion mirrors

limit performance of short pulse lasers in terms of fluence and pulse shapes. Within the laser damage competition, the testing was done by raster scan procedure for selected coating materials, designs and deposition methods. The mirrors showed damage threshold fluences from 1 up to 15 J/cm^2, see Fig. 4.24. In work [256], the commercially-available broadband high-reflectors were tested by pulse duration of 150 ps with the raster scan procedure. The work showed damage thresholds ranging from 2 to 8 J/cm^2 with the best performance of hafnia/silica and tantala/silica coatings. Silica coatings produced by e-beam and PIAD processes were tested by pulses of 60 ps in the study [173]. At 10on1 testing, the coatings showed damage thresholds around 15 J/cm^2. In [257], a ramp step (R/1) procedure was applied on dielectric coating stacks with 30 ps pulse duration and showed damage threshold values ranging from 6 J/cm^2 (HfO_2/SiO_2 PIAD) up to 11 J/cm^2 (HfO_2/SiO_2 e-beam). Comparing our LIDT results at 150-ps regime with the available literature, the determined thresholds are comparable to the ones already published.

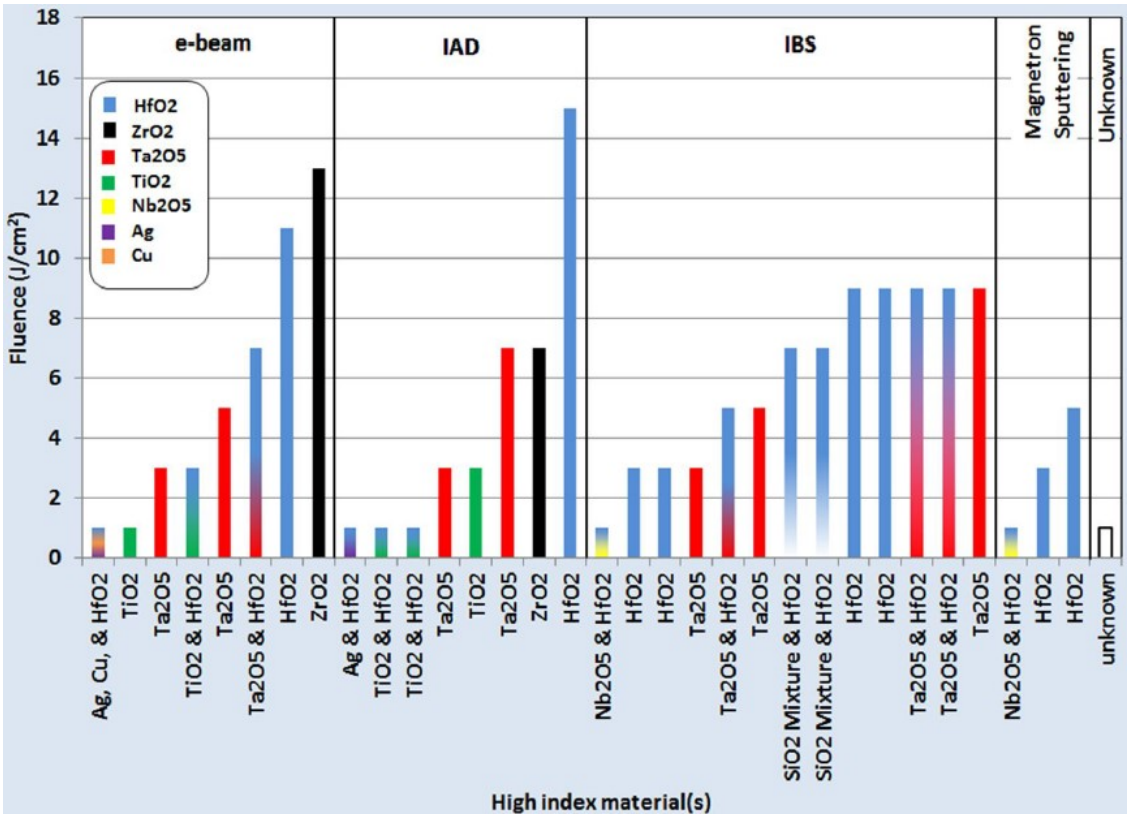

Figure 4.24: Experimental damage threshold fluence of the broadband short-pulse mirror coatings as a function of coating material and deposition process. Figure taken from [258].

4.6 Laser damage testing of monolayers at 100 fs

Using the LIDT setup at ELI Beamlines described in Sec. 3.8, we peformed tests of oxide coatings at 100-fs pulse regime for 1000on1 and 10000on1 procedures. For the given number of shots, a tested sample was irradiated 4x times with the same fluence on different spots. The irradiated sites were analyzed ex-situ using a 3D laser confocal microscope OLS5100 (Olympus) with 100x magnification objective. The damage threshold was determined as the highest fluence that is lower than the lowest fluence causing damage in the experiment.

To be consistent with error bars presented in this thesis, we take into account the 3σ deviations of effective beam area, pulse-to-pulse energies, and a half of pulse energy increment used in the LIDT testing. The values of the error bars calculated in this way are close to the value of 10.3% corresponding to the overall fluence measurement uncertainty determined by experienced laser operators at ELI Beamlines facility. The uncertainty takes into account random variations of pulse to pulse energy stability ($< 5\%$), pulse to pulse spatial profile stability (1.3%) as well as the systematic variations of energy meter calibration (3%), reference-absolute calibration ($< 5\%$) and spatial profile uncertainty (2%).

The tested samples were magnetron-sputtered monolayers of HfO_2, Nb_2O_5 and SiO_2 deposited on fused silica substrates. The physical thicknesses of HfO_2 and SiO_2 coatings were 150 nm whereas Nb_2O_5 was 200 nm thick.

The HfO_2, Nb_2O_5 and SiO_2 monolayers were tested in vacuum ($\approx 10^{-6}$ mbar) at the incidence angle of 45° by experimental fluences ranging from 0.01 up to 2.5 J/cm^2. The corresponding intrinsic LIDT fluences are shown in Fig. 4.25a). The highest damage threshold provides SiO_2 while Nb_2O_5 material is the most susceptible one to the damage initiation.

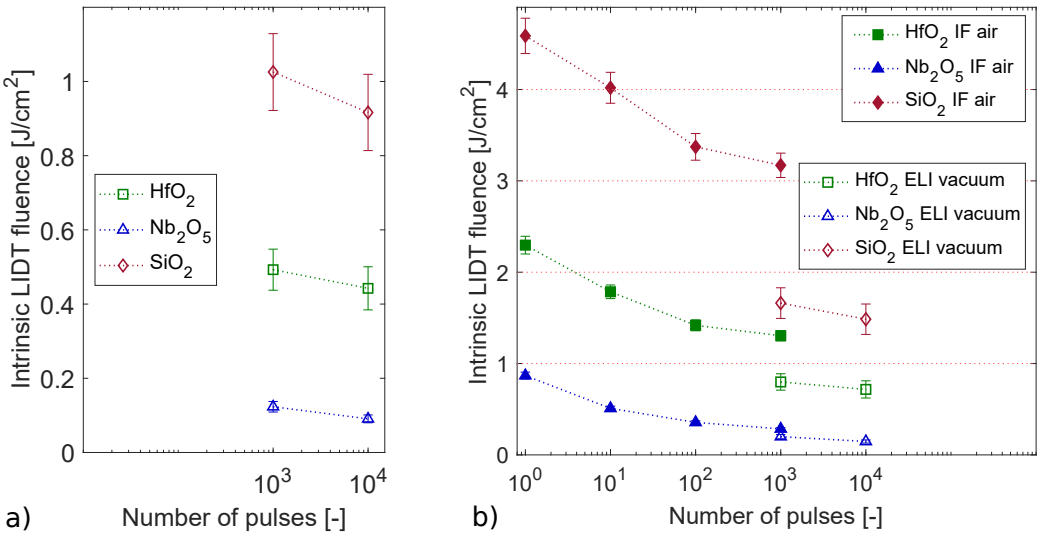

Figure 4.25: a) Intrinsic LIDT fluence of magnetron sputtered single layer coatings tested at 100 fs, 1050 nm in vacuum environment at 500 Hz repetition rate. The figure b) shows the LIDT rescaled to 500 fs pulse duration (τ) using the law: LIDT $\sim \tau^{0.3}$. The filled symbols correspond to the LIDT tests done with the 500-fs 1030-nm setup at Institut Fresnel working at a repetition rate of 10 Hz.

Using the scaling law of LIDT in dependence of τ pulse duration, i.e. $\sim \tau^{0.3}$ for oxides (see Sec. 2.3.4), we rescaled the determined LIDT to the pulse duration of 500 fs and compared these results to the ones obtained in air with 500-fs 1030-nm LIDT station at Institut Fresnel. The comparison is shown in Fig. 4.25b). The

1kon1 damage thresholds in vacuum are significantly lower than the thresholds of monolayers determined in air environment at a wavelength of 1030 nm.

The spots on samples tested for LIDT in ELI Beamlines facility were observed ex-situ via 3D confocal microscope which represented very sensitive tool for damage detection. Examples of damaged spots on Nb_2O_5, HfO_2 and SiO_2 monolayer are shown in Fig. 4.26.

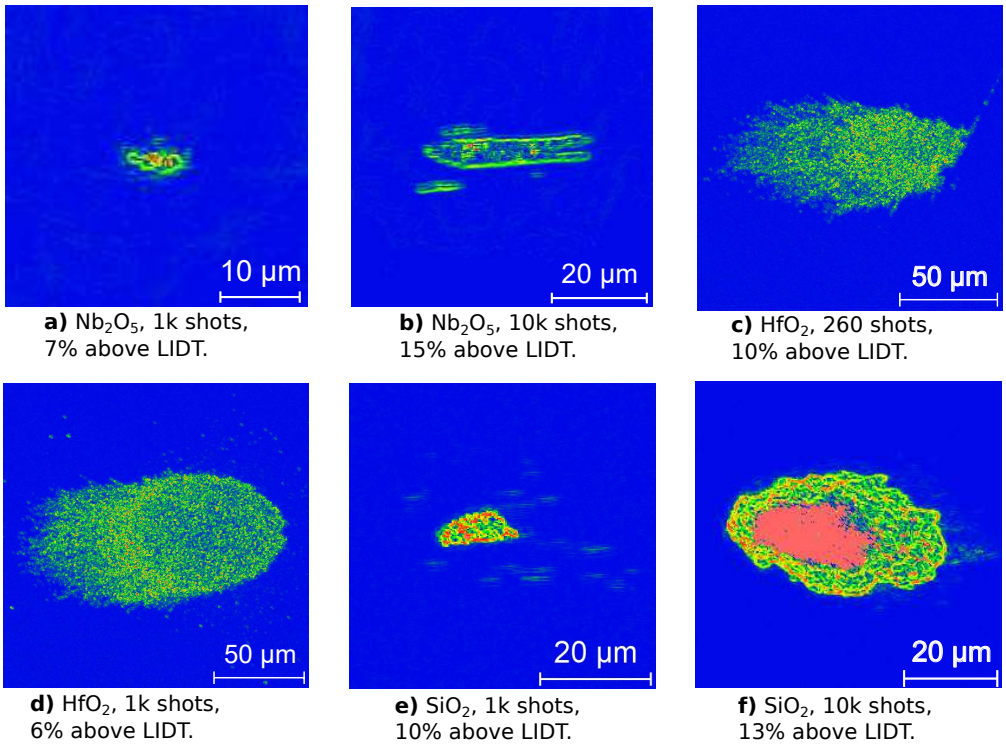

a) Nb_2O_5, 1k shots, 7% above LIDT.
b) Nb_2O_5, 10k shots, 15% above LIDT.
c) HfO_2, 260 shots, 10% above LIDT.
d) HfO_2, 1k shots, 6% above LIDT.
e) SiO_2, 1k shots, 10% above LIDT.
f) SiO_2, 10k shots, 13% above LIDT.

Figure 4.26: Damages on Nb_2O_5 (a-b), HfO_2 (c-d) and SiO_2 (e-f) oxide coatings induced by 100-fs 1050-nm 500 Hz laser. The images were captured ex-situ by OLS5100 confocal microscope.

At this point, it is not clear if the observed differences between results from ELI and IF are related to air/vacuum effect or to a metrology issue. [103] The work [154] done with IBS HfO_2 showed significant difference in LIDT tested at 50 fs in air and in vacuum ($\approx 10^{-7}$ mbar) for number of pulses larger than 1k, see Fig. 2.20 on page 59. For 1k pulses, the LIDT in air was by less 10 % higher than in vacuum, whereas for our test at 1k of pulses on magnetron-sputtered HfO_2, we have LIDT in air by $\approx 60\%$ higher than in vacuum. However, we should note that the comparison between studies is difficult since different testing conditions were applied (pressure, pulse duration, wavelength). From a metrology point of view, it was found that the scaling law is dependent on the temporal shape of the pulse. [103] In this work we did not go into such a deep analysis.

4.7 Laser damage testing at MHz repetition rate

The LIDT tests in high-repetition rate regime were performed with the station described in Sec. 3.9 on page 91. In these tests, we aimed to study the effect of number of pulses on the LIDT of dielectric thin films used in optical components. The high-repetition rate of used laser source allows to test films with high numbers of pulses in a short time. This regime is of interest for the industrial application related to GREAT project.

By contrast, to reach a low number of pulses is more difficult with the laser since the pulse picking for single pulse extraction is not enabled. In our high-repetition rate LIDT setup, the minimum number of used pulses is limited by an external mechanical shutter whose shortest opening time is 10 ms. Therefore, to get minimum number of pulses, we preferred the lowest accessible repetition rate of the LIDT station - 500 kHz. Another reason for using this repetition rate was to maintain the mechanical shutter undamaged after exposure to pulses at a wavelength of 515 nm.

Within this high-repetition rate LIDT campaign, each spot on a tested sample was irradiated by multiple pulses whose energy was regulated by the HWP position which was kept within the irradiation on a given site. For one attenuator position, the irradiation was usually repeated at 5 spots. The spot-spot distance was 500 µm. The used definition of LIDT was the highest used fluence that is lower than the minimum fluence causing damage. The damage detection was performed in-situ using BXFM Olympus optical microscope.

Coating material	Nb_2O_5			$HfO_2^\star$	SiO_2
Layer thickness	150 nm	300 nm	450 nm	500 nm	450 nm
n @515 nm	2.39			2.06	1.49
EFI max. (S-45)	0.32	0.31	0.51	0.42	0.50
Rep. rate	500 kHz			0.5–1.56 MHz	0.5–2.7 MHz

Table 4.3: Dielectric monolayers used for high-repetition rate LIDT testing at 45° angle of incidence with S-polarized beam (TE). EFI means Electric Field Intensity, n is the refractive index. All samples were produced by magnetron sputtering on fused silica substrate of 2 mm thickness and 1 inch diameter. $^\star HfO_2$ is not pure but contains $\sim 1-2$ % of SiO_2 admixture. [230]

4.7.1 Nb_2O_5

At the lowest repetition rate of the laser source - 500 kHz, we tested three magnetron-sputtered Nb_2O_5 monolayers of different thicknesses ranging from 150 nm to 450 nm, see Table 4.3. The tests were done for a broad range of number of pulses from 5000 up to 30 millions.

The LIDT results plotted in Fig. 4.27 indicate discrepancies between the intrinsic LIDT values of the three Nb_2O_5 samples. In Fig. 4.28, we compare electric field intensity distributions between the Nb_2O_5 monolayers. The 300 nm and 150 nm thick Nb_2O_5 show very similar electric field intensity maxima while the LIDT found for 300 nm thick Nb_2O_5 is higher than the thresholds of 150 nm coating. Thus, the differences between LIDT of Nb_2O_5 monolayers cannot be explained by electric field intensity distribution.

In study [259], it has been found there are some differences in absorption between the films with different thicknesses deposited by the same magnetron-sputtering machine. Therefore it is possible that the films have also different properties as regards the sub-ps LIDT, the films could have different non-linear absorption. In the high-repetition rate sub-ps regime, the laser radiation absorption is of high importance since the process can result in material heating and catastrophic damage. Examples of damaged spots on Nb_2O_5 coating are shown in Figs. 4.29a) and b).

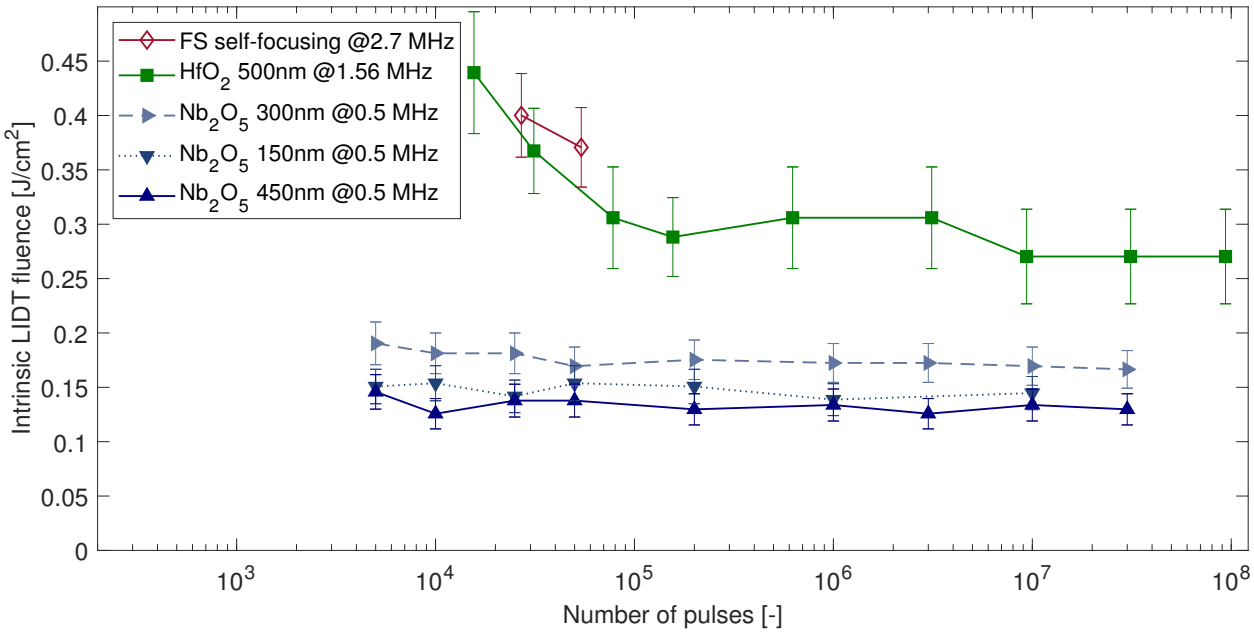

Figure 4.27: LIDT of Nb_2O_5 and HfO_2 monolayers tested at 0.5 MHz and 1.5 MHz repetition rates, respectively. The monolayers differed in their thicknesses as it is indicated in the legend. The determination of LIDT of SiO_2 thin film was not possible due to self-focusing effect in fused silica substrate occuring at 2.7 MHz. The error bars correspond to sum of 3σ deviations of beam size near focal plane, pulse-to-pulse energies and a half of energy increment in the test.

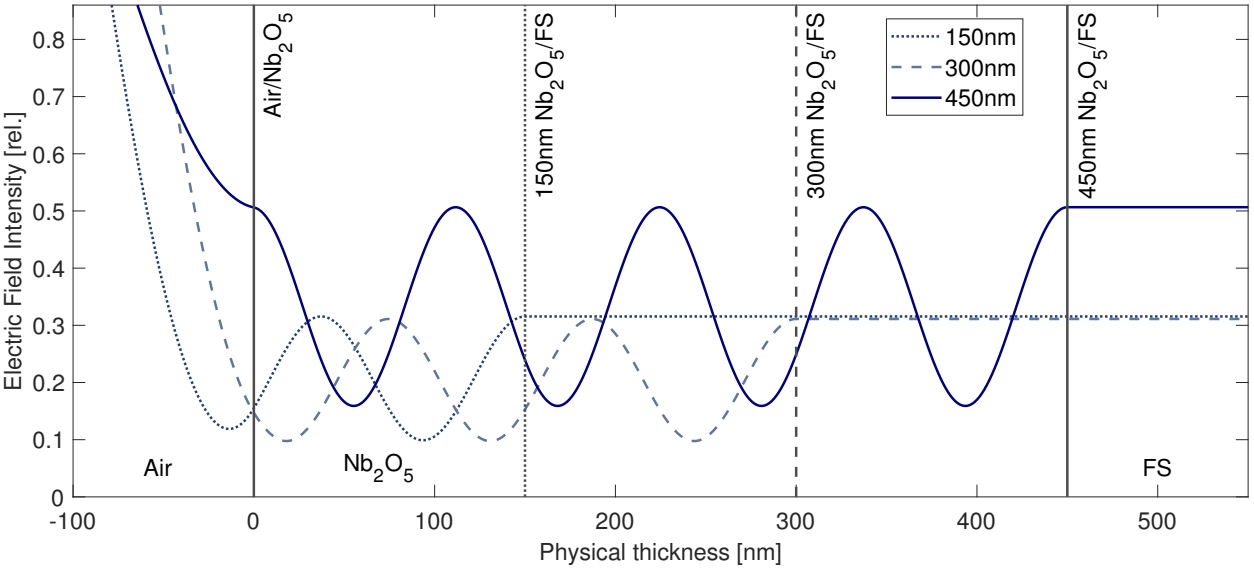

Figure 4.28: Electric Field Intensity distribution calculated for three Nb_2O_5 thin films of different physical thicknesses. The vertical lines correspond to interfaces between referenced environments.

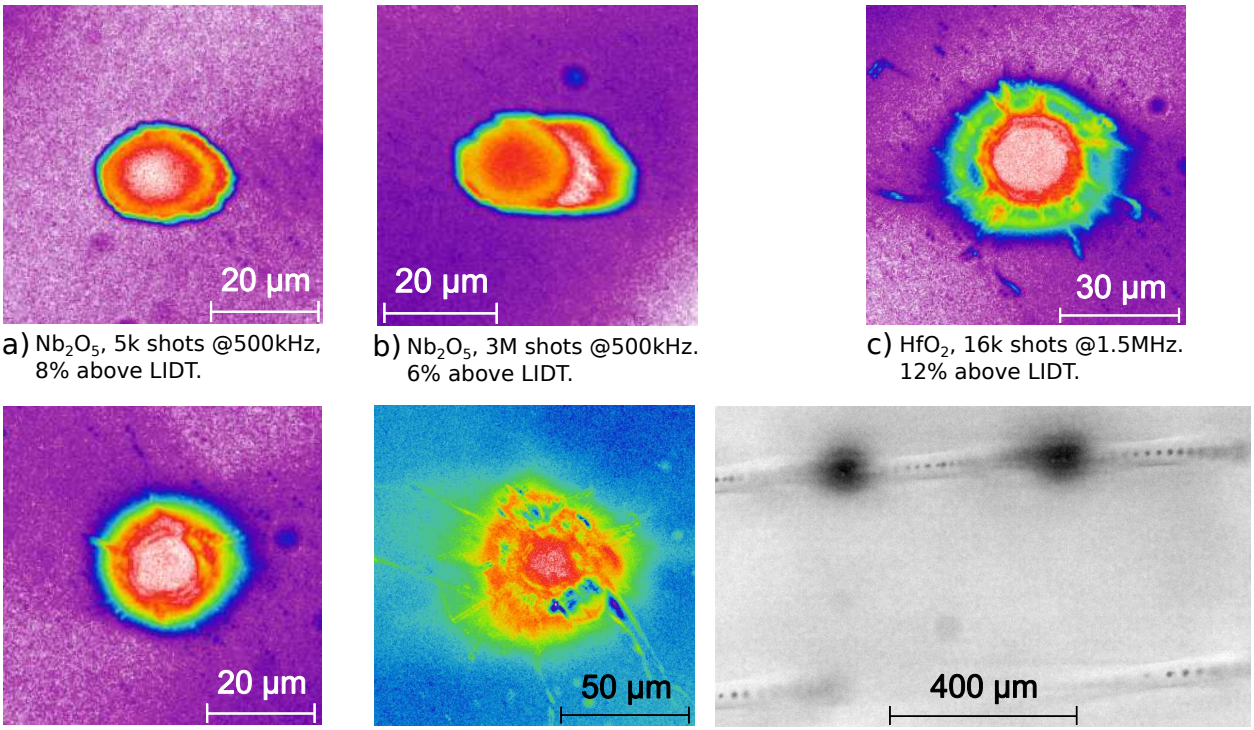

a) Nb_2O_5, 5k shots @500kHz, 8% above LIDT.

b) Nb_2O_5, 3M shots @500kHz. 6% above LIDT.

c) HfO_2, 16k shots @1.5MHz. 12% above LIDT.

d) HfO_2, 156k shots @1.5MHz. 14% above LIDT.

e) SiO_2, 27k shots @2.7MHz. 5% above LIDT.

f) Fused silica 2mm, ≥27k shots @2.7MHz.

Figure 4.29: Damaged spots on oxide coatings: 150 nm thick Nb_2O_5 (a-b), HfO_2 (c-d) and SiO_2 (e). The image f) corresponds to ex-situ observation revealing self-focusing inside fused silica substrate irradiated at 2.7 MHz. More information of coatings is given in Table 4.3.

4.7.2 HfO_2

The LIDT tests with HfO_2 monolayer containing a 1-2% admixture of SiO_5 were performed at 1.56 MHz. This repetition rate was used since at the lower repetition rate of 500 kHz, the damage formation was not observed even at a maximum pulse energy of 14 µJ corresponding to an intrinsic fluence of 0.52 J/cm^2. The tests at 1.56 MHz were performed for a broad range of number of pulses from 15600 up to 100 milions and the determined intrinsic LIDT fluences are shown in the Fig. 4.27. As opposed to the results with Nb_2O_5 samples irradiated at 500 kHz, these tests withf HfO_2 indicate effect of incubation between 15k and 100k. Starting at roughly 100k pulses, the damage threshold of HfO_2 for increased pulse numbers remains the same. Examples of damaged spots on HfO_2 caused by 16k and 156k shots are shown in Figs. 4.29c) and d), respectively.

4.7.3 SiO_2

In the case of 450 nm thick SiO_2 single layer coating, we did not find conditions allowing to study its LIDT using the MHz station. Already the in-situ surface observation indicated a different damage morphology (Fig. 4.29e) compared to that of Nb_2O_5 (Fig. 4.29a-b) or HfO_2 (Fig. 4.29c-d). The ex-situ inspection of spots irradiated at 2.7 MHz repetition rate showed damages inside the fused silica substrate (Fig. 4.29f) and suggests the self-focusing effect in the substrate as a possible explanation for damage initiation that could affect the resistance of SiO_2 coating.

Self-focusing can be described as a total collapse of the beam whose radius is reduced in the material. Therefore, the optical intensity increases which leads to the stronger self-focusing. The mechanism can continue up to the moment, when the optical material is damaged.

The question arising from self-focusing in fused silica at 515 nm is if it could be predicted theoretically. The self-focusing process can occur in the case that the optical power is higher than the self-focusing power P_{SF}, which is for a linearly polarized light defined using the Eq. (3.27) on page 78. [260] If we use the fused silica values of linear refractive index, $n = 1.46$ at 515 nm [261], and non-linear refractive index, $n_2 = (3 \pm 0.5) \times 10^{-20}$ m^2/W at $\lambda = 514$ nm [262], the self-focusing peak power P_{SF} is around 900 kW. Since the average power was around 25 W when the damage in fused silica was observed, the pulse energy of used laser working at 2.7 MHz repetition rate was around 9 µJ. Pulse duration should be 700 fs according to the laser manufacturer. For the mentioned values, the calculated peak power is around 13 MW which is higher than the P_{SF} power (900kW) and thus the self-focusing could occur.

We should note that the same peak power exists also in HfO_2 and Nb_2O_5, for which we did not observe any morphologies indicating self-focusing. We assume that self-focusing could be affected by a combination of nonlinear and thermal processes.

4.7.4 Discussion and conclusion of MHz tests

In the MHz repetition rate sub-ps regime, there is only a limited number of publications on LIDT of optical coatings. For $\sim 5 \cdot 10^{10}$ pulses at a repetition rate of 75 MHz and duration of 105 fs, it has been shown that uncoated niobate crystal has by 6% higher LIDT (0.84 mJ/cm^2) than the one coated by Nb_2O_5 antireflective coating (0.79 mJ/cm^2). [263] The work showed also significant impact of repetition rate on surface LIDT of Nb_2O_5 coated lithium niobate. Its LIDT at 75 MHz was $\sim 30\times$ lower that that at 100 kHz repetition rate.

The damage resistance of multilayer coatings composed of TiO_2, Ta_2O_5, HfO_2, or Al_2O_3 as high-index materials and SiO_2 as low index materials was studied at a repetition rate of 11.5 MHz. [264] At a wavelength of 1030 nm and a pulse duration of 1 ps, the linear bandgap dependency on intrinsic damage threshold was verified. The results suggest that thermal effects should not play a substantial role in the ultrashort pulse damaging process even at MHz repetition rates.

At a pulse duration of 120 fs, comparative measurements on a dielectric high reflector, a chirped mirror and metallic mirrors showed by at least a factor of 2.7 lower LIDT at 4.3 MHz than at 1 kHz. [265] The result was attributed to damage formation by thermal mechanisms whose presence was supported by heat transfer simulations.

The above-mentioned studies on the damage of optical coatings in MHz repetition rate regime indicate the complexity of physical processes in high-repetition rate regime. We should emphasize that it is difficult to compare the MHz studies because they differ in many parameters. For the development of laser components used in high-repetition rate regime, it is thus necessary to perform tests in conditions as close as possible to their applications in the laser systems.

The LIDT results in MHz repetition rate obtained in this manuscript are among the first ones for oxide optical coatings. The findings in this regime are critical for the development of high-repetition-rate ultrashort-pulse laser systems.

Since our results showed the damages inside fused silica substrate, the MHz station cannot be used for LIDT testing of SiO_2 thin film placed at the focal length from focusing lens. Another disadvantage of the used setup is that the effective beam diameter at the focal plane is only 45 µm which makes the beam profiling difficult even with high resolution cameras. For the sensor of 6.45 µm, we can calculate the maximum pixel intensity error, whose calcul was described in Sec. 3.4.7. In the case of an intensity peak at the pixel corner,

we get using the Eq. (3.32) the pixel intensity value which is 5% lower than the intensity peak of the Gaussian beam. By contrast, the pixel size error, calculated using the Eq. (3.31) is 29%. The difficulty with beam profile measurement may lead to erroneous determination of LIDT fluences.

Due to these limitations and the wavelength being unimportant for the GREAT project, we decided to move the dielectric tested samples from focal plane and to use the MHz experimental station for laser-induced contamination (LIC) tests with lower fluences. The LIC of oxide thin films will be the topic of Chapter 6.

4.8 Conclusion

In this chapter, we investigated monolayers of dielectric coatings that are used in optical components, including the designs of GWS. We firstly introduced deposition methods that are used to produce the coatings. Afterwards, we provided characterization of magnetron-sputtered amorphous oxides (HfO_2, Nb_2O_5, SiO_2) and PLD crystalline sesquioxides (Sc_2O_3, Y_2O_3, Lu_2O_3). We studied refractive indices and bandgaps of these materials. In the case of PLD films, we provide characterization done via XRD to determine their level of homogeneity. The information reported here on the characterisation of the optical properties of coating materials is an important input for the design of optical components developed within the GREAT project. The material characterization will specify the design constraints and options for the GWS and related application areas.

An essential part of the characterization of coatings for optical components is the testing of their damage thresholds. Thus, we devoted the remaining parts of this chapter to the LIDT testing of coating materials. With the 500-fs 1030-nm LIDT setup at Institut Fresnel we tested magnetron-sputtered amorphous oxides (HfO_2, Nb_2O_5, SiO_2) and PLD crystalline sesquioxides (Sc_2O_3, Y_2O_3, Lu_2O_3). The LIDT results of these materials are compared in Fig. 4.9. The magnetron-sputtered oxides are well-known materials that are used in optical components in sub-picosecond and picosecond regime. [76] In this work we found that also PLD crystalline sesquioxides have a potential for high-power resistant optical components for ultrashort-pulse regime. The well-grown PLD Sc_2O_3, Y_2O_3 and Lu_2O_3 show LIDT values at 500-fs 1030-nm close to the ones of magnetron-sputtered HfO_2 coating.

In the case of magnetron-sputtered oxides, we reported the LIDT results of dielectric oxides obtained by testing in total with five laser sources. The lasers used for testing were situated at Institut Fresnel and at the locations of GREAT project partners (HiLASE, Alphanov, ELI Beamlines). The laser sources allowed us to test oxides using a pulse duration ranging from 100 fs up to 150 ps with the main wavelength of 1 µm. Laser sources permitted us to test oxides with pulse durations from 100 fs to 150 ps with a main wavelength of 1 µm. A more detailed description of the LIDT stations used is given in Chapter 3.

In Fig. 4.30 we are comparing LIDT results of magnetron-sputtered oxides which were obtained using five laser sources. For pulses shorter than 10 ps, we show results in intrinsic LIDT, while the result at 150 ps is given in experimental fluence. The LIDTs correspond to the number of pulses in the order of 1k (or the closest determined value). It is 1k in the case of ELI, IF 10-Hz and HiLASE stations, whereas for Alphanov station we used 370 shots. The tests done with high-repetition rate setup at Institut Fresnel (IF MHz) enabled to compare data for Nb_2O_5 tested by 5k of shots and HfO_2 tested by 15k of shots. Aside from the IF MHz setup, which generated pulses at 0.5 µm with 500 kHz for Nb_2O_5 and 1.56 MHz for HfO_2 tests, the other setups emitted pulses at 1 µm with repetition rates less than or equal to 1 kHz.

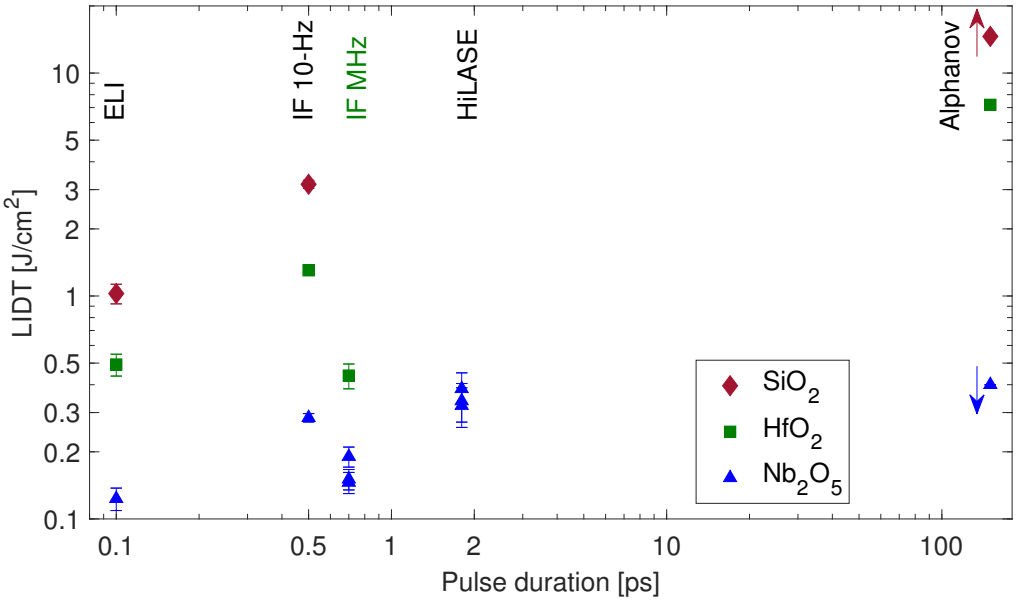

Figure 4.30: LIDTs of magnetron-sputtered oxide monolayers tested by five LIDT stations. The values from stations in ELI, HiLASE and from 10-Hz laser at Institut Fresnel (IF 10-Hz) correspond to 1k pulses, whereas the tests at Alphanov were done with ≈ 370 pulses and the tests with high-repetition rate MHz setup at Institut Fresnel (IF MHz) with 5k pulses for Nb_2O_5 and 15k pulses for HfO_2. Results for pulse durations shorter than 10 ps are given in intrinsic LIDT, whereas the LIDT value at 150 ps corresponds to experimental LIDT fluence. Except of IF MHz setup generating pulses at a wavelength of 0.5 µm with 500 kHz (Nb_2O_5) and 1.56 MHz (HfO_2), the setups emitted pulses at 1 µm with repetition rate ≤ 1 kHz. The LIDTs of SiO_2 and Nb_2O_5 at 150 ps regime were not detemined but the arrows indicate that LIDT of SiO_2 is higher than 14.6 J/cm^2 and LIDT of Nb_2O_5 is lower than 0.4 J/cm^2. The LIDT tests at HiLASE centre were performed with the effective beam diameter of 315 µm,[8] whereas other lasers had effective beam diameter ≤ 130 µm, see overview of laser beam parameters in Fig. 3.28.

Among the magnetron-sputtered materials, the highest damage threshold shows SiO_2, see Fig. 4.30. This statement is valid in all regimes, in which it was possible to test this material, i.e. at 100-fs, 500-fs and 150-ps.[9] When comparing the high-index materials, HfO_2 is shown to be more resistant, and this is true in all testing regimes, in which comparison with Nb_2O_5 is possible, i.e., at 100-fs, 500-fs, 700-fs, and 150-ps. Based on these results obtained with different LIDT setups, we recommend SiO_2 as a low-index and HfO_2 as a high-index coating material for use in high-power resistant optical components that will be implemented in sub-picosecond and picosecond systems such as the ones being developed in GREAT project. [8, 9]

[8] At the time of LIDT campaign at HiLASE, i.e. 2 months after the beginning of PhD, the only material available for LIDT testing was Nb_2O_5 of various thicknesses.

[9] In tests with high-repetition rate laser (IF MHz setup) we faced to the issue of self-focusing in fused silica, see Sec.4.7.

Chapter 5

Laser damage of mirrors and gratings

Dielectric coatings are an essential part of mirrors and gratings, whose damage resistance often represents the limiting parameter for power scaling of laser systems. In this chapter, we investigate the behaviour of reflective and diffractive optical components based on dielectric oxide coatings studied in the previous chapter. The experimental LIDTs of mirrors and gratings tested here will be compared to the theoretical LIDT values calculated using the simulation of the electric field intensity (EFI) distributions and knowledge of the intrinsic LIDT values of optical thin-film materials involved in the component's designs. Results of this work should be used for optimization of the components designed and fabricated in the GREAT consortium.

For the calculation of the EFI distributions within multilayer designs of mirrors, we will use the transfer matrix method that will be introduced in the first section of this chapter. We will then apply the matrix method for the highly reflective mirrors designed within the GREAT consortium. The predicted LIDTs of mirrors will be compared to experimental results obtained from tests performed by sub-ps pulses emitted at near-infrared wavelength. The tests of the mirrors were done with two LIDT stations: 500-fs 1030-nm setup at Institut Fresnel (Sec. 3.2) and 100-fs 1050-nm station at ELI Beamlines (Sec. 3.8). We will present an overview of LIDT results on mirrors for applied numbers of pulses ranging from 1 to 10k.

Within the GREAT project, we use either HfO_2 or Nb_2O_5 as high-index material in multilayer coatings. The selection of material is derived from the intended application. The material with excellent LIDT, HfO_2, is preferred for pulse compressive gratings that suffer from high concentration of pulse energy. By contrast, for laser systems operating in CW regime, in which GWS will be used for wavelength multiplexing, spectral stabilization or polarization conversion, the LIDT is less critical.[1] For these applications, the selected high-index material is thus Nb_2O_5, which has the advantage of a higher refractive index compared to HfO_2. Thus, to achieve the same level of reflectivity, a multilayer stack based on Nb_2O_5/SiO_2 layers requires lower number of layers than the HfO_2/SiO_2 design. The lower number of layers is advantageous since it reduces stress in the stack. A possible compromise is a combined multilayer, with HfO_2/SiO_2 in the closest layers to the air which show the high electric field intensities, and with Nb_2O_5/SiO_2 layers near the substrate. Such a design has both the high LIDT and the reduced stress due to its lower number of layers. However, the deposition of such advanced designs is more challenging.

In the fabrication process of GWS, a necessary phase is the etching of the grating pattern. The etching represents a separate technological discipline with variety of lithographic methods, which have their own material selection preferences. In this work, we will present a study of the effect of optical surface treatment

[1] The experimental setup for LIDT testing at CW regime was not available during the PhD because of mobility restrictions linked to covid19.

by Ti adhesion promoter and Cr hard mask on the LIDT. These materials are coated on optical surfaces in order to facilitate the process of etching. The Ti promoter is used to adhere photoresist to fused silica in order to ease the etching of shallow gratings in fused silica. The purpose of the Cr mask is to improve etching selectivity in the case of deep grating profiles.

Finally, we will estimate the LIDT of selected GWS designs that employ SiO_2 as a low-index and HfO_2 or Nb_2O_5 as high-index coating materials. In the GWS analyzed here, the grating profiles are etched in the high-index coating materials at the surface and the created structures are frequently the weakest parts of the designs, in which the damage is initiated. The findings of the presented study could be used to improve the next generation of GWS designs and production procedures. The experimental results on LIDT of GWS were not available at the time of writing this manuscript due to delays related to covid19 and technical issues with laser.

5.1 Electric Field Intensity in multilayer coatings

Functional multilayer stacks have a wide range of applications, including optical filters, antireflection coatings, and Fabry-Pèrot interferometers. We will briefly introduce here the transfer matrix method (TMM) which is used to anticipate the behavior of multilayer thin-film structures in a given configuration. The TMM method is based on the solution of frequency domain Maxwell's equations for a linear, non-dispersive, homogeneous and isotropic medium without free charges. The method describes light propagation across a multilayer system, given the following assumptions. [266]

- The thin film is considered as an optically isotropic medium with a refractive index n.
- The changes of refractive index occurs in the direction normal to the multilayer structure – normal inhomogeneity.
- A layer in the propagation axis is defined by two planes. The layer's other dimensions are infinite.
- The size of a layer's thickness is comparable to the wavelength of the incoming light.
- The incident wave is plane, monochromatic, and polarized linearly.
- The roughness of the substrate and the interfaces between layers are ignored.

In such conditions, the electric field is the solution of the Helmholtz equation that is derived from the Maxwell equations:

$$\Delta\mathcal{E} + \left|\vec{k}\right|^2 \mathcal{E} = 0. \tag{5.1}$$

The symbol $\mathcal{E}$ means the electric field and $\vec{k}$ is the wave vector, with

$$\left|\vec{k}\right|^2 = \omega^2\mu\varepsilon, \tag{5.2}$$

where ω means angular frequency, μ permeability and ε dielectric permittivity.

To study the electric field intensity distribution inside multilayer structure irradiated by the electromagnetic radiation, let us consider an interference stack consisting of N layers. An illustrative diagram of a stack with incoming wave $\vec{k}_0^+$ is given in Fig. 5.1. Each layer j has an refractive index n_j and a physical thickness d_j. The description of the interferential system requires calculation in terms of the amplitude of the electric field. For the calculation, a harmonic wave is considered. As shown in Fig. 5.1, the electric field $\mathcal{E}_j$ in layer j can be described as the sum of a forward-propagating component $\mathcal{E}_j^+$ and a backward-propagating component $\mathcal{E}_j^-$, i.e. $\mathcal{E}_j(z) = \mathcal{E}_j^+(z) + \mathcal{E}_j^-(z)$.

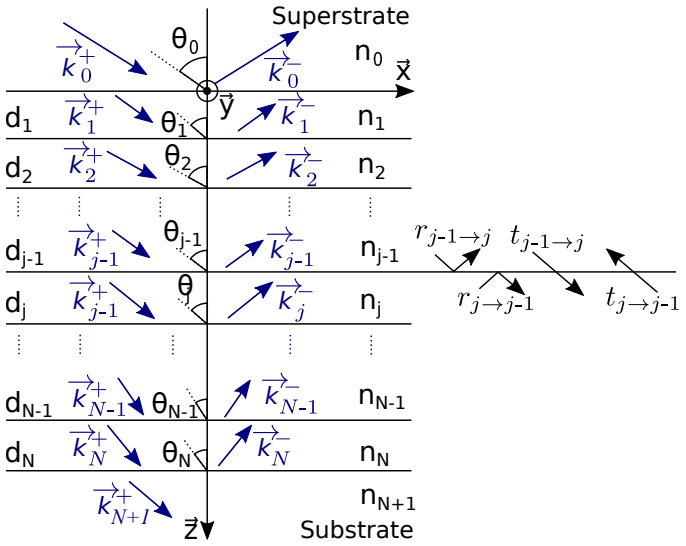

Figure 5.1: Diagram of interferential stack consisting of N layers. Incoming wave is $\vec{k}_0^+$. In layer j of refractive index n_j and physical thickness d_j, the electric field $\mathcal{E}_j$ is the sum of a forward-propagating component $\mathcal{E}_j^+$ and a backward-propagating component $\mathcal{E}_j^-$. θ_j means an angle of incidence in j-labeled layer. When falling on an interface, a part of electric field is reflected (and transmitted) with a reflection (transmission) coefficient in amplitude noted r and t respectively. The blue arrows indicate propagation vectors.

The calculation of the properties of the multilayer structure is based on the matrix method. [220] The way the waves interact is described by a matrix for a given environment, in which the waves pass (Environment matrix - C), and a matrix for the interface between two environments (Interface pass matrix - T).

5.1.1 Environment matrix

Solution of Helmholtz equation (Eq. 5.1) has the form of entire electric field $\mathcal{E}_j(z)$ containing the forward-propagating $\mathcal{E}_j^+(z)$ and backward-propagating $\mathcal{E}_j^-(z)$ components:

$$\begin{aligned}\mathcal{E}_j(z_j) &= \mathcal{E}_j^+(z_j) + \mathcal{E}_j^-(z_j)\\ &= A_j^+(z_j)e^{\imath k_j cos(\theta_j) z_j} + A_j^-(z_j)e^{-\imath k_j cos(\theta_j) z_j}\\ &= A_j^+(z_j)e^{\imath k_j cos(\theta_j) z_{j-1}} e^{\imath k_j cos(\theta_j) d_j} + A_j^-(z_j)e^{-\imath k_j cos(\theta_j) z_{j-1}} e^{-\imath k_j cos(\theta_j) d_j}\\ &= \mathcal{E}_j^+(z_{j-1})e^{\imath k_j cos(\theta_j) d_j} + \mathcal{E}_j^-(z_{j-1})e^{-\imath k_j cos(\theta_j) d_j},\end{aligned} \tag{5.3}$$

where θ_j means an angle of incidence in j-labeled layer, see Fig. 5.1. From Eq. (5.3), we can express relations between electric field components $\mathcal{E}_j^+(z_j), \mathcal{E}_j^-(z_j)$ and $\mathcal{E}_j^+(z_{j-1}), \mathcal{E}_j^-(z_{j-1})$ in matrix termed "Environment matrix (C)":

$$\begin{pmatrix}\mathcal{E}_j^+(z_j)\\ \mathcal{E}_j^-(z_j)\end{pmatrix} = \begin{pmatrix}e^{\imath k_j cos(\theta_j) d_j} & 0\\ 0 & e^{-\imath k_j cos(\theta_j) d_j}\end{pmatrix} \begin{pmatrix}\mathcal{E}_j^+(z_{j-1})\\ \mathcal{E}_j^-(z_{j-1})\end{pmatrix} = C \cdot \mathcal{E}_j(z_{j-1}). \tag{5.4}$$

5.1.2 Interface pass matrix

The interface pass matrix can be derived from conditions of continuity of tangential components:

$$\mathcal{E}_{j-1}^{tan}(z_{j-1}) = \mathcal{E}_{j}^{tan}(z_{j-1}) \tag{5.5a}$$

$$\mathcal{H}_{j-1}^{tan}(z_{j-1}) = \mathcal{H}_{j}^{tan}(z_{j-1}) \tag{5.5b}$$

The tangential components of magnetic fields in Eq. (5.5b) can be expressed using product of vectors of electric field and $\vec{z}$ vector multiplied by effective refractive index: $\widetilde{n}_j$:

$$\mathcal{H}_{j}^{tan} = \widetilde{n}_j \cdot \vec{z} \times \mathcal{E}_{j}^{tan} \tag{5.6}$$

Here, we should remind that the effective refractive indices differ between S (n_j^S) and P (n_j^S) polarizations:

$$\widetilde{n}_j^S = \frac{\alpha}{\omega\mu}, \tag{5.7a}$$

$$\widetilde{n}_j^P = -\frac{\omega\varepsilon}{\alpha}, \tag{5.7b}$$

where α is the component of the wave vector $\vec{k}$ that is perpendicular to the interfaces (along $\vec{z}$ axis in Fig. 5.1).

Then by dividing Eq. (5.6) using $\vec{z}\times$ and several arithmetic operations, we obtain using Eq. (5.5a) the relations between $\mathcal{E}_j^+(z_{j-1})$, $\mathcal{E}_j^-(z_{j-1})$ and $\mathcal{E}_{j-1}^+(z_j)$, $\mathcal{E}_{j-1}^-(z_{j-1})$ components that can be expressed in matrix termed "Interface pass matrix (T)":

$$\mathcal{E}_j(z_j) = \begin{pmatrix} \mathcal{E}_j^+(z_j) \\ \mathcal{E}_j^-(z_j) \end{pmatrix} = \frac{1}{2\widetilde{n}_j} \begin{pmatrix} \widetilde{n}_j + \widetilde{n}_{j-1} & \widetilde{n}_j - \widetilde{n}_{j-1} \\ \widetilde{n}_j - \widetilde{n}_{j-1} & \widetilde{n}_j + \widetilde{n}_{j-1} \end{pmatrix} \begin{pmatrix} \mathcal{E}_j^+(z_{j-1}) \\ \mathcal{E}_j^-(z_{j-1}) \end{pmatrix} = T \cdot \mathcal{E}_j(z_{j-1}). \tag{5.8}$$

5.1.3 Matrix of complete stack

As the electric field passes through the individual optical elements, we have to multiply the matrices of the elements. Matrix of complete stack M is matrix containing all interface pass and environment matrices:

$$\mathcal{E}_0 = T_{0\to1} \cdot C_{0\to1} \cdot T_{1\to2} \cdot C_{1\to2} \cdot .... \cdot C_{N\to N+1} \cdot T_{N\to N+1} \cdot \mathcal{E}_{N+1} = M \cdot \mathcal{E}_{N+1}. \tag{5.9}$$

It is useful to express the matrix of complete stack in the simplified form:

$$\begin{pmatrix} \mathcal{E}_0^+ \\ \mathcal{E}_0^- \end{pmatrix} = \begin{pmatrix} m_{11} & m_{12} \\ m_{21} & m_{22} \end{pmatrix} \begin{pmatrix} \mathcal{E}_{N+1}^+ \\ \mathcal{E}_{N+1}^- \end{pmatrix}. \tag{5.10}$$

5.1.4 Reflection and transmission coefficients

Assuming the substrate as a semi-infinite environment, there is no backward propagation in substrate and $\mathcal{E}_{N+1}^- = 0$. Then from the Eq. (5.10), we can determine the reflection and transmission coefficients:

$$r = \frac{\mathcal{E}_0^-}{\mathcal{E}_0^+} = \frac{m_{21}}{m_{11}}, \tag{5.11a}$$

$$t = \frac{\mathcal{E}_{N+1}^+}{\mathcal{E}_0^+} = \frac{1}{m_{11}}. \tag{5.11b}$$

The reflection R and transmission T factors in intensity are given by:

$$R = rr^*, \tag{5.12a}$$

$$T = \frac{n_{N+1}}{n_0} tt^*. \tag{5.12b}$$

The matrix formalism makes it possible to quickly determine the optical properties of a component by separating the phenomena related to layers and interfaces between them.

5.1.5 Electric Field Intensity

Using the matrix calculus introduced above, see Eq. (5.9), we can determine the forward $\mathcal{E}_j^+(z)$ and backward $\mathcal{E}_j^-(z)$ propagating electric field components for any z position across the stack of layers. However, to determine the electric field intensity, we must distinguish between the transversal electric (S) and transversal magnetic (P) polarizations. [161] In the case of S polarization, the entire electric field $\mathcal{E}_j(z)$ meets the continuity condition at the interfaces and its value is equal to the sum of the progressive $\mathcal{E}_j^+(z)$ and the retrograde $\mathcal{E}_j^-(z)$ part. The calculation of the electric field intensity for S-polarized radiation is thus done using the Eq. (3.13).

For P-polarized radiation, the electric field intensity calcul requires to separate components of electric field $\mathcal{E}_j(z)$ in tangential plane $\mathcal{E}_j^{\parallel}(z)$, i.e. parallel to the interface along x axis, and the component $\mathcal{E}_j^{\perp}(z)$ perpendicular to the environment interface, see Fig. 5.1. In principle, the calcul of electric field intensity is done using the Eq. (3.14) and the tangential components are summed, $\mathcal{E}_j^{\parallel}(z) = \mathcal{E}_j^{\parallel+}(z) + \mathcal{E}_j^{\parallel-}(z)$, while the normal components are substracted, $\mathcal{E}_j^{\perp}(z) = \mathcal{E}_j^{\perp+}(z) - \mathcal{E}_j^{\perp-}(z)$. [161]

5.2 Electric Field Intensity distribution of GREAT mirrors

Within the GREAT consortium, we had available HfO_2-SiO_2 and Nb_2O_5-SiO_2 multilayer coatings. The dielectric stacks were magnetron sputtered on fused silica substrates at IF by RCMO group. [222] The multilayer designs were suggested by the IFSW. The highly reflective mirrors represent intermediate step in fabrication process flow of Grating Waveguide Structures (GWS) that are intended to be used for pulse compression, wavelength stabilization or as polarization converters. The mirrors with their parameters are summarized in Table 5.1. For all mirrors, the low-index material is SiO_2 while the high-index coatings are Nb_2O_5 or HfO_2. All the reflective designs are intended for S-polarized beams.

Design	High-index material	Application wavelength [nm]	Angle of incidence [°]	Number of layers	GREAT application
A1D3	HfO_2	1030	51.4	41	Pulse compressor
A3D1	Nb_2O_5	976	61.7	28	Wavelength stabilization
A3D3	Nb_2O_5	976	55	29	Wavelength stabilization
A5D5	Nb_2O_5	1030	0	29	Polarization converter
CLASm	Nb_2O_5	1030	0	21	Quarter wave mirror
OPTm	Nb_2O_5	1030	0	27	LIDT enhanced mirror

Table 5.1: Summary of magnetron-sputtered GREAT mirrors and CLASm, OPTm reflective designs with basic parameters. The mirrors were available for LIDT tests. More detailed description of mirror designs is given in Appendix A.

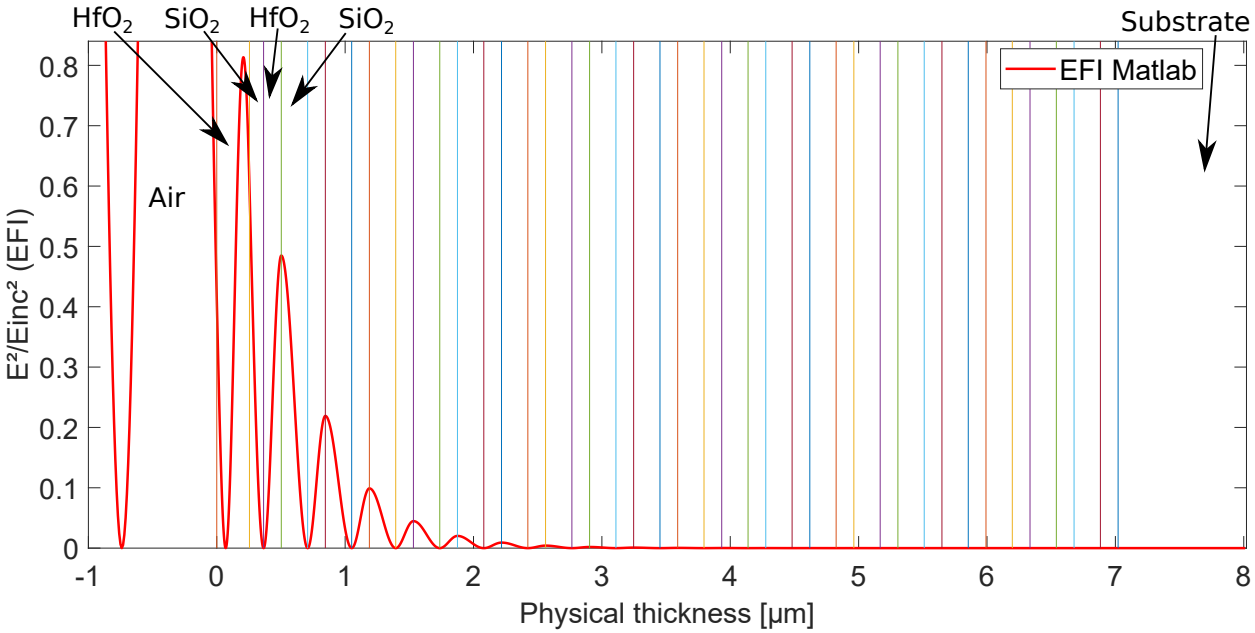

Figure 5.2: EFI distribution for A1D3 mirror design irradiated by S-polarized beam at 51.4° angle of incidence. The EFI is normalized to the incident electric field amplitude in air. The EFI distribution was calculated by transfer matrix method implemented in a MATLAB code. The layer which is exposed to air is HfO_2.

Using the transfer matrix method described above the electric field intensity (EFI) distribution was calculated for the mirrors fabricated in GREAT. An example of EFI distribution in a A1D3 multilayer coating made of two materials, high-index HfO_2 and low-index SiO_2, is given in Fig. 5.2. The determined EFI maxima in both high-index and low-index coating materials are listed in the Table 5.2. The EFI maxima are given for the LIDT test configurations and the final application configurations.

5.2.1 Calculated LIDT of mirror

Let us consider $EFI_{\mathrm{max,H}}$ and $EFI_{\mathrm{max,L}}$ as electric field intensity maxima for high-index and low-index material, respectively, which are valid for selected angle of incidence, polarization and wavelength. Let $F_{\mathrm{int,H}}$ and $F_{\mathrm{int,L}}$ be the intrinsic fluences of high-index and respectively low-index material. Then, from Eq. (3.20), we can express the theoretically expected LIDT fluence for high-index ($F_{\mathrm{ext,H}} = \frac{F_{\mathrm{int,H}}}{EFI_{\mathrm{max,H}}}$) and low index material ($F_{\mathrm{ext,L}} = \frac{F_{\mathrm{int,L}}}{EFI_{\mathrm{max,L}}}$). The calculated LIDT of the mirror or structure containing multiple materials is then determined by the material showing the lowest expected LIDT fluence:

$$F_{\mathrm{ext,mirror}} = \min\left[F_{\mathrm{ext,H}}, F_{\mathrm{ext,L}}\right]. \tag{5.13}$$

We will call in the following text the expected LIDT fluence determined using the knowledge of intrinsic LIDT of material as "calculated LIDT". By contrast, the experimental LIDT fluence of mirrors obtained directly from tests of the mirrors we will termed "measured LIDT".

In all fabricated mirror designs, the coating material more vulnerable to laser damage initiation is high-index material. The HfO_2 shows approximately 2x–2.4x lower intrinsic LIDT than SiO_2, and in the case of Nb_2O_5 its intrinsic LIDT is 5x–11x lower than SiO_2, see Fig. 4.9. [267] The difference in LIDTs between materials is dependent on number of shots. Thus, even in the case of A3D1 design with electric field

GREAT mirror design	High-index mate-rial	Pol-ari-zat-ion	AOI [°]	λ-LIDT [nm]	EFI max. @λ-LIDT			λ-Appl. [nm]	EFI max. @λ-Appl.			
					High-index layer	Low-index layer	L/H factor		High-index layer	Low-index layer	L/H factor	Corre-ction factor
A1D3	HfO2	S	51.4	1030	0.81	0.60	0.74	1030				1
		P			1.04	0.91	0.87					
A3D1	Nb2O5	S	61.7	1030	1.12	3.22	2.87	976	1.31	4.00	3.06	0.86
		P			0.55	0.87	1.60		0.51	0.90	1.77	1.08
A3D3	Nb2O5	S	55	1030	0.31	0.30	0.99	976	0.30	0.30	1.00	1.04
		P			0.72	0.71	0.99		0.68	0.68	1.00	1.05
A5D5	Nb2O5		0	1030	0.79	0.79	1.00	1030				1
CLASm	Nb2O5	S	0	1030	0.79	0.79	1.00	1030				1
		S	8	1050	0.78	0.78	1.00	1030	0.78	0.78	1.00	1.01
OPTm	Nb2O5	S	0	1030	0.50	1.18	2.36	1030				1
		S	8	1050	0.66	1.08	1.66	1030	0.53	1.15	2.18	1.25

Table 5.2: Electric Field Intensity maxima (EFI max.) for GREAT mirrors and CLASm, OPTm reflective designs calculated by Transfer Matrix Method using MATLAB code. The EFI is normalized to the incident electric field amplitude in air. The A3D1 and A3D3 mirrors were designed to application wavelength (λ-Appl.), which was different from wavelength available for LIDT tests (λ-LIDT). The L/H factor is the ratio between EFI maxima in high-index layer and low-index layer. Correction factor corresponds to the ratio between EFI maximum at wavelength of LIDT test and EFI maximum at application wavelength, see Eq. 5.15.

enhancement approximately 3x higher in low-index material (SiO_2) than in high-index material (Nb_2O_5), see L/H factor in the Table 5.2, the damage initiation should occur in the less electric field enhanced Nb_2O_5.

5.2.2 Correction factor to application wavelength

The GREAT mirror designs were developed for three laser wavelengths: 976 nm[2] , 1030 nm and 2050 nm. However, the testing of materials or multilayer structures was not possible at 976 nm or 2050 nm since we did not have access to laser sources operating at these wavelengths. A possible solution is to make prediction of LIDT by comparing the EFI maxima at intended application wavelength and the wavelength, at which the LIDT tests can be performed.

For the wavelengths close to 1 µm, we can consider LIDT rather independent on laser wavelength:[3] [255]

$$F_{int} = F_{ext}^{\lambda-\mathrm{LIDT}} \cdot EFI_{max}^{\lambda-\mathrm{LIDT}} = F_{ext}^{\lambda-\mathrm{Appl}} \cdot EFI_{max}^{\lambda-\mathrm{Appl}}, \tag{5.14}$$

then using the knowledge of EFI maximum at an application wavelength ($EFI_{max}^{\lambda-\mathrm{Appl}}$) and the EFI maximum at a wavelength available for the LIDT tests ($EFI_{max}^{\lambda-\mathrm{Appl}}$), we can determine the experimental LIDT fluence at application wavelength:

$$F_{ext}^{\lambda-\mathrm{Appl}} = F_{ext}^{\lambda-\mathrm{LIDT}} \cdot \frac{EFI_{max}^{\lambda-\mathrm{LIDT}}}{EFI_{max}^{\lambda-\mathrm{Appl}}}, \tag{5.15}$$

[2]For a wavelength of 976 nm, the LIDT testing should be performed at CW regime since this is relevant to operation of diode laser systems operating at this wavelength. However, due to mobility restrictions related to covid19, testing in CW regime was not available prior to the writing of this thesis. Nevertheless, we measured LIDT of mirrors in sub-ps regime as an indication of their quality. Drawback of this work is that we do not know about correlation to CW regime.

[3]At 2µm, however, this is not valid but still the LIDT calculation using comparison of EFI maxima between 1 µm and 2µm can give rough estimation.

even though the material or structure was tested at other wavelength that was available for LIDT tests (λ-LIDT). The ratio $\frac{EFI_{max}^{\lambda-\mathrm{LIDT}}}{EFI_{max}^{\lambda-\mathrm{Appl}}}$ in Eq. (5.15) we term "Correction factor" and its values for GREAT mirror designs are listed in the last column of Table 5.2.

5.3 LIDT tests of mirrors

The laser damage tests were carried out with the 6 magnetron sputtered mirror designs developed within GREAT. The list of mirrors together with testing and application parameters, i.e. polarization state, angle of incidence or wavelength, is summarized on the left side of Table 5.2. All designs were tested with the 500-fs, 1030-nm, 10-Hz LIDT station at Institut Fresnel. In the case of CLASm and OPTm mirrors, the LIDT tests were performed also with setup at ELI Beamlines by a pulse duration of 100 fs at a wavelength of 1050 nm and with a repetition rate of 500 Hz.

During the LIDT tests, each mirror was tested at an angle of incidence relevant to the designed application, see Table 5.2. It should be noted that the experimental LIDT fluence (F_{ext}) reported here refers to the effective area (A_{eff}) measured at the normal incidence, see Eq. (3.1). The determination of experimental LIDT fluences at an angle of incidence (AOI) is possible through the relation:

$$F_{ext}^{\mathrm{AOI}} = F_{ext} \times \cos(\mathrm{AOI}). \tag{5.16}$$

5.3.1 LIDT of mirrors at 500-fs 1030-nm in air

The testing of A1D3, A3D1, A3D3, A5D5, CLASm and OPTm mirrors was performed with 500-fs 1030-nm LIDT station described in Sec. 3.2 on page 69. To change the beam polarization from P to S, an additional HWP was placed before the last optical element - the lens with 30 cm focal length. For both polarizations, the beam profiling at focal plane by BP8.7 sensor from FemtoEasy showed the same effective beam diameter of ~ 85 µm at focus. All LIDT tests with mirrors were performed at focal plane, which was determined using a Nb_2O_5 tested at the beginning of LIDT campaign for different focal lens positions.

LIDT procedure and damage detection

The testing with mirrors was done with similar LIDT procedures as in Sec. 4.3.1 on page 105. The tests were repeated for 1on1, 10on1, 100on1 and 1000on1 procedures with a 10 Hz repetition rate. Each mirror was tested at an angle of incidence relevant to the intended application.

For the evaluation of irradiated spots, the in-situ observation with a 20× magnification of the objective mounted on a BXFM Olympus microscope was used in the case of A1D3, A3D1 and A3D3 designs. The results of A5D5 mirror were obtained ex-situ using a Zeiss Axiotech differential interference contrast microscope with an objective of 20× magnification. Based on previous results, the difference between the mentioned observation methods should not be significant, especially in the multiple-shot irradiation regimes. In the case of CLASm and OPTm designs, the damage inspection was done with three devices: in-situ imaging lens (VZM$^{\mathrm{TM}}$ 450 Zoom Imaging lens, Edmund Optics), ex-situ differential interference microscope (Zeiss Axiotech, Olympus) and additionally with confocal laser microscope (OLS5100, Olympus). The results of CLASm and OPTm designs presented here correspond to the last method, which was the most accurate since it enabled observation with 100× objective magnification and exact positioning across horizontal and vertical coordinates.

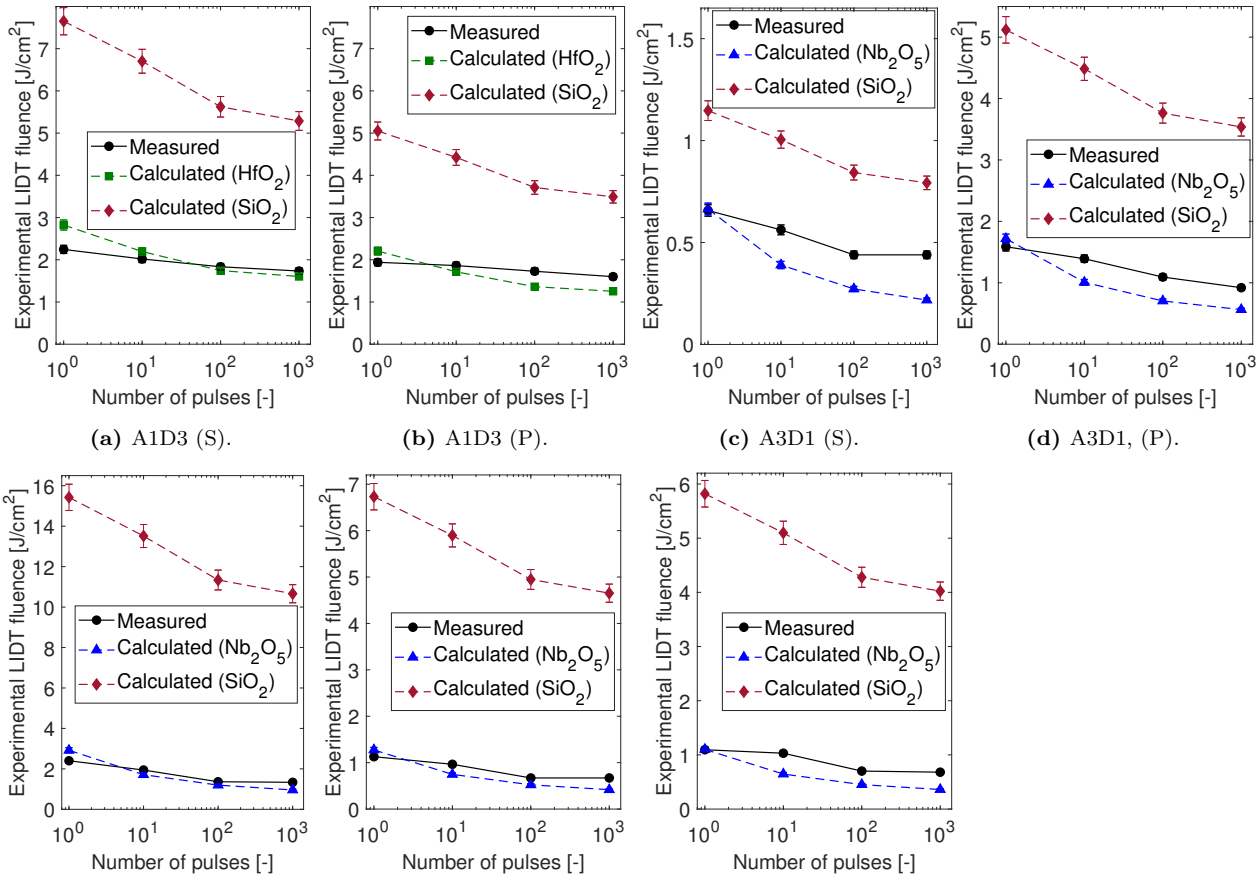

(a) A1D3 (S). **(b)** A1D3 (P). **(c)** A3D1 (S). **(d)** A3D1, (P).

(e) A3D3, (S). **(f)** A3D3, (P). **(g)** A5D5, (0° AOI).

Figure 5.3: Experimental and calculated laser-induced damage thresholds of mirror designs used in GWS. The results for A1D3 and A5D5 mirrors correspond to a wavelength of LIDT tests - 1030 nm, whereas the results for A3D1 and A3D3 designs were rescaled to application wavelength (976 nm) using Eq. (5.15). The angles of incidences (AOI) correspond to the intended application, see Table 5.2.

LIDT of mirror designs for GWS

The summary of both measured and calculated LIDT results of mirrors for GWS is shown in Fig. 5.3. The results plotted for A1D3 and A5D5 mirrors correspond to a wavelength of LIDT tests - 1030 nm, whereas the results for A3D1 and A3D3 designs were rescaled to application wavelength (976 nm) using Eq. (5.15). As expected a good agreement is found between measured and calculated LIDT. However, in all studied mirror designs, the decrease in measured LIDT with increasing number of pulses is less significant than the drop in calculated LIDT of high-index material. This might be connected to the formation of laser-induced defects which could differ between the tested single layer material and multilayer stacks, even though they were deposited by the same magnetron sputtering technique. The determined LIDTs are also related to the used detection method and the damages could differ on single layer versus stack, e.g. by color change.

Since the mirrors should be implemented in laser systems with long-term damage resistant optics, the 1000on1 LIDT results should be the most relevant for their qualification. For this pulse number, the measured LIDT was always higher than the calculated LIDT, which may thus be used as a careful (worst case) estimation. If we compare the 1000on1 LIDT between mirrors, the A1D3 in S-polarization shows, as expected,

the highest measured LIDT of 1.7 J/cm^2, see Fig 5.3. For the A1D3 design the high LIDT is a critical property since it is aimed for pulse compressor that is exposed to high energy densities. It is why the A1D3 design uses highly resistant HfO_2 as a high-index material. The 1000on1 experimental LIDT higher than 1 J/cm^2 shows also A3D3 mirror which should be a part of GWS for wavelength stabilization. The high LIDT is probably connected to the advantageously low EFI maximum in Nb_2O_5 material. The A3D3 mirror in S-polarized configuration has EFI maximum of 0.31 whereas the other designs have at least 0.55.

The graphs plotted in Fig. 5.3 show large discrepancies in calculated LIDTs between high-index (HfO_2 or Nb_2O_5) and low-index (SiO_2) materials. The calculated LIDT of low index material is significantly higher than the one of high-index material, the difference ranges from a factor of 1.7 (1on1, A3D1, S) up to 11 (1000on1, A3D3 and A5D5). Such a large difference in calculated LIDTs implies that there is a room for LIDT enhancement by adjusting the electric field intensity distribution to decrease the high EFI maxima in high-index material.

LIDT enhancement of Nb_2O_5-SiO_2 mirrors

In the case of GWS designs, a frequently used high-index material is Nb_2O_5 whose deposition is well mastered as well as the etching process needed for grating structure production. However, a drawback of this material lies in its low damage threshold which is around 3 to 5 times lower than that of HfO_2, see Fig. 4.9c) on page 106. The disadvantage of Nb_2O_5 can be overcome by proper design with optimized electric field distribution with peaks localized in low index SiO_2. Thus, we developed two Nb_2O_5/SiO_2 mirrors, one with classical (CLASm) and one with optimized (OPTm) design, to investigate their LIDT.

For both mirrors, CLASm and OPTm, the layer material interfacing to air was high-index Nb_2O_5. Designs were adapted to normal angle of incidence for a beam at a wavelength of 1030 nm. The CLASm design contained stack of 21 layers with each layer corresponding to Quarter Wave Optical Thickness (QWOT). The OPTm design has 27 layers. First 12 layers from incident beam have optimized thickness, specifically Nb_2O_5 layers have 0.5 QWOT while SiO_2 layers 1.6 QWOT. Each of the remaining 15 layers closer to the substrate has a QWOT thickness.

The simulation of EFI distribution based on transfer matrix method showed that CLASm design has the same EFI maximum in Nb_2O_5 and SiO_2 materials, see Table 5.2. By contrast, the OPTm design has EFI maximum in Nb_2O_5 approximately 2.4 times lower than in SiO_2. Since this value is still lower than the ratio between the intrinsic LIDTs of SiO_2 and Nb_2O_5, see Fig. 4.9c) on page 106, we consider the Nb_2O_5 material as the one limiting LIDT of these mirrors. Furthermore, since there is much larger relative difference between LIDTs of SiO_2 and Nb_2O_5 materials in multiple-shot regime, there should be a room for further experimental LIDT improvement of mirrors.

As anticipated, we observe higher experimental LIDT with OPTm design than in the case of CLASm design, see Fig. 5.4a) and b). However, we observe a quite different evolution of measured LIDT with increasing number of pulses between OPTm and CLASm designs. While for 1on1 and 10on1 procedures the measured LIDT for OPTm design is approximately two times higher than for CLASm, the difference is greatly reduced for 100on1 and 1000on1 procedures (to factors of 1.46 and 1.35 respectively). The CLASm design does not show decrease in LIDT with number of pulses. It might be possible that there are some material modifications but we do not observe them even with 3D laser confocal microscope.

In Fig. 5.4c) and d) we show measured LIDT of CLASm and OPTm mirrors in dependence on used detection method - in-situ imaging lens, ex-situ differential interference contrast and ex-situ confocal microscopy. We found that the observation method has impact on determined LIDT mainly in the case of 1on1 procedure. To compare the suitability of detection methods, we show damaged spots induced by 1on1 irradiation

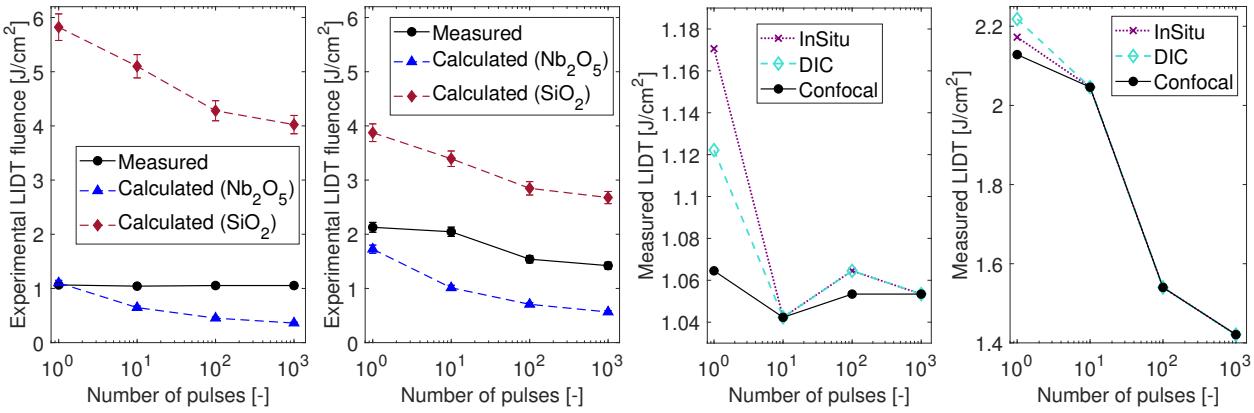

(a) CLASm (air, 500 fs). **(b)** OPTm (air, 500 fs). **(c)** CLASm - detection. **(d)** OPTm - detection.

Figure 5.4: Experimental laser-induced damage thresholds at 500 fs, 1030 nm, normal incidence and air environment. The LIDT of optical mirrors was investigated with the purpose to enhance damage resistance by design optimization. The results on figures a) and b) compare calculated and measured LIDTs, whereas figures c) and d) show only measured LIDTs determined using three observation devices: in-situ optical microscope (Zoom VZM 450 Edmund Optics) with imaging lens, ex-situ differential interference contrast (DIC) microscope (Zeiss Axiotech) and 3D laser confocal microscope (OLS5100 Olympus). The figures a) and b) show results correspoding to confocal microscopy.

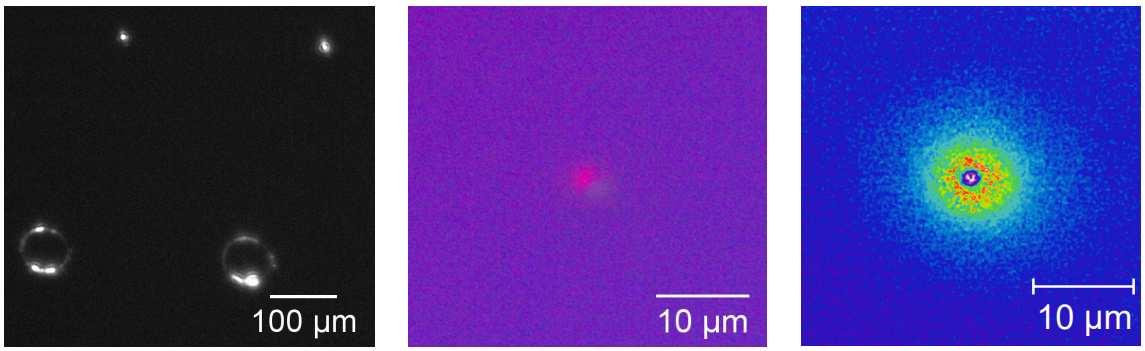

(a) In-situ imaging lens. **(b)** Ex-situ DIC microscopy. **(c)** Ex-situ confocal microscopy.

Figure 5.5: 1on1 damaged spots on CLASm mirror inspected by three observation techniques: a) in-situ imaging lens, b) ex-situ differential interference contrast (DIC) microscopy, and c) ex-situ 3D laser confocal microscopy. The figure a) shows at its upper part the damages induced by fluences that were $\sim 10\%$ higher than the LIDT determined by confocal microscopy. The 1on1 damages in lower part of image a) were generated using a pulse with $\sim 2\times$ higher fluence than the LIDT. Figures b) and c) show the same damage caused by a laser fluence that was by 7% higher than the determined LIDT.

in Fig. 5.5 containing images captured by in-situ imaging lens, ex-situ DIC microscopy and ex-situ confocal microscopy. The in-situ imaging lens enabled detection of material damages with up to $6.4\times$ magnification. In the case of CLASm design, the threshold detected with the in-situ method was around 10% higher than the LIDT determined by confocal microscopy. The Fig. 5.5 b) and c) show the same damage induced by a laser fluence that was by 7% higher than the determined LIDT. The image captured by confocal microscopy (Fig. 5.5c) shows considerably more details of the material modifications, confirming greater suitability for damage detection of this technique in comparison to DIC (Fig. 5.5b).

5.3.2 LIDT of mirrors at 100-fs 1050-nm

To validate mirrors for use in ultrashort lasers, we aimed to perform LIDT tests by pulse durations shorter than 500 fs. Thanks to the collaboration with ELI Beamlines facility, we had an access to LIDT setup operating with pulse duration of 100 fs. The setup was described in Sec. 3.8 on page 88. Since laser systems working in such high-intense 100 fs regime are facing with undesirable nonlinear optical effects in air, the optical components are placed in vacuum environment.

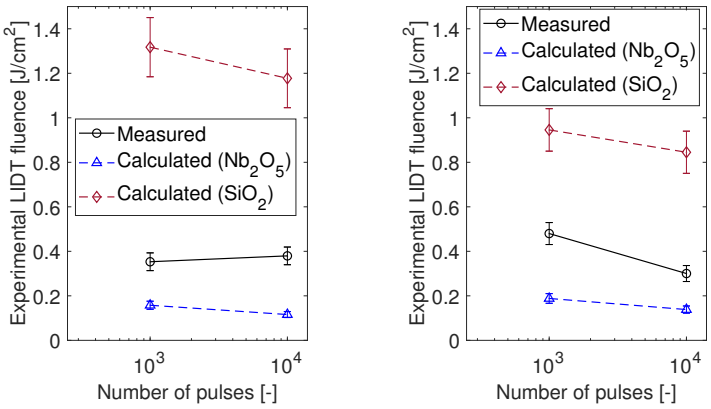

(a) CLASm (vacuum, 100 fs). **(b)** OPTm (vacuum, 100 fs).

Figure 5.6: Experimental LIDTs of optical mirrors investigated with the purpose to enhance damage resistance by design optimization. The results on figures a) and b) correspond to LIDT tests at 100 fs, 1050 nm, angle of incidence of 8° and a pressure of $\sim 10^{-6}$ mbar. The damage detection was done using 3D laser confocal microscope.

In this thesis, we used the 100 fs LIDT setup to test the single layers of the used materials and CLASm and OPTm mirror designs in high vacuum by pulses at a wavelength of 1050 nm. The damage testing of these two mirrors was done at an angle of incidence close to normal incidence (8° AOI), which is the operation angle of these mirrors suggested by designers. Otherwise, the testing procedure was similar to the one with monolayer coatings described in Sec. 4.6 on page 119. The experimental LIDT fluences of mirrors for 1000on1 and 10000on1 procedures are shown in Fig. 5.6 together with the calculated LIDTs.

If we compare the determined LIDTs of mirrors in vacuum, we see that OPTm mirror has higher 1000on1

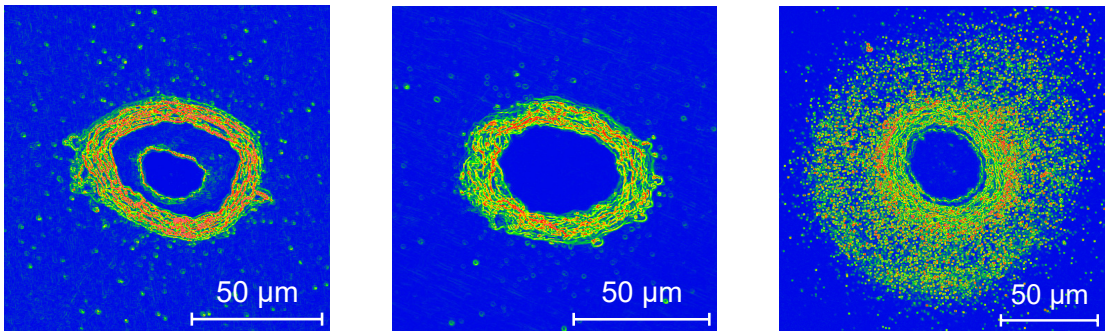

(a) CLASm, 2000 shots, 100 fs, vacuum. **(b)** OPTm, 240 shots, 100 fs, vacuum. **(c)** CLASm, 380 shots, 500 fs, air.

Figure 5.7: Damaged spots on CLASm and OPTm mirrors, induced by a laser fluence slightly higher than the determined LIDTs. The damage inspection was done using confocal microscope.

LIDT than CLASm. However, its 10000on1 threshold is lower than that of CLASm. The result could be affected by a defect which was not observed before the irradiation. In Fig. 5.7a) and b), we show examples of damaged spots on CLASm and OPTm mirrors, respectively. These damages were caused by fluences slightly higher (by 5-10%) than their LIDTs. We see similar morphology of ablated coatings on both mirrors.

The damage morphologies formed by 100 fs pulses in vacuum can be compared to the modified CLASm surface irradiated by pulses of 500 fs duration in air, Fig. 5.7. Although the fluences were close to the damage threshold in tests done by both LIDT setups, the damage morphologies differ significantly between each other. For the test done with pulse duration of 500 fs in air, the region around the damage shows lot of redeposited debris (Fig. 5.7c), and the visible surface modification covers a much broader area than in the case of damaged spots created by 100 fs pulses (Fig. 5.7a-b) in vacuum, where only little debris is observed. The difference in debris redeposition between vacuum and air was found on metals irradiated by sub-ps UV pulses in study [268] The effect of ambient gas pressure on debris redeposition was described on polymers irradiated by ns UV pulses. [269]

To compare LIDTs of mirrors tested by two LIDT stations operating with 100 fs and 500 fs pulse durations, we rescaled the 100-fs results to 500-fs using the scaling law: LIDT $\sim \tau^{0.3}$. Additionally, the LIDT results performed with the beam at a wavelength of 1050 nm were rescaled to the application wavelength of 1030 nm using the Eq. (5.15). The LIDT results of CLASm and OPTm mirrors corresponding to their application conditions, i.e. a wavelength of 1030 nm and normal incidence, determined by tests in air and vacuum, are shown in Fig. 5.8.

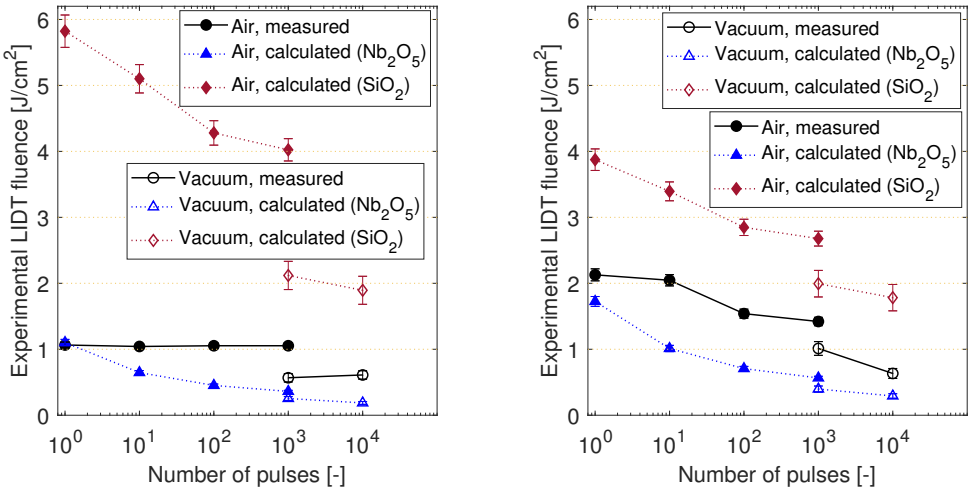

(a) CLASm mirror. **(b)** OPTm mirror.

Figure 5.8: Effect of environment on experimental LIDTs of optical mirrors. The LIDT results in vacuum obtained with a pulse duration (τ) of 100-fs were rescaled to 500 fs using the scaling law: LIDT $\sim \tau^{0.3}$. Additionaly, the LIDT results were rescaled to the application wavelength of 1030 nm using the Eq. (5.15). The tests in vacuum were done with a repetition rate of 500 Hz whereas the tests in air with 10 Hz.

For the same number of pulses (1k), the damage thresholds in vacuum are significantly lower than the ones determined in air. Similarly to the case of single layers tested at 100 fs (Sec. 4.6), the damage thresholds of mirrors tested at 100 fs in vacuum are significantly lower than the ones tested at 500 fs in air. We do not have clear explanation for this result, it might be related to an effect of environment [154] or a metrology issue. [103]

5.3.3 Summary of LIDT results on mirrors

As a final step of LIDT work on mirrors, we are comparing in the Fig. 5.9 the measured LIDTs to the calculated ones for all tested mirror designs. The plotted results correspond to the experimental LIDT conditions, i.e. no parametric scaling was used. The middle zone between the two straight dashed curves represents the validity zone of the model, which accounts for 21% of the variation in the LIDT tests. The variations of 21% correspond to the total budget of error contributors in the LIDT testing, which was summarized in Table 3.4 on page 83. For the determination of calculated LIDT, it is required not only the intrinsic LIDT of materials, but also the knowledge of electric field intensity distribution. We assume that the errors in EFI maxima calcul can be neglected since the layer thicknesses were very accurately monitored during the magnetron sputtering depositions. Moreover, with the perspective of the development of GWS, we were careful to determine the refractive indices very accurately.

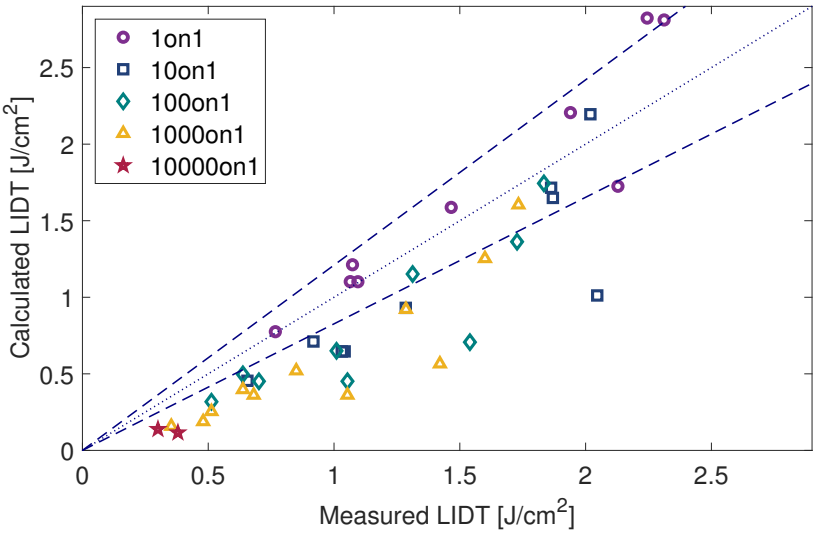

Figure 5.9: Comparison of measured and calculated LIDTs of mirrors. Results correspond to the LIDT testing conditions listed in Table 5.2, i.e. no parametric scaling was used.

Assuming the uncertainty of calculated LIDT we see that for the single shot tests the calculated LIDTs are in good agreement with the measured LIDT values. However, as the number of pulses increases, there are more cases where the measured LIDT is significantly higher than the calculated one.

One hypothesis why we see this discrepancy between measured and calculated values could be that the LIDT is linked to several factors, and not only to the EFI maximum value. The effect on LIDT could have the presence of maximum field inside the stack, the average or root mean square field of a given layer, or the field value at interfaces between two layers. The evolution of LIDT with number of shots could also be different if the film is in contact with air or embedded in the stack. It could be also possible that the single layer materials, from which the calculated LIDTs were derived, were not deposited with exactly the same conditions as mirrors and thus could have different density of defects and processes of laser-induced defect generation.

5.4 LIDT of GWS

Grating waveguide structures (GWS) are reflecting diffractive optical elements with periodic features in the form of sub-wavelength gratings integrated with planar waveguides and reflective dielectric stack, see Section 1.2.1. By a design selection of the whole GWS it is possible to achieve resonant effects that are more efficient than current grating-only-based devices commercially available today. GWS enable innovative solutions for laser beam adjustment, such as radial and azimuthal polarization selection, [21, 37, 38] spectral stabilization, [39], wavelength tuning, [17, 40], or pulse compression. [20, 25, 41]

For use of GWS in such applications, the laser damage resistance of the materials and components must be determined. Because these structures are based on resonant effects, their laser damage resistance is predicted to be linked to the electric-field distribution in the structure, as it has been found to be in dielectric multilayer stacks and gratings. [240, 270] Furthermore, the electric-field distribution can be quite sensitive to opto-geometrical factors, particularly the refractive index and layer thicknesses in a multilayer stack. [10] A deeper investigation on this problem is thus desirable in order to improve GWS effectiveness.

The fabrication of GWS involves multiple and complex steps that can modify the LIDT of final components compared to dielectric mirrors tested before. Within GREAT we have worked with partners to understand the effects of these fabrication steps. Here, we firstly present a study of effect of optical surface treatment by Ti adhesion promoter and Cr hard mask[4] on LIDT since these materials are used in the fabrication process of GWS. Afterwards, we will investigate and predict LIDT of selected GWS designs that use SiO_2 as a low-index and HfO_2 or Nb_2O_5 as high-index coating materials. The findings from this work can serve for the optimization of the next generation of GWS designs and their fabrication procedures.[5]

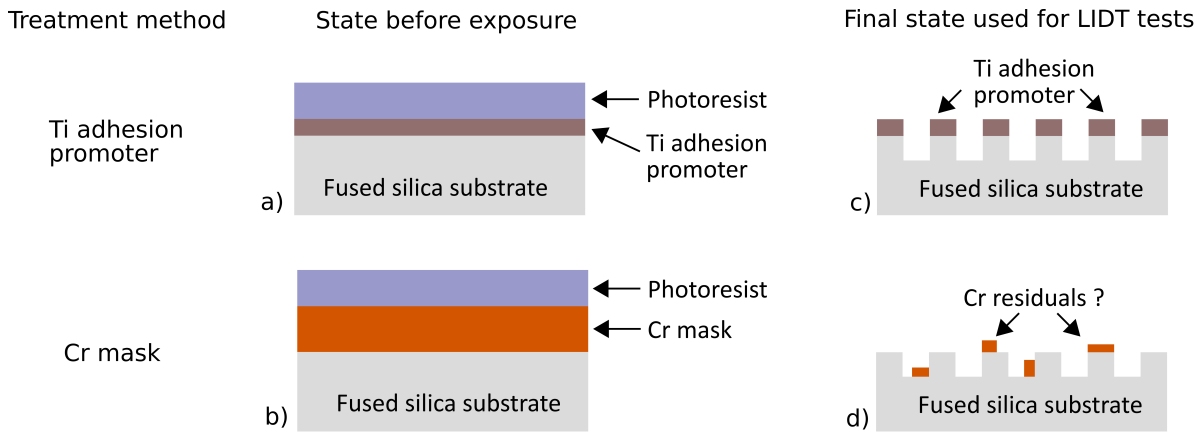

Figure 5.10: Schematic drawings with Ti adhesion promoter (a) and Cr mask layer (b) in the structures to be etched. Ti promoter is used to adhere photoresist to fused silica. Role of Cr mask is to enhance selectivity for etching of deep structures into fused silica. Cr mask layer is around 50 nm thick while Ti promoter has a sub-monolayer thickness. Figures (c) and (d) show final states of structures used for LIDT tests, by which we try to reply on question whether Ti adhesion promoter or potential presence of Cr residuals can affect LIDT of the whole structure.

[4] Cr mask is removed after etching, but there might be still some residuals, whose effect on LIDT we aim to investigate.

[5] The LIDT tests of GWS are out of scope of the thesis because of fabrication delays connected to covid19, but the results should be reported by the end of 2022.

5.4.1 Effect of Cr mask and Ti adhesion promoter on LIDT

Introduction

As a part of the GWS development process, it is important to evaluate any surface treatment that could affect LIDT of the final optical component. Therefore, we are investigating the effect of surface treatment by Ti adhesion promoter and Cr hard mask. The location of Ti adhesion promoter and Cr mask within the processed structures is schematically depicted in Fig.5.10. The both materials play important role in grating etching. Ti promoter is used to adhere consistently photoresist to fused silica, required for accurate grating profile production. Role of Cr mask is to enhance selectivity for etching of deep structures into fused silica. Cr mask layer is around 50 nm thick while Ti promoter has a sub-monolayer thickness.[6]

Chrome hard mask is widely used as an interlayer in lithography due to its ability to resist fluorine-based dry etching, which provides high selectivity to a variety of materials covering Si, SiO_2 [271–273], Nb_2O_5 [274] and Ta_2O_5 [275]. A Cr hard mask assists in achieving deep, high aspect ratio profiles with smooth, near-vertical sidewalls. After the creation of deep grating profiles, a process of wet etching is used to remove the Cr mask. However, it might be possible that some highly absorbent Cr remains on the sample surface after the wet etching and affects the LIDT of the optical structures.

A typical challenge in lithography is adhesion of a photoresist to a surface of interest. A process limiting adhesion to the photoresist's low-polar molecules is the production of polar OH bonds on the surface. Among the most utilized adhesion promoters that can guarantee consistent adhesion are HMDS (HexaMethylDiSilazane), TI-Prime, and diphenylsilanediol-derivatives (AR 300-80). HMDS adheres to the surface through its Si atoms that can be bound to the oxygen atoms of the surface releasing ammonia, whereas low-polar methyl groups offer excellent wetting and adhesion to the photoresist.

TI-Prime (MicroChemicals GmbH) is a highly diluted Ti compound that is spin coated onto a surface. TI-Prime forms a physically bonded TiO_x monolayer and by a soft-sintering process creates a hydrophobic surface. [276, 277] In this work we will refer to TI-Prime as Ti (adhesion) promoter. Similarly to the case of Cr hard mask, the presence of Ti adhesion promoter on an optical surface might affect the damage resistance of given component. Thus, in this study, we are analyzing the impact of Cr hard mask and Ti promoter on the LIDT of fused silica samples.

Samples to be tested

The 7 fused silica substrate samples intended for LIDT testing were prepared by Institut für Technische Optik of Universität Stuttgart (ITO USTUTT) and Department of Physics and Mathematics of the University of Eastern Finland (UEF). The specifications of these samples are summarized in Table 5.3.

On the sample #1 a Cr layer of a thickness of 50 nm was deposited with Q300T T Plus sputter (Quorum). The sample #2 contains a monolayer of the Ti adhesion promoter that was spin-coated with 2-min long soft-baking process at a temperature of 120°C. The substrate surface of sample #3 was not treated by any additional step and served as a reference sample. In the following text, we will use term "untreated" to emphasize no sample surface treatment with both Ti promoter and Cr mask.

On the surfaces of samples #5–7, the linear grating profiles were created. For the diffraction grating fabrication, the S1818 Shipley photoresist was spin-coated and afterwards direct laser patterning was applied. The photoresist patterns on samples #5–7 were transferred into fused silica substrates by inductively coupled plasma-reactive ion etching (ICP-RIE) process that resulted in a grating period of 25 µm[7] with a grating

[6] We estimate the Ti promoter layer thickness to be around 3 nm but this has to be confirmed.

[7] The grating profiles were created also with 100 µm pitch on different area on the sample surfaces.

Sample number	Mark	Treatment	Grating	Substrate diameter [mm]
#1	FS Cr	Cr mask	No	38
#2	FS Ti	Ti promoter	No	38
#3	FS	Untreated	No	38
#4	FS Ti Circular Grating	Ti promoter	Yes	38
#5	FS Cr Grating	Cr mask	Yes	25
#6	FS Ti Grating	Ti promoter	Yes	25
#7	FS Grating	Untreated	Yes	25

Table 5.3: Summary of samples intended for LIDT testing to evaluate the effect of treatment with Cr hard mask and Ti adhesion promoter. The term "untreated" means that the sample surface was not treated with either Cr or Ti.

depth of 600 nm. For photoresist residues removing, O_2 plasma was used. The sample #6 was treated with Ti adhesion promoter located between the substrate and photoresist, see Fig.5.10a). In the case of sample #5, the photoresist layer was applied on Cr hard mask, which was wet-etched and then removed by wet-etching solution. The grating profile on sample #7 was not treated with either Cr mask or Ti promoter.

The production of sample #4 with circular grating profile was very different from samples #5–7. As a resist AZ MIR 701 14 CP dilluted with EBR solvent was used. The grating period was patterned by scanning beam interference lithography (SBIL). The SBIL allowed to get circular grating with period of 881 nm, which is by more than one order of magnitude smaller than in the case of linear grating profiles ($\geq 25\,\mu$m) on samples #5–7. [8]

LIDT procedure and damage detection

The samples #1–7 were tested with the 500-fs, 1030-nm setup described in Sec. 3.2 on page 69. The LIDT tests were performed with TM-polarized radiation at incidence angle of 51.4° which was advantageous for the in-situ damage detection technique applied using an optical microscope with 20× magnification.

The tested samples were positioned at focal plane of the lens with 30 cm focal length. The effective beam diameter was around 85 µm. The LIDT tests were repeated for 1on1, 10on1 and 100on1 procedures. Usually a unique fluence was used for just one spot site. The pulse energy increment was around 2%. Knowing both energy and spatial profile, the fluence in the focal plane is calculated in terms of normal beam fluence, i.e. in a plane that is normal to the beam axis.

The damage threshold was determined as the highest fluence that is lower than the lowest fluence causing damage in the experiment. The results from this testing campaign will not be presented in intrinsic LIDT because we do not know all parameters about promoters and structuration needed for the electric field intensity simulation.

LIDT results and discussion

LIDT tests were performed within and outside the structured regions of samples, the results are shown in Fig. 5.11. Firstly, we focus on the unstructured regions, Fig. 5.11a). Our results indicate that LIDTs of fused silica treated by Cr mask (FS Cr) are close to the ones of untreated referenced sample (FS). In contrast, the

[8] For more details about sample production, please ask GREAT ESR8 Anton Savchenko and ESR5 Fangfang Li.

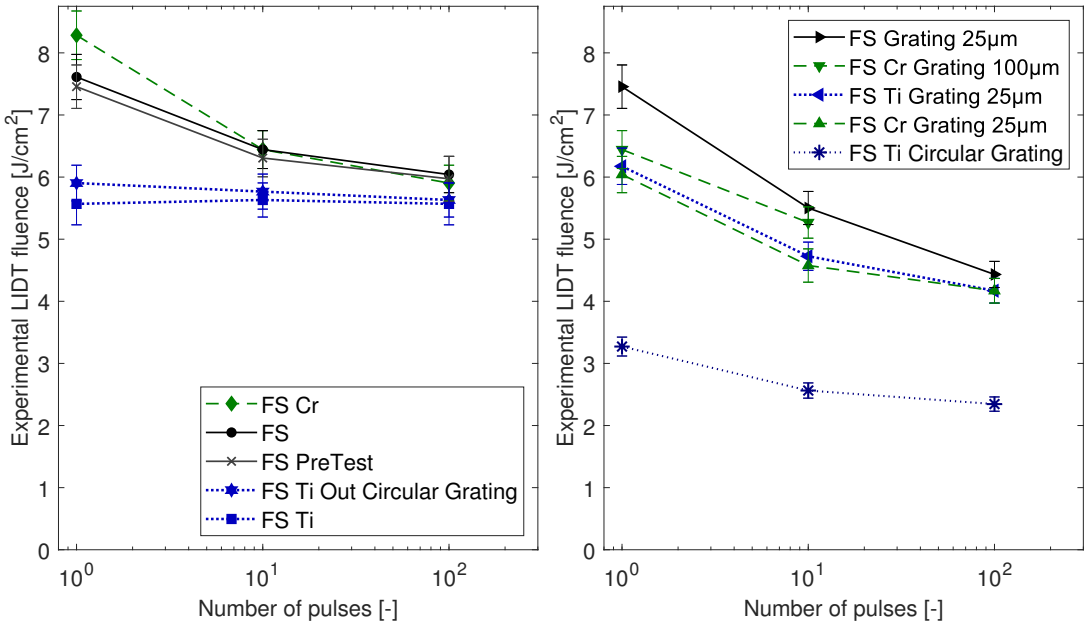

(a) Unstructured profiles.

(b) Structured grating profiles.

Figure 5.11: LIDT test results for the unstructured (a) and the structured grating (b) profiles. Effect of the treatment method on the LIDT. Fused silica substrates were coated either by Ti adhesion promoter or by Cr hard mask. FS Ti Out Circular Grating refers to an unstructured region on the sample #4 (Tab. 5.3). The values of 25 µm or 100 µm mean grating periods.

unstructured fused silica with Ti adhesion promoter (FS Ti) shows significantly lower single-shot LIDT than the reference sample. This might be connected to the used detection method that does not allow to observe some material changes caused by single-shot irradiation of untreated or Cr mask treated samples. In the multiple pulse regime, the difference in LIDTs between the Ti treated and non-treated samples is lower and for the 100on1 tests it is even within the indicated error bars. It seems the Ti promoter facilitates only the observation of any surface modification after 1on1 tests.

This result raises the question of whether the Ti promoter is not removed after the first shot but to confirm this hypothesis we have to do further inspection of irradiated spots. It might be also possible that the presence of TiO_2 monolayer lowers LIDT due to low LIDT of TiO_2. This hypothesis is supported by the fact that TiO_2 has a significantly lower bandgap (3.6 eV [124]) than fused silica (9 eV [278]). However, in the multi-shot regime that is relevant to industrial applications, unstructured samples treated by both Ti promoter or Cr mask show similar LIDT values to the untreated reference sample (FS).

We now turn our attention to the LIDT results with structured grating profiles, see Fig. 5.11b). We preferred to test the gratings with the lowest grating period (25 µm) since the beam size is limited. The highest LIDTs show the untreated reference grating profile. The lowest LIDTs exhibit circular grating profile treated with Ti adhesion promoter. For the grating period of 25 µm, there is no difference in LIDT between Ti and Cr treated samples. The Cr treated grating of 100 µm showed higher LIDT than that of 25 µm, which could be explained by the small beam size and non-homogeneous distribution of electric field intensity in the grating structure.

Similar to the case of unstructured substrates, we see that in the multi-pulse regime the values of differently treated linear gratings (Ti, Cr, untreated) with a period of 25 µm approach each other. For a number of

100 pulses, the LIDT values are practically the same, i.e., within the error bars. In the case of the circularly profiled grating, its damage threshold is significantly lower than that of the other structured samples. This could be due to the grating design, small grating period of 881 nm and duty cycle alternating over the sample surface. Such a design might result in a significantly higher electric field intensification. However, to confirm this hypothesis we do not have sufficiently precise sample characteristics.

If we compare the LIDT results between unstructured and structured profiles, Fig. 5.11, we see same single-shot LIDT within the indicated error bars for unstructured untreated reference sample (FS) and untreated grating profile (FS Grating 25 µm). Similarly for samples treated with Ti promoter, the unstructured substrate (FS Ti) shows single-shot LIDT close to the one of structured linear grating with 25 µm period (FS Ti Grating 25 µm). In all other cases if we compare samples with similar treatment method (untreated, Ti, Cr), the LIDT values related to grating structured profiles are lower than that of unstructured substrates. This could be a consequence of more enhanced electric field intensity in structured grating profiles than in the case of unstructured substrates.

Conclusion of treatment method effect on LIDT

To conclude, the tests performed on unstructured and structured substrates show that LIDT of samples treated by different methods (Ti promoter, Cr mask) converge to the same value with the increasing number of shots. At 100 shots, the LIDTs are same within the indicated error bars. The observed differences between single-shot LIDTs are not important for industrial applications requiring operation with higher numbers of pulses (> 100).

We should emphasize that purpose of these tests was only to compare LIDT between samples. Thus we did not calculate the intrinsic LIDT fluence. We also do not know material parameters of adhesion promoters and grating structures, so the electric field intensity calcul was not possible at this moment. To test the grating structures accurately, the raster scanning method should be applied in order to reveal any spots vulnerable to damage initiation within the large area of gratings.

5.4.2 Prediction of GWS LIDT

In the case of grating structures, the dependence of their LIDT on the electric field intensity maximum has been observed. [15] It has been found that the high peaks of electric field intensities take place in the grating pillars, on the opposite side of the incident wave. The relation between the EFI maximum and LIDT was confirmed by the detection of damage morphologies at the same locations, where the EFI maxima occur. [279, 280]

Within the GREAT project, we use Rigorous Coupled Wave Analysis to simulate the electric field distribution within GWS. The RCWA is a method for getting the exact solution of Maxwell's equations for electromagnetic diffraction by grating structures. [281,282] It is a noniterative, deterministic method that use state-variables to reach the solution without the presence of intrinsic numerical instabilities. The accuracy of the derived solution is primarily determined by the number of terms in the field space-harmonic expansion.

The RCWA technique investigates diffraction from surface structured gratings by dividing the grating into a large number of sufficiently thin planar grating layers to simulate the grating profile to an acceptable degree of accuracy. [282] The electromagnetic fields in each grating layer are calculated using the coupled-wave method. The electromagnetic boundary conditions, i.e. continuity of the tangential electric- and magnetic-field components, are then applied sequentially at the interfaces between the output regions, grating layers and input regions. This approach allows to calculate the reflected and transmitted diffracted field amplitudes and diffraction efficiencies.

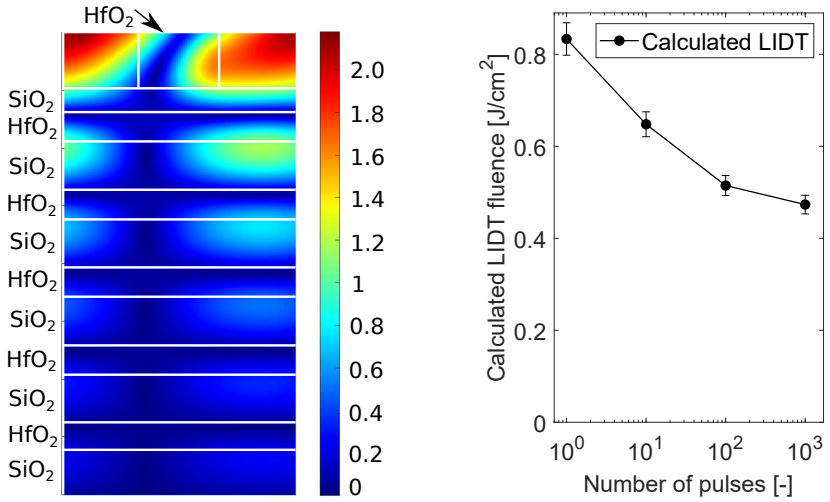

(a) **(b)**

Figure 5.12: Electric field distribution (a) and calculated LIDT (b) for GWS design termed A1D3 based on magnetron sputtered HfO_2 and SiO_2 layers. The design should be implemented into laser systems for pulse compression at a wavelength of 1030 nm.

In this work, computations are done for a lossless, isotropic non-conducting medium interacting with monochromatic plane waves of TE or TM polarization. An example of electric field distribution calculated by RCWA method is shown on Fig. 5.12a). The simulation is done for A1D3 GWS design that should be used for pulse compression. Since the high damage resistance is a key attribute for this application, the HfO_2 was selected as a high-index material. Indeed, the simulation shows that the electric field maximum is localized at a pillar of HfO_2 and thus the resistance of this material determines the resistance of the whole GWS design.

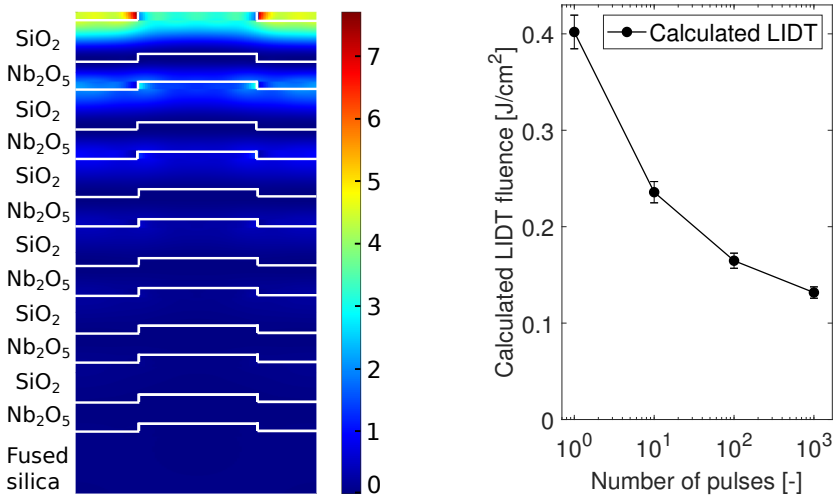

(a) **(b)**

Figure 5.13: Electric field intensity distribution (a) and calculated LIDT (b) for GWS design termed A5D3 based on magnetron sputtered Nb_2O_5 and SiO_2 layers. The 12-layer coating design should operate in laser systems as output coupler with $\sim 4\%$ transmittance at 1030 nm.

Knowing both electric field intensity maximum and instrinsic LIDT of the material, we calculated experimental LIDT fluences (Eq. 3.20) for number of pulses ranging from 1 up to 1k, see Fig. 5.12b). We found a LIDT value of A1D3 GWS to be around 0.5 J/cm^2 for 1k shots (500 fs, 1030 nm). By contrast, the LIDT of A5D3 GWS design (Fig. 5.13a) intended for polarization conversion in CW regime, has a predicted 1000on1 LIDT value of $\approx$ 0.13 J/cm^2, see Fig. 5.13b). The significantly lower LIDT of A5D3 design than that of A1D3 is connected to the used high-index material, which was Nb_2O_5. As mentioned above, the Nb_2O_5 has lower LIDT but it is more convenient for GWS fabrication by partners in GREAT consortium working with several lithography methods. Finally, we should emphasize that LIDT is of lower importance for components operating in CW regime than for pulse compressors interacting with sub-ps pulses.

5.5 Conclusion

This Chapter 5 was focused on optical components consisting of low-index and high-index coating materials that were investigated in Chapter 4. Firstly, we introduced the transfer matrix method used for electric field intensity calcul in multilayer coatings. Afterwards, the method was applied to the designs of GREAT mirrors with the aim to be used to calculate LIDTs of mirrors using the knowledge of intrinsic LIDT of particular coating materials. Furthermore, the tranfer matrix method allowed us to determine correction factors connecting the LIDT results obtained at a wavelength of 1030 nm to the predicted LIDTs at component application wavelengths.

In the next part of this Chapter, we presented LIDT results measured with mirrors. The tests were performed in both air and vacuum environments and the effect of environment was discussed. We found lower LIDT for mirror tested in high vacuum environment than in air. The experimentally obtained results were compared to the calculated LIDT values. While in the single-pulse mode the results agreed with the calculated prediction, in the multiple-pulse regime this was not the case and the measured LIDT was often larger than the calculated predicted value, see Fig. 5.9 on page 140. Since the light reflecting multilayers were not deposited in the same production cycle as the monolayers, whose intrinsic LIDT was used in calculation, it might be possible that the multilayers have lower density of laser-induced defects. The process of laser-induced defect formation may vary depending on whether the oxide layer is in contact with air or embedded in the stack. This could explain the higher LIDT of experimental values in comparison to calculated ones.

Finally, we focused our attention to laser damage resistance of GWS designs. As part of the grating profile manufacturing process, optical surfaces are frequently coated with Ti adhesion promoters or Cr hard masks. Thus, we investigated the effect of this fabrication step on LIDT of GWS. We found that the LIDTs of samples treated by different methods (Ti promoter, Cr mask, untreated) converge to the same value with the increasing number of shots, if we take into account error bars. For 100 pulses, the LIDTs are practically same since they differ only within the indicated error bars. Therefore, the effect of treatment with Ti promoter of Cr mask does not play significant role for components that should be used in industrial laser systems operating with high numbers of pulses.

In the final section of this chapter, we performed the LIDT predictions for the selected GWS designs. The prediction is based on the knowledge of intrinsic LIDT of particular coating materials and simulation of the electric field distribution using the Rigorous Coupled Wave Analysis method. Our calculation shows a 1000on1 LIDT of 0.5 J/cm^2 for the design with HfO_2 as a high-index material and 0.13 J/cm^2 for the design with high-index Nb_2O_5. The LIDT testing of GWS, designed and fabricated by GREAT project partners, should be performed in the months after the submission of this thesis.

Chapter 6

MHz-laser-induced contamination of oxide thin films in air

Diode-pumped high-repetition rate sub-ps lasers, such as the ones related to applications of the GREAT project, are used in the industrial sector for very accurate material processing including cutting, drilling, welding and marking. For reliable operation of these lasers, the power handling capabilities of dielectric coatings in components implemented in these lasers have to be studied. When these coatings are exposed to high intensities of laser radiation, the laser energy can be coupled to the dielectrics through nonlinear ionization processes, which can lead to damage onset. This onset has been studied in Chapters 3, 4, and 5 using single shots or moderate number of pulses (up to 10k shots). For high-repetition rate lasers irradiating materials with large numbers of pulses, billions in the case of MHz regime, the damage resistance is reduced by complex processes. In the multiple pulse regime, laser-induced defects can be generated easing the ionization process by making accessible new energy levels within the bandgap electronic structure. [128,144] If the laser pulses are emitted with high repetition rate, then the dielectrics can suffer from heat accumulation, which can cause stress or failure. [265,283] Damage resistance of components in high repetition rate lasers relates also to damage growth process initiated by localized defects. [87,253,257,284]

Due to the complexity of the processes that lead to laser damage, it is critical to validate optical components using tests that are as close to the applications as possible. Only such tests can be used to predict the lifetime of optical components and their power handling capabilities. However, even when components exhibit high LIDT fluence, their long-term reliability may be restricted to fluences much lower than the LIDT value. [285] This reduction in reliable laser operation lifetime can be linked to an unwanted deposition process, detrimental phenomenon known as laser-induced contamination (LIC). [11,286]

The LIC process refers to the growth of a nanometric highly absorbing layer on an irradiated optical surface, see Fig. 6.1. LIC is the result of interaction between a laser beam, an optical surface and outgassing species in surrounding environment. A contamination layer is typically created by organic compounds or other molecules on optical components that undergo photopolymerization due to laser irradiation. [287–289] Irradiation of the contamination-based layer causes chemical reactions yielding a loss of volatility of the contaminants. A thin LIC deposit is thus formed under the beam, which modifies the optical component properties, resulting in transmission (for optics with antireflective coating) or reflection loss (for optics with reflective coating). [290] The contamination-based layer may cause irreversible damage to the optics surface (e.g. microcracks), leading to laser failure. [286,291]

The LIC formation leading to optical damage in sealed laser systems was firstly documented in 1994 [167],

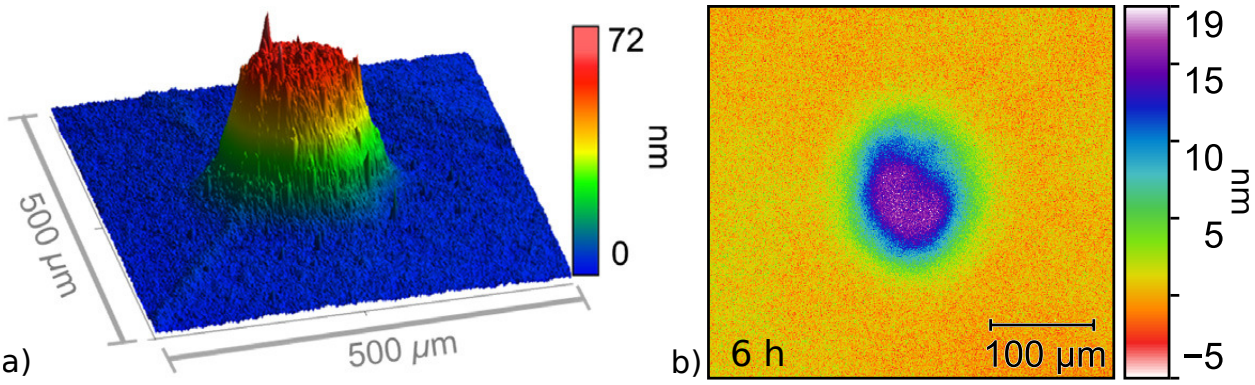

Figure 6.1: Examples of laser-induced contamination deposits for: a) dielectric mirror [11], b) magnetron-sputtered SiO_2 layer of 450 nm thickness irradiated for 6 h. Both samples were exposed to 700 fs/515 nm/3 MHz laser with $\sim$ 35 W of mean power.

but it is still a serious concern in today's high performance laser systems. [292,293] The LIC effect has mostly been explored in the context of space applications. [294, 295] It has been proven that LIC caused unreliable and short-term operation of ns UV lasers used in spaceflight missions. [285,291,296] In work [297], it has been demonstrated that coating optics with fluorinated films is a potential strategy for preventing the formation of an organic contamination layer.

For the fs/ps pulse duration regime, the LIC has been observed on gratings irradiated in vacuum by a beam with a wavelength of 1030 nm. [293] It has been found that the contaminated surface of the gratings can be cleaned using a radio frequency plasma source, whose regular application can ensure the reliable operation of the laser source. In the same work it has also been observed LIC at 515 nm. Usually the effect is enhanced with higher photon energy.

Although LIC proved to be critical for lasers operating in vacuum and identified as a major risk for use of lasers in space [294, 296], it has been discovered that LIC also occurs in high-power lasers operating in air. [298] Recently, the study [11] on dielectric mirrors irradiated by sub-ps pulses at MHz repetition rate revealed LIC formation in air, see Fig. 6.1a). Therefore, the study of LIC formation is of paramount importance for MHz laser applications. Thanks to the advances in laser technologies and their applications, the complexity of the physical processes and the considerable number of parameters involved, LIC formation is still an active topic for research.

In this work, we investigate LIC growth on the dielectric oxide coatings developed for GREAT applications, which are in air environment. The LIC tests were done using a sub-picosecond (700 fs) laser emitting high-repetition rate pulses (3.3 MHz) at a wavelength of 515 nm. The experiments were performed in similar conditions as in the work [11]. An advantage of the work presented in this chapter is the knowledge of coating designs and deposition procedures that allowed to make a systematic parametric study.

Compared to the near-infrared laser radiation, the photons at a wavelength of 515 nm enable to perform laser tests that accelerates the contamination layer formation process. [11] This is crucial since the standard laser specification is a few tens of thousands of hours, and it is inconvenient to do laboratory investigations with such long durations. The irradiated spots on the surface of the samples are inspected via multiple detection methods enabling analysis of contamination deposits. Such detailed investigation is necessary to develop new designs of optical components that will be more resistant to LIC formation and ensure long-term reliable laser operation required for industrial applications.

We will firstly describe the experimental setup used for LIC tests. Then we will present results as a

function of LIC test duration and applied laser radiation experimental fluence. The results will be reported as a parametric study, in which we will show how changes in coating material, thickness, and deposition method affect the LIC growth dynamics. Afterwards, we will introduce the characterization methods that we use for LIC deposit inspection. In the next section we will try to study whether there is a correlation between the formation of the contamination layer and the thermal effects caused by its presence. Finally, we will summarize the findings and propose future directions for LIC research.

6.1 Experiments

There are various experimental setups available in the scientific community for conducting LIC tests. Some of the setups [294, 296, 299–303] were used to test optics intended for space applications, with an emphasis on study in the nanosecond UV regime. In this case, a high vacuum chamber is utilized to simulate space conditions, and the contamination growth is regulated by inserting a selected contaminant into the chamber. Studies on molecular contamination under nanosecond UV laser irradiation were also undertaken in high-power laser facilities specialized on fusion research. [304–307] In these facilities, the highly powerful pulses are emitted with a very low repetition rate, limiting the total number of laser pulses used in experiments.

To study surface modifications and contamination growth, a variety of diagnostic methods have been used. The in situ techniques include measurements of transmission loss [291], laser-induced fluorescence [308] or infrared thermography. [11] Among the ex-situ diagnostics, the relevant tools for contamination investigation are differential interference contrast microscopy, confocal fluorescence microscopy, optical profilometry, and atomic force microscopy (AFM). [11, 160]

Using these facts, we designed a laser damage testing station that enables in-situ sample monitoring as well as real-time transmission loss measurements and possible thermal monitoring with infrared thermography. Since applications of GREAT project operate in an ambient air environment, we used our experimental station for LIC tests in air. The air properties (water content, pressure, temperature) were however not controlled in our study. In this work, we analyzed contamination deposits using ex-situ techniques covering optical profilometry, fluorescence microscopy, X-ray photoelectron spectroscopy, scattering-type scanning near field optical microscopy and absorption measurements.

6.1.1 Experimental setup

The LIC tests are done with a high-power industrial laser source (EOLITE Chinook) that generates pulses at a repetition rate of 3.3 MHz with a duration of 700 fs at a wavelength of 515 nm. The average power was ~ 35 W, which corresponds to a pulse energy of 10 µJ. Generated laser pulses are reflected by three mirrors, see the schematic drawing in Fig. 6.2, and directed to a fused silica planoconvex lens (LENS) of 20 cm focal length.

By moving the lens along a motorized linear stage, the beam size on the front side of sample was adjusted to have a suitable fluence for the LIC tests, i.e. slightly lower than the LIDT value. Moving the lens enabled us to reduce the fluence on the sample while maintaining the full power of the laser source. Therefore, no power reduction through a combination of half-wave plate (HWP) and thin-film polarizer (TFP) was used. The combination of these elements was solely used for power reduction in the laser damage tests performed to determine the position of the focal plane.

During the LIC tests, the average power transmitted through a sample was recorded by a calorimeter (EM, Ophir L50(150)A-BB-35) to detect possible decreases in transmission which could be caused by contamination or damage. We determined the 3σ deviation of pulse energy stability to be 1.3%, see Sec. 3.9.1 on page 91.

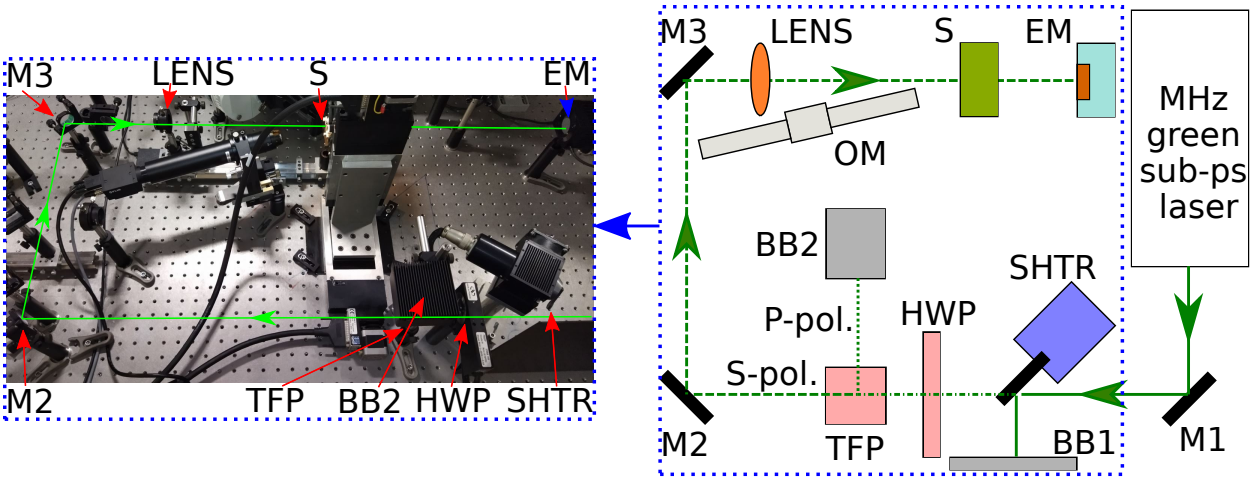

Figure 6.2: Experimental setup with sub-ps green high-repetition rate laser source used for LIC tests. S – tested sample, MX – x-th mirror, SHTR – shutter, BBX – x-th beam blocker, OM – optical microscope (Zoom VZM 450 Edmund Optics), HWP – half-wave plate, TFP – UVFS thin film polarizer (transmission of S vertical polarization 99 %, reflection of P horizontal polarization 99.5 %, 420-1244E Eksma Optics), EM - energy meter (calorimeter, Ophir L50(150)A-BB-35).

The irradiation of a sample was carried out with linear polarization at an incidence angle close to normal ($< 5°$). The slight inclination from normal incidence was used to protect the lens from heating caused by the reflected beam that was directed to an additional beam blocker.

In contrast to LIDT tests with setup described in Sec. 3.9 on page 91, the LIC tests were not performed at focal plane but for lens-sample distances longer than focal length. It implies the LIC tests were done with diverging beam incident to the sample front side plane, at which the effective beam diameter was $\approx 130\mu$m. This was done to decrease the experimental fluence to and avoid damages inside or at rear side of the sample and to obtain larger LIC deposits.

Throughout the LIC tests, we monitored the state of the tested sample front side. The monitoring was carried out using imaging optics with a long working distance objective and a CMOS camera. The imaging optics was protected from the bright scattered green laser light by a filter. For more sensitive observation, the front side of sample was illuminated by a fiber halogen lamp.

The thicknesses of contamination deposits were measured ex-situ by optical profilometry, see Sec. 6.1.6. Examples of deposits observed by this method are shown in Fig.6.1. A more detailed description of ex-situ fluorescence microscopy, X-ray photoelectron spectroscopy and scattering-type scanning near-field optical microscopy will be given in Sec. 6.3 devoted to material characterization.

6.1.2 Beam Profile measurement

The beam profile was measured with high-resolution BeamPro 8.7 camera (FemtoEasy) for tens of lens positions near focal length as can be seen in Fig. 6.3. The camera sensor of 3.45 µm pixel length was placed instead of holder with sample (S), see Fig 6.2, in normal incidence to the beam. The beam incident to the tested sample had profile close to Gaussian one with $M^2 \leq 1.3$.

To avoid high laser light exposure to the CMOS sensor, the beam profiling was carried out in low power mode (2.1 MHz repetition rate, ~ 130 mW). Furthermore, the pulse energy was reduced by a neutral density

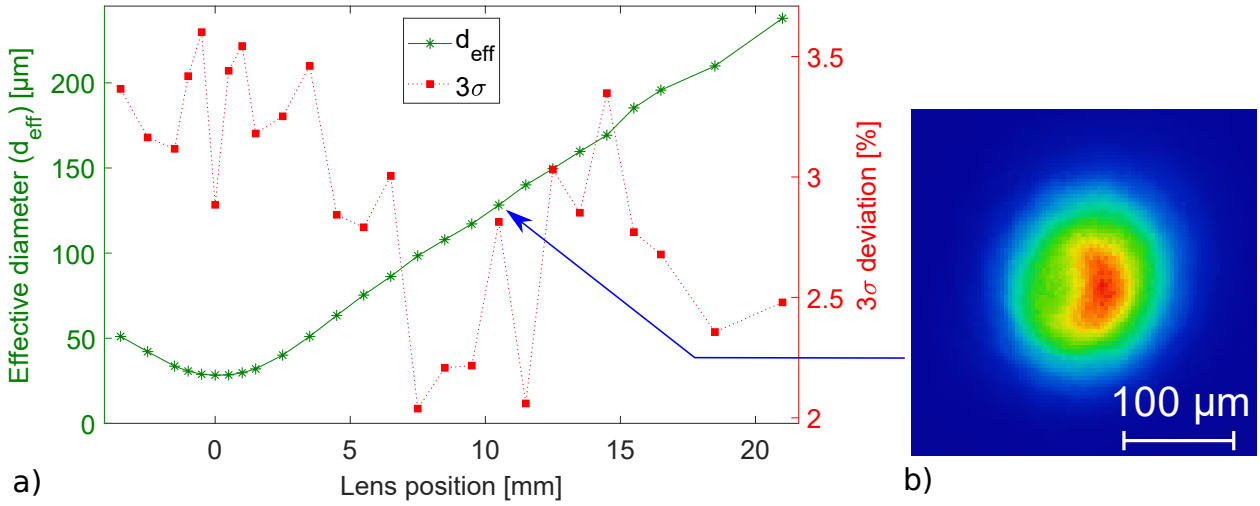

Figure 6.3: Beam profile of MHz sub-ps green laser measured with a sensor of 3.45 µm pixel length: a) effective beam diameter (d_{eff}) and 3σ standard deviation of effective area as a function of lens position; b) beam profile corresponding approximately to the lens position used for LIC tests with effective beam diameter around 130 µm. For lens positions > 0, the CMOS sensor of the beam profiler is farther from the lens than the focal plane.

filter (ND3-4) and the combination of HWP and TFP. We applied minimum exposure time of 39 µs, which corresponds to ≈ 82 pulses and ≈ 44 frames per second.

For one lens position, 100 frames were recorded. The effective beam areas were analyzed using the maximum exposure value detected on one pixel, i.e. no averaging method was used. The dependence of effective beam diameter on lens position is shown in Fig. 6.3 with the beam profile corresponding to the one used for LIC tests. At the focal plane, the effective beam diameter was ≈ 30 µm, whereas the diameter used for LIC tests was around 130 µm. We found values of $3\,\sigma$ deviations of beam area reaching up to $\approx 3.5\%$.

6.1.3 Samples

The samples tested for LIC growth were dielectric oxide single layer coatings whose parameters are listed in Table 6.1. We tested SiO_2, HfO_2 and Nb_2O_5 single layers on fused silica substrates. The SiO_2 coatings were deposited by magnetron sputtering (MS) and plasma-ion assisted deposition (PIAD). In the case of HfO_2, the fabrication methods were MS, PIAD and ion-beam sputtering (IBS). The Nb_2O_5 coatings were made only by MS.

The LIC tests are performed on coatings with thicknesses ranging from 131 nm up to 475 nm. Except an IBS layer coated on 6 mm thick fused silica and a 150 µm thin substrate of a sample dedicated for ex-situ XPS analysis (Sec. 6.3.2), the substrate was 2 mm thick fused silica. The coatings were deposited at Institut Fresnel, with the exception of IBS HfO_2 coating produced by Laboratoire Matériaux Avancés.

6.1.4 Test procedure

The LIC tests with the coated samples were performed at full laser power of $\approx 35\,W$ for a large scale of durations ranging from 2 seconds up to 6 hours. The duration of LIC test was given by switching the amplifier of the laser source on and off; not by the operation of mechanical shutter.[1] The irradiation of a

[1] This precaution was introduced to prevent damage to the mechanical shutter.

Material	Deposition	Thickness [nm]	Producer
SiO_2	MS	150; 300; 450	IF
	PIAD	475	
HfO_2	MS	150; 450	IF
	PIAD	150; 300	
	IBS	131	LMA
Nb_2O_5	MS	150	IF

Table 6.1: Single-layer coating materials intended for laser-induced contamination tests. The coatings produced by magnetron-sputtering (MS) and by plasma-ion assistance deposition (PIAD) were coated at Institut Fresnel (IF) on 2 mm thick fused silica substrates. The ion-beam sputtered (IBS) coating was deposited in Laboratoire Matériaux Avancés (LMA) on 6 mm thick fused silica.

tested sample was stopped either if catastrophic damage was detected with the in-situ microscope, to avoid contamination by surface debris, or at the end of the intended irradiation time for further ex-situ analysis. After irradiation of a given spot on the sample was completed, the next test was performed at a sufficient distance from the previous one to avoid any laser-induced surface modification before the given test. The usual distance between the irradiated spots was 1 mm and the effective beam diameter was $\approx 130\,\mu m$.

6.1.5 Error contributors

We estimate the uncertainty in LIC thickness measurement via optical profilometry to be around ± 1 nm. Another source of uncertainty is connected to focal plane determination. Due to the chosen step in lens positions and sensitivity of used in-situ imaging, we assume uncertainty in focal plane determination around ± 0.5 mm. This causes an uncertainty in the effective beam areas and thus in the values of fluences for LIC testing of about 10%. Thus, we consider this error contributor to be significantly larger than the pulse-to-pulse variations of beam sizes or pulse energies.

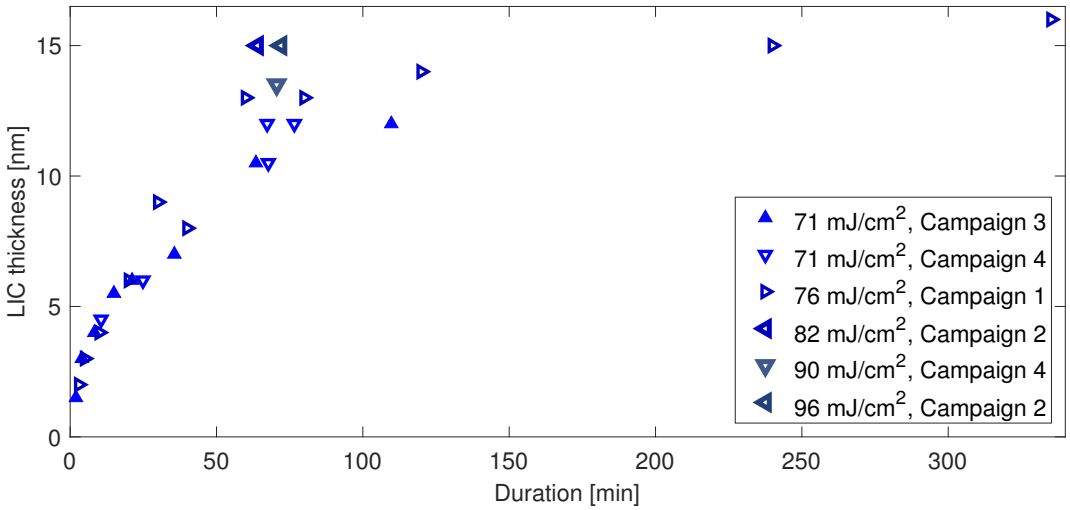

Figure 6.4: LIC deposit thicknesses on 450 nm thick MS SiO_2 coating show good experimental reproducibility across four LIC test campaings. The legend shows experimental fluences. The LIC deposit thicknesses correspond to the maxima found on spot areas analyzed using the optical profilometer.

Despite these uncertainties, our comparison of results between the LIC campaigns (Fig. 6.4) indicates good experimental reproducibility.[2] This is valid for both the initial growth rate of the LIC deposit and the maximum height at which it saturates. The comparison of LIC deposit growth dynamics between four campaigns was done for 450 nm thick SiO_2 coatings produced by magnetron-sputtering in the same deposition batch. The results suggest a trend that a slight increase in the irradiation fluence of the coating tends to result in a modest increase in the LIC deposit thickness. This generalization is valid assuming that the uncertainty of the LIC thickness measurement by used optical profilometer is approximately ± 1 nm.

6.1.6 Optical Profilometry with Low Coherence Interferometry

A non-contact non-destructive method which allows to get information about the surface profile with a vertical resolution in nanometer scale is optical profilometry. The method is based on principle similar to Michelson's interferometer, see Fig. 6.5a). [309] A white light source beam is split in an objective into two waves, one is directed to a reference mirror and the other to the sample. If the two waves, coming from the reference mirror and the sample, are in phase, we get constructive interference on the camera. If these waves are out of phase, we have destructive interference.

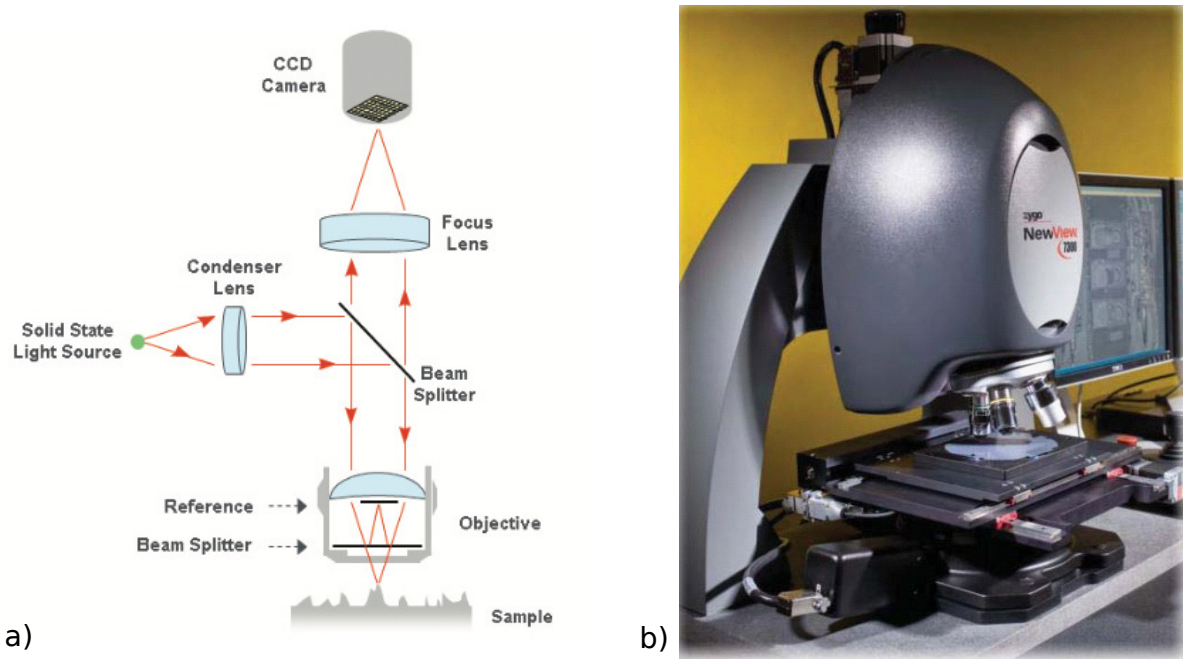

Figure 6.5: Optical profilometry: a) schematic drawing from [309]; b) Zygo NewView 7300 device used in this work.

Using a piezoelectric device, we can perform a vertical scan of the sample surface to record interferences mapping the surface profile. We use light of large spectral bandwidth (white light), which is connected via the uncertainty principle to low coherence length. Therefore, we can observe interferences only in a small region of beam path differences, i.e. only for small range of sample vertical positions. Thus, the spectrally broad light source increases the sensitivity required for LIC deposit measurement at nanometer scale.

[2] The LIC campaigns were conducted over 2 years, during which we recorded a decrease in laser source power of only few percents.

In this work, we used optical profilometer - device Zygo NewView 7300 shown in Fig. 6.5b). Evidence of the high sensitivity of the LIC deposit measurements is shown in Fig. 6.6, which compares spots on 300 nm thick PIAD HfO_2 irradiated for durations ranging from 3 s up to 2 h 22 min. We see that already after 3 s long irradiation, we were able to detect a LIC deposit of 1 nm thickness. The series of spots correspond to the LIC deposit growth shown in Fig. 6.11 for 300 nm thick monolayer of HfO_2 produced by PIAD method. An example of LIC deposit observation via optical profilometer for a 450 nm thick magnetron-sputtered SiO_2 coating, irradiated for 6 hours long test, was shown in Fig. 6.1b).

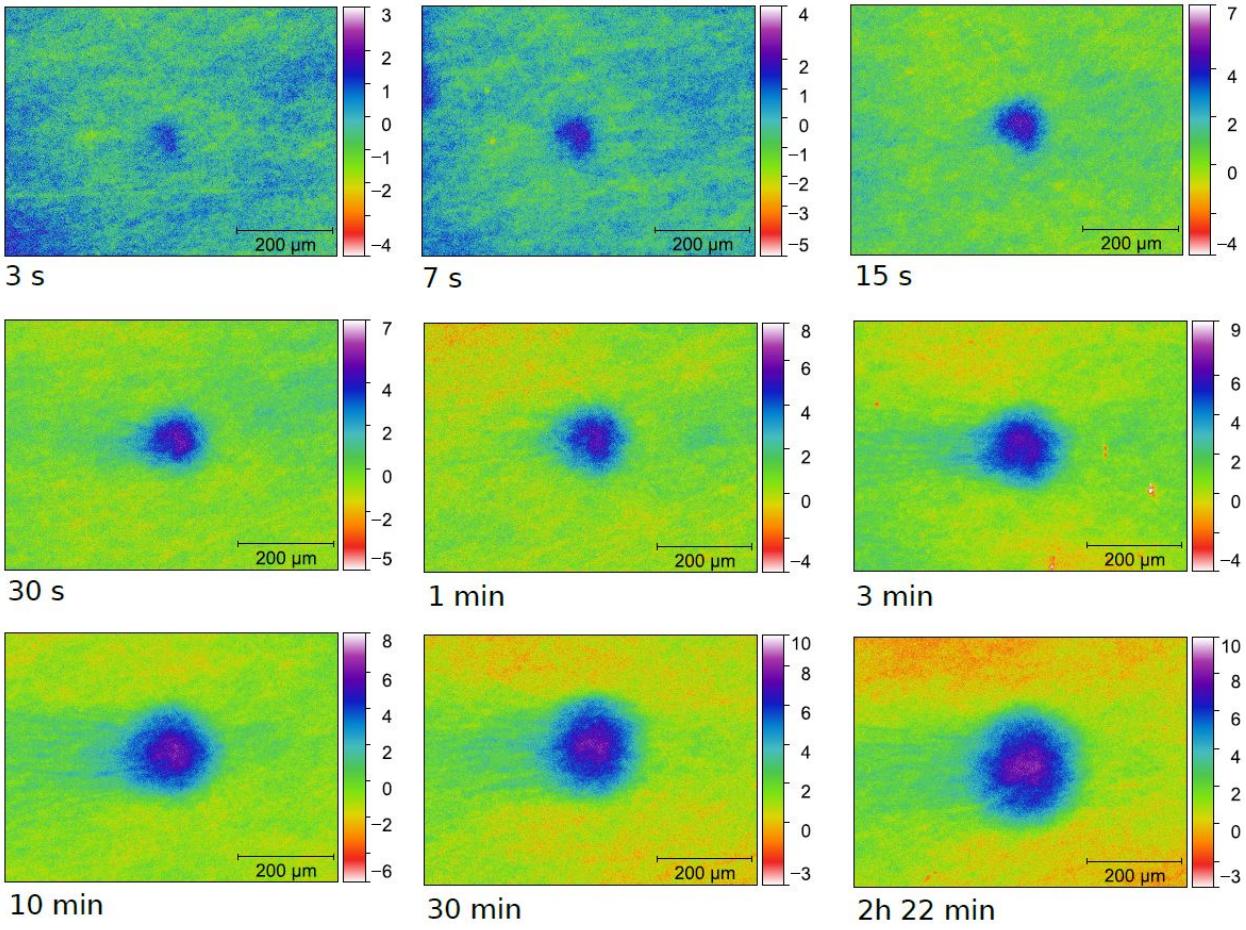

Figure 6.6: Laser-induced contamination deposits on PIAD HfO_2 coating of 300 nm thickness irradiated by pulses of 515 nm laser wavelength at a repetition rate of 3.3 MHz and power of ≈ 35 W.

6.2 Parametric study

In this work, we aimed to study the LIC growth dynamics, dependence of LIC deposit thickness on test duration. Thanks to the access to numerous samples, whose parameters are listed in Table 6.1, we could study the LIC growth dynamics as a function of coating material, its deposition method and thickness. The LIC deposit thicknesses presented in this section correspond to the maxima found on spot areas analyzed using the optical profilometer.

In majority of LIC tests we use experimental fluences between 70 and 80 mJ/cm^2, which is 1-2 orders of magnitude lower fluence than the LIDTs of dielectric coating monolayers determined with 500-fs 1030-nm 10-Hz setup, see Fig. 4.9c) on page 106. The results presented in the parametric study are expressed in experimental fluences to enable comparison with previous parts of this thesis. In Table 6.2, we list correspoding values of used mean and peak intensities.

Experimental fluence [mJ/cm^2]	Mean intensity [kW/cm^2]	Peak intensity [GW/cm^2]
50	165	71
60	198	86
70	231	100
80	264	114
90	297	129

Table 6.2: Conversion between physical quantities. Majortity of LIC tests was done with experimental fluences between 70 and 80 mJ/cm^2.

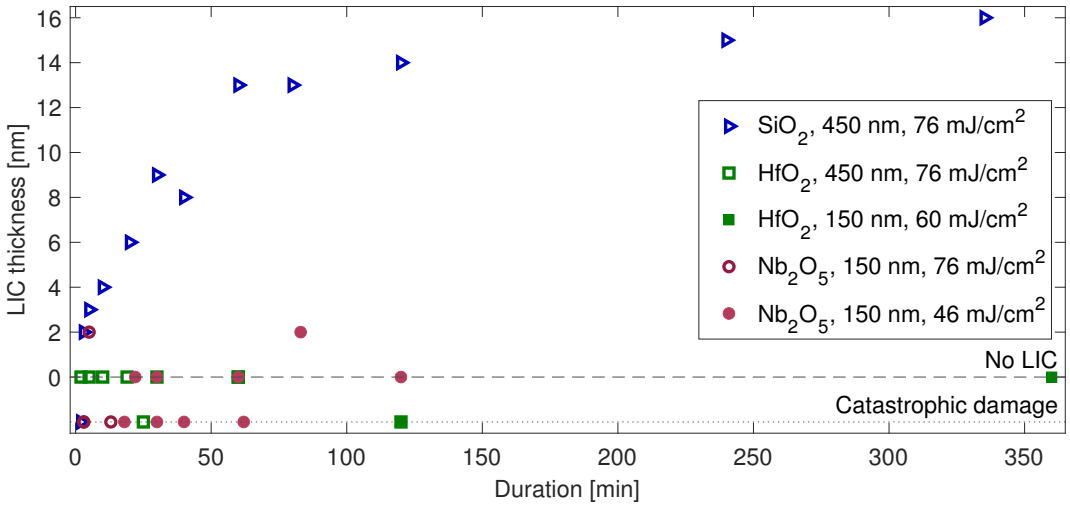

Figure 6.7: Effect of material on LIC dynamics. All results refer to samples deposited by magnetron sputtering and tested in the same LIC campaign. On the irradiated sites of HfO_2, we did not detected any contamination deposit. In the case of Nb_2O_5, the growth of contamination layers thicker than 2 nm was not possible, since the irradiation conditions were close to damage threshold at 3.3 MHz repetition rate.

6.2.1 Effect of material

In Fig. 6.7, we summarized results for three magnetron-sputtered coating materials: SiO_2, HfO_2 and Nb_2O_5, obtained within the same LIC test campaign. At the experimental fluence of 76 mJ/cm^2, the LIC deposits thicker than 2 nm were clearly observed only for SiO_2 coating, while for HfO_2 samples we either did not detect any surface modification or in some cases catastrophic damage. In the case of 150 nm thick HfO_2, we did not detect any LIC deposit even after 6 hours long irradiation using fluence of $\approx$ 60 mJ/cm^2. For 150 nm

thick Nb_2O_5, it was also hard to find good conditions for LIC growth since this material is susceptible to damage at conditions we used. Nevertheless, in two cases we found 2 nm thick LIC deposits.[3]

If we focus on the LIC deposit growth dynamics on SiO_2 coating, we can distinguish between growth phase and saturation period. Already after 3 min long irradiation we found LIC deposit of 2 nm thickness. For 5 min long irradiation it was 3 nm. LIC deposit thickness of 4 nm was reached after 10 min, and 6 nm after 20 min long irradiation. These results thus indicate that the LIC thickness growth rate is highest at the beginning of irradiation (up to 1 nm per minute) and gradually decreases. After 60 min long irradiation, the rate of LIC deposit thickness growth is noticeably reduced ($\leq$ 1 nm per hour) and deposit thickness saturates.

6.2.2 Effect of thickness

The effect of coating thickness on LIC growth dynamics was studied with magnetron-sputtered SiO_2 coatings and with HfO_2 produced by PIAD. For the SiO_2 coatings with the thicknesses of 150, 300 and 450 nm, the results plotted in Fig. 6.8 show clear correlation between the coating and LIC deposit thicknesses. The results suggest linear dependence of the final (saturated) LIC deposit thickness and the initial growth rate on the coating thickness.

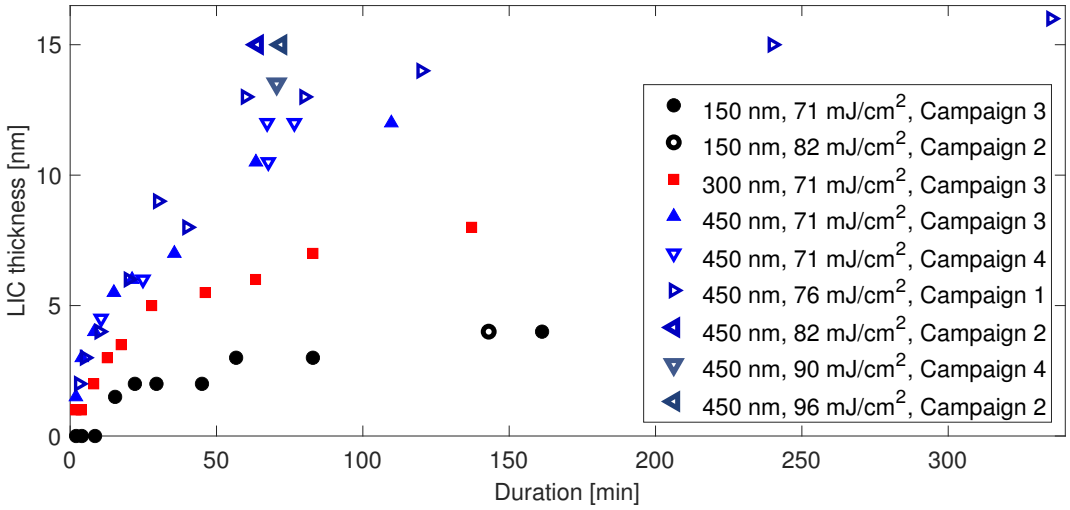

Figure 6.8: Effect of MS SiO_2 coating thickness on LIC growth dynamics. The results of LIC deposits obtained in four campaigns are close to each other, indicating a good experimental reproducibility.

The impact of coating thickness on LIC deposit growth dynamics was also investigated with PIAD deposited HfO_2 monolayers.[4] The results for detected LIC deposits on 150 nm and 300 nm thick HfO_2 monolayers are plotted in Fig. 6.9. For 150 nm thick PIAD HfO_2, we found LIC deposit thickness saturation after $\approx$ 20 min long irradiation at the level of 4 nm. In the case of 300 nm thick PIAD HfO_2, the saturation occurred also after $\approx$ 20 min but the LIC deposits were around 7 nm thick. Assuming the uncertainty of the LIC thickness measurement $\pm$1 nm, the hypothesis of linear dependence of saturated LIC deposit thickness

[3] We performed several tests on 150 nm thick MS Nb_2O_5 coating also with repetition rates from 1 to 2 MHz to decrease the material overload and susceptibility to be damaged. However, we did not find good conditions to study LIC growth dynamics on this material.

[4] The PIAD deposition of HfO_2 monolayers thicker than 400 nm is technologically challenging.

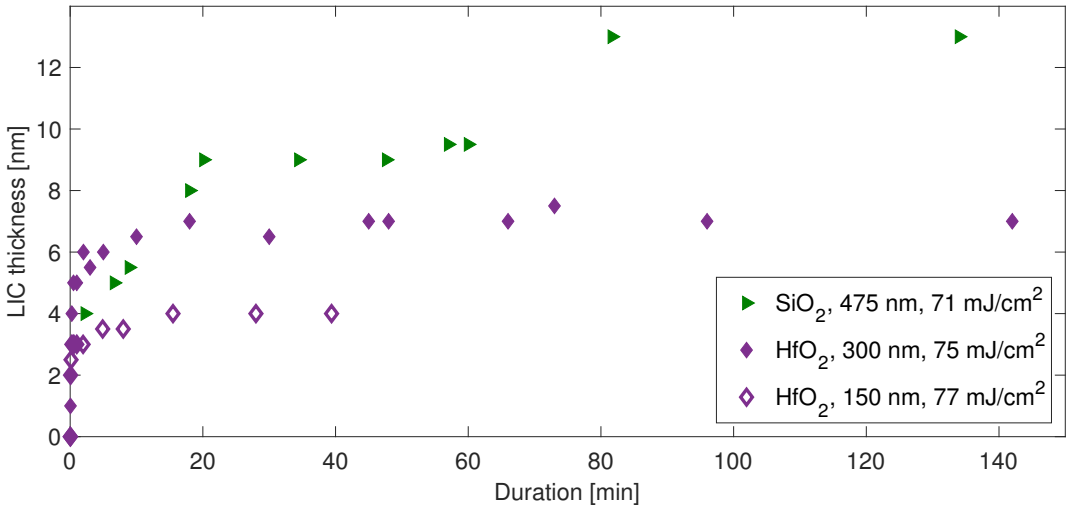

Figure 6.9: Effect of PIAD material and HfO_2 coating thickness on LIC growth.

on coating thickness is still valid. The PIAD SiO_2 coating was the thickest coating (475 nm) and shows also thicker LIC deposits (up to 13 nm) than ones detected on HfO_2.

In comparison to LIC deposit growth dynamics with MS SiO_2 (Fig. 6.8), the growth in the early phase of irradiation seems to be much faster on PIAD coatings (Fig. 6.9). For instance, in the case of 300 nm thick PIAD HfO_2, we detected a LIC deposit of 3 nm thickness already after 8 sec long irradiation, and 5 nm after 30 sec. The very dynamic growth of LIC deposit on the PIAD HfO_2 is evidenced also from images of irradiated spots in Fig. 6.6 captured by the optical profilometer.

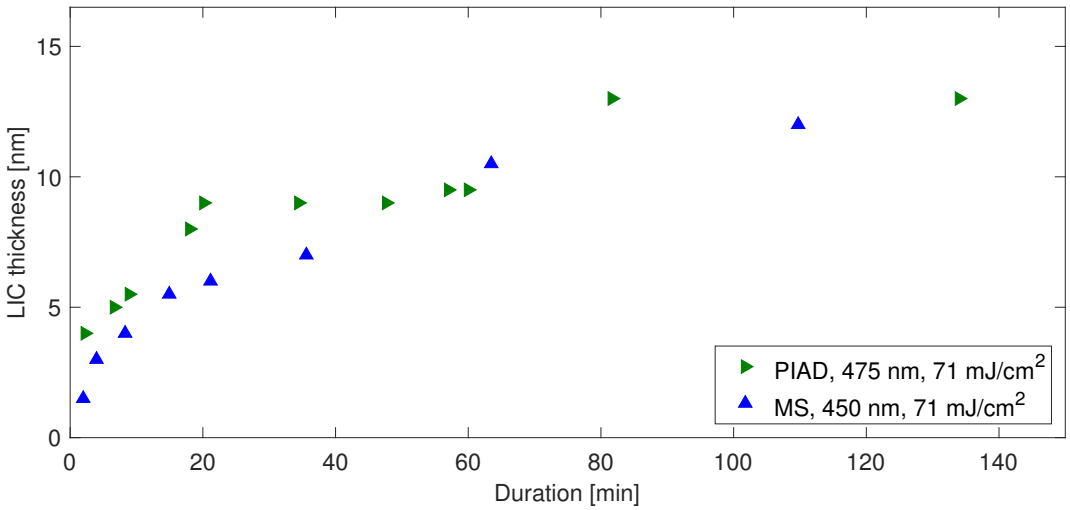

Figure 6.10: Effect of deposition method on LIC growth on SiO_2 coatings, which were produced by plasma-ion assistance deposition (PIAD) or by magnetron sputtering (MS).

6.2.3 Effect of deposition method

Within this work on laser-induced contamination, we compared LIC growth dynamics across the deposition methods for both SiO_2 and HfO_2 coatings. Comparison of LIC thicknesses between MS and PIAD deposited SiO_2 coatings of similar thicknesses (PIAD 475 nm, MS 450 nm) is shown in Fig. 6.10. The main difference in dynamics is at the earliest phase of irradiation. After 2 min long LIC test, PIAD coating showed 4 nm thick deposit whereas for MS one it was only 1.5 nm. The PIAD SiO_2 thus shows faster growth than the MS SiO_2 coating within the first 40 minutes of irradiation. For LIC test durations longer than 40 minutes, the difference in LIC deposit thicknesses between the samples is not significant.

In the case of HfO_2, we compared material responses to the laser irradiation of MS, PIAD and IBS deposited coatings, see Fig. 6.11. We found no LIC deposits on irradiated spots of MS and IBS coated HfO_2 even after 6 hours long tests. At the same time, we observed that these coatings are susceptible to catastrophic damage formation when irradiated at a fluence of 76 mJ/cm^2. In the case of MS HfO_2, a catastrophic damage was observed even at 60 mJ/cm^2. The only deposition method that allowed the observations of contamination growth dynamics on HfO_2 coating was the PIAD.

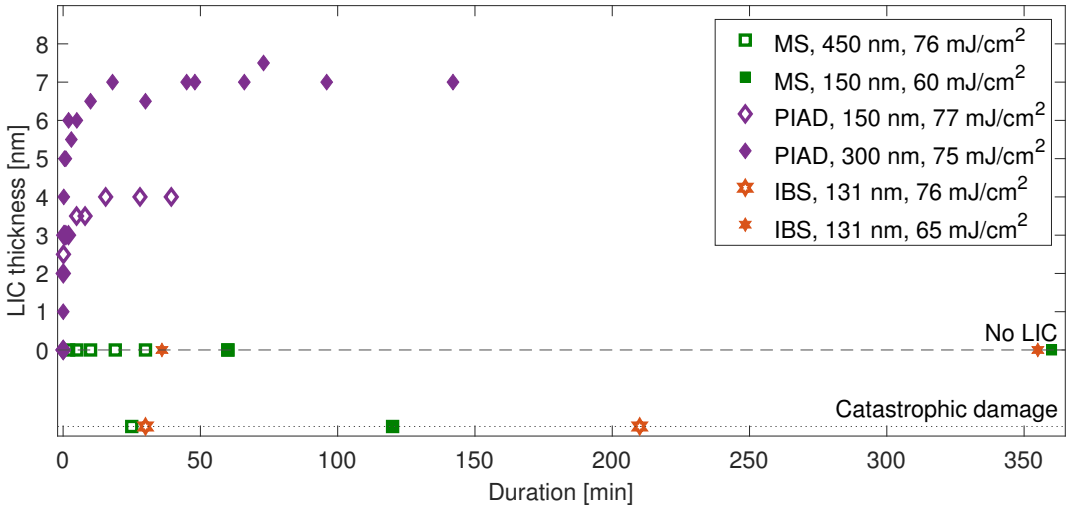

Figure 6.11: Effect of HfO_2 deposition method and coating thickness on LIC growth.

6.3 Characterization of the LIC deposits

In this section, we summarize results obtained with the characterization techniques: fluorescence, X-ray photoelectron spectroscopy and scattering-type scanning near-field optical microscopy. We used these methods to analyze LIC deposits on thin-film coatings in order to get maximum information about deposit topography, chemical composition, or optical properties to go further in the understanding of LIC.

6.3.1 Fluorescence

The absorption of photons at excitation wavelength leads to an excitation of electrons, which later relax back to the ground state and release a part of stored energy in emitted photons. The emitted photons have lower energies than the original excitation ones. The more an organic molecule is able to conjugate electrons, the

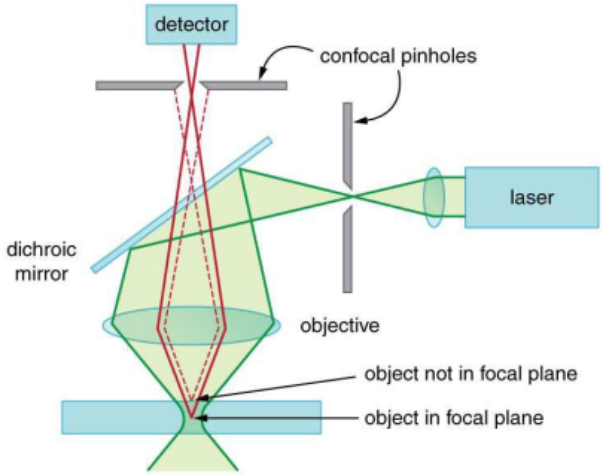

Figure 6.12: Schematic of confocal microscope for fluorescence measurements. Schematics is taken from [310].

more its emission spectrum is red-shifted. The red shifted spectra have, for example, carbon-based structures such as aromatic compounds and alkenes.

We investigated some of the irradiated spots by ex-situ fluoresence confocal microscopy, since the contamination layer may produce photo-luminescence signal that could help to gain insights on its composition. We acquire fluorescence images to detect differences in the chemical composition of the LIC deposits obtained for different irradiation times. For this purpose, we use a confocal microscope allowing imaging with high resolution. The term confocal refers to the fact that two pinholes are placed in the beam path from laser source to detector, see Fig. 6.12, in order to obtain a clear image of the viewed object by filtering the light which is not focused. [310] If we wish to image the fluorescent object in 3D, we have to scan it plane by plane.

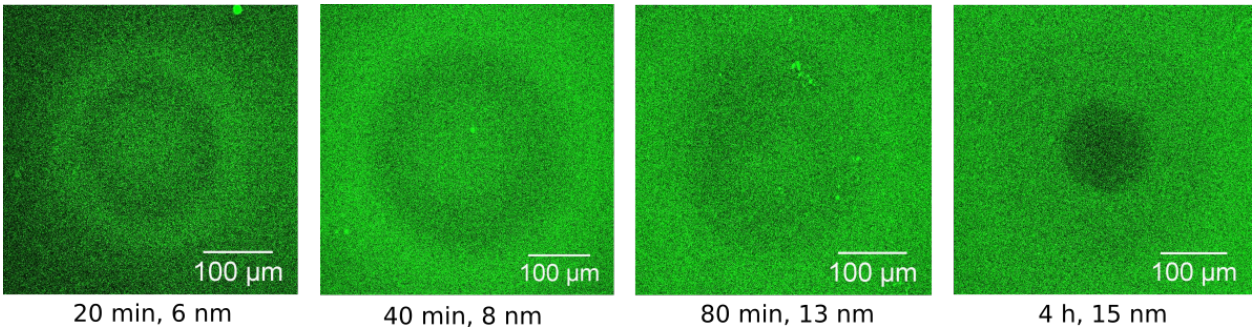

Figure 6.13: Spots on MS SiO_2 coating of 450 nm thickness observed by ex-situ confocal fluorescence microscope (Leica TCS SPE). Excitation wavelength was 405 nm. Images were captured using 10x objective magnification with the light spectrum ranging from 455 to 800 nm. The labels below the images indicate the exposure duration and LIC deposit thickness determined by the optical profilometer.

We used a confocal microscope (Leica TCS SPE) with an excitation wavelength of 405 nm and detection range from 455 to 800 nm. In Fig. 6.13, we show 2D images of spots on 450 nm thick MS SiO_2 coating. The fluorescence images show spots that were tested for LIC growth by green laser light exposures ranging from 20 minutes to 4 hours.

The evolution of changes in the irradiated spot images suggests that the deposits have an inhomogeneous

chemical nature. We first observe the growth of the deposited area - up to 80 minutes. Subsequently, a second transformation of the deposit occurs which further reduces the fluorescence yield. Such material transformation when saturation is reached was reported for UV nanosecond pulses in vacuum. [303] A possible reason why we see darker central region in the case of the 4 hour long test is that the contamination layer may absorb some of the fluorescent or excitation light.

Another hypothesis is that the LIC deposit could act as an interferential layer. This effect was described in details by G. Reaidy [160,303], who found that the effective refractive index of LIC deposit can be lower than that of the surrounding fused silica substrate due to its nanometric porosity. Such a layer exhibits slightly antireflective characteristics which were observed during the early phase of the LIC deposit evolution. In our case, the antireflective characteristics could explain the observed dark spot while the surrounding areas absorb the light and induce fluorescence more easily.

For deeper investigation of LIC deposits, it might be useful to measure transmission and reflection spectra of the contaminated spots, which is challenging due to the small thickness of the deposit. We should also irradiate the LIC deposits by other excitation wavelength, yielding more fluorescence light. Ideally a fluorescence excitation spectra could be acquired. Finally, at this point the signal of studied LIC deposits have not given information on their composition, but only on the evolution and the structure.

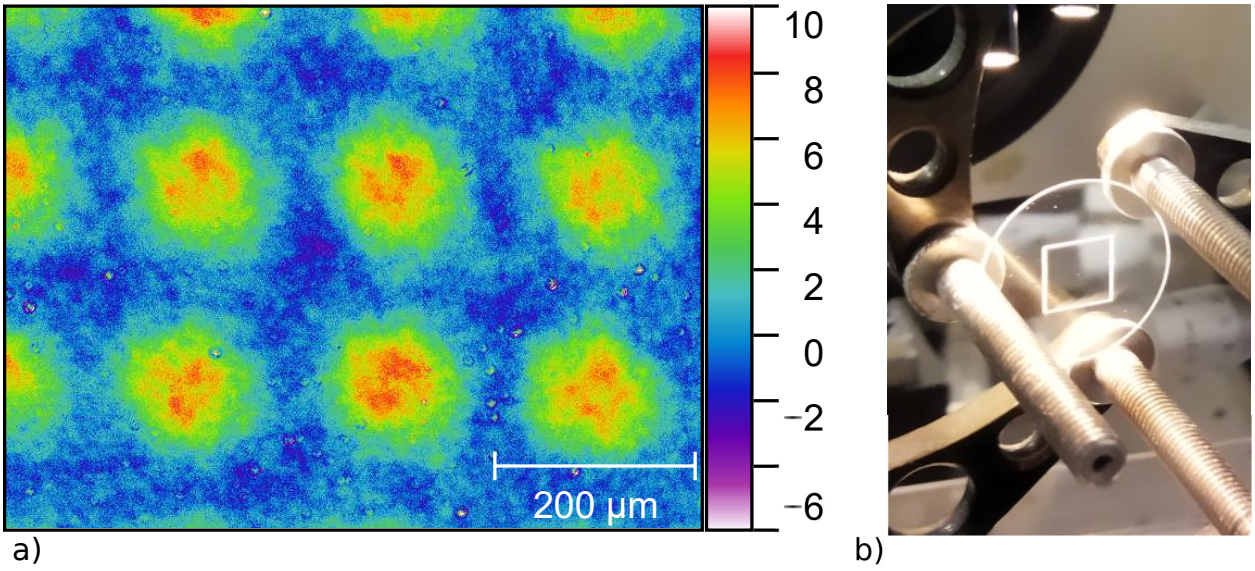

Figure 6.14: Preparation of contaminated sample for XPS analysis: a) image captured by the optical profilometer showing a part of area with 5x5 spots of LIC deposits on 450 nm thick PIAD SiO_2 coating; b) the same sample containing 150 µm thick substrate placed in the holder. The square inside the rounded sample was laser cut to be studied further using a XPS device.

6.3.2 XPS analysis

To be able to reply on question from where the LIC deposit originates, we need to know its chemical composition. The elements that are present near the material surface (in the depth up to 10 nm) can be determined by X-ray photoelectron spectroscopy (XPS). [311, 312] Surface characterization by XPS is performed by irradiating a material in vacuum with soft x-ray radiation[5] and measuring the kinetic energy

[5] In our case we used a Mg source emitting at 1253.6 eV.

of the emitted photoelectrons. XPS is a surface-sensitive quantitative spectroscopic technique based on photoelectric effect that can determine the chemical state, electronic structure and density of electronic states in a material in addition to the elemental composition. XPS is a measuring technique that can identify the chemical bonding and composition in the top few atomic layers of a material's surface. [313]

Due to size constrains of the sample in the XPS apparatus [314], we did not analyse the same samples, for which the results are shown in the parametric study of LIC (Sec. 6.2), but we had to cut a sample of 1 inch diameter to a size smaller than 1 cm^2. Therefore, we firstly generated several identical LIC deposits on 150 µm thin SiO_2 substrate of high optical quality and then the sample was accurately cut by laser beam directed by a galvoscanner, see Fig. 6.14. We used such a thin substrate (coverslip) to facilitate cutting with the laser beam.

Prior to cutting, the substrate was coated with 450 nm thick SiO_2 layer deposited by PIAD method. To increase the sensitivity of XPS measurement[6], we created an array of 5x5 spots on the SiO_2 coating, see Fig. 6.14a). Each of these irradiations lasted 30 min and resulted in LIC deposit thicknesses of around 8 nm. At this irradiation time the mean growth is done, but we are not yet in the saturation zone, see Fig. 6.8.

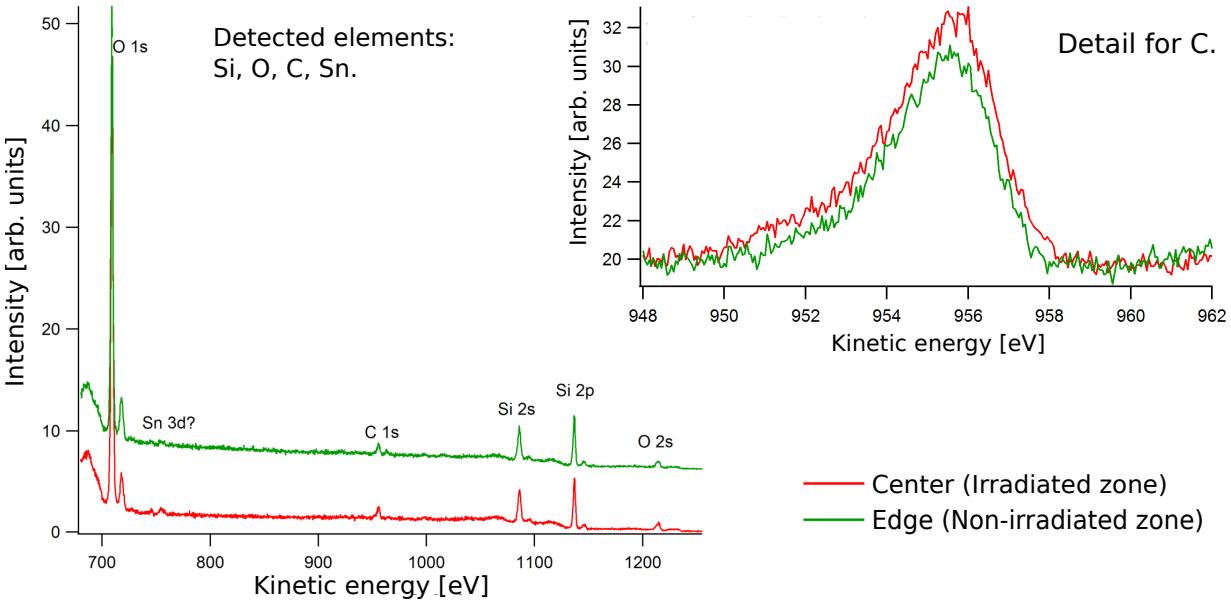

Figure 6.15: Comparison of spectra between the two analyzed zones on SiO_2 sample: center part with array of LIC deposits (red) and edge of sample which was not irradiated by the laser. This XPS analysis revealed presence of Si, O, C and Sn. The largest difference between the two analyzed zones, detailed in the inset for C, suggests that there may be carbon compounds characteristic to the LIC.

Afterwards, a laser-cut square sample, see Fig. 6.14b), containing the array of LIC deposits was moved to PIIM laboratory (Physique des Interactions Ioniques et Moléculaires), where the XPS measurement was performed. The XPS measurement was performed on LIC and no-LIC zones on SiO_2 sample, see Fig. 6.15, in order to determine the effect of 30 min long irradiation on the chemical composition of the surface. The spectra of the examined zone are similar and we can detect the presence of silicon, carbon, oxygen and tin. The main difference in spectral characteristic between the two analyzed zones was found for carbon. As shown in the inset in Fig. 6.15, the carbon peak is slightly higher in the irradiated zone. This increment suggests

[6]Spot analyzed by the used XPS has a diameter of around 300 µm.

that the LIC deposit is at least partially composed of carbonaceous material. Nevertheless, the difference between zones were minor and additional studies probing the vibrational modes of adsorbed species are needed to understand the nature of such carbonaceus species.

6.3.3 Scattering-type scanning near-field optical microscopy

As a part of our investigation on LIC, we analyzed a spot on 450 nm thick magnetron-sputtered SiO_2 coating via ultra-resolution method called scattering-type scanning near-field optical microscopy (s-SNOM). [315] The s-SNOM technique uses a focused light beam that illuminates the sharp tip, see Fig. 6.16a), which approaches and scans sample to produce a topographic image simultaneously with the optical signal from the tip-sample interaction. Compared to the atomic force microscopy (AFM), in the s-SNOM method, the scattered light is also recorded, thereby generating an optical image. In principle, a lighted particle can increase optical fields in its vicinity, which are modulated by the presence of a sample. As a result of this near-field interaction, the scattered light conveys information about the sample's local optical properties. Excitation of a sample can be used to get particular contrast, for example, molecular vibrations provide a spectroscopic fingerprint that can be used to identify chemical composition. The mechanical and the optical resolution of s-SNOM is given by the radius of curvature at metallized tip apex.

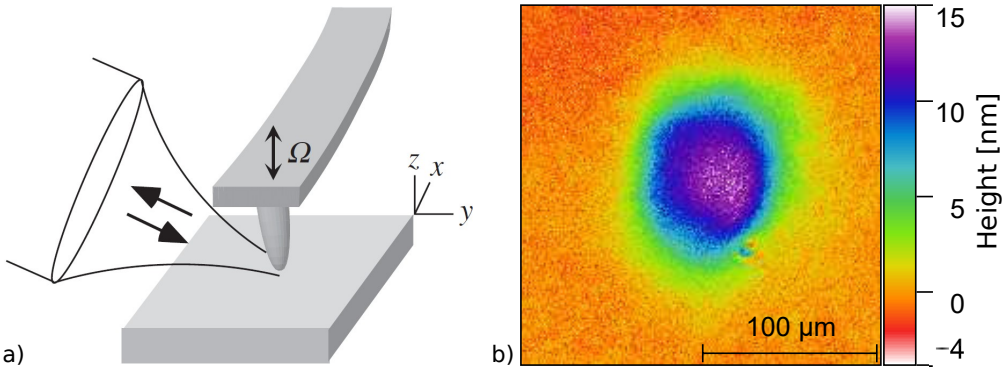

Figure 6.16: Characterization of magnetron-sputtered 450 nm thick SiO_2 coating: a) principle of s-SNOM (image taken from [315]) and b) spot captured by the optical profilometer. The spot is intended to be analyzed by s-SNOM.

The spot on SiO_2 was irradiated for 70 minutes and using the optical profilometer we determined the deposit thickness of 13.5 nm, see Fig. 6.16b). Afterwards, we analyzed the deposit using a Neaspec-Attocube s-SNOM system, which enables to capture a maximum squared area with a 80 µm long edge. The system allows to achieve resolution limit in height around 5 nm, if the investigated sample is clean and smooth.

Despite the deposit thickness larger than the resolution limit of used s-SNOM device, we did not identify any sample surface abnormality that could be related to LIC deposit. A possible reason could be low contrast on sample surface, since the spot diameter is around 100 µm whereas the imaged area with s-SNOM was chosen to be a square with a 15 µm long edge. Since the LIC spot diameter is larger than the area, analyzed by s-SNOM, centered over the LIC region where the changes are quite homogeneous, see Fig. 6.16b), we did not observe any changes even with the high lateral and axial resolution (100 nm and $\sim$ 5 nm respectively). Thus, for future measurements via s-SNOM, we recommend to analyze a deposit of diameter ideally around 10 µm with high height contrast. In this case, the size of the investigated object is smaller than the maximum scan size and one can also improve the lateral resolution down to 20 nm instead of 100 nm by increasing the number of points recorded over a smaller scan region.

6.4 Thermal effects

To advance our understanding of LIC, we explored the thermal effects associated with deposit growth. Indeed, the formation of a contamination layer under the laser spot leads to absorption of a fraction of the laser power which can lead to an increase in local temperature. Furthermore, the coupling of laser radiation in the coating due to linear or nonlinear absorption processes can also lead to heat accumulation, which can contribute to the LIC process both in its initiation and growth phases.

In our experimental conditions the laser fluence reached 71 mJ/cm^2 with a pulse repetition rate of 3.3 MHz. Under these conditions, the increase in surface temperature could play an important role in the laser-induced deposition process. The adsorption and sticking coefficient of volatized compounds on surfaces are temperature-dependent processes and thermal effects have already been suggested as a possible contribution of LIC. [11]

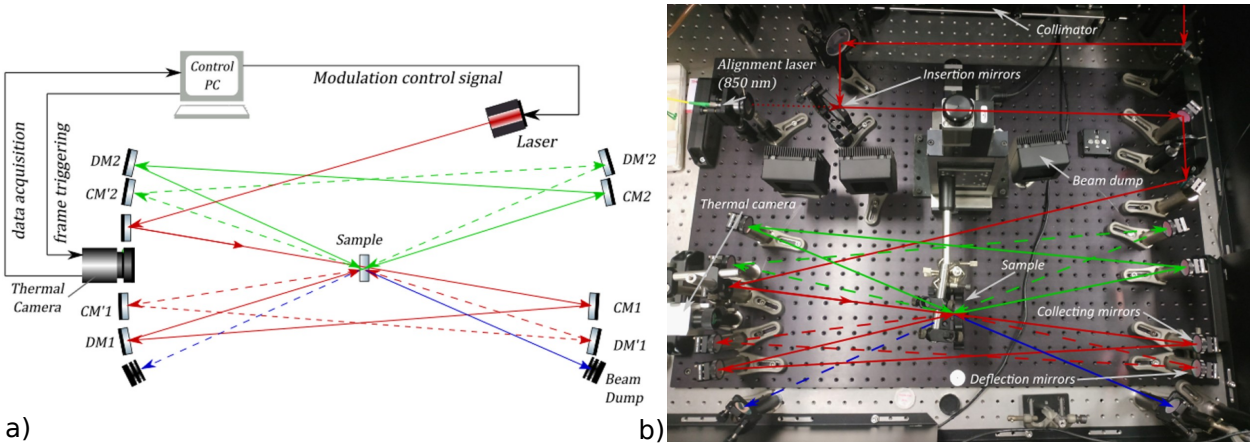

Figure 6.17: Lock-In Thermography setup at a wavelength of 1 µm used for absorption measurement: a) schematic, b) photograph. For clarity, the beam color is modified after each pass. The sample works as a beam splitter with directions for reflected and transmitted beams. Figure taken from [316].

6.4.1 Absorption measurements

The observed LIC deposit growth on tested coatings might be connected to thermal effects as it was shown in study [11] performed at similar irradiation conditions to our work. Since the thermal effects are linked to the absorption in thin-film coatings, we carried out measurement of absorption using Lock-In Thermography (LIT) method with a setup developed in PhD work of Camille Petite. [316] The setup uses a high-power CW laser at 1.07 µm with accessible output power up to 1.5 kW. Using reflective components, see Fig. 6.17, the incident laser beam is recycled to be transmitted or reflected by the measured sample multiple times in order to increase the sensitivity (signal-to-noise ratio) of absorption measurement. The multipass setup allowed the measurement of absorption at the ppm level with a precision of 11 %.

In Table 6.3, we summarize absorption measurement results for SiO_2 and HfO_2 coatings produced by both magnetron sputtering and electron beam deposition with plasma-ion-assistance. We found broad range of absorption values between the measured coated samples, covering 2 orders of magnitude. The result is surprising since the samples were not irradiated before the absorption measurement. A possible reason of such large discrepancy in absorption could be related to local defects whose nature (emissivity, size) is not

Material	Deposition	Batch	Thickness	Absorption	LIC presence
			[nm]	[ppm]	
SiO_2	MS	#1	150	7.4	yes
SiO_2	MS	#1	300	106	yes
SiO_2	MS	#1	450	8.7	yes
SiO_2*	PIAD	#3	300	5.1	-
SiO_2	PIAD	#4	475	564	yes
SiO_2*	PIAD	#5	600	7.6	-
HfO_2	MS	#2	150	6.3	no
HfO_2	MS	#2	450	10.3	no
HfO_2	PIAD	#6	300	231	yes
HfO_2*	PIAD	#7	300	18	-
HfO_2*	PIAD	#8	600	29	-
FS Corning 7980	-		0	2.0	-

Table 6.3: Results of absorption measurement at 1 µm done for coatings of different thicknesses deposited on fused silica substrate (FS Corning 7980). Coating deposition method was either magnetron sputtering (MS) or electron-beam deposition with plasma-ion-assistance (PIAD). The LIC presence and the absorption measurement were not studied with the same samples. However, the results of LIC presence correspond to the absorption measurement results done for the same coating material of the same coating thickness, deposited by the identical method in the same deposition batch. For FS, the LIC presence was not studied. The symbol * refers to data taken from [259].

known at this moment. Other causes might handling with the coated samples and different histories that could lead to some surface contamination. We emphasize that care should be taken to the parameters used during deposition process as well as to the cleanliness of surrounding environment. We also point out that these absorption measurements were made at a laser wavelength of 1 µm, and one expects higher absorption at 0.5 µm. For more details, please see [316].

6.4.2 Calculations

Considering the high repetition rate in our irradiation conditions (3.3 MHz) corresponding to 0.3 µs between each shot, the temperature cannot relax back to the ambient temperature between two pulses. The order of magnitude of the τ_r thermal relaxation time is: [316]

$$\tau_r = \frac{w^2}{4D}, \tag{6.1}$$

where D means the thermal diffusivity of the material ($1 \cdot 10^{-6}\,m^2/s$ for fused silica) and w the beam radius incident on the sample. In our case, the beam radius is around 95 µm (at $1/e^2$) which corresponds to the thermal relaxation time of 2 ms. During the high repetition rate irradiation, the temperature should increase to a steady state regime in which the losses compensate for the heat coupled in the coating and deposit by laser absorption. In this case, assuming a semi-infinite material with a surface heat source, the temperature attained using a CW laser can be estimated using the following relationship:

$$\Delta T^{\circ}_{max} = \frac{AP}{2wK\sqrt{\frac{\pi}{2}}}, \tag{6.2}$$

where A is the absorption and K means the thermal conductivity (1.38 W/m/K for fused silica). In our test conditions ($P = 35$ W, $w = 95$ µm), the temperature reached in steady state can therefore be evaluated as a function of absorption: $\Delta T^{\circ}_{max} \approx A \cdot 1.1 \cdot 10^5$ °C. For magnetron sputtered 450 nm thick SiO_2 coating, the absorption measured with Lock-In Thermography is in the order of 10 ppm at 1 µ, see Table 6.3. The absorption of 10 ppm could lead to an increase of temperature by approximately 1.1°C. In our case of irradiation at 0.5 µm, the temperature increase may be higher if the absorption scales with the wavelength. The calculation is of course a gross approximation but it is intended to obtain an order of magnitude of the expected temperature increase. Other simulations could be done e.g. with Finite Elements Method [265], but we will not report them here.

6.4.3 Thermographic measurement

To go further in this investigation, we have implemented an in situ thermographic measurement to experimentally evaluate a possible correlation between temperature increase and LIC growth. We have used a thermal camera (FLIR A655) operating in the Long Wave InfraRed band (8 to 13 µm) with the integration time of 10 ms and the emissivity set to 0.85 for the sample under consideration. The camera was equipped with a macro objective providing a spatial resolution of 100 µm in the imaging configuration, and it was thermally calibrated by the manufacturer. We present in Fig. 6.18 the experimental configuration.

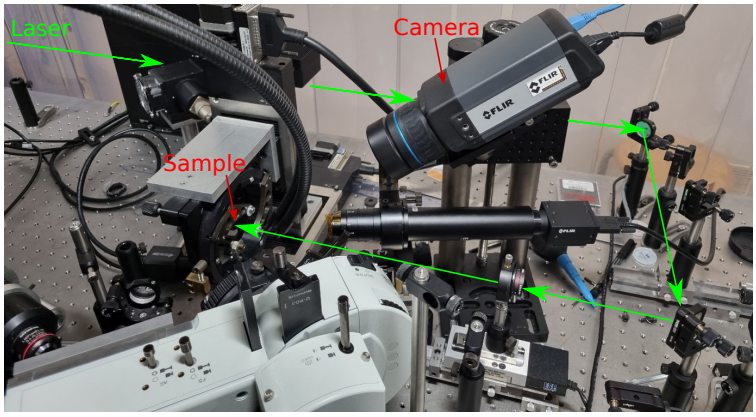

Figure 6.18: Experimental configuration for temperature monitoring.

Experiments were conducted on a magnetron-sputtered 450 nm thick SiO_2 coating. The temperature evolution was recorded during 80 min long laser exposure at 3.3 MHz with a mean power of 35 W and effective beam diameter of 130 µm. After the exposure, the spot was analyzed ex-situ via the optical profilometer and a LIC deposit thickness of around 12 nm was found.

The thermal measurements indicate an increase in temperature of only around 1 °C, see Fig. 6.19a). Furthermore, the temperature increase is not spatially resolved, see Fig. 6.19b). Therefore, these thermal measurements suggest that the LIC formation is mainly a cold process, as opposed to pyrolysis process for instance.

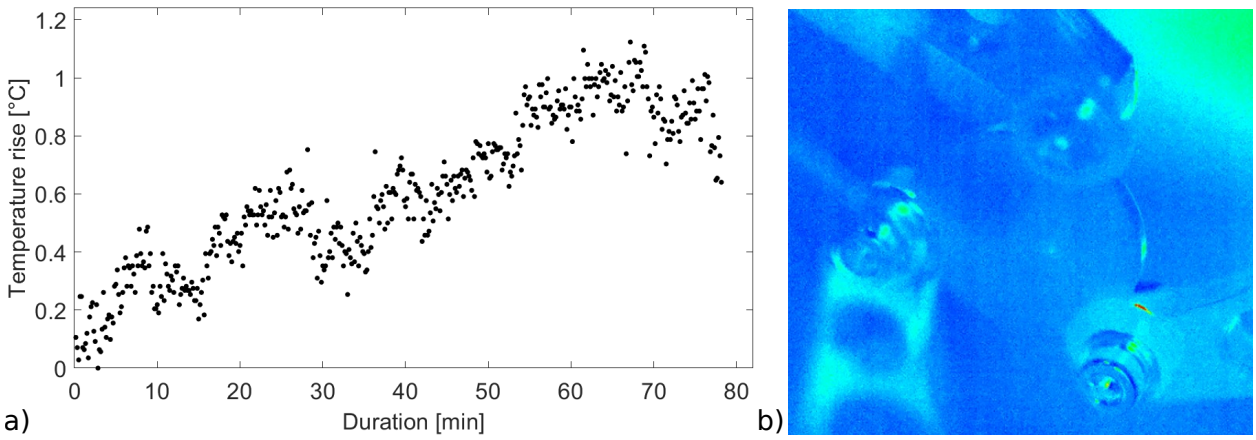

Figure 6.19: Evolution of temperature on 450 nm thick MS SiO_2 coating during the irradiation inducing LIC: a) temperature rise as a function of duration. Exposure time of the camera was 10 ms and the deposit covered a bit more than one pixel. b) Photograph of irradiated sample captured by thermal camera.

6.5 Conclusion

In this Chapter, we tested SiO_2, HfO_2, Nb_2O_5 dielectric coatings in air irradiated by pulses of 700 fs duration with a repetition rate of 3.3 MHz. The aim of this work was to investigate LIC deposit growth on the materials used in optical component designs developed within GREAT project. We found that there is a significant effect of coating material and deposition method on LIC growth dynamics, see Table 6.4.

	MS	PIAD	IBS
SiO_2	LIC	LIC	
HfO_2	No LIC / Damage	LIC	No LIC / Damage
Nb_2O_5	LIC$\leq$ 2 mm / Damage		

Table 6.4: Summary of LIC test results in dependence on coating material and deposition method.

For SiO_2 produced by both MS and PIAD, we found experimental conditions for LIC and studied the dependence of the LIC deposit thickness on irradiation duration and layer thickness. In the case of HfO_2 coating material, we found LIC deposits only on PIAD deposited samples. The results for MS and IBS HfO_2 indicate susceptibility to damage growth. The catastrophic damages were detected also on surfaces of MS Nb_2O_5, for which we did not find LIC deposits thicker than 2 nm.

Our main observations from the parametric study of LIC deposit growth are following:

- We observe a correlation between LIC deposit saturation thickness and coating thickness (which, to the best of our knowledge, has never been reported before). The dependence is approximately linear and was observed for MS SiO_2 and PIAD HfO_2 samples.
- Among the tested samples, the largest saturation thickness of 16 nm was found in the case of 450 nm thick MS SiO_2 coating irradiated for 6 h.
- In the early phase of irradiation, the PIAD samples show more dynamic growth of LIC deposit than MS coatings. The growth rate on 300 nm thick PIAD HfO_2 is 20 times faster than on 450 nm thick MS SiO_2.

In this work, we characterized LIC deposit via optical profilometry, fluorescence microscopy, XPS analysis and s-SNOM. The ex-situ optical profilometry allowed us observe deposit morphology in 3D dimensions. Measurement with fluorescence microscopy shows darker regions on irradiated spots than for the surroundings. It also shows a material transformation during the LIC process. The reduced fluorescence yield at 405 nm may be caused by light absorption in the contamination layer.

To get information about chemical composition of LIC, we analyzed deposit on PIAD SiO_2 coating by XPS spectroscopy with weak spatial resolution. We found a slight difference in spectra for carbon between an irradiated zone and a non-irradiated zone of coating, which suggests that there might be some carbon compounds characteristic to the LIC. However, the changes between zones were small, and more research into the vibrational modes of adsorbed species is required to understand the source of LIC deposit growth.

The characterization of a LIC deposit on MS SiO_2 via s-SNOM device did not allow us to identify any sample surface abnormality that could be related to LIC deposit. One possible explanation is that the sample surface has a low height contrast. For further study, another analytical method called Rutherford Backscattering Spectrometry could be used. In study [317], the method sucessfully confirmed contamination of SiO_x coating and detected signal of silicium.

Our not spatially resolved observation during thermal measurements as well as rough calculation of material temperature change indicate an increase in temperature of only around 1 °C. These results suggest that LIC formation occurs in a cold environment and support the hypothesis of photoactivated polymerization of contaminants on the surface of the optic. If there is a possible thermal component of the LIC process, it can only be triggered by the transient peak temperatures. To investigate this further, several actions can be done:

- Time resolved numerical simulations.
- Comparing the LIC deposits of pulsed lasers to CW lasers.
- Making pump-probe measurements to get time resolved temperature information.

The study presented in this chapter might be useful for further development of design coatings mitigating LIC growth.

Conclusion

The main motivation of this thesis was to investigate laser-induced damage thresholds (LIDT) of coating materials and structures and to contribute to the development of reflective component designs with enhanced LIDT that will be implemented in lasers used e.g in industry. These goals were attained by testing non-traditional coating materials, advanced designs of optical components and by exploring the effect of thin-film deposition method on laser damage resistance. The testing was performed with available experimental stations operating under conditions as close as possible to the intended application of the coating-based reflective components.

In the fields of industrial material processing, telecommunications or biochemistry, there is a need of functional damage resistant components, that can adjust laser wavelength, polarization or pulse duration. Such adjustment of laser light properties can be done using Grating Waveguide Structures (GWS), whose development is a key task of GREAT project [8], described in the first part of this thesis. Within the GREAT project, we tested the damage resistance of coatings and structures corresponding to the different stages of the GWS production chain, i.e. single-layer coatings, multi-layer reflective structures and the first generation of grating structures which were etched into substrates.

To be able to improve the resistance of state-of-the-art optical components, we should understand physical mechanisms that lead to damage in dielectric coating materials. Therefore, in Chapter 2 we reviewed the knowledge of laser-induced damage on dielectric materials. Although this review has concentrated on the laser-induced damage in sub-ps regime, we also introduced physical effects that are related to damage formation by longer pulse durations or CW irradiation. Such an overview is useful because the mechanism leading to damage is not only dependent on pulse duration but also, for example, repetition rate or number of pulses. Damage formation during sub-ps pulse irradiation with a high repetition rate may be associated with the same thermal phenomena as damage formation in the CW regime.

When a dielectric material is irradiated by pulses of sub-ps duration, electrons in its structure can absorb photon energy via non-linear processes including multi-photon ionization. Despite the efficient excitation of material in sub-ps regime, indicating that LIDT should not be dependent on beam size, we found that this statement is not unequivocal in the published literature. Thus, in Chapter 3, we elaborated a detailed metrology study about the effect of beam size on LIDT determined by pulses of 500 fs duration emitted at a wavelength of 1030 nm. The study underlines the difficulty of LIDT measurements with very focused laser beams, which could be related to beam deformation due to self-focusing in the lens. We determined focusing conditions that are suitable for LIDT testing of optical components that will be implemented in lasers with larger beams than the beam used for testing. To evaluate the tests of such optical components accurately, we provided a synthesis of identified contributors to errors. As the major error contributor in the best case scenario, we determined inaccuracy of beam size measurement.

To qualify the coatings and structures for use in thin-disk, fiber or diode laser systems operating in different regimes, we tested within this thesis their laser damage resistance with five LIDT setups located in

Institut Fresnel in Marseille and GREAT partner institutions: Alphanov technological center in Bordeaux, HiLASE centre and ELI Beamlines facility (both in Dolní Břežany near Prague). These LIDT setups are described in Chapter 3. Overall, the access to these setups enabled testing with pulse durations ranging from 100 fs up to 150 ps, at wavelengths from 515 nm to 1050 nm, at repetition rates from 10 Hz to 3.3 MHz and with effective beam diameters from 40 µm up to 315 µm. However, the main conclusions about LIDT summarized in the following paragraphs are related to the tests with sub-ps near-infrared sub-1-kHz lasers.

Thanks to the collaboration with producers of dielectric coatings, we studied in Chapter 4 LIDT of monolayer coatings deposited by different deposition methods. Using the 500-fs 1030-nm 10-Hz LIDT station, we performed tests with pulsed-laser deposited crystalline sesquioxides (Sc_2O_3, Y_2O_3, Lu_2O_3) and amorphous metal oxides (HfO_2, Nb_2O_5, SiO_2) coated by magnetron sputtering. We found that the LIDTs of sesquioxides are comparable to each other and in the multiple pulse test regime show values close to those of widely used HfO_2 coatings. The work suggests that pulsed-laser deposition is a potential production method of sesquioxide coatings for use in high-power resistant optical components of ultrashort pulsed lasers. However, the single crystal nature of PLD coatings has to be taken into account during the design of components based on multilayer PLD stacks.

In Chapter 5, we expanded our LIDT study to the optical components developed within the GREAT project: dielectric mirrors and gratings. We used the transfer matrix method to determine the electric field maxima in materials of coatings incorporated in the mirrors. Using these values and the intrinsic LIDTs of monolayers (from Chapter 4) we made predictions of LIDTs for mirrors. We compared the calculated LIDTs to the experimentally obtained data for mirrors. The results from this study are useful inputs for further steps in development of damage resistant mirrors with optimized electric field intensity distribution.

In next part of Chapter 5, we analysed optical surfaces treated with Ti adhesion promoter and Cr hard mask forming thin layers, because manufacturers of diffractive optical components frequently use them to facilitate grating etching. We found that the LIDTs of the treated surfaces are similar to the untreated surface, when they are tested by 100 pulses. Thus, the treatment of optical surfaces by Ti promoter or Cr mask does not significantly affect the LIDT of whole dielectric structures and optical components used in industrial lasers operating with high numbers of pulses. Finally, we predicted LIDT for GWS using the electric field intensity values obtained by Rigorous Coupled Wave Analysis (RCWA) and knowledge of LIDTs for individual coating materials. These data should be used to identify conditions that are critical for reliable operation of laser systems equipped with GWS for pulse compression or polarization adjustment.

The lifetime of optical components in industrial high-repetition rate laser systems can be limited by a detrimental effect called laser-induced contamination (LIC). In Chapter 6, we explored the effect on monolayer dielectric coatings in air environment irradiated by 700-fs long pulses emitted at a wavelength of 515 nm with a repetition rate of 3.3 MHz. We found that there is a significant effect of coating material and deposition method on LIC growth dynamics. For magnetron-sputtered SiO_2 and plasma-ion-assistance deposited HfO_2 coatings we found approximately linear dependence of LIC deposit thickness on coating thickness. This relationship could suggest that LIC growth is connected to thermal effects driven by absorption in the dielectric coatings but we could not evidence this link using time-averaged thermal measurements. The findings of this study may be beneficial in the upcoming development of coatings designs that reduce LIC growth.

The studies carried out within this thesis show the complexity of the processes involved in laser damage field. Among many perspectives to explore, this thesis encourages to:

- Study of pulsed-laser deposited coatings including HfO_2 and multilayer reflective components.
- Extend LIDT and LIC studies with repetition rates ranging from around 100 kHz up to GHz regime. It should be possible to determine the relaxation time of coating materials after the irradiation by sub-ps

pulses. For the development of high power laser systems it might be useful to identify the repetition rates, for which the thermal effects start to play significant role in given coating materials.

- LIDT testing of coating materials and structures with a large number of pulses (e.g. 10^8). Since the reproduction of these tests takes long time, it should be supported with damage threshold characteristic curve modeling.
- Testing of GWS structures in conditions close to their intended applications.

Bibliography

[1] M. Soileau, "Laser-Induced Damage Phenomena in Optics: A Historical Overview," in *Laser-Induced Damage in Optical Materials*, D. Ristau, Ed., 3–8, CRC Press (2014).

[2] W. Koechner, "Damage of Optical Elements," in *Solid-State Laser Engineering*, W. T. Thodes, A. Adibi, T. Asakura, *et al.*, Eds., **1**, 680–701, Springer, New York, NY (2006).

[3] D. Bäuerle, *Introduction*, 3–12. Springer Berlin Heidelberg, Berlin, Heidelberg (2011).

[4] R. R. Gattass and E. Mazur, "Femtosecond laser micromachining in transparent materials," *Nature Photonics* **2**, 219–225 (2008).

[5] B. Neuenschwander, B. Jaeggi, M. Schmid, *et al.*, "Surface Structuring with Ultra-short Laser Pulses: Basics, Limitations and Needs for High Throughput," *Physics Procedia* **56**, 1047–1058 (2014).

[6] Y. Wang, S. Tomilov, and C. J. Saraceno, "High-power modelocked thin-disk oscillators as potential technology for high-rate material processing," *Advanced Optical Technologies* **10**, 247–261 (2021).

[7] G. Quaranta, G. Basset, O. J. F. Martin, *et al.*, "Recent Advances in Resonant Waveguide Gratings," *Laser Photonics Rev.* **12**, 1800017 (2018).

[8] "Grating Reflectors Enabled laser Applications and Training (GREAT) Innovative Training Network." https://itn-great.eu/. Accessed: 2022-02-24.

[9] "Grating Reflectors Enabled laser Applications and Training "GREAT" - project proposal," (2018). Innovative Training Networks (ITN) Call: H2020-MSCA-ITN-2018.

[10] L. Gallais, M. Rumpel, M. Moeller, *et al.*, "Investigation of laser damage of grating waveguide structures submitted to sub-picosecond pulses," *Applied Physics B* **126**(4), 69 (2020).

[11] G. Gebrayel El Reaidy and L. Gallais, "Analysis of laser-induced contamination at 515 nm in the sub-ps/MHz regime," *Optical Engineering* **60** (2020).

[12] S. Gales, D. L. Balabanski, F. Negoita, *et al.*, "New frontiers in nuclear physics with high-power lasers and brilliant monochromatic gamma beams," *Physica Scripta* **91**(9), 093004 (2016).

[13] A. Bunkowski, O. Burmeister, T. Clausnitzer, *et al.*, "Diffractive Optics for Gravitational Wave Detectors," *Journal of Physics: Conference Series* **32**, 333–338 (2006).

[14] N. Bonod and J. Neauport, "Diffraction gratings: from principles to applications in high-intensity lasers," *Advances in Optics and Photonics* **8**, 156 (2016).

[15] J. Neauport, E. Lavastre, G. Razé, *et al.*, "Effect of electric field on laser induced damage threshold of multilayer dielectric gratings," *Optics Express* **15**(19), 12508 (2007).

[16] M. Rumpel, *Applications of Grating Waveguide Structures in Solid-State Lasers*. PhD thesis, Universität Stuttgart (2019).

[17] T. Dietrich, S. Piehler, C. Röcker, *et al.*, "Passive compensation of the misalignment instability caused by air convection in thin-disk lasers," *Optics Letters* **42**, 3263 (2017).

[18] T. Dietrich, S. Piehler, M. Rumpel, *et al.*, "Highly-efficient continuous-wave intra-cavity frequency-doubled Yb:LuAG thin-disk laser with 1 kW of output power," *Optics Express* **25**, 4917 (2017).

[19] M. Eckerle, T. Dietrich, F. Schaal, *et al.*, "Novel thin-disk oscillator concept for the generation of radially polarized femtosecond laser pulses," *Optics Letters* **41**, 1680 (2016).

[20] M. Rumpel, M. Moeller, C. Moormann, *et al.*, "Broadband pulse compression gratings with measured 99.7% diffraction efficiency," *Opt. Lett.* **39**, 323 (2014).

[21] M. A. Ahmed, M. Haefner, M. Vogel, *et al.*, "High-power radially polarized Yb:YAG thin-disk laser with high efficiency," *Optics Express* **19**, 5093 (2011).

[22] M. A. Ahmed, M. Rumpel, A. Voss, *et al.*, "Applications of sub-wavelength grating mirrors in high-power lasers," *Adv. Opt. Technol.* **1**, 381–388 (2012).

[23] M. Abdou Ahmed, F. Beirow, A. Loescher, *et al.*, "High-power thin-disk lasers emitting beams with axially-symmetric polarizations," *Nanophotonics* **0**, 1–11 (2021).

[24] M. M. Vogel, M. Rumpel, B. Weichelt, *et al.*, "Single-layer resonant-waveguide grating for polarization and wavelength selection in Yb:YAG thin-disk lasers," *Opt. Express* **20**, 4024 (2012).

[25] M. Flury, A. V. Tishchenko, and O. Parriaux, "The Leaky Mode Resonance Condition Ensures 100% Diffraction Efficiency of Mirror-Based Resonant Gratings," *Journal of Lightwave Technology* **25**, 1870–1878 (2007).

[26] G. A. Golubenko, A. S. Svakhin, V. A. Sychugov, *et al.*, "Total reflection of light from a corrugated surface of a dielectric waveguide," *Soviet Journal of Quantum Electronics* **15**, 886–887 (1985).

[27] "Institut für Strahlwerkzeuge (IFSW)." https://www.ifsw.uni-stuttgart.de/en/. Accessed: 2022-02-22.

[28] R. Weber, A. Michalowski, M. Abdou-Ahmed, *et al.*, "Effects of Radial and Tangential Polarization in Laser Material Processing," *Physics Procedia* **12**, 21–30 (2011).

[29] A. Giesen, H. Hügel, A. Voss, *et al.*, "Scalable concept for diode-pumped high-power solid-state lasers," *Applied Physics B* **58**, 365–372 (1994).

[30] A. Giesen and J. Speiser, "Fifteen Years of Work on Thin-Disk Lasers: Results and Scaling Laws," *IEEE Journal of Selected Topics in Quantum Electronics* **13**(3), 598–609 (2007).

[31] "Department of Physics and Mathematics of University of Eastern Finland." https://www.uef.fi/en/unit/department-of-physics-and-mathematics. Accessed: 2022-02-22.

[32] "ALPHaNOV: Optics and Lasers Technology Center." https://www.alphanov.com/en/who-are-we/missions-organisation. Accessed: 2022-02-22.

[33] "Optoelectronics Research Centre." https://www.orc.soton.ac.uk/who-we-are. Accessed: 2022-02-23.

[34] R. Mears, L. Reekie, I. Jauncey, *et al.*, "Low-noise erbium-doped fibre amplifier operating at 1.54 µm," *Electronics Letters* **23**(19), 1026 (1987).

[35] "Laboratoire Hubert Curien." https://laboratoirehubertcurien.univ-st-etienne.fr/en/the-lab/presentation.html. Accessed: 2022-02-23.

[36] "MarTec Photonics." https://martec-photonics.eu/. Accessed: 2022-03-02.

[37] M. Rumpel, M. Haefner, T. Schoder, *et al.*, "Circular grating waveguide structures for intracavity generation of azimuthal polarization in a thin-disk laser," *Optics Letters* **37**, 1763 (2012).

[38] T. Kämpfe, S. Tonchev, A. V. Tishchenko, *et al.*, "Azimuthally polarized laser mode generation by multilayer mirror with wideband grating-induced TM leakage in the TE stopband," *Optics Express* **20**, 5392 (2012).

[39] S. Piehler, T. Dietrich, M. Rumpel, *et al.*, "Highly efficient 400 W near-fundamental-mode green thin-disk laser," *Optics Letters* **41**, 171 (2016).

[40] A. Tishchenko and V. Sychugov, "High grating efficiency by energy accumulation in a leaky mode," *Optical and Quantum Electronics* **32**(6/8), 1027–1031 (2000).

[41] M. Rumpel, A. Voss, M. Moeller, *et al.*, "Linearly polarized, narrow-linewidth, and tunable Yb:YAG thin-disk laser," *Optics Letters* **37**, 4188 (2012).

[42] S. Tonchev, T. Kämpfe, and O. Parriaux, "High efficiency, high selectivity ultra-thin resonant diffractive elements," *Optics Express* **20**, 26714 (2012).

[43] N. Lyndin, T. Kämpfe, S. Tonchev, *et al.*, "Transverse-mode selective resonant grating-mirrors for high power and high brightness emission," *Optics Express* **23**, 17275 (2015).

[44] B. Mangote, L. Gallais, M. Commandré, *et al.*, "Femtosecond laser damage resistance of oxide and mixture oxide optical coatings," *Opt. Lett.* **37**, 1478 (2012).

[45] O. Parriaux, V. A. Sychugov, and A. V. Tishchenko, "Coupling gratings as waveguide functional elements," *Pure and Applied Optics: Journal of the European Optical Society Part A* **5**, 453–469 (1996).

[46] R. Paschotta, *Field guide to laser pulse generation*, no. FG14 in SPIE field guides, SPIE Press, Bellingham, Wash (2008).

[47] T. Eidam, S. Hanf, E. Seise, *et al.*, "Femtosecond fiber CPA system emitting 830 W average output power," *Optics Letters* **35**, 94 (2010).

[48] W. Koechner, *Solid-state laser engineering*, no. 1 in Springer series in optical sciences, Springer, New York, NY, 6th rev. and updated ed ed. (2006).

[49] S. Weiler, A. Hangst, C. Stolzenburg, *et al.*, "Frequency doubled high-power disk lasers in pulsed and continuous-wave operation," in *Proc. SPIE*, E. Beyer and T. Morris, Eds., **8239**, 823907, (San Francisco, California, USA) (2012).

[50] C. Gaida, M. Gebhardt, T. Heuermann, *et al.*, "Ultrafast Tm-doped fiber amplifier with 1 kW average output power," in *2019 Conference on Lasers and Electro-Optics Europe & European Quantum Electronics Conference (CLEO/Europe-EQEC)*, cj_10, IEEE, (Munich, Germany) (2019).

[51] M. Kraus, M. A. Ahmed, A. Michalowski, *et al.*, "Microdrilling in steel using ultrashort pulsed laser beams with radial and azimuthal polarization," *Optics Express* **18**, 22305 (2010).

[52] M. Meier, V. Romano, and T. Feurer, "Material processing with pulsed radially and azimuthally polarized laser radiation," *Applied Physics A* **86**, 329–334 (2007).

[53] V. G. Niziev and A. V. Nesterov, "Influence of beam polarization on laser cutting efficiency," *Journal of Physics D: Applied Physics* **32**, 1455–1461 (1999).

[54] R. Dorn, S. Quabis, and G. Leuchs, "Sharper Focus for a Radially Polarized Light Beam," *Physical Review Letters* **91**, 233901 (2003).

[55] S. Quabis, G. Kihara Rurimo, M. Schardt, *et al.*, "Investigation of Longitudinal and Transverse Electric Field Components in Strongly Focused Radially Polarized Light Beam," in *International Symposium on Optical Memory and Optical Data Storage*, WC3, OSA, (Honolulu, Hawaii) (2005).

[56] M. D. Levenson, "Wavefront Engineering for Photolithography," *Physics Today* **46**, 28–36 (1993).

[57] V. P. Kalosha and I. Golub, "Toward the subdiffraction focusing limit of optical superresolution," *Optics Letters* **32**, 3540 (2007).

[58] Y. I. Salamin, "Mono-energetic GeV electrons from ionization in a radially polarized laser beam," *Optics Letters* **32**, 90 (2007).

[59] H. Kawauchi, K. Yonezawa, Y. Kozawa, *et al.*, "Calculation of optical trapping forces on a dielectric sphere in the ray optics regime produced by a radially polarized laser beam," *Optics Letters* **32**, 1839 (2007).

[60] Y. Zhao, Q. Zhan, Y. Zhang, *et al.*, "Creation of a three-dimensional optical chain for controllable particle delivery," *Optics Letters* **30**, 848 (2005).

[61] H. Ishitobi, I. Nakamura, N. Hayazawa, *et al.*, "Orientational Imaging of Single Molecules by Using Azimuthal and Radial Polarizations," *The Journal of Physical Chemistry B* **114**, 2565–2571 (2010).

[62] T. A. Nieminen, N. R. Heckenberg, and H. Rubinsztein-Dunlop, "Forces in optical tweezers with radially and azimuthally polarized trapping beams," *Optics Letters* **33**, 122 (2008).

[63] Z. Man, Z. Bai, S. Zhang, *et al.*, "Redistributing the energy flow of a tightly focused radially polarized optical field by designing phase masks," *Optics Express* **26**, 23935 (2018).

[64] C. Gu and P. Yeh, "Form birefringence dispersion in periodic layered media," *Optics Letters* **21**, 504 (1996).

[65] J. E. Wolfe, S. R. Qiu, and C. J. Stolz, "Fabrication of mitigation pits for improving laser damage resistance in dielectric mirrors by femtosecond laser machining," *Applied Optics* **50**, C457 (2011).

[66] C. N. Danson, C. Haefner, J. Bromage, *et al.*, "Petawatt and exawatt class lasers worldwide," *High Power Laser Science and Engineering* **7**, e54 (2019).

[67] C. Kittel, *Introduction to Solid State Physics*, Wiley, 8 ed. (2004).

[68] J. Patterson and B. Bailey, *Solid-State Physics*, Springer Berlin Heidelberg, Berlin, Heidelberg (2010).

[69] A. Hervy, *Multidielectrics coatings improvement for high power lasers with femtosecond pulses*. PhD thesis, Ecole polytechnique, Palaiseau, France (2015).

[70] L. Emmert and W. Rudolph, "Femtosecond Laser-Induced Damage in Dielectric Materials," in *Laser-Induced Damage in Optical Materials*, D. Ristau, Ed., 127–152, CRC Press, Boca Raton, FL (2014).

[71] R. M. Wood, *Laser-induced damage of optical materials*, Series in optics and optoelectronics, Institute of Physics, Bristol (2003). OCLC: ocm51779491.

[72] R. W. Boyd, *Nonlinear optics*, Academic Press, San Diego, CA, 2nd ed ed. (2003).

[73] J.-C. Diels and W. Rudolph, *Ultrashort laser pulse phenomena: fundamentals, techniques, and applications on a femtosecond time scale*, Optics and photonics, Elsevier / Academic Press, Amsterdam ; Boston, 2nd ed ed. (2006).

[74] K. Hirao, *Active glass for photonic devices: photoinduced structures and their application*, Springer, Berlin; London (2011). OCLC: 751525484.

[75] ISO 21254-1:2011, "Lasers and laser-related equipment – test methods for laser-induced damage threshold – part 1: Definitions and general principles," tech. rep., International Organization for Standardization, Geneva, Switzerland (2011).

[76] C. J. Stolz and R. A. Negres, "Ten-year summary of the Boulder Damage Symposium annual thin film laser damage competition," *Optical Engineering* **57**, 1 (2018).

[77] R. Wood, "Laser-Induced Damage by Thermal Effects," in *Laser-Induced Damage in Optical Materials*, D. Ristau, Ed., 9–24, CRC Press (2014).

[78] G. Duchateau, M. D. Feit, and S. G. Demos, "Strong nonlinear growth of energy coupling during laser irradiation of transparent dielectrics and its significance for laser induced damage," *Journal of Applied Physics* **111**, 093106 (2012).

[79] S. C. Jones, P. Braunlich, R. T. Casper, *et al.*, "Recent Progress On Laser-Induced Modifications And Intrinsic Bulk Damage Of Wide-Gap Optical Materials," *Optical Engineering* **28** (1989).

[80] M. Chorel, *Study of high damage threshold optical coatings used in environment with very low hygrometry for fusion class laser system*. PhD thesis, Université de Bordeaux (2019).

[81] M. Sozet, *Study of the laser-induced damage of reflective components in the sub-picosecond regime*. PhD thesis, Ecole Centrale Marseille (2016).

[82] M. Sparks, D. L. Mills, R. Warren, *et al.*, "Theory of electron-avalanche breakdown in solids," *Physical Review B* **24**, 3519–3536 (1981).

[83] S. Papernov, "Defect-Induced Damage," in *Laser-Induced Damage in Optical Materials*, D. Ristau, Ed., 25–74, CRC Press (2014).

[84] B. C. Stuart, M. D. Feit, S. Herman, *et al.*, "Nanosecond-to-femtosecond laser-induced breakdown in dielectrics," *Physical Review B* **53**, 1749–1761 (1996).

[85] A. Joglekar, H. Liu, G. Spooner, *et al.*, "A study of the deterministic character of optical damage by femtosecond laser pulses and applications to nanomachining," *Applied Physics B* **77**, 25–30 (2003).

[86] M. Sozet, J. Néauport, E. Lavastre, *et al.*, "Laser damage density measurement of optical components in the sub-picosecond regime," *Optics Letters* **40**, 2091 (2015).

[87] M. Sozet, S. Bouillet, J. Berthelot, *et al.*, "Sub-picosecond laser damage growth on high reflective coatings for high power applications," *Optics Express* **25**, 25767 (2017).

[88] B. C. Stuart, M. D. Feit, A. M. Rubenchik, *et al.*, "Laser-Induced Damage in Dielectrics with Nanosecond to Subpicosecond Pulses," *Physical Review Letters* **74**, 2248–2251 (1995).

[89] A.-C. Tien, S. Backus, H. Kapteyn, *et al.*, "Short-Pulse Laser Damage in Transparent Materials as a Function of Pulse Duration," *Physical Review Letters* **82**, 3883–3886 (1999).

[90] M. Lenzner, J. Krüger, S. Sartania, *et al.*, "Femtosecond Optical Breakdown in Dielectrics," *Physical Review Letters* **80**, 4076–4079 (1998).

[91] P. Martin, S. Guizard, P. Daguzan, *et al.*, "Subpicosecond study of carrier trapping dynamics in wide-band-gap crystals," *Physical Review B* **55**, 5799–5810 (1997).

[92] T. Apostolova and Y. Hahn, "Modeling of laser-induced breakdown in dielectrics with subpicosecond pulses," *Journal of Applied Physics* **88**, 1024–1034 (2000).

[93] A. Kaiser, B. Rethfeld, M. Vicanek, *et al.*, "Microscopic processes in dielectrics under irradiation by subpicosecond laser pulses," *Physical Review B* **61**, 11437–11450 (2000).

[94] M. Mero, J. Zeller, and W. Rudolph, "Ultrafast Processes in Highly Excited Wide-Gap Dielectric Thin Films," in *Femtosecond Laser Spectroscopy*, P. Hannaford, Ed., 305–329, Springer-Verlag, New York (2005).

[95] D. Du, X. Liu, G. Korn, *et al.*, "Laser-induced breakdown by impact ionization in SiO_2 with pulse widths from 7 ns to 150 fs," *Applied Physics Letters* **64**(23), 3071–3073 (1994).

[96] M. Lenzner and W. Rudolph, "Laser-Induced Optical Breakdown in Solids," in *Strong Field Laser Physics*, T. Brabec, Ed., **134**, 243–257, Springer New York, New York, NY (2008). Series Title: Springer Series in Optical Sciences.

[97] B. Rethfeld, "Unified Model for the Free-Electron Avalanche in Laser-Irradiated Dielectrics," *Physical Review Letters* **92**, 187401 (2004).

[98] M. V. Klein and T. E. Furtak, *Optics*, Wiley, New York, 2nd ed ed. (1986).

[99] P. P. Rajeev, M. Gertsvolf, P. B. Corkum, *et al.*, "Field Dependent Avalanche Ionization Rates in Dielectrics," *Physical Review Letters* **102**, 083001 (2009).

[100] M. Mero, J. Liu, W. Rudolph, *et al.*, "Scaling laws of femtosecond laser pulse induced breakdown in oxide films," *Physical Review B* **71**, 115109 (2005).

[101] L. Englert, B. Rethfeld, L. Haag, *et al.*, "Control of ionization processes in high band gap materials via tailored femtosecond pulses," *Optics Express* **15**(26), 17855 (2007).

[102] C. W. Carr, J. B. Trenholme, and M. L. Spaeth, "Effect of temporal pulse shape on optical damage," *Applied Physics Letters* **90**, 041110 (2007).

[103] A. Ollé, J. Luce, N. Roquin, *et al.*, "Implications of laser beam metrology on laser damage temporal scaling law for dielectric materials in the picosecond regime," *Review of Scientific Instruments* **90**, 073001 (2019).

[104] D.-B. L. Douti, *Laser induced damage and ultrashort-pulse laser excitation of optical thin films*. PhD thesis, Université d'Aix-Marseille (2015).

[105] B. Rethfeld, D. S. Ivanov, M. E. Garcia, *et al.*, "Modelling ultrafast laser ablation," *Journal of Physics D: Applied Physics* **50**, 193001 (2017).

[106] B. Rethfeld, O. Brenk, N. Medvedev, *et al.*, "Interaction of dielectrics with femtosecond laser pulses: application of kinetic approach and multiple rate equation," *Applied Physics A* **101**, 19–25 (2010).

[107] B. Rethfeld, "Free-electron generation in laser-irradiated dielectrics," *Physical Review B* **73**, 035101 (2006).

[108] B. H. Christensen and P. Balling, "Modeling ultrashort-pulse laser ablation of dielectric materials," *Physical Review B* **79**, 155424 (2009).

[109] P. Audebert, P. Daguzan, A. Dos Santos, *et al.*, "Space-Time Observation of an Electron Gas in SiO_2," *Physical Review Letters* **73**, 1990–1993 (1994).

[110] S. Mao, F. Quéré, S. Guizard, *et al.*, "Dynamics of femtosecond laser interactions with dielectrics," *Applied Physics A* **79**, 1695–1709 (2004).

[111] F. Quéré, P. Grua, H. Bercegol, *et al.*, "Interaction of an intense laser field with a dielectric containing metallic nanoparticles," *Applied Physics B: Lasers and Optics* **78**, 825–828 (2004).

[112] L. Englert, M. Wollenhaupt, L. Haag, *et al.*, "Material processing of dielectrics with temporally asymmetric shaped femtosecond laser pulses on the nanometer scale," *Applied Physics A* **92**, 749–753 (2008).

[113] M. Wollenhaupt, L. Englert, A. Horn, *et al.*, "Control of Ionization Processes in High Band Gap Materials," *Journal of Laser Micro/Nanoengineering* **4**, 144–151 (2009).

[114] J. R. Gulley and T. E. Lanier, "Model for ultrashort laser pulse-induced ionization dynamics in transparent solids," *Physical Review B* **90**, 155119 (2014).

[115] J. Liao and J. R. Gulley, "Time–frequency control of ultrafast plasma generation in dielectrics," *Journal of the Optical Society of America B* **31**, 2973 (2014).

[116] N. Medvedev and B. Rethfeld, "A comprehensive model for the ultrashort visible light irradiation of semiconductors," *Journal of Applied Physics* **108**, 103112 (2010).

[117] B. Rethfeld, H. Krutsch, and D. Hoffmann, "Tracing Laser-Induced Dielectric Breakdown in Solids," *Contributions to Plasma Physics* **50**, 16–20 (2010).

[118] O. Brenk and B. Rethfeld, "Electron dynamics in transparent materials under high-intensity laser irradiation," *Optical Engineering* **51**, 121810–1 (2012).

[119] N. S. Shcheblanov and T. E. Itina, "Femtosecond laser interactions with dielectric materials: insights of a detailed modeling of electronic excitation and relaxation processes," *Applied Physics A* **110**, 579–583 (2013).

[120] N. Sanner, O. Utéza, B. Chimier, *et al.*, "Toward determinism in surface damaging of dielectrics using few-cycle laser pulses," *Applied Physics Letters* **96**, 071111 (2010).

[121] K. J. Wædegaard, D. B. Sandkamm, A. Mouskeftaras, *et al.*, "Probing ultrashort-pulse laser excitation of sapphire: From the initial carrier creation to material ablation," *EPL (Europhysics Letters)* **105**, 47001 (2014).

[122] L. Gallais, D.-B. Douti, M. Commandré, *et al.*, "Wavelength dependence of femtosecond laser-induced damage threshold of optical materials," *Journal of Applied Physics* **117**, 223103 (2015).

[123] A. H. Guenther and J. K. McIver, "To scale or not to scale," in *Proc. SPIE*, H. E. Bennett, L. L. Chase, A. H. Guenther, *et al.*, Eds., **2114**, 488, (Boulder, CO) (1994).

[124] L. Gallais and M. Commandré, "Laser-induced damage thresholds of bulk and coating optical materials at 1030 nm, 500 fs," *Applied Optics* **53**, A186 (2014).

[125] C. B. Schaffer, A. Brodeur, and E. Mazur, "Laser-induced breakdown and damage in bulk transparent materials induced by tightly focused femtosecond laser pulses," *Measurement Science and Technology* **12**, 1784–1794 (2001).

[126] D. M. Simanovskii, H. A. Schwettman, H. Lee, *et al.*, "Midinfrared Optical Breakdown in Transparent Dielectrics," *Physical Review Letters* **91**, 107601 (2003).

[127] T. Q. Jia, H. X. Chen, M. Huang, *et al.*, "Ultraviolet-infrared femtosecond laser-induced damage in fused silica and CaF_2 crystals," *Physical Review B* **73**, 054105 (2006).

[128] D.-B. Douti, L. Gallais, and M. Commandré, "Laser-induced damage of optical thin films submitted to 343, 515, and 1030 nm multiple subpicosecond pulses," *Optical Engineering* **53**, 122509 (2014).

[129] M. Jupé, L. Jensen, A. Melninkaitis, *et al.*, "Calculations and experimental demonstration of multi-photon absorption governing fs laser-induced damage in titania," *Optics Express* **17**, 12269 (2009).

[130] N. Bloembergen, "Laser-induced electric breakdown in solids," *IEEE Journal of Quantum Electronics* **10**, 375–386 (1974).

[131] D. Nguyen, L. A. Emmert, I. V. Cravetchi, *et al.*, "$Ti_xSi_{1-x}O_2$ optical coatings with tunable index and their response to intense subpicosecond laser pulse irradiation," *Applied Physics Letters* **93**, 261903 (2008).

[132] L. O. Jensen, M. Mende, H. Blaschke, *et al.*, "Investigations on SiO_2/HfO_2 mixtures for nanosecond and femtosecond pulses," in *Proc. SPIE*, G. J. Exarhos, V. E. Gruzdev, J. A. Menapace, *et al.*, Eds., **7842**, 784207, (Boulder, Colorado) (2010).

[133] S. Juodkazis, T. Kondo, A. V. Rode, *et al.*, "Three-dimensional recording and structuring of chalcogenide glasses by femtosecond pulses," in *Proc. SPIE*, I. Miyamoto, H. Helvajian, K. Itoh, *et al.*, Eds., **5662**, 179–184 (2004).

[134] B. Mangote, *Laser damage behavior of optical thin films in subpicosecond regime.* PhD thesis, Université Paul Cézanne - Aix-Marseille III (2011).

[135] A. Melninkaitis, T. Tolenis, L. Mažulė, *et al.*, "Characterization of zirconia– and niobia–silica mixture coatings produced by ion-beam sputtering," *Applied Optics* **50**, C188 (2011).

[136] G. Abromavicius, R. Buzelis, R. Drazdys, *et al.*, "Influence of electric field distribution on laser induced damage threshold and morphology of high reflectance optical coatings," in *Proc. SPIE*, G. J. Exarhos, A. H. Guenther, K. L. Lewis, *et al.*, Eds., **6720**, 67200Y, (Boulder, CO) (2007).

[137] J. A. Britten, W. A. Molander, A. M. Komashko, *et al.*, "Multilayer Dielectric Gratings for Petawatt-Class Laser Systems," in *Proc. SPIE*, G. J. Exarhos, A. H. Guenther, N. Kaiser, *et al.*, Eds., **5273**, 1, (Boulder, CO) (2004).

[138] M. Sozet, E. Lavastre, J. Néauport, *et al.*, "Laser damage metrology in the sub-ps range for the PETAL facility," in *Pacific-Rim Laser Damage 2018: Optical Materials for High-Power Lasers*, J. Shao, T. Jitsuno, and W. Rudolph, Eds., 29, SPIE, (Yokohama, Japan) (2018).

[139] J. Dijon, M. Poulingue, and J. Hue, "Thermomechanical model of mirror laser damage at 1.06 µm. Part 1: nodule ejection.," in *Proc. SPIE*, G. J. Exarhos, A. H. Guenther, M. R. Kozlowski, *et al.*, Eds., **3578**, 387, (Boulder, CO) (1999).

[140] L. Gallais, X. Cheng, and Z. Wang, "Influence of nodular defects on the laser damage resistance of optical coatings in the femtosecond regime," *Opt. Lett.* **39**, 1545–1548 (2014).

[141] N. Bloembergen, "Role of Cracks, Pores, and Absorbing Inclusions on Laser Induced Damage Threshold at Surfaces of Transparent Dielectrics," *Applied Optics* **12**, 661 (1973).

[142] A. Rosenfeld, M. Lorenz, R. Stoian, *et al.*, "Ultrashort-laser-pulse damage threshold of transparent materials and the role of incubation," *Applied Physics A: Materials Science & Processing* **69**, S373–S376 (1999).

[143] A. Chmel, "Fatigue laser-induced damage in transparent materials," *Materials Science & Engineering B* **49**, 175–190 (1997).

[144] M. Mero, B. R. Clapp, J. C. Jasapara, *et al.*, "On the damage behavior of dielectric films when illuminated with multiple femtosecond laser pulses," *Optical Engineering* **44**(5), 1 – 7 (2005).

[145] M. Li, S. Menon, J. P. Nibarger, *et al.*, "Ultrafast Electron Dynamics in Femtosecond Optical Breakdown of Dielectrics," *Physical Review Letters* **82**, 2394–2397 (1999).

[146] D. N. Nguyen, L. A. Emmert, D. Patel, *et al.*, "Transient phenomena in the dielectric breakdown of HfO_2 optical films probed by ultrafast laser pulse pairs," *Applied Physics Letters* **97**, 191909 (2010).

[147] L. A. Emmert, M. Mero, D. N. Nguyen, *et al.*, "Femtosecond pulse S on 1 LIDT in dielectric materials: Comparison of Experiment and Theory," in *Proc. SPIE*, G. J. Exarhos, V. E. Gruzdev, J. A. Menapace, *et al.*, Eds., **7842**, 784211, (Boulder, Colorado) (2010).

[148] ISO 21254-1:2011, "Lasers and laser-related equipment – test methods for laser-induced damage threshold – part 2: Threshold determination," tech. rep., International Organization for Standardization, Geneva, Switzerland (2011).

[149] L. A. Emmert, M. Mero, and W. Rudolph, "Modeling the effect of native and laser-induced states on the dielectric breakdown of wide band gap optical materials by multiple subpicosecond laser pulses," *J. Appl. Phys.* **108**, 043523 (2010).

[150] K. Xiong, J. Robertson, and S. J. Clark, "Passivation of oxygen vacancy states in HfO_2 by nitrogen," *Journal of Applied Physics* **99**, 044105 (2006).

[151] D. N. Nguyen, L. A. Emmert, W. Rudolph, *et al.*, "The effect of nitrogen doping on the multiple-pulse subpicosecond dielectric breakdown of hafnia films," in *Proc. SPIE*, G. J. Exarhos, V. E. Gruzdev, D. Ristau, *et al.*, Eds., **7504**, 750402, (Boulder, CO) (2009).

[152] L. Lamaignère, "Quartz and Glasses," in *Laser-Induced Damage in Optical Materials*, D. Ristau, Ed., 264–283, CRC Press, Boca Raton, FL (2014).

[153] W. Riede, P. Allenspacher, H. Schröder, *et al.*, "Laser-induced hydrocarbon contamination in vacuum," in *Proc. SPIE*, G. J. Exarhos, A. H. Guenther, K. L. Lewis, *et al.*, Eds., **5991**, 59910H, (Boulder, CO) (2005).

[154] D. N. Nguyen, L. A. Emmert, P. Schwoebel, *et al.*, "Femtosecond pulse damage thresholds of dielectric coatings in vacuum," *Optics Express* **19**, 5690 (2011).

[155] N. Sanner, B. Bussiere, O. Utéza, *et al.*, "Influence of the beam-focus size on femtosecond laser-induced damage threshold in fused silica," in *Proc. SPIE*, J. Neev, S. Nolte, A. Heisterkamp, *et al.*, Eds., **6881**, 68810W, (San Jose, CA) (2008).

[156] O. Uteza, B. Bussiere, F. Canova, *et al.*, "Laser-induced damage threshold of sapphire in nanosecond, picosecond and femtosecond regimes," *Applied Surface Science* **254**, 799–803 (2007).

[157] S. Martin, A. Hertwig, M. Lenzner, *et al.*, "Spot-size dependence of the ablation threshold in dielectrics for femtosecond laser pulses," *Applied Physics A: Materials Science & Processing* **77**, 883–884 (2003).

[158] A. Hertwig, S. Martin, J. Krüger, *et al.*, "Interaction area dependence of the ablation threshold of ion-doped glass," *Thin Solid Films* **453-454**, 527–530 (2004).

[159] B. C. Stuart, M. D. Feit, S. Herman, *et al.*, "Optical ablation by high-power short-pulse lasers," *J. Opt. Soc. Am. B* **13**, 459–468 (1996).

[160] G. Gebrayel El Reaidy, *Experimental evaluation and modeling of laser-induced contamination on space optics.* PhD thesis, Université d'Aix-Marseille (2018).

[161] K. Ohta and H. Ishida, "Matrix formalism for calculation of electric field intensity of light in stratified multilayered films," *Applied Optics* **29**, 1952 (1990).

[162] A. Olle, *Etude de la dépendance temporelle de l'endommagement laser de matériaux diélectriques à 1054 nm en régime sub-picoseconde et picoseconde.* PhD thesis, Ecole Centrale Marseille (2020).

[163] L. G. DeShazer, B. E. Newnam, and K. M. Leung, "Role of coating defects in laser-induced damage to dielectric thin films," *Applied Physics Letters* **23**, 607–609 (1973).

[164] N. L. Boling and G. Dubé, "Laser-induced inclusion damage at surfaces of transparent dielectrics," *Applied Physics Letters* **23**, 658–660 (1973).

[165] R. H. Picard, D. Milam, and R. A. Bradbury, "Statistical analysis of defect-caused laser damage in thin films," *Applied Optics* **16**, 1563 (1977).

[166] J. Reif, S. Petzoldt, A. P. Elg, *et al.*, "The role of defects in laser surface damage thresholds of fluoride crystals," *Applied Physics A Solids and Surfaces* **49**, 199–204 (1989).

[167] F. E. Hovis, B. A. Shepherd, C. T. Radcliffe, *et al.*, "Optical damage at the part per million level: the role of trace contamination in laser-induced optical damage," in *Proc. SPIE*, H. E. Bennett, L. L. Chase, A. H. Guenther, *et al.*, Eds., **2114**, 145, (Boulder, CO) (1994).

[168] J.-Y. Natoli, L. Gallais, H. Akhouayri, *et al.*, "Laser-induced damage of materials in bulk, thin-film, and liquid forms," *Applied Optics* **41**, 3156 (2002).

[169] Y. Xu, D. H. Dunlap, L. A. Emmert, *et al.*, "Laser-driven detonation wave in hafnium oxide film: Defect controlled laser damage and ablation," *Journal of Applied Physics* **128**, 123101 (2020).

[170] B. Mangote, L. Gallais, M. Zerrad, *et al.*, "A high accuracy femto-/picosecond laser damage test facility dedicated to the study of optical thin films," *Review of Scientific Instruments* **83**, 013109 (2012).

[171] M. Garcia-Lechuga, G. Gebrayel El Reaidy, H. Ning, *et al.*, "Assessing the limits of determinism and precision in ultrafast laser ablation," *Applied Physics Letters* **117**, 171604 (2020).

[172] B. Zhou, A. Kar, M. J. Soileau, *et al.*, "Invariance of the r^2-ln(F) relationship and attainable precision in ultrafast laser ablation experiments," *Optics Express* **29**, 5635 (2021).

[173] T. A. Laurence, R. A. Negres, S. Ly, *et al.*, "Role of defects in laser-induced modifications of silica coatings and fused silica using picosecond pulses at 1053 nm: II. Scaling laws and the density of precursors," *Opt. Express* **25**, 15381–15401 (2017).

[174] D. Ashkenasi and A. Rosenfeld, "Material processing of dielectrics with femtosecond lasers," in *Laser Applications in Microelectronic and Optoelectronic Manufacturing IV*, J. J. Dubowski, H. Helvajian, E.-W. Kreutz, *et al.*, Eds., **3618**, 102 – 113, International Society for Optics and Photonics, SPIE (1999).

[175] O. Armbruster, A. Naghilou, M. Kitzler, *et al.*, "Spot size and pulse number dependence of femtosecond laser ablation thresholds of silicon and stainless steel," *Applied Surface Science* **396**, 1736–1740 (2017).

[176] A. Naghilou, O. Armbruster, and W. Kautek, "Femto- and nanosecond pulse laser ablation dependence on irradiation area: The role of defects in metals and semiconductors," *Applied Surface Science* **418**, 487–490 (2017).

[177] B.-M. Kim, M. D. Feit, A. M. Rubenchik, *et al.*, "Effects of high repetition rate and beam size on hard tissue damage due to subpicosecond laser pulses," *Applied Physics Letters* **76**, 4001–4003 (2000).

[178] A. Naghilou, O. Armbruster, M. Kitzler, *et al.*, "Merging Spot Size and Pulse Number Dependence of Femtosecond Laser Ablation Thresholds: Modeling and Demonstration with High Impact Polystyrene," *The Journal of Physical Chemistry C* **119**, 22992–22998 (2015).

[179] O. Armbruster, A. Naghilou, and W. Kautek, "The Role of Defects in Pulsed Laser Matter Interaction," in *Advances in the Application of Lasers in Materials Science*, P. M. Ossi, Ed., **274**, 39–61, Springer International Publishing, Cham (2018). Series Title: Springer Series in Materials Science; Excellent LID introduction.

[180] J. B. Ashcom, R. R. Gattass, C. B. Schaffer, *et al.*, "Numerical aperture dependence of damage and supercontinuum generation from femtosecond laser pulses in bulk fused silica," *J. Opt. Soc. Am. B* **23**, 2317–2322 (2006).

[181] S. R. Foltyn, "Spotsize effects in laser damage testing," *Laser Induced Damage in Optical Materials* **669**, 368–379 (1982).

[182] L. Lamaignère, M. Balas, R. Courchinoux, *et al.*, "Parametric study of laser-induced surface damage density measurements: Toward reproducibility," *Journal of Applied Physics* **107**, 023105 (2010).

[183] L. Lamaignère, A. Ollé, M. Chorel, *et al.*, "Round-robin measurements of the laser-induced damage threshold with sub-picosecond pulses on optical single layers," *Optical Engineering* **60** (2020).

[184] M. Scherer, "Magnetron sputter-deposition on atom layer scale," *Vak. Forsch. Prax.* **21**, 24–30 (2009).

[185] A. V. Smith and B. T. Do, "Bulk and surface laser damage of silica by picosecond and nanosecond pulses at 1064 nm," *Applied Optics* **47**, 4812 (2008).

[186] E. T. J. Nibbering, G. Grillon, M. A. Franco, *et al.*, "Determination of the inertial contribution to the nonlinear refractive index of air, N_2, and O_2 by use of unfocused high-intensity femtosecond laser pulses," *Journal of the Optical Society of America B* **14**, 650 (1997).

[187] Y. E. Geints, A. M. Kabanov, A. A. Zemlyanov, *et al.*, "Kerr-driven nonlinear refractive index of air at 800 and 400 nm measured through femtosecond laser pulse filamentation," *Applied Physics Letters* **99**, 181114 (2011).

[188] A. Börzsönyi, Z. Heiner, A. Kovács, *et al.*, "Measurement of pressure dependent nonlinear refractive index of inert gases," *Optics Express* **18**, 25847 (2010).

[189] V. Loriot, E. Hertz, O. Faucher, *et al.*, "Measurement of high order Kerr refractive index of major air components: erratum," *Optics Express* **18**, 3011 (2010).

[190] J. Schwarz, P. Rambo, M. Kimmel, *et al.*, "Measurement of nonlinear refractive index and ionization rates in air using a wavefront sensor," *Optics Express* **20**, 8791 (2012).

[191] A. V. Mitrofanov, A. A. Voronin, D. A. Sidorov-Biryukov, *et al.*, "Post-filament self-trapping of ultrashort laser pulses," *Optics Letters* **39**, 4659 (2014).

[192] Aurel Stratan, Alexandru Zorila, Laurentiu Rusen, *et al.*, "Measuring effective area of spots from pulsed laser beams," *Optical Engineering* **53**, 1–11 (2014).

[193] M. Chyla, M. Smrz, and T. Mocek, "High-energy, picosecond regenerative thin-disk amplifier at 1 kHz," in *Proc. SPIE*, W. A. Clarkson and R. K. Shori, Eds., **8235**, 82351W, (San Francisco, California, USA) (2012).

[194] J. Vanda, "Progress in design of advanced LIDT station in HiLASE project," in *Proc. SPIE*, J. Kovačičinová and T. Vít, Eds., **9442**, 94421E, (Liberec, Czech Republic) (2015).

[195] P. Cech, J. Vanda, M.-G. Muresan, *et al.*, "Laser-Induced Damage Threshold Testing at HILASE," *MM Science Journal* **2019**, 3657–3661 (2019).

[196] T. Willemsen, U. Chaulagain, I. Havlíčková, *et al.*, "Large area ion beam sputtered dielectric ultrafast mirrors for petawatt laser beamlines," *Optics Express* **30**, 6129 (2022).

[197] P. K. Velpula, D. Kramer, and B. Rus, "Femtosecond Laser-Induced Damage Characterization of Multilayer Dielectric Coatings," *Coatings* **10**, 603 (2020).

[198] M. Ďurák, D. Kramer, P. K. Velpula, *et al.*, "Comparison of different LIDT testing protocols for PW and multi-PW class high-reflectivity coatings," in *SPIE Laser Damage*, G. J. Exarhos, V. E. Gruzdev, J. A. Menapace, *et al.*, Eds., 100140O, (Boulder, CO, United States) (2016).

[199] A. R. Meadows, J. Cupal, P. Hříbek, *et al.*, "Femtosecond optical parametric amplification in BBO and KTA driven by a Ti:sapphire laser for LIDT testing and diagnostic development," in *SPIE Optics + Optoelectronics*, J. Hein, Ed., 102380E, (Prague, Czech Republic) (2017).

[200] M. Ďurák, P. K. Velpula, D. Kramer, *et al.*, "Laser-induced damage threshold tests of ultrafast multilayer dielectric coatings in various environmental conditions relevant for operation of ELI beamlines laser systems," *Optical Engineering* **56**, 011024 (2016).

[201] T. A. Laurence, D. A. Alessi, E. Feigenbaum, *et al.*, "Mirrors for petawatt lasers: Design principles, limitations, and solutions," *Journal of Applied Physics* **128**, 071101 (2020).

[202] Y. Chen, D. Hahner, M. Trubetskov, *et al.*, "Comparison of magnetron sputtering and ion beam sputtering on dispersive mirrors," *Applied Physics B* **126**, 82 (2020).

[203] D. Ristau and H. Ehlers, "Thin Film Optical Coatings," in *Springer Handbook of Lasers and Optics*, F. Träger, Ed., 373–396, Springer New York, New York, NY (2007).

[204] D. Zambrano, R. Villarroel, R. Espinoza-González, *et al.*, "Mechanical and microstructural properties of broadband anti-reflective TiO_2/SiO_2 coatings for photovoltaic applications fabricated by magnetron sputtering," *Solar Energy Materials and Solar Cells* **220**, 110841 (2021).

[205] S.-H. Jeong, J.-K. Kim, B.-S. Kim, *et al.*, "Characterization of SiO_2 and TiO_2 films prepared using rf magnetron sputtering and their application to anti-reflection coating," *Vacuum* **76**, 507–515 (2004).

[206] A. Zahoor, C. Xu, T. Shahid, *et al.*, "Effects of O_2 flux on structure, optical properties and hydrophobicity of highly emissive antireflective HfO_2 thin films by magnetron sputtering," *Vacuum* **197**, 110824 (2022).

[207] K. Sun, X. Tang, C. Yang, *et al.*, "Preparation and performance of low-emissivity Al-doped ZnO films for energy-saving glass," *Ceramics International* **44**, 19597–19602 (2018).

[208] B. Barman, S. K. Swami, and V. Dutta, "Fabrication of highly conducting ZnO/Ag/ZnO and AZO/Ag/AZO transparent conducting oxide layers using RF magnetron sputtering at room temperature," *Materials Science in Semiconductor Processing* **129**, 105801 (2021).

[209] L. Wang, C. Zhao, L. Zhao, *et al.*, "Effect of O_2/Ar flow ratio and heat treatment on the structure and properties of SiO_2 film prepared by magnetron sputtering," *Physica B: Condensed Matter* **630**, 413537 (2022).

[210] T. Minami, "Substitution of transparent conducting oxide thin films for indium tin oxide transparent electrode applications," *Thin Solid Films* **516**, 1314–1321 (2008).

[211] F. Craciun, T. Lippert, and M. Dinescu, "Pulsed Laser Deposition: Fundamentals, Applications, and Perspectives," in *Handbook of Laser Micro- and Nano-Engineering*, K. Sugioka, Ed., 1–33, Springer, Cham (2020).

[212] K. B. Masood, P. Kumar, M. A. Malik, *et al.*, "A comprehensive tutorial on the pulsed laser deposition technique and developments in the fabrication of low dimensional systems and nanostructures," *Emergent Mater.* **4**, 737–754 (2021).

[213] M. Filipescu, A. Palla-Papavlu, A. Bercea, *et al.*, "Antireflective coatings with high damage threshold prepared by laser ablation," *Appl. Phys. A* **125**, 815 (2019).

[214] A. Bercea, M. Filipescu, A. Moldovan, *et al.*, "Optical coatings for ELI experiments prepared by laser ablation," *Rom. J. Phys.* **63**(606) (2018).

[215] E. N. Sirjita, L. Rusen, S. Brajnicov, *et al.*, "Properties of Hafnium and Aluminium Silicates Coatings Obtained by PLD," *Coatings* **11**, 753 (2021).

[216] J. J. Prentice, J. A. Grant-Jacob, D. P. Shepherd, *et al.*, "Yb-doped mixed-sesquioxide films grown by pulsed laser deposition," *J. Cryst. Growth* **491**, 51–56 (2018).

[217] K. A. Sloyan, T. C. May-Smith, M. N. Zervas, *et al.*, "Crystalline garnet Bragg reflectors for high power, high temperature, and integrated applications fabricated by multi-beam pulsed laser deposition," *Appl. Phys. Lett.* **101**, 081117 (2012).

[218] P. H. Lissberger, "Optical applications of dielectric thin films," *Reports on Progress in Physics* **33**, 197–268 (1970).

[219] H. Ehlers and D. Ristau, *Production strategies for high-precision optical coatings*, 103–140. Elsevier (2018).

[220] H. A. Macleod, *Thin-film optical filters*, Institute of Physics Pub, Bristol ; Philadelphia, 3rd ed ed. (2001).

[221] D. Depla, S. Mahieu, and J. Greene, "Sputter Deposition Processes," in *Handbook of Deposition Technologies for Films and Coatings*, P. M. Martin, Ed., ch. 5, 253–296, William Andrew Publishing, Boston, third ed. (2010).

[222] J. Zideluns, *Optical monitoring methods and strategies for magnetron sputtered thin-film filters*. PhD thesis, Ecole Centrale Marseille (2022).

[223] D. Rasic, R. Sachan, M. F. Chisholm, *et al.*, "Room Temperature Growth of Epitaxial Titanium Nitride Films by Pulsed Laser Deposition," *Crystal Growth & Design* **17**, 6634–6640 (2017).

[224] D. Rasic and J. Narayan, "Epitaxial Growth of Thin Films," in *Crystal Growth*, V. Glebovsky, Ed., ch. 5, IntechOpen, Rijeka (2019).

[225] T. Venkatesan, X. Wu, A. Inam, *et al.*, "Laser processing of high-T_c superconducting thin films," *IEEE J. Quantum Electron.* **25**, 2388–2393 (1989).

[226] H. M. Smith and A. F. Turner, "Vacuum Deposited Thin Films Using a Ruby Laser," *Appl. Opt.* **4**, 147 (1965).

[227] J. J. Prentice, J. A. Grant-Jacob, S. V. Kurilchik, *et al.*, "Particulate reduction in PLD-grown crystalline films via bi-directional target irradiation," *Appl. Phys. A* **125**, 152 (2019).

[228] G. A. Govindassamy, J. J. Prentice, J. G. Lunney, *et al.*, "Effect of laser repetition rate on the growth of Sc_2O_3 via pulsed laser deposition," *Appl. Phys. A* **128**, 577 (2022).

[229] T. C. May-Smith, A. C. Muir, M. S. B. Darby, *et al.*, "Design and performance of a ZnSe tetra-prism for homogeneous substrate heating using a CO_2 laser for pulsed laser deposition experiments," *Appl. Opt.* **47**, 1767–1780 (2008).

[230] H. Hagedorn, W. Lehnert, J. Pistner, *et al.*, "Plasma assisted reactive magnetron sputtering of demanding interference filters," in *SVC TechCon 2012*, O–24, (Santa Clara, CA, USA) (2012).

[231] Y. Nigara, "Measurement of the optical constants of yttrium oxide," *Jpn J Appl Phys* **7**, 404–408 (1968).

[232] A. Belosludtsev, K. Juškevičius, L. Ceizaris, *et al.*, "Correlation between stoichiometry and properties of scandium oxide films prepared by reactive magnetron sputtering," *Appl. Surf. Sci.* **427**, 312–318 (2018).

[233] L. Gao, F. Lemarchand, and M. Lequime, "Refractive index determination of SiO_2 layer in the UV/Vis/NIR range: spectrophotometric reverse engineering on single and bi-layer designs," *Journal of the European Optical Society: Rapid Publications* **8**, 13010 (2013).

[234] L. Gao, F. Lemarchand, and M. Lequime, "Exploitation of multiple incidences spectrometric measurements for thin film reverse engineering," *Optics Express* **20**, 15734–15751 (2012).

[235] O. Stenzel, S. Wilbrandt, M. Schürmann, *et al.*, "Mixed oxide coatings for optics," *Appl. Opt.* **50**, C69–C74 (2011).

[236] E. C. Freeman and W. Paul, "Optical constants of rf sputtered hydrogenated amorphous Si," *Phys. Rev. B* **20**, 716–728 (1979).

[237] C. Kränkel, "Rare-Earth-Doped Sesquioxides for Diode-Pumped High-Power Lasers in the 1-, 2-, and 3-µm Spectral Range," *IEEE J. Sel. Top. Quantum Electron.* **21**, 250–262 (2015).

[238] Y. Kuzminykh, A. Kahn, and G. Huber, "Nd^{3+} doped Sc_2O_3 waveguiding film produced by pulsed laser deposition," *Opt. Mater.* **28**, 883–887 (2006).

[239] S. Chen, Y. Zhao, Z. Yu, *et al.*, "Femtosecond laser-induced damage of HfO_2/SiO_2 mirror with different stack structure," *Appl. Opt.* **51**, 6188 (2012).

[240] A. Hervy, L. Gallais, G. Chériaux, *et al.*, "Femtosecond laser-induced damage threshold of electron beam deposited dielectrics for 1-m class optics," *Opt. Eng.* **56**, 011001 (2016).

[241] M. Mende, S. Schrameyer, H. Ehlers, *et al.*, "Laser damage resistance of ion-beam sputtered Sc_2O_3/SiO_2 mixture optical coatings," *Appl. Opt.* **52**, 1368 (2013).

[242] C. S. Menoni, E. M. Krous, D. Patel, *et al.*, "Advances in ion beam sputtered Sc_2O_3 for optical interference coatings," in *Proc. SPIE*, **7842**, 784202 (2010).

[243] E. M. Krous, D. Patel, P. Langston, *et al.*, "Scandium oxide thin films deposited by dual ion beam sputtering for high-power laser applications," in *Optical Interference Coatings*, FA10, OSA, (Tucson, AZ, USA) (2010).

[244] D. Grosso and P. Sermon, "Scandia optical coatings for application at 351 nm," *Thin Solid Films* **368**, 116–124 (2000).

[245] J. Aarik, H. Mändar, M. Kirm, *et al.*, "Optical characterization of HfO_2 thin films grown by atomic layer deposition," *Thin Solid Films* **466**, 41–47 (2004).

[246] F. Rainer, W. H. Lowdermilk, D. Milam, *et al.*, "Scandium oxide coatings for high-power UV laser applications," *Appl. Opt.* **21**, 3685 (1982).

[247] F. Rainer, W. H. Lowdermilk, D. Milam, *et al.*, "Materials for optical coatings in the ultraviolet," *Appl. Opt.* **24**, 496 (1985).

[248] S. Tamura, S. Kimura, Y. Sato, *et al.*, "Laser-damage threshold of Sc_2O_3/SiO_2 high reflector coatings for a laser wavelength of 355 nm," *Thin Solid Films* **228**, 222–224 (1993).

[249] S. J. Beecher, J. A. Grant-Jacob, P. Hua, *et al.*, "Ytterbium-doped-garnet crystal waveguide lasers grown by pulsed laser deposition," *Optical Materials Express* **7**, 1628 (2017).

[250] A. Hervy, L. Gallais, D. Mouricaud, *et al.*, "Electron-beam deposited materials for high-reflective coatings: Femtosecond LIDT," in *Optical Interference Coatings (OIC) 2013*, FA.4, OSA, (Whistler, Canada) (2013).

[251] L. Gallais, B. Mangote, M. Zerrad, *et al.*, "Laser-induced damage of hafnia coatings as a function of pulse duration in the femtosecond to nanosecond range," *Appl. Opt.* **50**, C178–C187 (2011).

[252] D. N. Nguyen, L. Emmert, M. Mero, *et al.*, "The effect of annealing on the subpicosecond breakdown behavior of hafnia films," in *Proc. SPIE*, **7132**, 71320N (2008).

[253] P. K. Velpula, M. Ďurák, D. Kramer, *et al.*, "Evolution of femtosecond laser damage in a hafnia–silica multi-layer dielectric coating," *Optics Letters* **44**, 5342 (2019).

[254] M. Rasedujjaman and L. Gallais, "Polarization dependent laser damage growth of optical coatings at sub-picosecond regime," *Optics Express* **26**, 24444 (2018).

[255] D.-B. Douti, T. Bégou, F. Lemarchand, *et al.*, "Analysis of laser energy deposition leading to damage and ablation of HfO_2 and Nb_2O_5 single layers submitted to 500 fs pulses at 1030 and 343 nm," *Applied Physics A* **122**, 653 (2016).

[256] K. R. P. Kafka, E. A. Chowdhury, R. A. Negres, *et al.*, "Test station development for laser-induced optical damage performance of broadband multilayer dielectric coatings," in *SPIE Laser Damage*, G. J. Exarhos, V. E. Gruzdev, J. A. Menapace, *et al.*, Eds., 96321C, (Boulder, CO, United States) (2015).

[257] R. A. Negres, C. W. Carr, T. A. Laurence, *et al.*, "Laser-induced damage of intrinsic and extrinsic defects by picosecond pulses on multilayer dielectric coatings for petawatt-class lasers," *Optical Engineering* **56**, 011008 (2016).

[258] C. J. Stolz, R. A. Negres, K. Kafka, *et al.*, "150-ps broadband low dispersion mirror thin film damage competition," in *SPIE Laser Damage*, G. J. Exarhos, V. E. Gruzdev, J. A. Menapace, *et al.*, Eds., 96320C, (Boulder, CO, United States) (2015).

[259] C. Petite, R. Marcouillé, A. Moreau, *et al.*, "Multipass lock-in thermography for the study of optical coating absorption," *Applied Optics* **61**, 978 (2022).

[260] R. Paschotta, *Encyclopedia of laser physics and technology*, Wiley-VCH, Weinheim (2008). OCLC: ocn229464595.

[261] I. H. Malitson, "Interspecimen Comparison of the Refractive Index of Fused Silica," *Journal of the Optical Society of America* **55**, 1205 (1965).

[262] D. Milam, "Review and assessment of measured values of the nonlinear refractive-index coefficient of fused silica," *Applied Optics* **37**, 546 (1998).

[263] I. Pipinytė, R. Grigonis, K. Stankevičiūtė, *et al.*, "Laser-induced-damage threshold of periodically poled lithium niobate for 1030 nm femtosecond laser pulses at 100 kHz and 75 MHz," in *Proc. of SPIE Vol. 8786*, J. Shao, T. Jitsuno, and W. Rudolph, Eds., 87861N, (Shanghai, P. R. China) (2013).

[264] I. B. Angelov, M. von Pechmann, M. K. Trubetskov, *et al.*, "Optical breakdown of multilayer thin-films induced by ultrashort pulses at MHz repetition rates," *Optics Express* **21**, 31453 (2013).

[265] B. J. Nagy, L. Gallais, L. Vámos, *et al.*, "Direct comparison of kilohertz- and megahertz-repetition-rate femtosecond damage threshold," *Optics Letters* **40**, 2525 (2015).

[266] L. N. Acquaroli, "Matrix method for thin film optics," (2018). [arXiv:1809.07708v1 [physics.optics]].

[267] M. Stehlik, G. Govindassamy, J. Zideluns, *et al.*, "Sub-picosecond 1030 nm laser-induced damage threshold evaluation of pulsed-laser deposited sesquioxide thin films," *Optical Engineering* **61** (2022).

[268] S. Preuss, A. Demchuk, and M. Stuke, "Sub-picosecond UV laser ablation of metals," *Applied Physics A Materials Science & Processing* **61**, 33–37 (1995).

[269] G. Koren and U. P. Oppenheim, "Laser ablation of polymers in pressurized gas ambients," *Applied Physics B Photophysics and Laser Chemistry* **42**, 41–43 (1987).

[270] T. Willemsen, M. Jupé, M. Gyamfi, *et al.*, "Enhancement of the damage resistance of ultra-fast optics by novel design approaches," *Opt. Express* **25**, 31948 (2017).

[271] A. Milenin, C. Jamois, R. Wehrspohn, *et al.*, "The SOI planar photonic crystal fabrication: patterning of Cr using Cl_2/O_2 plasma etching," *Microelectronic Engineering* **77**, 139–143 (2005).

[272] A. Milenin, C. Jamois, T. Geppert, *et al.*, "SOI planar photonic crystal fabrication: Etching through $SiO_2/Si/SiO_2$ layer systems using fluorocarbon plasmas," *Microelectronic Engineering* **81**, 15–21 (2005).

[273] F. Messow, C. Welch, A. Eifert, *et al.*, "Deep single step vertical ICP–RIE etching of ion beam sputter deposited SiO_2/Si multilayer stacks," *Microelectronic Engineering* **113**, 70–73 (2014).

[274] M. Taimoor, A. Alatawi, S. Reuter, *et al.*, "Single-step inductively coupled plasma etching of sputtered Nb_2O_5/SiO_2 multilayer stacks using chromium etch mask," *Journal of Vacuum Science & Technology A: Vacuum, Surfaces, and Films* **35**, 041302 (2017).

[275] M. F. A. Muttalib, R. Y. Chen, S. J. Pearce, *et al.*, "Optimization of reactive-ion etching (RIE) parameters for fabrication of tantalum pentoxide (Ta_2O_5) waveguide using Taguchi method," *EPJ Web of Conferences* **162**, 01003 (2017).

[276] N. Arjmandi, "Resist Homogeneity," in *Updates in Advanced Lithography*, S. Hosaka, Ed., InTech (2013).

[277] M. Zakharova, V. Vlnieska, H. Fornasier, *et al.*, "Development and Characterization of Two-Dimensional Gratings for Single-Shot X-ray Phase-Contrast Imaging," *Applied Sciences* **8**, 468 (2018).

[278] L. Sudrie, A. Couairon, M. Franco, *et al.*, "Femtosecond Laser-Induced Damage and Filamentary Propagation in Fused Silica," *Physical Review Letters* **89**, 186601 (2002).

[279] S. Hocquet, J. Neauport, and N. Bonod, "The role of electric field polarization of the incident laser beam in the short pulse damage mechanism of pulse compression gratings," *Applied Physics Letters* **99**, 061101 (2011).

[280] F. Kong, Y. Jin, H. Huang, *et al.*, "Laser-induced damage of multilayer dielectric gratings with picosecond laser pulses under vacuum and air," *Optics & Laser Technology* **73**, 39–43 (2015).

[281] M. G. Moharam, T. K. Gaylord, E. B. Grann, *et al.*, "Formulation for stable and efficient implementation of the rigorous coupled-wave analysis of binary gratings," *Journal of the Optical Society of America A* **12**, 1068 (1995).

[282] M. G. Moharam, T. K. Gaylord, D. A. Pommet, *et al.*, "Stable implementation of the rigorous coupled-wave analysis for surface-relief gratings: enhanced transmittance matrix approach," *Journal of the Optical Society of America A* **12**, 1077 (1995).

[283] S. M. Eaton, H. Zhang, P. R. Herman, *et al.*, "Heat accumulation effects in femtosecond laser-written waveguides with variable repetition rate," *Optics Express* **13**(12), 4708 (2005).

[284] Y. Hao, M. Sun, Y. Guo, *et al.*, "Asymmetrical damage growth of multilayer dielectric gratings induced by picosecond laser pulses," *Optics Express* **26**, 8791 (2018).

[285] H. A. Abdeldayem, E. Dowdye, J. Canham, *et al.*, "Contamination and radiation effects on spaceflight laser systems," in *Proc. SPIE*, E. W. Taylor, Ed., **5897**, 589705, (San Diego, California, USA) (2005).

[286] F. E. Hovis, B. A. Shepherd, C. T. Radcliffe, *et al.*, "Mechanisms of contamination-induced optical damage in lasers," in *Proc. SPIE*, H. E. Bennett, A. H. Guenther, M. R. Kozlowski, *et al.*, Eds., **2428**, 72–83, (Boulder, CO) (1995).

[287] D. Wernham, J. Alves, F. Pettazzi, *et al.*, "Laser-induced contamination mitigation on the ALADIN laser for ADM-Aeolus," in *Proc. SPIE*, G. J. Exarhos, V. E. Gruzdev, J. A. Menapace, *et al.*, Eds., **7842**, 78421E, (Boulder, Colorado) (2010).

[288] M. Otto, "Airborne molecular contamination: quality criterion for laser and optical components," in *Proc. SPIE*, A. L. Glebov and P. O. Leisher, Eds., **9346**, 93460F, (San Francisco, California, United States) (2015).

[289] C. T. Scurlock, "A phenomenological study of the effect of trace contamination on lifetime reduction and laser-induced damage for optics," in *Proc. SPIE*, G. J. Exarhos, A. H. Guenther, N. Kaiser, *et al.*, Eds., **5647**, 86, (Boulder, CO) (2005).

[290] H. Schröder, P. Wagner, D. Kokkinos, *et al.*, "Laser-induced contamination and its impact on laser damage threshold," in *Proc. SPIE*, G. J. Exarhos, V. E. Gruzdev, J. A. Menapace, *et al.*, Eds., **8885**, 88850R, (Boulder, Colorado, USA) (2013).

[291] D. Kokkinos, H. Schroeder, K. Fleury-Frenette, *et al.*, "Laser optics in space failure risk due to laser induced contamination," *CEAS Space Journal* **9**, 153–162 (2016).

[292] P. Zhang, Y. Jiang, J. Wang, *et al.*, "Improvements in long-term output energy performance of Nd:glass regenerative amplifiers," *High Power Laser Science and Engineering* **5**, e23 (2017).

[293] Z. Hubka, J. Novák, I. Majerová, *et al.*, "Mitigation of laser-induced contamination in vacuum in high-repetition-rate high-peak-power laser systems," *Applied Optics* **60**, 533 (2021).

[294] P. Chen, R. Hedgeland, L. Ramsey, *et al.*, "Contamination control of space-based laser instruments," in *Proc. SPIE*, O. M. Uy, S. A. Straka, J. C. Fleming, *et al.*, Eds., **6291**, 629104, (San Diego, California, USA) (2006).

[295] H. Schröder, S. Borgmann, W. Riede, *et al.*, "Investigation of laser induced deposit formation under space conditions," in *International Conference on Space Optics — ICSO 2008*, J. Costeraste, E. Armandillo, and N. Karafolas, Eds., 22, SPIE, (Toulouse, France) (2017).

[296] W. Riede, H. Schroeder, G. Bataviciute, *et al.*, "Laser-induced contamination on space optics," in *Proc. SPIE*, G. J. Exarhos, V. E. Gruzdev, J. A. Menapace, *et al.*, Eds., **8190**, 81901E, (Boulder, Colorado) (2011).

[297] B. H. Weiller, J. D. Fowler, and R. M. Villahermosa, "Contamination resistant coatings for enhanced laser damage thresholds," in *Proc. SPIE*, G. J. Exarhos, V. E. Gruzdev, J. A. Menapace, *et al.*, Eds., **8530**, 85302A, (Boulder, Colorado, USA) (2012).

[298] S. Möller, A. Andresen, C. Merschjann, *et al.*, "Insight to UV-induced formation of laser damage on LiB_3O_5 optical surfaces during long-term sum-frequency generation," *Optics Express* **15**(12), 7351 (2007).

[299] U. Leinhos, K. Mann, A. Bayer, *et al.*, "Long-term laser induced contamination tests of optical elements under vacuum at 351 nm," in *Proc. SPIE*, G. J. Exarhos, V. E. Gruzdev, J. A. Menapace, *et al.*, Eds., **7842**, 78422E, (Boulder, Colorado) (2010).

[300] F. E. Hovis, B. A. Shepherd, C. T. Radcliffe, *et al.*, "Contamination damage in pulsed 1-µm lasers," in *Proc. SPIE*, H. E. Bennett, A. H. Guenther, M. R. Kozlowski, *et al.*, Eds., **2714**, 707, (Boulder, CO) (1996).

[301] D. Kokkinos, P. Gailly, M. P. Georges, *et al.*, "Real-time measurement of temperature variation during nanosecond pulsed-laser-induced contamination deposition," *Applied Optics* **54**, 10579 (2015).

[302] I. Balasa, M. Hippler, H. Schröder, *et al.*, "Enhancement of contamination growth and damage by absorption centers under UV irradiation," in *Proc. SPIE*, G. J. Exarhos, V. E. Gruzdev, J. A. Menapace, *et al.*, Eds., **9237**, 92372A, (Boulder, Colorado, United States) (2014).

[303] G. Gebrayel El Reaidy, F. R. Wagner, D. Faye, *et al.*, "Study of the first stages of laser-induced contamination," *Optical Engineering* **57**, 1 (2018).

[304] K. Bien-Aimé, C. Belin, L. Gallais, *et al.*, "Impact of storage induced outgassing organic contamination on laser induced damage of silica optics at 351 nm," *Optics Express* **17**, 18703 (2009).

[305] O. Favrat, B. Mangote, I. Tovena-Pécault, *et al.*, "Study of organic contamination induced by outgassing materials. Application to the Laser MégaJoule optics," *Applied Surface Science* **293**, 132–137 (2014).

[306] X. Cheng, X. Miao, H. Wang, *et al.*, "Surface Contaminant Control Technologies to Improve Laser Damage Resistance of Optics," *Advances in Condensed Matter Physics* **2014**, 1–7 (2014).

[307] E. S. Field and D. E. Kletecka, "Impact of contamination and aging effects on the long-term laser damage resistance of $SiO_2/HfO_2/TiO_2$ high reflection coatings for 1054 nm," *Optical Engineering* **58**, 1 (2019).

[308] H. Schröder, S. Becker, Y. Lien, *et al.*, "Fluorescence monitoring of organic deposits," in *Proc. SPIE*, G. J. Exarhos, A. H. Guenther, K. L. Lewis, *et al.*, Eds., **6720**, 67200O, (Boulder, CO) (2007).

[309] "White Light Interferometry." https://www.nanoscience.com/techniques/optical-profilometry/white-light-interferometry/. Accessed: 2022-07-14.

[310] M. Ghafoor, "Synthesis of high refractive index materials for manufacturing apochromatic lens by 3D printing," (2017).

[311] F. A. Stevie and C. L. Donley, "Introduction to x-ray photoelectron spectroscopy," *Journal of Vacuum Science & Technology A* **38**, 063204 (2020).

[312] J. F. Moulder, W. F. Stickle, P. E. Sobol, *et al.*, *Handbook of X-ray photoelectron spectroscopy*, Perkin-Elmer Corporation, Eden Prairie (1992). Accessed: 2022-07-15.

[313] G. Greczynski and L. Hultman, "A step-by-step guide to perform x-ray photoelectron spectroscopy," *Journal of Applied Physics* **132**, 011101 (2022).

[314] E. Salomon, M. Minissale, F. R. Lairado, *et al.*, "Pyrene Adsorption on a Ag(111) Surface," *The Journal of Physical Chemistry C* **125**, 11166–11174 (2021).

[315] F. Keilmann and R. Hillenbrand, "Near-field microscopy by elastic light scattering from a tip," *Philos. Trans. Royal Soc. A* **362**, 787–805 (2004).

[316] C. Petite, *Composants optiques en couches minces pour lasers de forte puissance continue*. PhD thesis, Ecole Centrale Marseille (2022).

[317] D. Lupinski, D. Balitsky, A. Dobroc, *et al.*, "Entre tenue au flux laser et Vieillissement des cristaux ONL - le point de vue du producteur (Cristal Laser)." Atelier Tenue au flux Laser, Toulouse 28-29 june, 2022.

Appendices

Appendix A

Mirror designs

Here we will provide description of mirror designs developed within the project GREAT and CLASm and OPTm mirrors aiming to study LIDT enhancement by optimizing EFI distribution. The mirrors with their parameters were summarized in Table 5.1 on page 131 and their electric field intensity maxima were listed in Table 5.2 on page 133. All mirrors were designed for S (TE) polarization. A1D3, A5D5, CLASm and OPTm have application wavelength of 1030 nm, whereas A3D1 and A3D3 976 nm. We will firstly list in Table A.1 the values of measured and simulated transmittances at wavelengths of interest in this thesis. Then, for each mirror, we will provide table describing its design and figures with transmission spectra and electric field intensity distribution. More information about the mirror designs and the thickness monitoring during magnetron-sputtering deposition is in the thesis of Janis Zideluns [222].

Mirror	Wavelength	Transm. measured	Transmittance simulated			
		(Mixed pol.) (0° AOI)	(Mixed pol.) (0° AOI)	(Mixed pol.) (Appl. AOI)	(P pol.) (Appl. AOI)	(S pol.) (Appl. AOI)
[-]	[nm]	[-]	[-]	[-]	[-]	[-]
A1D3	1030	6.97E+01	6.31E+01	1.64E-02	3.28E-02	2.58E-05
A3D1	1030	1.02E-01	1.05E-01	1.58E-01	3.16E-01	2.63E-04
	976	3.09E+01	3.15E+01	5.41E-02	1.08E-01	1.63E-04
A3D3	1030	7.07E-03	6.08E-03	5.87E-02	1.17E-01	4.25E-05
	976	5.36E+00	4.72E+00	1.76E-02	3.52E-02	1.91E-05
A5D5	1030	-2.10E-03	8.64E-04	8.64E-04	8.64E-04	8.64E-04
CLASm	1030	2.51E-02	1.65E-02	1.65E-02	1.65E-02	1.65E-02
	1050	2.75E-02	1.88E-02	1.88E-02	1.88E-02	1.88E-02
OPTm	1030	2.60E-02	1.66E-02	1.66E-02	1.66E-02	1.66E-02
	1050	1.73E-02	7.41E-03	7.41E-03	7.41E-03	7.41E-03

Table A.1: Transmittances of mirrors at wavelengths of interest in this thesis (see Table 5.2). The right column corresponds to S polarization and application angle of incidence (AOI) given in Table 5.1. all values of A5D5, CLASm and OPTm designs correspond to 0° AOI.

A1D3

Layer	Material	n	Thickness
[-]	[-]	[-]	[nm]
0	FS	1.45	
1	HfO_2	2.03	138
2	SiO_2	1.47	205
3	HfO_2	2.03	138
4	SiO_2	1.47	205
5	HfO_2	2.03	138
6	SiO_2	1.47	205
7	HfO_2	2.03	138
8	SiO_2	1.47	205
9	HfO_2	2.03	138
10	SiO_2	1.47	205
11	HfO_2	2.03	138
12	SiO_2	1.47	205
13	HfO_2	2.03	138
14	SiO_2	1.47	205
15	HfO_2	2.03	138
16	SiO_2	1.47	205
17	HfO_2	2.03	138
18	SiO_2	1.47	205
19	HfO_2	2.03	138
20	SiO_2	1.47	205
21	HfO_2	2.03	138

Layer	Material	n	Thickness
[-]	[-]	[-]	[nm]
22	SiO_2	1.47	205
23	HfO_2	2.03	138
24	SiO_2	1.47	205
25	HfO_2	2.03	138
26	SiO_2	1.47	205
27	HfO_2	2.03	138
28	SiO_2	1.47	205
29	HfO_2	2.03	138
30	SiO_2	1.47	205
31	HfO_2	2.03	138
32	SiO_2	1.47	205
33	HfO_2	2.03	138
34	SiO_2	1.47	205
35	HfO_2	2.03	138
36	SiO_2	1.47	205
37	HfO_2	2.03	138
38	SiO_2	1.47	205
39	HfO_2	2.03	138
40	SiO_2	1.47	110
41	HfO_2	2.03	255
	air	1	

Table A.2: A1D3 mirror design with refractive indices n @1030nm and physical thicknesses of layers.

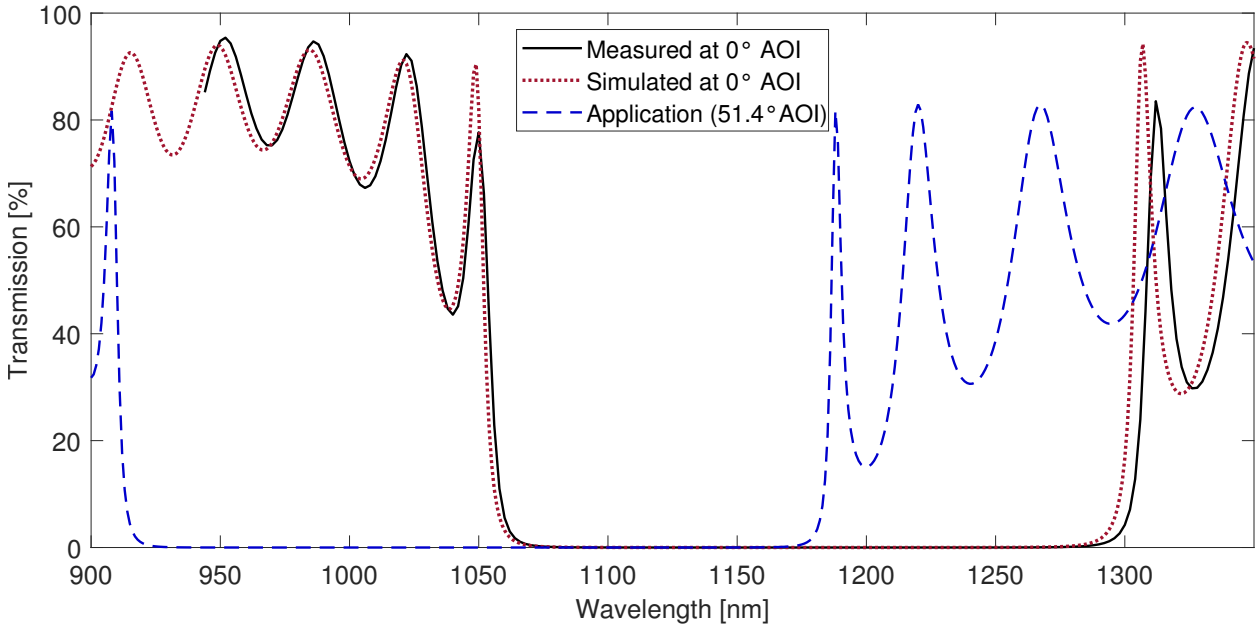

Figure A.1: Transmission spectra of A1D3 mirror measured and simulated at 0° AOI and transmission spectrum for its application conditions (51.4° AOI, S polarization).

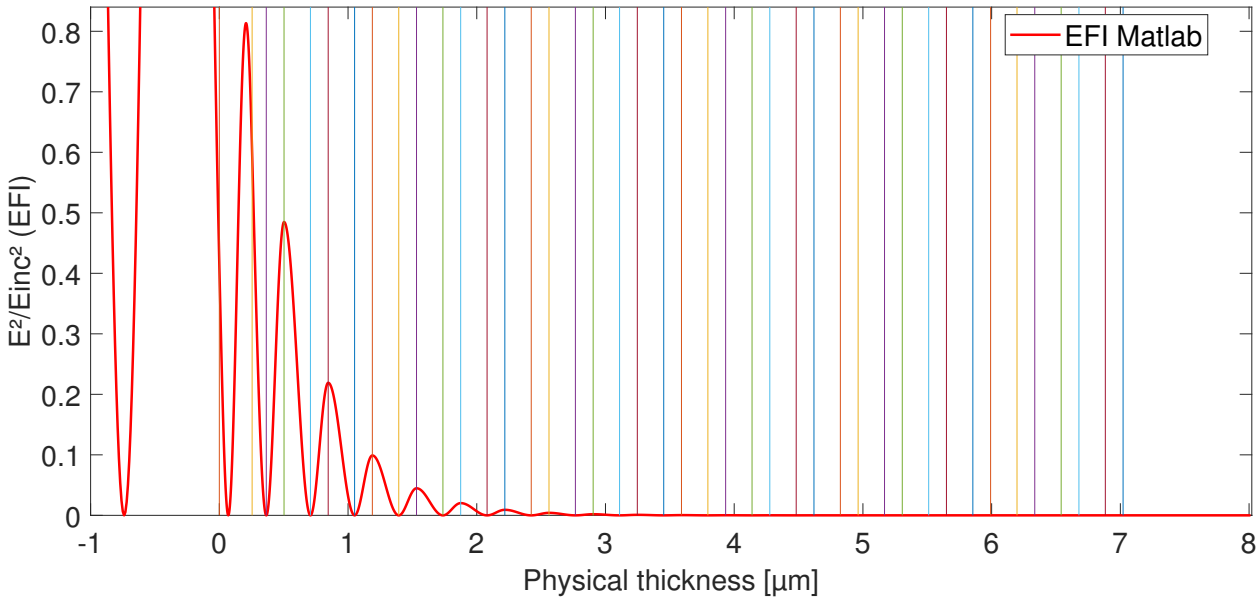

Figure A.2: Electric Field Intensity distribution within A1D3 mirror (51.4° AOI, S polarization, wavelength of 1030 nm). The physical thickness 0 corresponds to the interface between air and HfO_2.

A3D1

Layer	Material	n	Thickness
[-]	[-]	[-]	[nm]
0	FS	1.45	
1	Nb_2O_5	2.26	117
2	SiO_2	1.47	205
3	Nb_2O_5	2.26	117
4	SiO_2	1.47	205
5	Nb_2O_5	2.26	117
6	SiO_2	1.47	205
7	Nb_2O_5	2.26	117
8	SiO_2	1.47	205
9	Nb_2O_5	2.26	117
10	SiO_2	1.47	205
11	Nb_2O_5	2.26	117
12	SiO_2	1.47	205
13	Nb_2O_5	2.26	117
14	SiO_2	1.47	205

Layer	Material	n	Thickness
[-]	[-]	[-]	[nm]
15	Nb_2O_5	2.26	117
16	SiO_2	1.47	205
17	Nb_2O_5	2.26	117
18	SiO_2	1.47	205
19	Nb_2O_5	2.26	117
20	SiO_2	1.47	205
21	Nb_2O_5	2.26	117
22	SiO_2	1.47	205
23	Nb_2O_5	2.26	117
24	SiO_2	1.47	205
25	Nb_2O_5	2.26	117
26	SiO_2	1.47	205
27	Nb_2O_5	2.26	117
28	SiO_2	1.47	205
	Air	1	

Table A.3: A3D1 mirror design with refractive indices n @1030nm and physical thicknesses of layers.

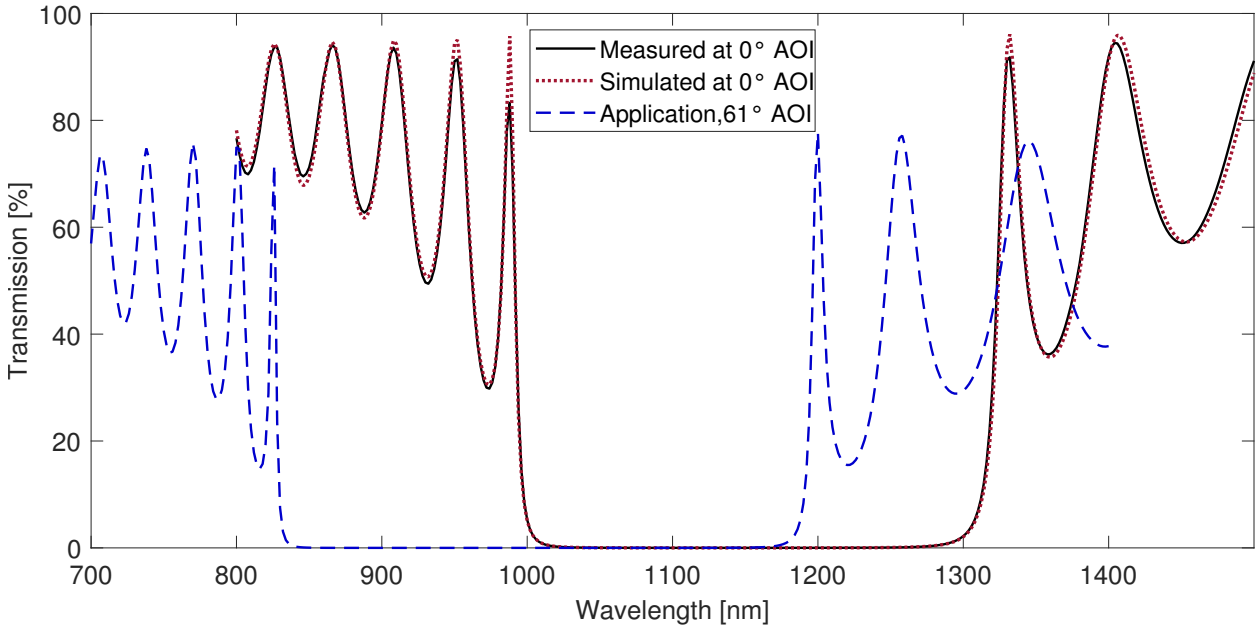

Figure A.3: Transmission spectra of A3D1 mirror measured and simulated at 0° AOI and transmission spectrum for its application conditions (61° AOI, S polarization).

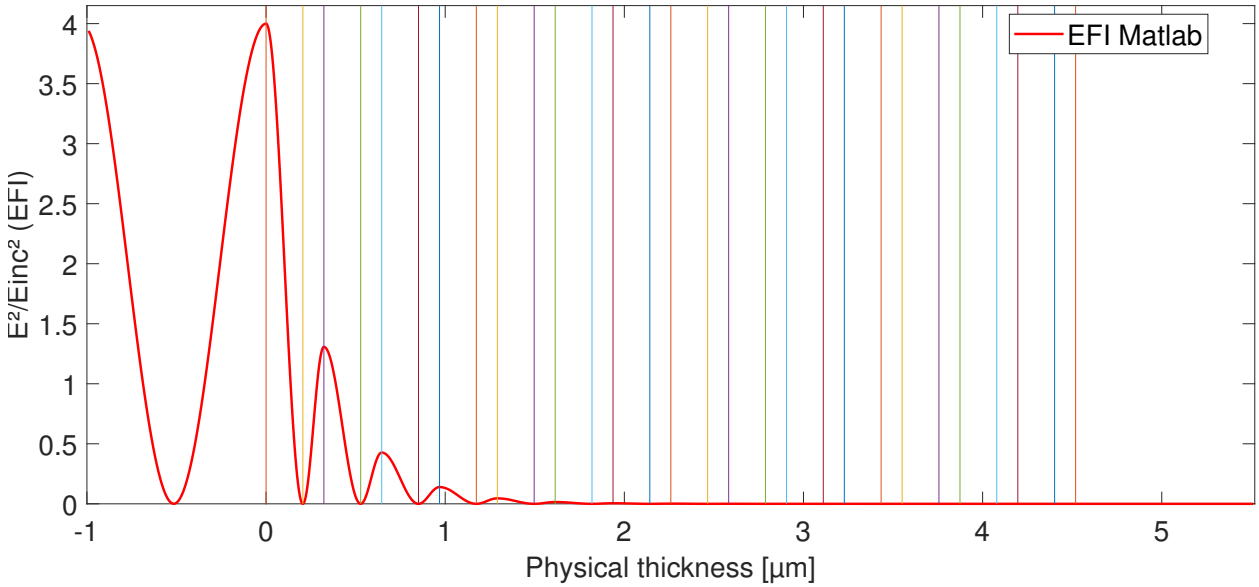

Figure A.4: Electric Field Intensity distribution within A3D1 mirror (61.7° AOI, S polarization, wavelength of 976 nm). The physical thickness 0 corresponds to the interface between air and Nb_2O_5.

A3D3

Layer	Material	n	Thickness
[-]	[-]	[-]	[nm]
0	FS	1.45	
1	Nb_2O_5	2.26	116
2	SiO_2	1.47	198
3	Nb_2O_5	2.26	116
4	SiO_2	1.47	198
5	Nb_2O_5	2.26	116
6	SiO_2	1.47	198
7	Nb_2O_5	2.26	116
8	SiO_2	1.47	198
9	Nb_2O_5	2.26	116
10	SiO_2	1.47	198
11	Nb_2O_5	2.26	116
12	SiO_2	1.47	198
13	Nb_2O_5	2.26	116
14	SiO_2	1.47	198
15	Nb_2O_5	2.26	116

Layer	Material	n	Thickness
[-]	[-]	[-]	[nm]
16	SiO_2	1.47	198
17	Nb_2O_5	2.26	116
18	SiO_2	1.47	198
19	Nb_2O_5	2.26	116
20	SiO_2	1.47	198
21	Nb_2O_5	2.26	116
22	SiO_2	1.47	198
23	Nb_2O_5	2.26	116
24	SiO_2	1.47	198
25	Nb_2O_5	2.26	116
26	SiO_2	1.47	198
27	Nb_2O_5	2.26	116
28	SiO_2	1.47	198
29	Nb_2O_5	2.26	116
	Air	1	

Table A.4: A3D3 mirror design with refractive indices n @1030nm and physical thicknesses of layers.

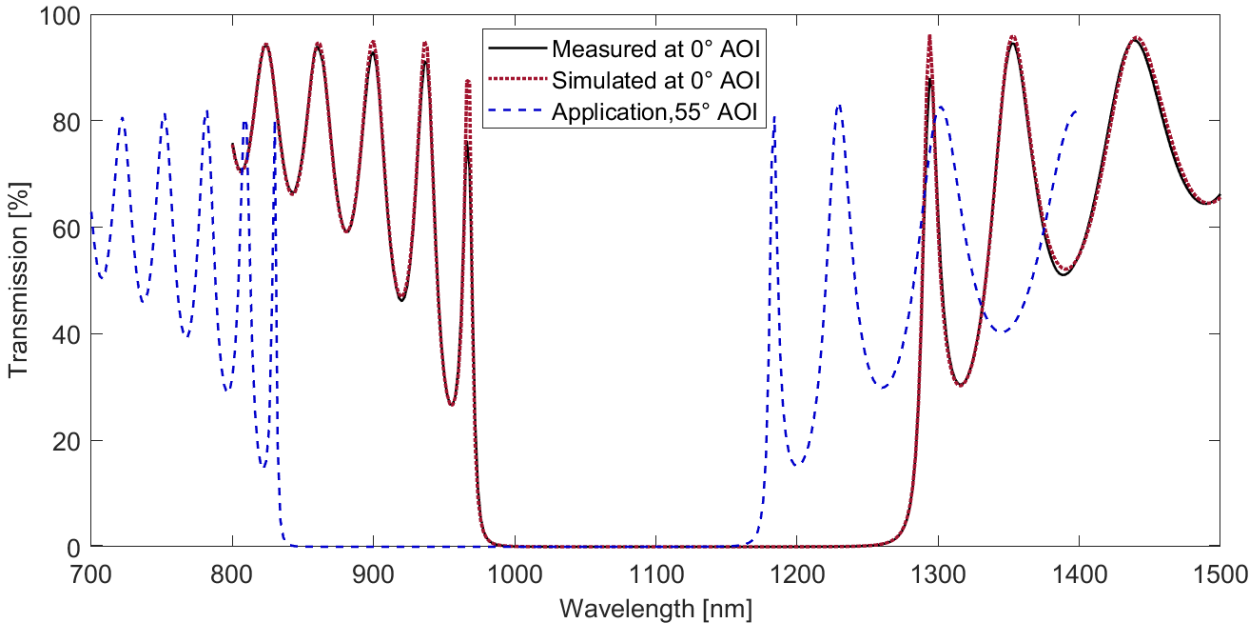

Figure A.5: Transmission spectra of A3D3 mirror measured and simulated at 0° AOI and transmission spectrum for its application conditions (55° AOI, S polarization).

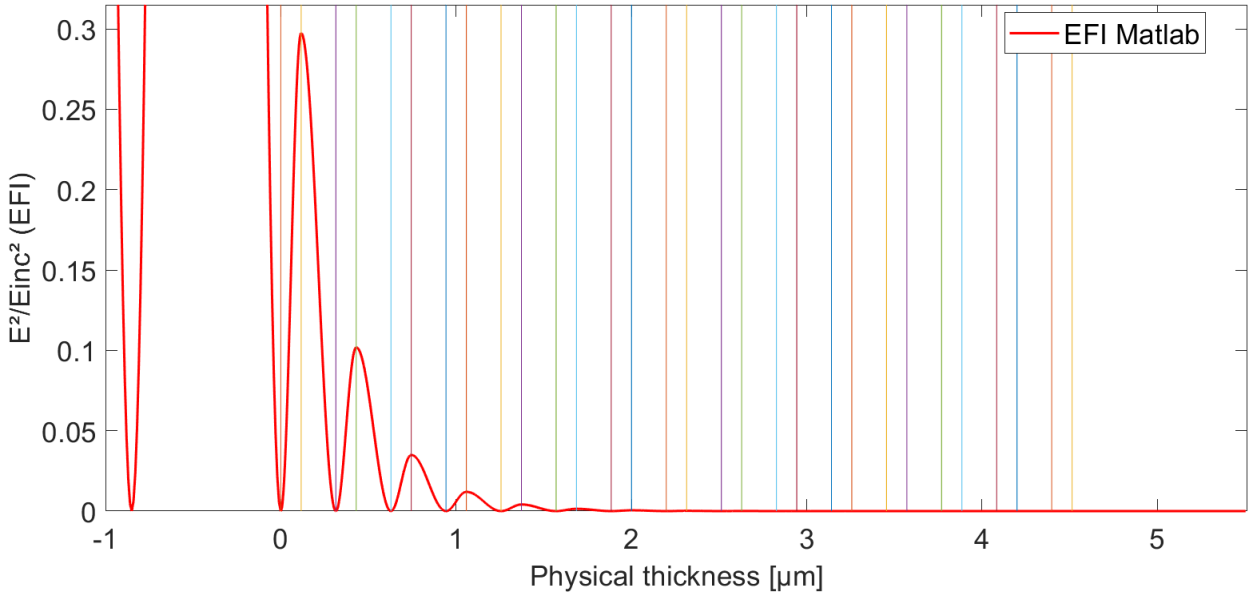

Figure A.6: Electric Field Intensity distribution within A3D3 mirror (55° AOI, S polarization, wavelength of 976 nm). The physical thickness 0 corresponds to the interface between air and Nb_2O_5.

A5D5

Layer	Material	n	Thickness
[-]	[-]	[-]	[nm]
0	FS	1.45	
1	Nb_2O_5	2.26	114
2	SiO_2	1.47	174
3	Nb_2O_5	2.26	114
4	SiO_2	1.47	174
5	Nb_2O_5	2.26	114
6	SiO_2	1.47	174
7	Nb_2O_5	2.26	114
8	SiO_2	1.47	174
9	Nb_2O_5	2.26	114
10	SiO_2	1.47	174
11	Nb_2O_5	2.26	114
12	SiO_2	1.47	174
13	Nb_2O_5	2.26	114
14	SiO_2	1.47	174
15	Nb_2O_5	2.26	114

Layer	Material	n	Thickness
[-]	[-]	[-]	[nm]
16	SiO_2	1.47	174
17	Nb_2O_5	2.26	114
18	SiO_2	1.47	174
19	Nb_2O_5	2.26	114
20	SiO_2	1.47	174
21	Nb_2O_5	2.26	114
22	SiO_2	1.47	174
23	Nb_2O_5	2.26	114
24	SiO_2	1.47	174
25	Nb_2O_5	2.26	114
26	SiO_2	1.47	174
27	Nb_2O_5	2.26	114
28	SiO_2	1.47	174
29	Nb_2O_5	2.26	570
	Air	1	

Table A.5: A5D5 mirror design with refractive indices n @1030nm and physical thicknesses of layers.

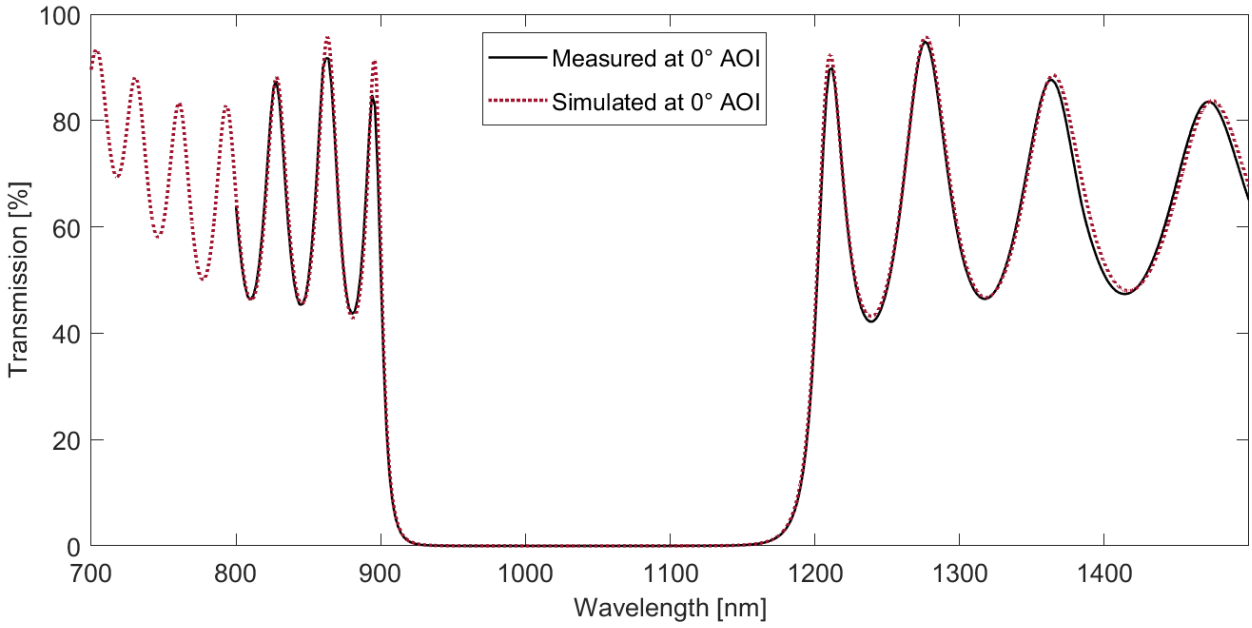

Figure A.7: Transmission spectra of A5D5 mirror measured and simulated at 0° AOI.

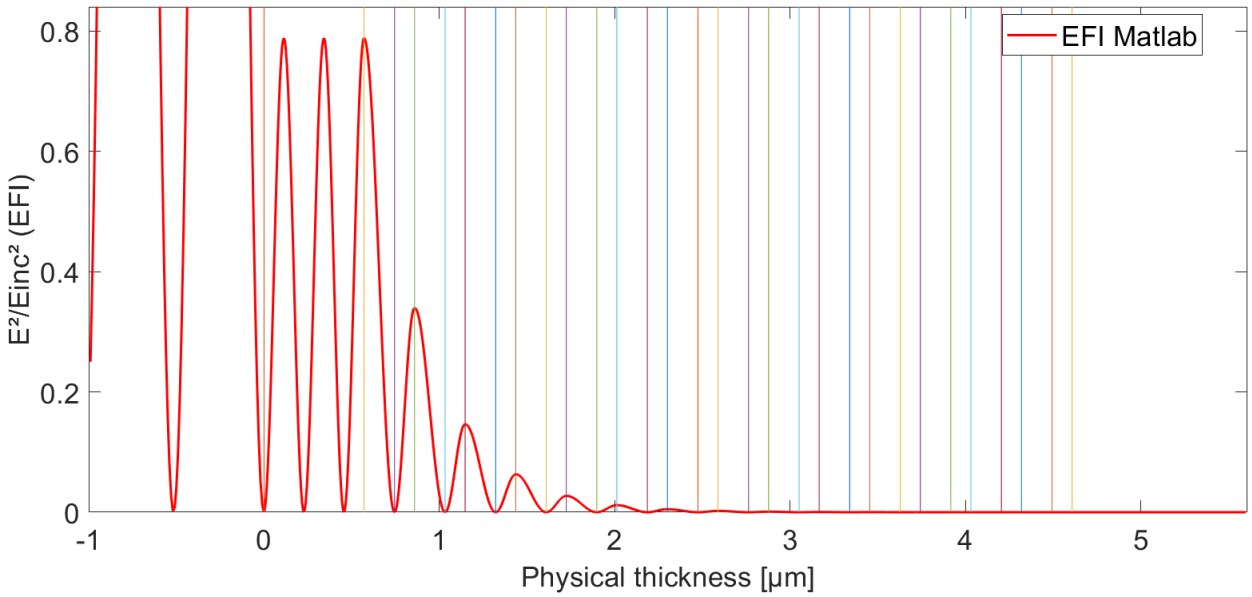

Figure A.8: Electric Field Intensity distribution within A5D5 mirror (0° AOI, wavelength of 1030 nm). The physical thickness 0 corresponds to the interface between air and Nb_2O_5.

CLASm

Layer	Material	n	Thickness
[-]	[-]	[-]	[nm]
0	FS	1.45	
1	Nb_2O_5	2.26	114
2	SiO_2	1.47	174
3	Nb_2O_5	2.26	114
4	SiO_2	1.47	174
5	Nb_2O_5	2.26	114
6	SiO_2	1.47	174
7	Nb_2O_5	2.26	114
8	SiO_2	1.47	174
9	Nb_2O_5	2.26	114
10	SiO_2	1.47	174
11	Nb_2O_5	2.26	114

Layer	Material	n	Thickness
[-]	[-]	[-]	[nm]
12	SiO_2	1.47	174
13	Nb_2O_5	2.26	114
14	SiO_2	1.47	174
15	Nb_2O_5	2.26	114
16	SiO_2	1.47	174
17	Nb_2O_5	2.26	114
18	SiO_2	1.47	174
19	Nb_2O_5	2.26	114
20	SiO_2	1.47	174
21	Nb_2O_5	2.26	114
	Air	1	

Table A.6: CLASm mirror design with refractive indices n @1030nm and physical thicknesses of layers.

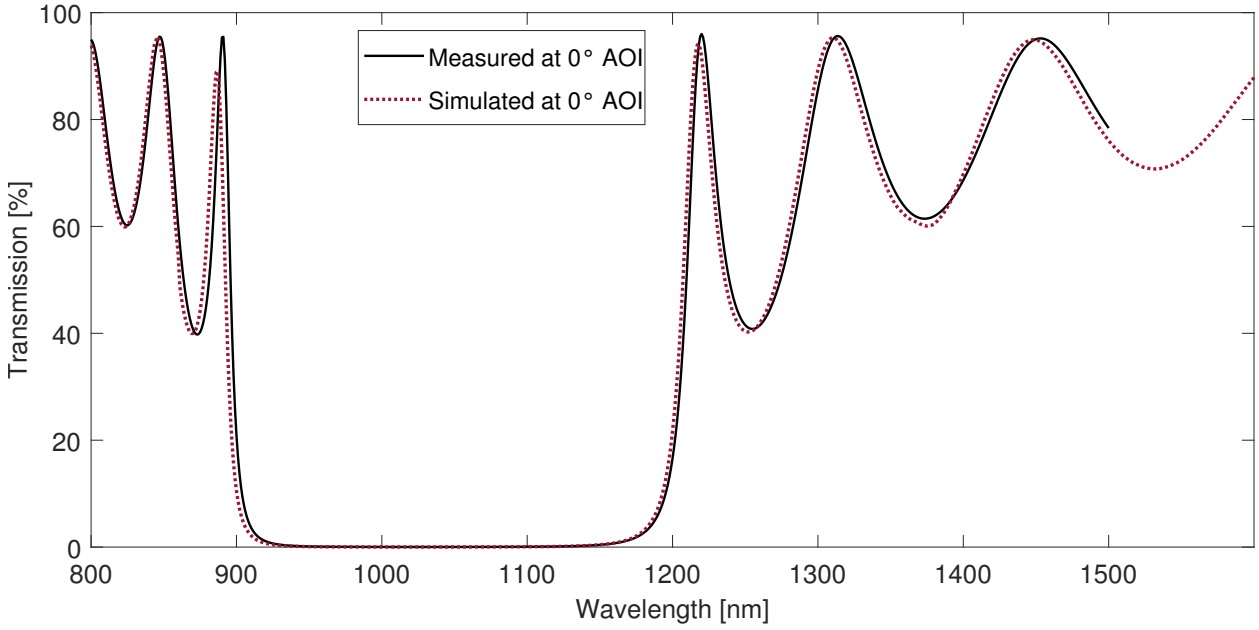

Figure A.9: Transmission spectra of CLASm mirror measured and simulated at 0° AOI.

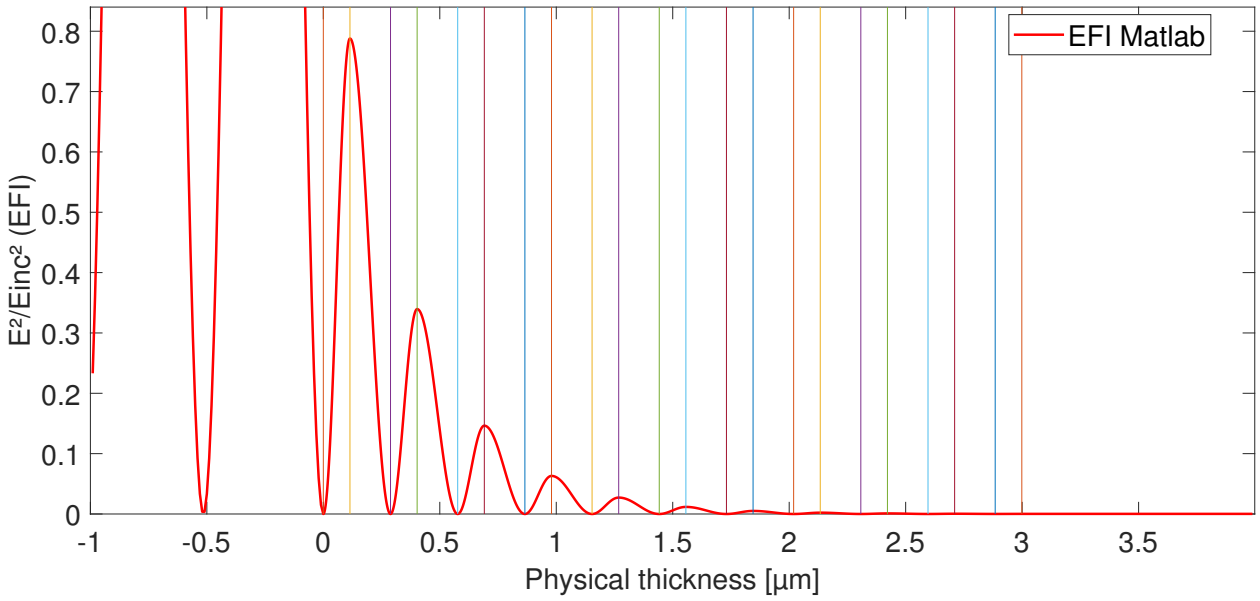

Figure A.10: Electric Field Intensity distribution within CLASm mirror (0° AOI, wavelength of 1030 nm). The physical thickness 0 corresponds to the interface between air and Nb_2O_5.

OPTm

Layer	Material	n	Thickness
[-]	[-]	[-]	[nm]
0	FS	1.45	
1	Nb_2O_5	2.26	114
2	SiO_2	1.47	174
3	Nb_2O_5	2.26	114
4	SiO_2	1.47	174
5	Nb_2O_5	2.26	114
6	SiO_2	1.47	174
7	Nb_2O_5	2.26	114
8	SiO_2	1.47	174
9	Nb_2O_5	2.26	114
10	SiO_2	1.47	174
11	Nb_2O_5	2.26	114
12	SiO_2	1.47	174
13	Nb_2O_5	2.26	114
14	SiO_2	1.47	174

Layer	Material	n	Thickness
[-]	[-]	[-]	[nm]
15	Nb_2O_5	2.26	114
16	SiO_2	1.47	279
17	Nb_2O_5	2.26	57
18	SiO_2	1.47	279
19	Nb_2O_5	2.26	57
20	SiO_2	1.47	279
21	Nb_2O_5	2.26	57
22	SiO_2	1.47	279
23	Nb_2O_5	2.26	57
24	SiO_2	1.47	279
25	Nb_2O_5	2.26	57
26	SiO_2	1.47	279
27	Nb_2O_5	2.26	57
	Air	1	

Table A.7: OPTSm mirror design with refractive indices n @1030nm and physical thicknesses of layers.

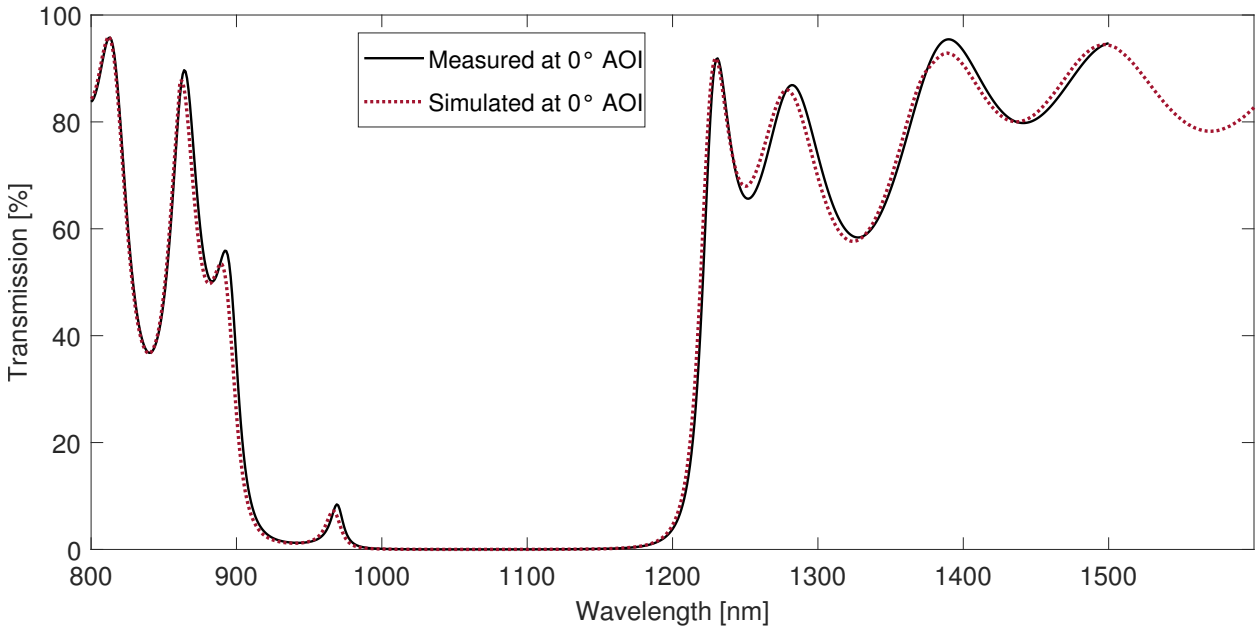

Figure A.11: Transmission spectra of OPTm mirror measured and simulated at 0° AOI.

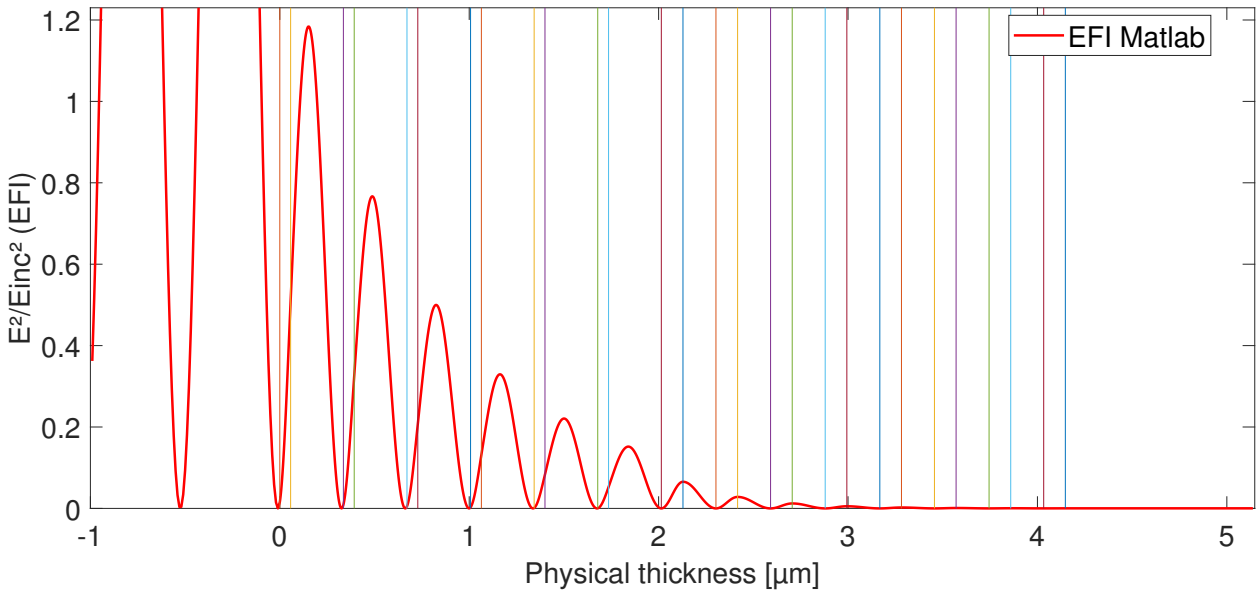

Figure A.12: Electric Field Intensity distribution within OPTm mirror (0° AOI, wavelength of 1030 nm). The physical thickness 0 corresponds to the interface between air and Nb_2O_5.

Appendix B

MATLAB – script calculating Electric Field Intensity on single layer

```
clear all;
close all;
clc;

% Calcul of Electric Field Intensity (EFI) distribution within a monolayer.
E0p = 1; % Electric field amplitude in air.
lambda = 1030; % Laser wavelength in nm.
d = 450; % Monolayer thickness in nm.
Theta0 = 45*pi/180; % AOI Incidence angle.

% Refractive indices at 1030nm.
n0 = 1; % Air at 1030nm.
n1 = 2.26; % 2.261425; % Nb2O5 at 1030nm - measured.
n2 = 1.45; % 1.45; % Fused Silica substrate (SiO2) at 1030nm.

% Angels defined by Snells law.
Theta1 = asin(n0/n1*sin(Theta0));
Theta2 = asin(n1/n2*sin(Theta1));

% Wavelength numbers
k0 = 2*pi*n0*cos(Theta0)/lambda;
k1 = 2*pi*n1*cos(Theta1)/lambda;
k2 = 2*pi*n2*cos(Theta2)/lambda;

%% Polarization S.
% n0_eff = n0*cos(Theta0);
% n1_eff = n1*cos(Theta1);
% n2_eff = n2*cos(Theta2);
```

```
%% Polarization P.
    n0_eff = n0/cos(Theta0);
    n1_eff = n1/cos(Theta1);
    n2_eff = n2/cos(Theta2);

% Reflection and transmission coefficients.
% First interface at z=0.
r01 = (n0_eff - n1_eff)/(n0_eff + n1_eff);
t01 = 2*n0_eff/(n0_eff + n1_eff);
r10 = -r01;  % r10 = (n1_eff - n0_eff)/(n0_eff + n1_eff);
t10 = 2*n1_eff/(n0_eff + n1_eff);
% Second interface at z=d.
r12 = (n1_eff - n2_eff)/(n1_eff + n2_eff);
t12 = 2*n1_eff/(n1_eff + n2_eff);

% Phase difference for one-direction pass.
phi = 2*pi*n1*d*cos(Theta1)/lambda;

% Fresnel coefficients
% The sum of reflected waves from monolayer.
r = r01 + (t10*t01*r12*exp(2i*phi))/(1-r12*r10*exp(2i*phi));

% The sum of transmitted waves through monolayer.
t = t01*t12*exp(1i*phi)/(1-r12*r10*exp(2i*phi));

R = (abs(r))^2;
T = n2_eff./n0_eff*(abs(t))^2;
RpT = R+T;

E0m = r*E0p; % Amplitude of reflected waves.

%% S Polarization - Amplitudes inside monolayer.
% E1m = E0p*(t-(1+r)*exp(1i*k1*d))/(exp(-1i*k1*d)-exp(1i*k1*d));
%% Reflected from 2nd interface.
% E1p = E0p*(1+r) - E1m; % Transmitted through 1st interface.

%% P Polarization - Amplitudes inside monolayer defined using .
E1m = E0p*(t-(1+r)*exp(1i*k1*d))/(exp(-1i*k1*d)-exp(1i*k1*d))*cos(Theta0)/cos(Theta1);
%% Reflected from 2nd interface.
E1p = E0p*(1+r)*cos(Theta0)/cos(Theta1) - E1m; % Transmitted through 1st interface.

z_min = -1*d;
z_max = 2*d;
Niter = 1000;
pas_z = (z_max-z_min)/(Niter-1);
```

```
% S polarization;
% for ii = 1:Niter
%     z(ii) = z_min+pas_z*ii;
%     if z(ii)<=0
%         Es(ii) = E0p*exp(1i*k0*z(ii)) + E0m*exp(-1i*k0*z(ii));
%     elseif z(ii)<d & z(ii)>0    % 0<z(ii)<=d
%         Es(ii) = E1p*exp(1i*k1*z(ii)) + E1m*exp(-1i*k1*z(ii));
%     else
%         Es(ii) = t*E0p*exp(1i*k2*z(ii));
%     end
%     EFI=abs(Es/E0p).^2; % Electric field intensity
% end

% P polarization;
for ii = 1:Niter
    z(ii) = z_min+pas_z*ii;
    if z(ii)<=0
        Epx(ii) = (E0p*exp(1i*k0*z(ii)) + r*E0p*exp(-1i*k0*z(ii)))*cos(Theta0);
        Epz(ii) = (E0p*exp(1i*k0*z(ii)) - r*E0p*exp(-1i*k0*z(ii)))*sin(Theta0);
    elseif z(ii)<d & z(ii)>0  % 0<z(ii)<=d
        Epx(ii) = (E1p*exp(1i*k1*z(ii)) + E1m*exp(-1i*k1*z(ii)))*cos(Theta1);
        Epz(ii) = (E1p*exp(1i*k1*z(ii)) - E1m*exp(-1i*k1*z(ii)))*sin(Theta1);
    else
        Epx(ii) = t*E0p*exp(-1i*k2*d)*exp(1i*k2*z(ii))*cos(Theta0);
        Epz(ii) = Epx(ii)*tan(Theta2);
    end
    EFI=abs(Epx/E0p).^2+abs(Epz/E0p).^2; % Electric field intensity
end

index1 = find(z > 0, 1, 'first'); % Find the first index within layer.
index2 = find(z < d, 1, 'last'); % Find the last index within layer.
EFILayerMax=max(EFI(index1:index2)); % EFI maximum within layer.

figure
plot(z,EFI)
legend('EFI') % At z=0 is air/layer interface;

EFIt=transpose(EFI);
zt=transpose(z);
Tab=table(zt,EFIt);
```